UNIVERSIDADE FEDERAL DO CEARÁ
CENTRO DE CIÊNCIAS
DEPARTAMENTO DE QUÍMICA ORGÂNICA E INORGÂNICA
PROGRAMA DE PÓS-GRADUAÇÃO EM QUÍMICA

RAQUEL DE ANDRADE BESSA

HIERARCHICAL CARTRIDGES BASED ON POROUS MATERIALS DISPERSED ON BACTERIAL CELLULOSE

FORTALEZA
2021

RAQUEL DE ANDRADE BESSA

HIERARCHICAL CARTRIDGES BASED ON POROUS MATERIALS DISPERSED ON BACTERIAL CELLULOSE

PhD thesis presented at Chemistry Graduated Program in Chemistry from Federal University of Ceará, as partial requisition in obtaining the Chemistry PhD title. Concentration Field: Chemistry.

Supervisor: Prof. Dr. Adonay Rodrigues Loiola
Co-Supervisor: Dra. Morsyleide de Freitas Rosa

FORTALEZA
2021

Dados Internacionais de Catalogação na Publicação
Universidade Federal do Ceará
Biblioteca Universitária
Gerada automaticamente pelo módulo Catalog, mediante os dados fornecidos pelo(a) autor(a)

B465h Bessa, Raquel de Andrade.
Hierarchical cartridges based on porous materials dispersed on bacterial cellulose / Raquel de Andrade Bessa. – 2021.
204 f. : il. color.

Tese (doutorado) – Universidade Federal do Ceará, Centro de Ciências, Programa de Pós-Graduação em Química, Fortaleza, 2021.
Orientação: Prof. Dr. Adonay Rodrigues Loiola.
Coorientação: Profa. Dra. Morsyleide de Freitas Rosa.

1. Zeólita. 2. Adsorção. 3. Hierarquização. 4. Celulose bacteriana. I. Título.

CDD 540

RAQUEL DE ANDRADE BESSA

HIERARCHICAL CARTRIDGES BASED ON POROUS MATERIALS DISPERSED ON BACTERIAL CELLULOSE

PhD thesis presented at Chemistry Graduated Program in Chemistry from Federal University of Ceará, as partial requisition in obtaining the Chemistry PhD title. Concentration Field: Chemistry.

Approved in 08/03/2021

EXAMINATORS

Prof. Dr. Adonay Rodrigues Loiola (Supervisor)

Universidade Federal do Ceará (UFC)

Dra. Morsyleide de Freitas Rosa (Co-supervisor)

Embrapa Agroindústria Tropical

Prof. Michael W. Anderson

The University of Manchester

Prof. Dra. Sibele Berenice Castella Pergher

Universidade Federal do Rio Grande do Norte (UFRN)

Dr. Luelc Sousa da Costa

Universidade Estadual de Campinas (Unicamp)

Prof. Dr. Luiz Gonzaga de França Lopes

Universidade Federal do Ceará (UFC)

To God and to my mommy Maria Vilma de Andrade Bessa (*in memoriam*).

ACKNOWLEDGMENTS

I have to start these acknowledgements with the Federal University of Ceará, in particular, the Chemistry Postgraduate Program, thanking them for the infrastructure, support and providing me with the opportunity to pursue my scientific career. To professors Luiz Lopes and Izaura Cirino that were the heads of school during my course, and to their secretaries that were always available to help me regarding all the questions that I had. I hope that they keep this environment of excellence and continue being very important to other future students, as well. To all the professors that I had the opportunity to learn from, both in classes and from their personal experience.

This study was financed in part by the Coordenação de Aperfeiçoamento Pessoal de Nível Superior – Brasil (CAPES) Finance Code 001, in both the national and international studies (Programa de Doutorado Sanduíche no Exterior, Finance Code 001 - 88881.189392/2018-01).

I would like to thank my main Brazilian lab, Laboratório de Materiais Nanoestruturados, especially to my supervisor Prof. Adonay Loiola, with whom I have been working for 10 years now. He helped me to build an ideal in science and in life, thank you for being here in all the great and bad moments, celebrating and holding my hand, teaching me that science is more than writing papers and performing experiments. And to all my co-workers that taught me and helped me even when they thought it was not helpful, for all the great and crazy moments that we lived building a working space together. To all the undergraduate students that helped me in my experiments during this journey.

To my second Brazilian lab at Embrapa, Laboratório de Tecnologia da Biomassa. This was an experience that I was willing to have, for being a well-known research institute, and having so many aspects to be followed, it helped me to develop many soft skills and I also learnt more about something new to my field, as the cellulose. Thus, I thank Dr Morsyleide Rosa for accepting to supervise me during this time, and for being such a great example of how women can be successful in Science and Technology. I am also saying a big thank you to those who helped me a lot during my internship in this lab: André, who was helping me since day 1, and the lab technicians Adriano and Lilian Chayn.

To my UK lab, Centre for Nanoporous Materials, especially to Prof Mike Anderson for supervising me during my 12 months in The University of Manchester, and for showing me a very approachable way of being a researcher and other ways of doing Science. I am also very happy that I was able to share my lab days with Dr Martin Attfield, Adam and all the other

students, as well as Prof Robert Dryfe and his research group that always helped me and treated me as one of theirs.

I would also like to thank all the other members of staff that I met and who helped me with equipment training, performing analyses, building access, etc. In particular, to The Mill (UoM) labs: Prof Stuart Holmes and Maria, and from the NMR centre (UoM). To Dr Maria Fátima from Laboratório de Microbiologia de Alimentos. To Prof Regina Paula and Prof Judith Feitosa from LabPol for the help with freeze-drying and other procedures when we were in need, and to the students that were always available: Venícios and Irisvan. To Prof Marcos Sasaki from Laboratório de Raios-X for all the help with XRD. To Central Analítica-UFC/CT-INFRA/MCTI-SISANO/Pró-Equipamentos CAPES for the SEM, in particular to Prof. Emílio de Castro and the members of staff that gave their best effort to help me during the analyses. To the staff from Central Analítica PGQUIM that are always happy to help us.

To Prof Ronaldo Nascimento and all of my friends in his group, for accepting me as part of their group from the very first day in this University and helping with so many analyses and their support to develop our work. Especially to Mayza, who is my first best friend, who helped me in everything, not only in my scientific career and became my another sister, to Juliene and Fátima, my laughing partners in wine sessions and the ones that have so much in common with me in life outside the lab.

To all the friends that I made outside of the lab during my stay in Manchester, starting with my house buddies Zubier and Yasmin; to all the members of the church community for making the catholic chaplaincy a welcoming environment for all the students in both masses and student dinners, and for teaching me so much about the culture, weather, etc.; and of course, to my brazilian-mancunian Family for making my days happier and easier in so many ways. To all the other friends that this year abroad brought to me by having the same financial program and sometimes, the same problems. Also, to the friends that shared tears and joy in this PhD life. To my friends from the catholic movement (Cursillo) in Fortaleza and the rest of Brazil that always prayed and helped me to be stronger and to keep this journey going.

To my Family for supporting in every step that I took in chemistry so far and all the things that we had together that made this journey possible. And to those that were my family when I needed. To my boyfriend Martin for being so supportive and helpful during this time that we have been together, in a way that I could not have with anyone else, the light in my days.

I am aware that this already became a huge acknowledgements section and I know that I should write down so many more names, but I hope that this shows how I could not have

gone through this journey by myself, scientifically and personally. Also, the complexity of obtaining this title requires many soft skills that I obtained during this time, which are crucial for pushing through all of this but will not be written on any certificate, so I will mention them here. In every semester of this PhD course, I had a big problem to solve, so this inspired my creativity and problem-solving skills; I was reborn in every new beginning that I had to go through (and I had many of them), this shows how I can restart or change projects. I became the mother that my mom needed, and then, that my family did, and this gave me a painful leadership; in the middle of everything happening, I was still able to write the reports, perform experiments, and be the best that I could for my research, and this gives me the ability of project management. For all of this, I must thank myself too for being strong and resilient to keep this journey, and also to God that was always by side, giving me hope for the best at the end of everything.

“Each individual is different and if you can blend that together and synergise their interactions I think that’s the way you get the best results.” (FLANIGEN, E. M.)

RESUMO

O presente trabalho trata da formação de cartuchos hierárquicos por meio de impregnação de Celulose Bacteriana com materiais nanoporosos: argila mesoporosa, zeólitas microporosas A e X, e uma zeólita A multiporosa. Celulose foi produzida com sucesso por organismos *Komagataeibacter* e todos os materiais nanoporosos obtidos por rota hidrotérmica. A influência da oxidação das nano fibrilas de celulose foi estudada, bem como diferentes concentrações para os componentes. Várias técnicas de caracterização como difração de raios-x (DRX), espectroscopia na região do infravermelho com transformada de Fourier (IV), ressonância magnética nuclear do estado sólido (RMN), microscopia eletrônica de varredura (MEV), microscopia eletrônica de transmissão (MET), análises termogravimétricas (TG) e isotermas de adsorção/dessorção N_2 foram empregadas para investigar propriedades, físicas, químicas e texturais das amostras. A cristalinidade para os componentes é mantida em todos os estudos realizados e diferenças são observadas para a amostra com zeólita A multiporosa sugerindo mudanças pela reidratação da estrutura da zeólita quando interage com a estrutura de celulose. Pelos resultados de IV e RMN, é observado o efeito positivo que os grupos carboxilato exercem na interação entre celulose e material nanoporoso. Nas imagens de MEV, as nano fibras são empurradas juntas formando folhas mais bem formadas nos aerogéis oxidados, onde os cristais estão distribuídos. Mesmo que as nano fibras envolvam os cristais na estrutura formada, a porosidade não é prejudicada e para todos os estudos, há melhoramento na estabilidade térmica dos materiais finais. A presença de mesoporos na estrutura zeolítica é ainda mais benéfica e quando são realizados testes de troca iônica com Ca^{2+} e adsorção, melhorias são observadas para os valores de remoção e q_e. A seletividade para Pb^{2+} na presença de Cd^{2+} é aperfeiçoada como resultado de melhor processo de difusão intra-partícula e a partir dos modelos cinéticos, o modelo de pseudo-segunda ordem é melhor ajustado aos dados experimentais sugerindo que a quimissorção é o processo que rege a adsorção. Assim, materiais hierárquicos usando celulose bacteriana, e ainda melhor, apresentando uma estrutura multiporosa conectada, permitem os íons Pb^{2+} moverem-se para o interior dos poros na estrutura zeolítica e apresentam um uso potencial para dispositivos tanto adsortivos como analíticos de Pb^{2+}.

Palavras-chave: zeólita; adsorção; hierarquização; celulose bacteriana.

ABSTRACT

The present work deals about the formation of hierarchical cartridges by means of Bacterial Cellulose impregnation with nanoporous materials: mesoporous clay, microporous zeolites A and X, and a multiporous zeolite A. Cellulose was successfully produced by *Komagataeibacter* organisms and all the nanoporous materials obtained by hydrothermal route. The oxidation influence of the cellulose nanofibrils was studied, as well as different weight concentrations for the components. Several characterization techniques such as X-ray diffraction (XRD), Fourier-transform infrared spectroscopy (FTIR), solid-state nuclear magnetic resonance (NMR), scanning electron microscopy (SEM), transmission electron microscopy (TEM), thermal analyses (TGA), and N_2 adsorption–desorption isotherms were employed to investigate physical, chemical, and textural properties of the samples. The crystallinity for the components is kept in all the studies performed and differences are seen for the sample with multiporous zeolite A suggesting changes due to rehydration of the zeolite structure when interacting with cellulose structure. From the IR and NMR results, it is observed the positive effect that the carboxylate groups play in the interaction between cellulose and nanoporous material. In SEM images, nanofibers are pushed together forming better-assembled laminae in the oxidized aerogels where the crystals are distributed. Even that the nanofibers entangle the crystals in the structure, the porosity is not damaged and for all the studies, there are improvements in the thermal stability for the final materials. The presence of the mesopores in the zeolite structure is even more beneficial and when performing Ca^{2+} ionic exchange and adsorption experiments, improvements are observed to removal and q_e values. The selectivity for Pb^{2+} in presence of Cd^{2+} is enhanced as result from improved intraparticle diffusion and from the kinetic models, the pseudo-second order model fits better to the experimental data suggesting chemisorption as the governing process in adsorption. Thus, hierarchical materials using bacterial cellulose, and even better, having a connected multiporous structure, allow the Pb^{2+} to move into the inner pores on the zeolite structure and present a potential use for either Pb^{2+} adsorptive or analytical devices.

Keywords: zeolite; adsorption; hierarchization; bacterial cellulose.

LIST OF FIGURES

LIST OF TABLES

LIST OF ABBREVIATIONS AND LETTERS

a.u.	Arbritrary unities
BC	Bacterial Cellulose
BET	Brunauer-Emmett-Teller
BJH	Barret-Joyner-Halenda
CCD	Charged coupled device
CEAS	Chemical Engineering and Analytical Sciences
CNPEM	Centro Nacional de Pesquisa em Energia e Materiais
CSDS	Cambridge Structural Database System
CTAB	Cetyltrimethylammonium bromide
DAS	Dynamic Angle Spinning
DI	Deionized
DOR	Double Rotation
DFT	Density Functional theory
EDS	Energy dispersive spectroscopy
EDTA	Ethylenediamine tetraacetic acid
eg	Exempli gratia, meaning “for example.”
FAU	Faujasite
FEG	Field emission gun
FT-IR	Fourier transform infrared
FWHM	Full-width at half maximum
ICDD	International Centre for Diffraction Data
ICSD	International Crystalline Structure Database
i.e.	Id est, meaning “that is.”
IR	Infrared
IUPAC	International Unione of Pure and Applied Chemistry
IZA	International Zeolite Association
LDH	Layered Double Hydroxides
LNNano	Laboratório Nacional de Nanotecnologia
LTA	Linde type A
MAS	Magic angle spinning
MCM	Mobil composition of matter
MOF	Metal organic framework

MQ MAS	Multiple Quantum magic angle spinning
NMR	Nuclear magnetic resonance
PCH	Porous clay heterostructures
PDF	Powder Diffraction File
PVDF	Polyvinylidene fluoride
Rpm	Rotations per minute
RSS	Residual sum of squares
SBA	Santa Barbara amorphous
SEM	Scanning Electron Microscopy
TEM	Transmission Electron Microscopy
TEMPO	2,2,6,6-tetramethylpiperidine-1-oxyl
TGA	Thermogravimetric analyses
TPHAC	3[(trimethoxysilyl)propyl]hexadecyldimethylammonium chloride
TPOAC	3[(trimethoxysilyl)propyl]octadecyldimethylammonium chloride
VOC	Volatile Organic Compound
WD	Working distance
XRD	X-ray diffraction
ZSM-5	Zeolite Socony Mobil–5

CONTENTS

1 INTRODUCTION

Industrial and technological development can be accompanied by the generation of toxic residues with potential to cause several dysfunctions in the human body as toxic metals or VOC's.[1-3] Among the most concerning compounds, the environmental regulations for toxic metals are becoming stricter, demanding the development of new methods and materials for their effective removal from industrial effluents. There are several methods currently available for wastewater treatment, including chemical precipitation, ion exchange, adsorption, membrane filtration and electrochemical treatment technologies.[4; 5]

Adsorption, which has become one of the leading techniques in wastewater treatment, relies strongly on the adsorbent properties, so its correct choice is paramount.[6] Several materials can be used for this purpose as biossorbents, activated carbon,[7; 8] MOF's,[9] zeolites[10] and graphene oxide[11]. However, usually some limitations can be faced in their applications due to high costs or regeneration.

Zeolites were firstly identified in 1756 and since then, around 250 structures have been discovered. According to the definition proposed by the International Zeolite Association (IZA), they are defined as any silica-based crystalline microporous solid in which some of the silicon atoms are replaced by other elements T (either trivalent or tetravalent).[12; 13] Their unique structures grant them remarkable properties such as crystallinity, uniform microporosity, high surface area, and high acidity, which make them widely used in catalysis and adsorption.[14] In 1991, Davis reported the main industrial use for zeolites as detergent builders, especially for zeolites with low Si/Al that are able to exchange M^{+} ions with Ca^{2+} coming from hard water.[15] Liang *et al*., 2017 reported that most part of commercial processes in petroleum refining and petrochemical industries use zeolite-based catalysts, especially for epoxidation, condensation, acylation, and amination processes. When the zeolites are deactivated, they can be easily reactivated by combustion, pyrolysis or other thermal treatments.[16]

Some applications although, require larger pores and the mesoporous materials with ordered structure show up as efficient in such cases. The first materials with such characteristics were reported in 1992 by Mobil Co.[17] In their approach, ionic surfactants are used with inorganic ions forming the mesopores. When used with clays, it may give rise to a similar structure called Porous Clay Heterostructures (PCH) as reported by Galarneau *et al*., 1995.[18]

However, in both cases, such properties can be hindered by mass transference issues when accessing the inner sites, or by difficulties in their recovery at the end of their use. The presence of larger pores in hierarchical structures can overcome these issues enhancing

transport and diffusion properties. In adsorption processes, usually the hierarchical materials present higher adsorption performance, improved access to the active sites and selectivity, as well as better reuse. Among a wide range of materials with some kind of hierarchy, zeolites stand out compared to other adsorbents and materials.[19; 20]

Their properties as ionic exchange and adsorption ability, as well as their relatively low costs, are responsible for this.[21; 22] In order to obtain hierarchical zeolites, their inherent micropores should be interconnected to the other pore systems with different and complementary roles from each other in the system.[23; 24] This can be achieved using different routes like the post-synthesis modification, the use of soft-templates on the starting gel, and the formation of composites with a macro/mesoporous material. The combination of more than one strategy can commonly give rise to macroporous monoliths with a specific shape and functional surface formed by the zeolite covering.[25; 26]

Cellulose is a potential candidate in the composite approach, being used in other types of hierarchical materials.[27-30] In addition, zeolites and cellulose composites can be produced and used in different applications.[31-33] Among the sources of cellulose nanofibres, certain bacteria strain can be highlighted since they excrete this polymer with the same chemical structure as the vegetal cellulose, but with higher purity, i.e., without other components usually hard to remove, and with a crystalline nanofibrillar structure, as well as adjustable chemical and physical properties.[34-36]

In this work, hierarchical cartridges are proposed using bacterial cellulose (BC) nanofibrils as supports for the preparation of a novel aerogel-like cartridge in combination with different nanoporous materials and the application of one of them for Pb^{2+} adsorption.

2 AIMS

2.1 General

To obtain a novel aerogel-like cartridge to be used in Pb^{2+} adsorption by combination of bacterial cellulose nanofibrils and a nanoporous material.

2.2 Specific

- To synthesize hierarchical cartridges formed by bacterial cellulose nanofibrils and different nanoporous materials;
- To characterize the formed materials by different techniques;
- To evaluate the interaction between BC and the nanoporous materials;
- To investigate the oxidation for cellulose in the cartridges' formation;
- To evaluate the weight composition for the cartridges;
- To measure the ionic exchange capacity for Ca^{2+} to some of the cartridges formed with zeolites A both micro and multiporous and zeolite X;
- To compare the performance for cartridges with zeolite A in both microporous and multiporous forms as Pb^{2+} adsorbents;
- To identify the adsorption process for the hierarchical cartridge using selectivity for Pb^{2+} and Cd^{2+} multicomponent system, and kinetic tests for Pb^{2+}.

3 THEORETICAL BACKGROUND

The background for materials used in this work, namely zeolites and mesoporous materials, cellulose, and composites and aerogels, as well as the structure hierarchization, is presented in this section. The adsorption process and the techniques applied for the characterization are also described in the following sections. This aims to present the main properties and characteristics for the materials and the information that can be expected from them when the characterizations are used.

3.1 Materials

3.1.1 Zeolites and Mesoporous Materials

Zeolites are a class of microporous materials with structure formed by molecular channels and cavities. Initially, the term zeolite was related only to microporous aluminosilicates, nevertheless, nowadays it encompasses any silica-based microporous crystalline solid where some of the Si atoms are substituted for other T elements that can be tri or tetravalent. The resulting tridimensional structure is formed by TO_4 (T = Si, Al, P, Ge, Ga, etc.) tetrahedra linked by shared oxygen atoms.[12; 13]

This way, their basic building units are formed by the TO_4 tetrahedra, the primary units. Secondary units are formed from the linkage of such units forming non-chiral polyhedra with edges, corners, and faces in common. The basic units are characteristic of each topology. They are identified by a lowercase 3-letter code in italic (excepting for the double rings with 4, 6 and 8 members). Figure 1 presents the formation of some structures changing one of the building units. Observe that when a drawing is presented, only the T atoms are shown in edges and the T–O–T bridges are the straight lines.[37; 38]

The building units also form cages and cavities that give rise to one of the main properties for zeolites. In Figure 1, the sodalite cage is connected to one of the double-rings to produce each structure. For example, on the left side, the coupling of sodalite cage and the d4r ring frames the LTA structure, whilst on the right side, the coupling of the same sodalite cage with d6r rings creates the Faujasite structure. The cavities are not presented in the image. The International Zeolite Association suggests that each zeolitic structure should be represented by a 3-caption letter code that does not include numbers or other types of characters.[38] The types

of structures do not depend on the composition, atoms distribution, unit cell dimensions or symmetry.[37]

Figure 1 - Secondary building units forming different zeolite structures: LTA and FAU

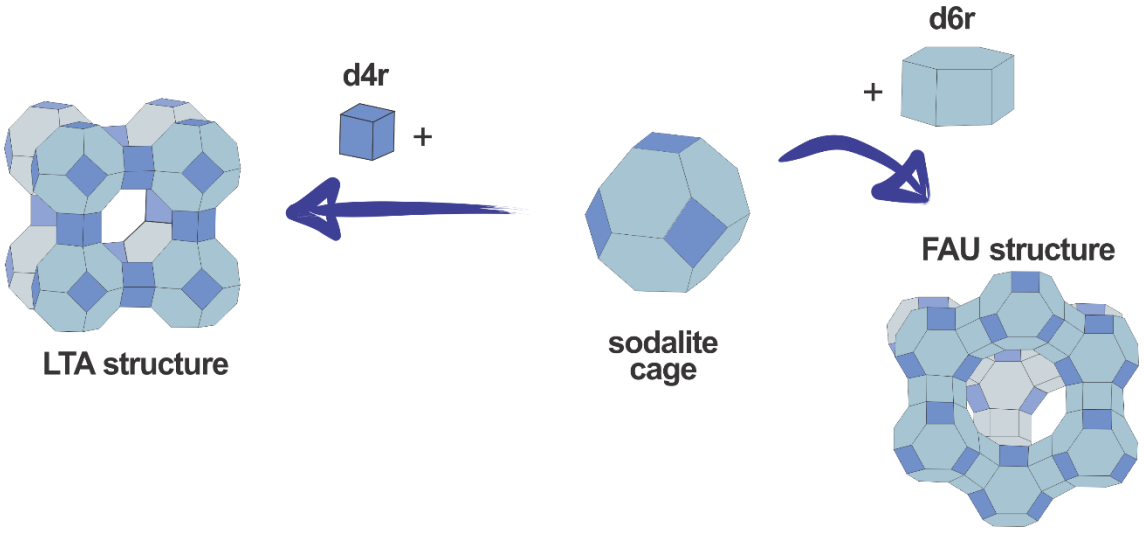

Source: Author (2021).

Today, 250 framework structures are known[39] and there is a broad range of applications that they can be used, as consequence of specific chemical composition, as well as unique pore system. This way, the search for new structures is always explored with new synthesis strategies to tune the final properties on the products.[40]

Usually, they are obtained by hydrothermal crystallization of a gel. The reaction medium should contain the structural atoms (depending on the product desired, the silica source can be crucial; other zeolites can also be used involving a dissolution-recrystallization process), solvents (by dilution of some synthesis gels, different zeolitic phases can be formed), templates or structure directing agents and mineralizers. The synthesis conditions vary from a few hours until several days, in basic medium (mainly), and temperatures below 200 °C in low autogenous pressure.[12; 40]

From their unique structure, some properties can be observed such as high hydration degree, low density due to the large voids volume when dehydrated, thermal and chemical stability, ionic exchange depending on the number and nature of cationic sites and their accessibility, electrical conductivity, adsorption capacity depending on the pore aperture and void volume, shape selectivity and catalytic capacity.[13; 41]

When the zeolites possess high cation exchange capacity, they are mainly used as ion exchangers and adsorbents. In catalytic applications, a more siliceous framework is required with cationic protons residing at well-separated exchange sites. In addition to that, their

molecular structure can lead to shape and/or size selective conversions imposing steric constrains to the adsorbed molecules. Significant efforts has been taken to use such materials in emerging areas as sensors and membranes.[41]

Even though, the microporosity limited the use of zeolites in adsorptive and catalytic processes with smaller molecules. In the 1990's, a new class of materials enhanced the range of molecules and applications for porous materials.[42] Mesoporous molecular sieves were first reported by Mobil Oil Co with M41S family in 1992,[17] and in 1998, the Santa Barbara Amorphous family, SBA.[43] MCM-41 and SBA-16 are the most published materials nowadays and they are similar to each other, since both of them present mesopores ordered hexagonally, but the latter has interconnectivity among the pores with micropores over the silica walls, achieved by the use of co-polymers.[44]

In many applications that the mesoporous materials can be used, some clays are presented as a low-cost alternative material as well as raw materials in many syntheses.[45-47] From 1930, their study becomes more evident in such field and their modification is suggested by some different ways getting with more well-defined approaches as observed for the Tubular Silicate Layered-Silicate, Folder Sheet Mechanism 16 and PCH's.[44; 48; 49]

Clays can be defined as naturally occurring or synthetic materials fine grained with some plasticity and hardening by drying or firing. Other properties are commonly observed like layered structure, anisotropy of the layers or particles and possibility of surface modification.[50] Some common modifications to produce enhanced porosity can use moderate acid leaching; intercalation of organic molecules, where alkylammonium salts or organic compounds can be easily inserted in the interlayer voids; pillared clays, with metallic oxides are inserted as pillars between the layers; and as PCH's, when the natural cations for the clay are changed by cationic surfactants, following with a silica source being added to produce combined mesoporosity.[48]

Figure 2 presents two structures for mesoporous materials (MCM-41 and PCH) that can be formed using surfactants by different synthetic routes. In both cases, the surfactant acts as a structure directing agent: in the first approach, the surfactant molecules are assembled in micelles, due to their amphiphilic property. Those micelles can be spherical or cylindrical, assuming hexagonal or cubic arrays, for example. The inorganic precursor is some silica source that becomes the building units for the walls of the mesoporous material. For PCH's formation, other molecules can be used as surfactants and co-surfactants (usually a neuter amine), and it also has the ability of compensation for negative charges in the clay's lamellae. The silica source is used as pillarizing agent to form the porous structure in the clay minerals.[44; 48]

Figure 2 - Mesoporous structures formed by different synthetic routes using surfactants

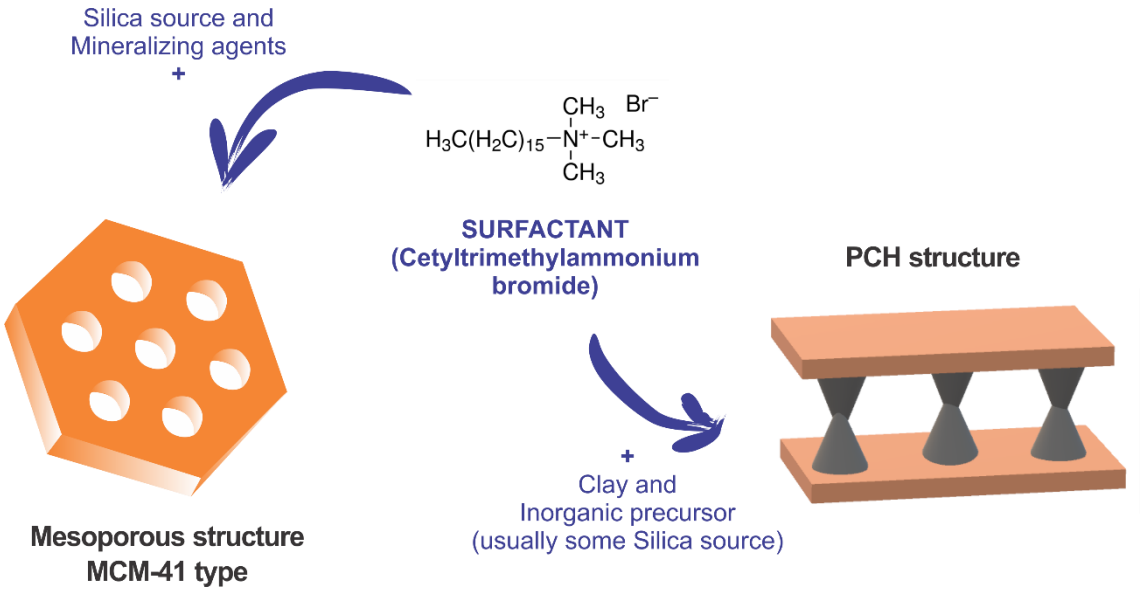

Source: Author (2021).

3.1.2 Cellulose

Cellulose is the most abundant polymer in Earth and its major source is the vegetal cellulose. The chemical formula is $(C_6H_{10}O_5)_n$ and it is formed by non-branched linear chains of β-D-glucose connected by β(1-4) bonds forming the cellobiose unity. For having surface hydroxyl groups in abundance, properties as hydrophilicity and biodegradability are found, as well as the chemical modification possibility.[51; 52 36]

The cellulose can be found in different crystalline forms (I, II, III and IV) where cellulose I is its natural form, with Iα structure triclinic and the dominate polymorph for most algae and bacteria, whilst the monoclinic structure, Iβ, is dominant for higher plant cell wall and tunicates. Both are coexistent in various proportions depending on the cellulose source. This impacts on the hydrogen bonds between the planes and Iα presents lower thermal stability.[51]

The vegetal cellulose is usually together to lignin and hemicellulose and therefore, further purification is required before it can be used for practical applications.[53] A wide range of microorganisms can synthesize much pure cellulose.[54-57] Among them, several bacterium genus, as *Achromobacter*, *Acrobacter*, *Agrobacterium Pseudomonas*, *Rizobium*, *Sarcina*, *Alcaligenes*, *Zoogloea* and *Komagataeibacter*. The latter is well-known for being a "super productor" organism since it is able to produce high amounts of cellulose in organized way without any pathogenic characteristics.[34]

It can be extracted from fruits, flowers, food and drinks.[58-62] Also known as *Acetobacter* or *Gluconacetobacter*, they are strictly aerobic bacteria, gram-negatives, in stick form, that oxidize sugars or ethanol during the process.[34; 63] It is reported that they produce cellulose as protection from UV radiation and aggressive chemical environments or even to improve the nutrients transportation.[36; 64] There is a growing limit for the pellicles to be formed, when all the bacteria are imprisoned and thus, inactivating it for the insufficient oxygen supply.[52]

It possesses a unique tridimensional nanostructure formed by a cellulose network with fibres considerably lower than the vegetal ones with high purity, crystallinity, and mechanical strength. In addition to that, there is also high water retention.[34]

Usually, the BC production includes two main steps for the pellicles to be obtained: cellular growing and culture. The main factors affecting their morphology, composition and properties are the culture medium used, reactor design (statically reactor, for example, results in higher amounts)[35; 53], temperature, oxygen availability, pH and additives.[64] The nutrients can

be substituted by industrial residues lowering the costs without damaging considerably the productivity and yield.[65-69]

One of the most known biochemical pathways for cellulose production involves the glucose conversion to cellulose, in steps with the intermediates: glucose 6-phosphate (G6P), glucose 1-phosphate (G1P) and uridine diphosphate glucose (UDP-glucose), and controlled by specific enzymes.[34] Equations (1) to (4) below represent the main steps in this process:

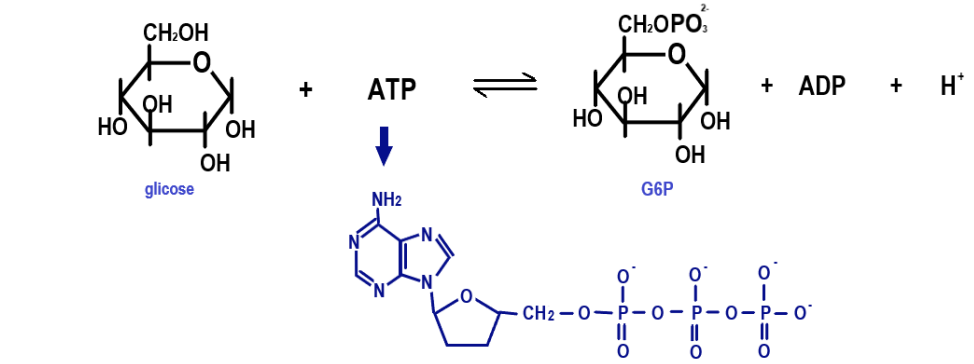

(1)

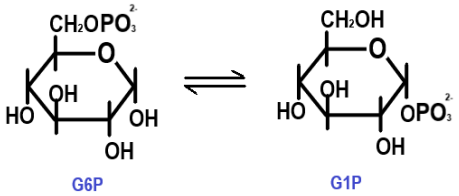

(2)

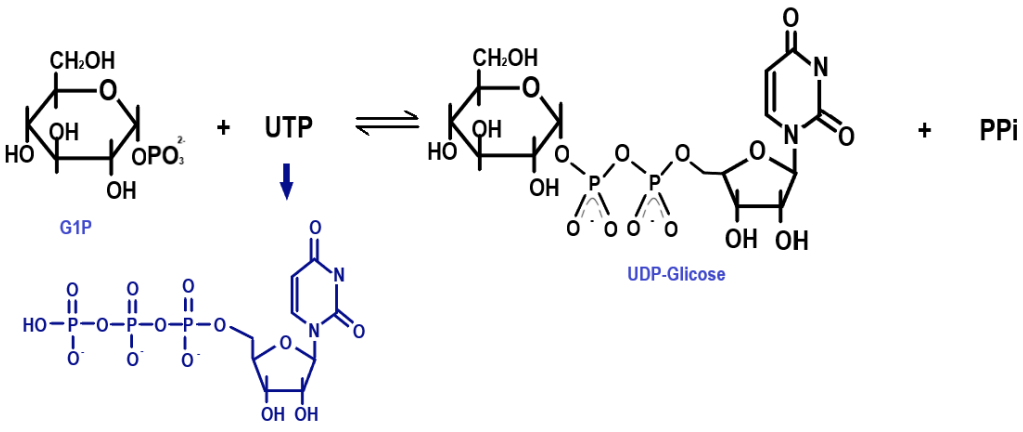

(3)

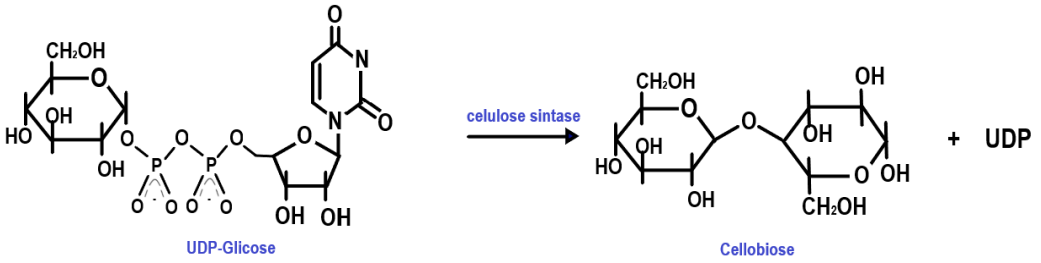

(4)

Initially (1), there is the phosphorylation of glucose to G6P by glucokinase enzyme converting a molecule of Adenosine triphosphate (ATP) to Adenosine diphosphate (ADP). Following to it (2), the G6P molecule is converted to G1P through the phosphoglucomutase enzyme. Then (3), G1P is isomerized in a reaction with uridine triphosphate (UTP) catalysed by the UDP-glucose pyrophosphorylase enzyme releasing a pyrophosphate (PPi) and getting the UDP-glucose, which is the cellulose precursor. Finally (4), the cellulose synthase (a complex enzyme in the bacterium membrane) polymerizes the cellobiose units in cellulose fibrils.

In the cellular wall for the bacterium, each pore produces a cellulose chain and they join in groups of 10-15 forming a nanofiber, organized with others in a way that fibrillar ribbons with around 50-80 nm diameter are formed.[64] The presence of strong interactions, both intra and intermolecular, among the hydroxyl groups of the formed products, bacterial cellulose is highly self-assembled.[36; 63]

From the final properties observed to Bacterial cellulose pellicles, several applications are possible. In the last decades, a wide range of applications has been studied, and due to its biocompatibility, the biomedical ones are extensively reported, including the use as biomaterial for artificial skin, artificial blood vessels and microvessels, wound dressing of burn ulcers, and dental implants.[63; 70]

It can also present improvements to purification processes from the mechanical strength, good chemical stability, ultrafine nanofibrillar network and high surface area that are closely related to adsorption efficiency.[70-72] Moreover, it can be used as a support for nanoparticles used in either adsorptive[73-75] or catalytic applications.[76; 77]

In addition to those, BC can also be used in electrical, optical, and magnetic materials. A good example of this use is the lithium-ion batteries where it can be used as separator, with adequate porosity and desirable affinity with the liquid electrolyte and lithium electrode becoming a high-performance separator for this purpose.[78; 79] Thus, bacterial cellulose based materials are becoming more popular in several scientific areas and are promising in the development of new or improved products.

3.1.3 Hierarchization

In nature, living organisms found in hierarchy an important characteristic to allow their evolution over the years. This can be noticed as organizational features in a community, fluid and response distribution or porous systems. In materials sciences, a bright future is expected with those attributes and several issues can be overcome, since this design can be used from molecular until macroscopic dimensions with high control and accuracy.

Hierarchy is a Greek word that was initially used to describe sanctification rankings in churches and nowadays remain with this organizational aspect, being used in natural, ecological, social, and even technical systems. Porous materials can be benefited with the improvement of chemical properties as well as mass transport.[26; 80] Table 1 shows some of the applications that can be benefited with the progress in hierarchy for sciences, that range from energy conversion and storage to fine biomedicine.

It is important to notice that different materials are widely used, particularly hierarchically porous carbons and metal oxides. Most of the improvements observed in the applications presented in the table are related to the presence of bigger pores enhancing properties like transport and diffusion of the main compounds. It can also be observed in almost all the applications the presence of materials with a defined shape, films or monoliths which is a characteristic highly desired to practical production.[19]

Table 1 - Main improvements in applications using hierarchical materials.

Application	**Improvements**	**Hierarchical materials**
Energy conversion		
Dye sensitized solar cells	- Dyes can be loaded inside the materials; - Macrochannels play a role as light harvesters, allowing deep penetration of light adsorption, resulting in high power conversion efficiency;	- TiO_2, ZnO and the composites based on them;
Photocatalytic hydrogen production	- Enhanced separation and transfer of photo-generated electrons and holes, improving its photo-electrochemical properties and H_2 evolution rate;	- Beta zeolite with CdS and Pt nanoparticles highly dispersed in the mesopores; - Bionanocomposite foam of $Zn_xCd_{1-x}S$ organized into the hierarchical architecture of bacterial cellulose;
Fuel cells	- Interconnected hierarchical macro-nanoporosity are essential on both the electrodes to allow a better dispersion for the active catalyst and facilitate diffusion due to the open network around the active catalysts;	- Porous carbon/graphene as support to the catalysts;
Energy storage		
Supercapacitors	- Enhancement of pseudocapacitive properties due to fast ion/electron transfer; - Structural degradation alleviation caused by volume expansion during the cycling process;	- Carbon- and/or graphene-based hierarchically porous structures;
Lithium ion batteries	- Good access of the electrolyte to the electrode surface; - Shortening the Li^+ insertion/extraction pathway; - Facilitating charge across the electrode/electrolyte interface;	- Carbon; - Graphene; - Metal oxides; - Polyanion compounds; - Porous Si and Ge;
Lithium Sulfur batteries	- Improving both rate and capacity retention performance of the electrode;	- Pore-structured carbon pillars; - Carbon monoliths;

Application	Improvements	Hierarchical materials
	- Alleviation of volume expansion; - Utilization efficiency of sulfur in the cathode;	- Multi-walled carbon nanotubes@mesoporous carbon; - Porous hollow carbon nano-onions; - 3-D free standing graphene-based porous carbon film;
Lithium air batteries	- Facilitation of electrolyte permeation and oxygen diffusion; - Providing sites to accommodate Li_2O_2 deposition;	- Nitrogen-doped micron-sized honeycomb-like porous carbon; - Carbon; - 3D interconnected macro-mesoporous air electrodes with functionalized graphene sheets; - Highly crystalline α-MnO_2 with hierarchical bimodal porous structure; - Free-standing porous carbon derived from graphene oxide gel in nickel foam; - MnO_2/hierarchically porous carbon nanocomposite;
Sodium Ion batteries	- Good access of the electrolyte to the electrode surface; - Shortening the Na^+ insertion/extraction pathway; - Facilitating charge across the electrode/electrolyte interface;	- Carbon; - Sandwich-like hierarchically porous carbon/graphene composite; - Hollow V_2O_5 nanospheres with exposed facets; - Porous $Li_4Ti_5O_{12}$ microspheres; - 3D porous $Na_3V_2(PO_4)_3$/C electrode; - 3D porous $NaTi_2(PO_4)_3$/C structure;
Photocatalysis and catalysis		
Photocatalysis	- Improvement on adsorption efficiency by light harvesting and light scattering effect in macropores; - High hydroxyl group concentration;	- Titanium oxide-based porous structures; - Other metal oxide-based porous structures (Cerium, Zinc and Iron);

Application	Improvements	Hierarchical materials
Catalysis Adsorption and separation	- Improved catalytic activity due to the special structure and morphology; - Good Chemical stability; - Excellent thermal stability; - Enhancement on diffusion through hierarchically porous structure; - Improved accessibility and matter transport;	- Polymer semiconductor-based porous structures; - Silicon-based porous structures; - Metal-based porous structures; - Metal oxide-based porous structures; - Noble metals loaded/doped on metal oxide-based porous structures; - Zeolite-based porous structures; - Metals loaded on hierarchically structured porous supports;
Adsorption of water-soluble pollutants	- Enhanced adsorption performance compared with single-sized porous materials due to their improved accessibility and high surface area;	- Carbon materials; - Metal oxides or bimetal oxides; - Hybrid materials as SiC fibers, Si-C-N, metal-organic frameworks and layered double hydroxide; - Porous Iron oxide superstructures;
Adsorption of heavy metals and metal ions	- Rapid diffusion and transportation of guest molecules; - Promote access to the active sites;	- Metal oxides; - Metal phosphonates; - Porous silicas with binding groups; - Carbon spheres; - LDH;
Adsorption of air pollutants: VOC and special organic molecules	- Higher adsorption capacity; - adsorption-desorption rate constants are higher than the plain materials; - High selectivity to toxic VOCs; - Reuse;	- Ceramic monoliths coated with silicalite-1 nanoparticles; - Porous polymers; - Aerogels; - Carbon-based hybrid adsorbent; - Superabsorbent hierarchically porous sponges from cellulose; - Macro-mesoporous carbon monoliths;

Application	Improvements	Hierarchical materials
CO_2 capture	- Improved mass transport by the macropores; - High surface area and pore volume;	- Porous PVDF/nano-SiC foams; - Hydrophobic monolithic porous silica; - Carbon monoliths; - Zeolites; - Porous organic polymers; - N-doped carbon microflowers;
Separation	- Faster separation rate at much lower backpressure;	- Macro-mesoporous monolithic silica materials; - Silica spheres; - Metal oxide-based columns;
Sensing	- Facilitates gas diffusion and mass transport; - Improves the sensitivity and response time of the gas sensor;	- Metal oxide semiconductors, specially ZnO; - Other metal/bimetal oxide-based semiconductors; - Graphene-based porous structures; - Ionic liquids; - Zeolitic based materials; - Porous SiO_2 films;
Biomedicine		
Bone tissue engineering	- Improved bioactive behaviour; - Porosity in the range required for implants;	- Bioactive ceramics; - Calcium phosphate-based scaffolds; - Titanium scaffold-based porous structures; - Biodegradable polymer-based porous structures;
Drug delivery systems	- Facilitate drug molecules to diffuse and transport through the pores;	- Nanoporous silica film; - Microparticles of metal oxides; - 3D aluminosiloxane hybrid gel network;
Enzyme immobilization	- High enzyme leadings; - Quick enzyme immobilization rates; - Tunable pore sizes according to the enzymes' diameter.	- Mussel-inspired polydopamine microcapsules with different wall structures; - ZnO-CaO-SiO_2-P_2O_5 bioactive nanostructures;

Application	Improvements	Hierarchical materials
		- Meso-macroporous-giant-porous bioactive glass/poly-ε-caprolactone composite scaffolds; - Diatom-derived carbon and gold-bearing replica microparticles; - LDH/Al_2O_3 composites; - Porous chitosan-PEG-SiO_2 biohybrid; - MgO templated porous carbon; - Porous $NaCoPO_4$-Co_3O_4 hollow microspheres.

Source: adapted from Sun *et al.*, 2016.[19]

In some of the applications presented in the Table 1, zeolites can be used, and due to their intrinsic microporosity, the growing interest for such materials is increasing over the years, as presented in Figure 3. Also, in some of the previous examples, only the zeolites are the main materials used in industry. For zeolites to be considered as hierarchically porous materials, they must present not only the micropores in zeolitic structure, but also other pores interconnected. The expression, although, is usually employed in a broad sense, where just having a secondary porosity is considered as a hierarchical material. Another aspect that should be observed when defining a material in hierarchical group is related to its role, in order to be different and complementary.[23; 24; 26]

Figure 3 - Graphs with publications distributed in 20 years for "Hierarchical" and "pores" presented in red; the ones with the terms “hierarchical” and "zeolite" are presented in blue

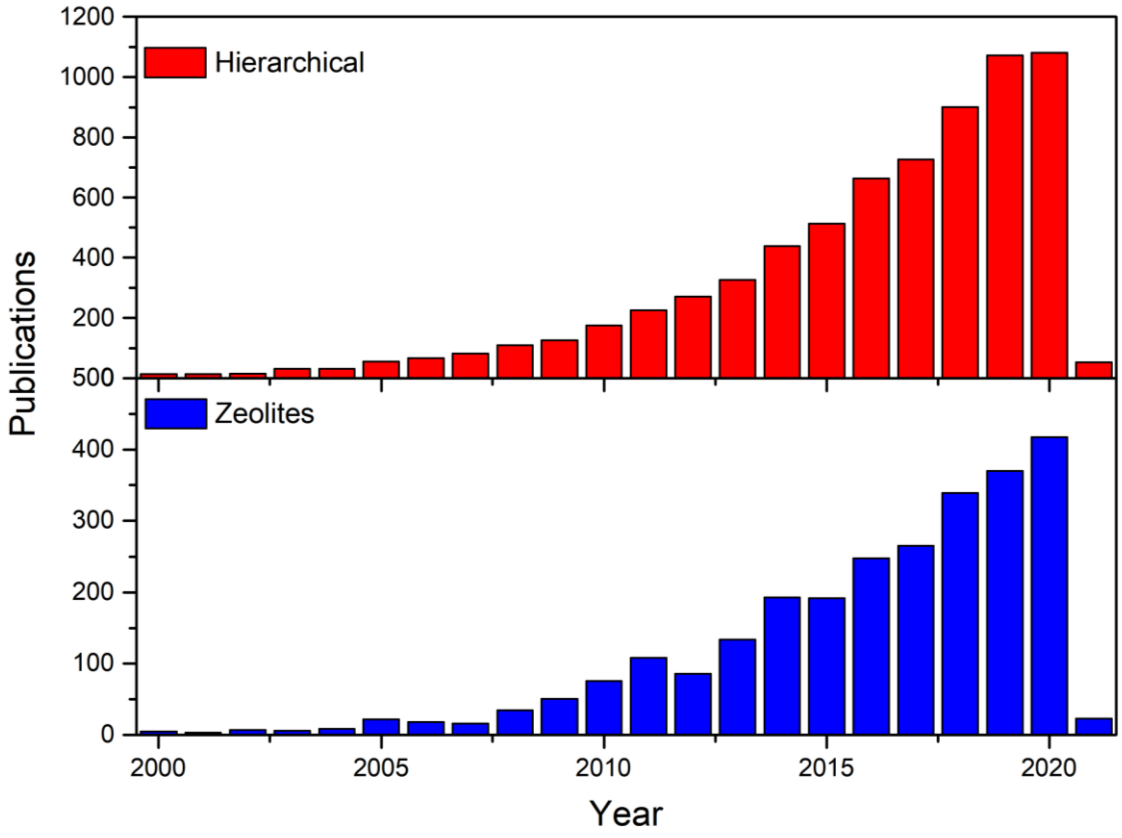

Source: Author (2021). Research using *Web of Science* database on 16/01/2021.

The mesopores introduction to the microporous structure can be inefficient for molecular transport if it is not correctly located in the crystal. To develop such materials, a careful design is required to not only create bigger pores, but also locate them harmonically with the micropores.[24] The main interest for this approach is to allow big molecules access

zeolite micropores and shorten the diffusional path for molecules that fit in those small pores. Thus, they act increasing the external surface area, maximizing intracrystalline diffusion and minimizing deactivation. Transport improvements are the basic requirement in a hierarchical material.[23; 26]

According to Schwieger *et al*. 2016,[26] hierarchy can be classified as:

a) structural, where a high stable network is achieved repeating structural elements;
b) transport, it allows the fast fluids distribution in a flow;
c) compositional, organizing some parts of a material leads to a system with a variable composition locally and systematically.

Advantages on their use are several syntheses approaches, controllable macroscopic morphologies, tunable porous structures and functions and a wide range of applications, for example. At the same time, it can be challenging since some synthesis procedures are expensive and hard-working, as well as it is not easy to obtain materials with high amount of secondary porosity. The perspectives for the hierarchical zeolites syntheses rely on preparation in a wide range of Si/Al ratios, keeping the inherent zeolite properties in cheap and easy methodologies.[23; 24]

Materials containing both micro and mesoporosity were usually discussed by means of composites formed by zeolite units with mesoporous amorphous phases. This could be achieved by mesoporous materials partial crystallization, zeolites seeds in a mesoporous matrix, treatment with surfactants, desilication and dealumination of zeolite structures and the use of templates.[81; 82] Nowadays, many of those approaches are still used but focused on making them interconnected and having different holes to the process. The most used methodologies are the post-synthesis modification, but other methodologies can be found easily. For the proper methodology choice, it is important to consider the aim of the study, since it will have impact at the characteristics of formed materials.

These types of materials can be observed in literature since late 1960's, where after leaching natural and synthetic zeolites with H_4EDTA, Kerr[83] reported increment to stability of those zeolites; but only in 2000, Matsukata group[84] brought them into light of discussions after studies on mesopores formation by silicon extraction in a ZSM-5 zeolite, showing that it was possible to obtain intracrystalline mesoporosity preserving still the original microporosity.

Other preparation procedures can be used to obtain this class of materials, using both bottom-up and top-down approaches, and the final materials can be classified as composites with different materials or purely zeolitic. The combination of more than one

strategy has potential use and the three basic techniques that are commonly used in addition to others are the surfactant design, sol-gel control, and post-treatment.[23; 25; 26]

When in composites, at least one additional material is used along to the zeolite. This secondary material can be porous by itself or just act helping the intercrystalline porosity formation. Usually, it results in macroporous monoliths with specific shape and functional surface formed by zeolite recovery. This combines different pores levels in a wide range and is very promising in industry since it inserts a lot of beneficial properties to the final material that can be related to the new geometry as well as to new properties associated to the synergy originated from their mixture.[26]

Figure 4 - Representation for types of hierarchy in zeolitic systems and examples of obtaining each of them.

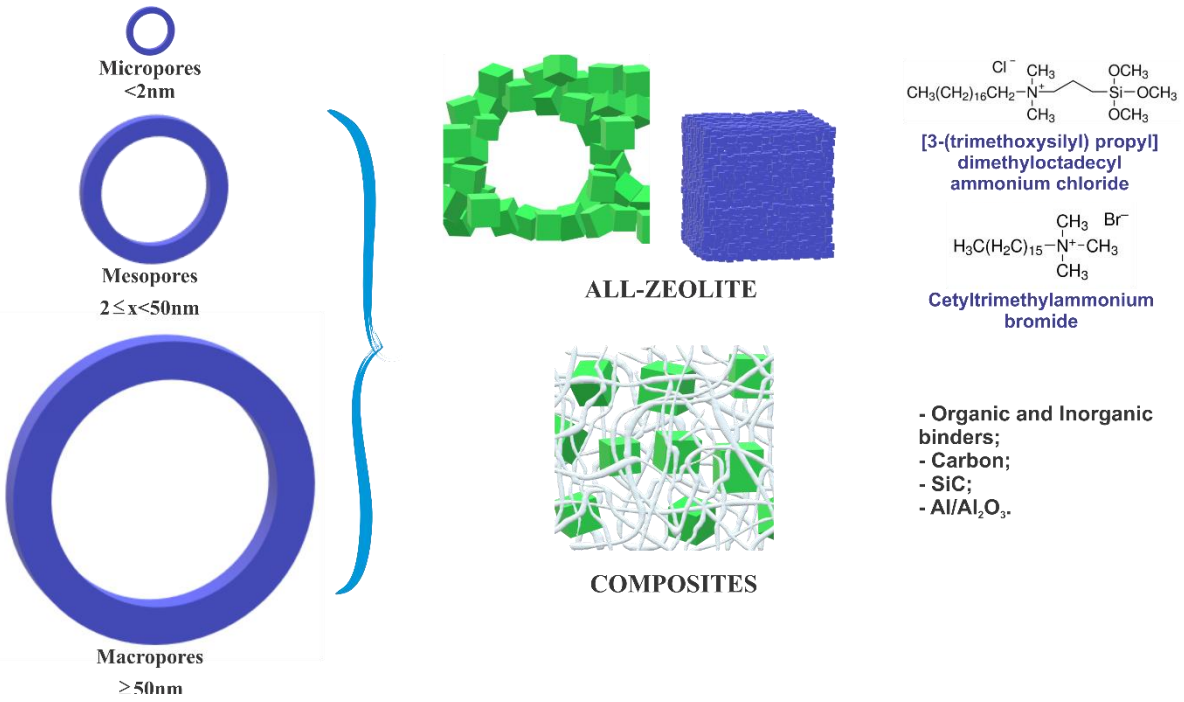

Source: Author (2021).

In Figure 4, the three pore types are presented with dimensions as suggested by IUPAC[85] and two zeolitic materials can be obtained mainly, depending on the strategy that is used in the synthesis: “All-zeolite” materials, where commonly surfactants are used, and “Composites”, with different substances along with the zeolite. The first ones have some advantages as good pore connectivity, high degree of additional porosity and different zeolites structures can be obtained, and the second ones, usually present well-defined shape, mechanical stability, and the size dan shape of the macropore system can be tailored.

One of the approaches to obtain purely zeolitic hierarchical material involves a bottom-up strategy with soft-templates. A very promising route uses two different molecules to produce the desired hierarchy; one of them directs the mesophase formation and the other, the micropores. However, it usually results in phase mixture containing the amorphous mesostructured and the microporous crystalline zeolite structure instead of an interconnected structure presenting both micro and mesopores.[23; 82]

To overcome these issues related to phase separation, the bifunctional surfactants come up. These molecules, commonly called amphiphilic organosilanes, are most probable to form ordered mesopores and micropores simultaneously. There is a hydrophilic part with silicon next to a quaternary ammonium, that allows the formation of covalent bonding with inorganic species by hydrolysis and condensation reactions as well as zeolite directing agent, and a long hydrophobic tail, that directs the mesopores within the structure via self-assembly of micelles. This can be used to obtain efficiently different zeolites with a micro-meso hierarchical structure.[23; 86]

Hardly a surfactant will modulate the zeolite crystal growth into a mesoporous structure since they are expelled from the aluminosilicate domain during the zeolite crystallization process, while organic molecules capable to interact strongly with the growing crystal surface can effectively modulate the crystallization process of inorganic materials. This is the key to the design of the bifunctional surfactants: amphiphilic molecules that contained a hydrolysable methoxysilyl moiety, a quaternary ammonium and a hydrophobic alkyl chain moiety.[87]

The molecule 3[(trimethoxysilyl)propyl]hexadecyldimethylammonium chloride (TPHAC) was used as mesopore-directing organosilane surfactant in 2006 by Ryoo group[87; 88] that synthesized it to be used in conventional alkaline zeolite synthesis mixtures. A MFI structure was obtained firstly, but other zeolite structures were also produced using the same principle ever since, like zeolites LTA,[89] MTW[90] and FAU.[91] In a typical experiment, it is obtained by reacting 3-(chloropropyl)trimethoxysilane with N,N-dimethylhexadecylamine in anhydrous methanol at 110 °C for 36 h in a Teflon-lined stainless-steel autoclave and concentrated at the end in a rotary evaporator. A similar molecule with an octadecyl organic chain instead of the hexadecyl can be used for the same purpose without big issues to the products and the facility of being commercialized from Sigma-Aldrich or Acros.[92]

Using molecules like this, it is possible to obtain zeolitic phases with a narrow mesopore distribution that can be adjusted changing some parameters as hydrophobic chain

length, time, temperature, and silanes content. Also, different morphologies can be found in literature like a house of cards structure or crystals with a rough surface.[86]

3.1.4 Composites and aerogels

As stated in the previous section, hierarchical zeolites can also be obtained by inserting the crystals in a polymeric matrix, presenting improved properties.[26] Cellulose is being used with several materials to get an enhanced structure with some hierarchy. Liu *et al*., 2019[93] used thin films formed by polyamide and oxidized cellulose nanofibrils for desalination with improved permeability due to the cellulose particles. Araújo *et al*., 2018[94] obtained a tri-dimensional structure by deposition of Cu nanoparticles over bacterial cellulose nanofibrils with antimicrobial efficiency. Fan *et al*., 2018[95] in their turn, report a material with high filtration efficiency for particle matter when using bacterial nanocellulose covered with protein nanoparticles and wood pulp cellulose.

Several works also report the combination of cellulose with different zeolites or other porous materials for the antibacterial purpose,[33; 96] in both gaseous[32; 97] and liquid[31] adsorption systems or even in art.[98]

An interesting way of using them in those applications can be as aerogels. Aerogel is a solid porous material with an opened structure formed by a network with interconnected nanostructures and porosity above 80%. They can also be considered as the dried counterpart of gels.[99] When the gels are dried using evaporation, xerogels are produced where the pores that were filled with liquid phase collapse and there is a high shrinkage.[100]

Cryogels are obtained from freeze-drying processes and can be referred as aerogels, if the pores occupy a high percentage of the sample volume.[99-101] Buchtová and Budtova[102] compared the property differences among the three types of materials. According to their findings, the morphology of the formed cartridges changes in a way that the aerogels present the gel structure preserved whilst the so-called cryogels present thin sheets with large and interconnected pores in a few micrometers' diameter. Moreover, the shrinkage, density, and surface area (ca. 10 and 49 $m^2 g^{-1}$) are lower for the cryogels.

Thus, the drying technique used is crucial for the final morphology. In general, surface tension for the liquid must be avoided, so the conventional drying methods are not efficient, and the tridimensional structure is destroyed. The most common techniques are the supercritical drying and the freeze-drying. In practice, for the supercritical drying, the gel is heated in a closed vessel until Temperature and Pressure are above the critical point for the liquid inside the gel, and as a result, the final materials are usually hydrophobic. To the freeze-drying, the liquid gel is firstly frozen and then dried by sublimation. It is also interesting to observe that the latter requires more time, but the first one, high costs since it uses a high

pressure vessel, so the choice for the lyophilization can be explained even if the original structure is changed by the ice crystals formed when the liquid crystallizes.[100; 101]

The temperature gradient during the freezing step can also promote changes to the aerogels formed, as observed by Zhang *et al.*[103] By comparing the effects for the use of liquid Nitrogen, ultra-freezer and conventional freezer, the authors proved that the liquid Nitrogen being used as freezing agent inhibits more effectively the self-assembly in cellulose aerogels, resulting in a more uniform and smooth surface.

Foam is another term that can be used for such materials. According to Lavoine and Bergström,[104] the preparation method can be the same as for the aerogels and cryogels, but the pores formed at the solid porous material are higher than 50 nm with porosity over 50%. For them, aerogel is a mesoporous (pore size in the range 2–50 nm) solid material with high porosity over 90%.

Sol is a liquid phase where colloidal particles are dispersed. Gel is the respective solid structure in which the clusters are filled with another substance, usually a liquid. The transformation from sol to gel is called gelation and nowadays this approach is the most popular to obtain aerogels. Initially, polycondensation reactions take place forming small clusters with ca. 2 nm. They aggregate forming bigger particles 4- 7 nm, and the temperature is adjusted for the gelation take place, following with ageing of the gel formed and then, dried.[100; 101]

The most known aerogels are the silica aerogels, or silicates with silica as the main component, but also aerogels formed by organic polymers (mixture phenol-furfural with poly-(dimethylsiloxane), 2,3- didecyloxyanthracene with ethanol, polyacrylonitrile, polyisocianates, resorcinol with formaldehyde, or melamine with formaldehyde are some examples),[100; 105] carbon, and inorganic species as zirconia, titania, alumina, and chalcogenides.[105]

Specifically, about cellulose aerogels, there are some advantages related to their biodegradability, availability since it is the most abundant biopolymer. Besides, the presence of hydroxyl groups over the structure allows a stable tridimensional network to be formed without the use of cross-linking agent. Among them, the bacterial cellulose aerogels are superior avoiding the use of chemical reagents to purify or to obtain the nanofibrils.[101]

Such materials in adsorption or separation processes are usually used for bulky molecules, but the main application is for oil separation. Pereira *et al.*[106] silanized bacterial cellulose nanofibrils with methyltrimethoxysilane after partial oxidation of the structure. In this study, the authors reported aerogels with high hydrophobicity and mechanical properties, allowing reuse with high absorption for different organic solvents. For the same purpose, He *et al.*[107] propose the formation of SiO_2 particles over the surface of the bacterial cellulose

nanofibers observing fast absorption rates in the oil-water mixture and low energetic dissipation.

Cellulose aerogels were prepared by Bendahou *et al*.,[108] using oxidized date palm tree nanofibres and nanozeolite particles. As a result, the cartridges formed present improved thermal conductivity and mechanical properties, combining the inter-cellulose films mesoporosity and the zeolite microporosity. Valencia *et al*.[109] used this approach for foams used in CO_2/N_2 separation processes. Mixing gelatin and nanocellulose from softwood fibers, colloidal zeolite silicalite-1 was impregnated with the highest amount reported so far, 90%. This resulted highly mechanically stable hybrid foams where the cellulosic matrix does not block the zeolite pores.

3.2 Adsorption

Adsorption is a mass transference operation that studies the ability of certain solids in taking over their surface some substances that are present in liquid or gaseous medium, allowing the from the medium. Because of that, this is one of the most popular methods for wastewater treatment, improving as a separation and purification method, in the last decade.[6] As a surface phenomenon, a higher surface area is beneficial for the process and porous materials are usually used as adsorbents.

Fechine *et al*., 2020 highlights the clay nanomaterials, magnetic nanomaterials, and MOFs.[110] The MOF's capacity for gas adsorption is also presented by Furukawa *et al*. showing their use for storage of hydrogen, methane, and carbon dioxide, as well as separation experiments for hydrocarbons and toxic molecules.[111] The same effect is observed for zeolites, since both present well-defined channels that allow molecules to diffuse to the inner surface.[112] Many other materials have potential for use as adsorbents, as graphene, activated carbon, carbon nanotubes, mesoporous silica, chitosan, red mud, alumina, clays, and bioadsorbents from rice husk, coconut waste, sugar cane bagasse, wheat bran, orange peel waste, sawdust, apple pomace, fungal and algal biomass, yeast, and egg shell.[21]

When referring to adsorption processes, usually the solids are called adsorbents and the species that are adsorbed on the surface, adsorbate. Usually, three different mechanisms can drive the process: steric (the pore sizes for the adsorbent had characteristic dimensions that molecules are excluded depending on their size), equilibrium (the solids have different abilities to uptake the adsorbates, related to their structures) and kinetic (the species present different diffusivities).[6] Experimental studies with zeolites can present information about uptake capacities and the thermodynamical parameters, as well as spectroscopic studies about the adsorbate molecule, and diffraction and NMR analyses regarding the location of the adsorbates in the pores.[112]

Depending on the strength of the adsorbent-adsorbate interaction, the process can be classified in physisorption or physical adsorption, and chemisorption or chemical adsorption. When the first one is the governing process in the system, the adsorption process is not specific, reversible, usually faster, and it happens in the whole adsorbent surface. The intermolecular bonds between the molecules in the fluid and the solid surface are higher than the molecules in the fluid, several layers of molecules can be observed, and as it does not involve the formation or cleavage of chemical bonds, the adsorbate nature is not modified. The chemisorption on the other hand, is highly specific and it happens in specific active sites on the solid.[6; 112]

To identify this feature and many other, it is essential that the appropriate equilibrium correlation is stablished and thus, be able to predict parameters and the quantitative comparison with other materials and processes. About equilibrium relations, adsorption isotherms must be used to describe the adsorption interaction, crucial to optimizing the process. A wide range of isotherms can be used for this, with several adsorbate molecules like Langmuir, Freundlich, Brunauer–Emmett–Teller, Redlich–Peterson, Dubinin–Radushkevich, Temkin, Toth, Koble–Corrigan, Sips, Khan, Hill, Flory–Huggins, and Radke–Prausnitz.[6; 110; 113; 114]

Another study that can be performed regarding the adsorption process is a kinetic study. From that, it is possible to determine better operating conditions for the process and it is expressed as removal rate of the adsorbent in a time. This implies on mass transference to the inner of the adsorbent particle, and the different processes that can lead to it are external mass transference, pore diffusion and surface diffusion. One of the main parameters determined from it is the maximum contact time that the adsorbate should spend with the adsorbent to reach the equilibrium. As important as this, some mathematical models can be used to identify the main mechanism that controls the process, among them, the pseudo first order and pseudo second order are the most used ones, together with the diffusion models: Weber and Morris, and Boyd.[6; 110; 115] The equations for the models used in this work are presented further in Experimental section.

Observing the comparisons of kinetics, thermodynamics, and regeneration of tetramethylammonium hydroxide adsorption in aqueous solution for three different materials showed that even though it is usually reported the adsorptive behaviour of some materials in relation to the surface area, the results presented the opposite, when using graphene oxide, zeolite NaY and granular activated carbon.[116] Thus, it is important to analyze other factors that might have influence like operational parameters (temperature, pH, and solvent), characteristics from the adsorbate (polarity, size, solubility, and acidity/basicity) or the adsorbent (surface area, pore size, density, surface functional groups, and hydrophobicity).[6]

Among the water chemical pollution studies presented by Armon and Hänninen, ocean acidification, toxic metals, and persistent organic endocrine disrupting compounds are cited.[117] In a research on Web of Science searching platform, the combination of “Adsorption” and the terms “dye”, “gas” or “metal” for articles and proceeding papers, show respectively 7, 13 and 23% of the results (on 18/01/2020). This trend happens because the heavy metals pollution is one of the most serious environmental problems nowadays with potential to cause several dysfunctions in the human, and adsorption is one of the main and efficient methods to remove them.[2; 4; 5]

Among the toxic metals, lead can be highlighted, since it interferes in neurological development and endocrine function, for example. Its main source in industrial effluents is due to lead-acid batteries wastewater, but also electroplating, electrical, and steel industries.[1; 4] A recent study about lead exposure in some countries showed the legacy of lead exposure as the main source to keep populations in high income countries continuously exposed, whilst for low income countries, there is also a lack of regulations or inability to enforce regulations.[118] In 2007, another study reported the Brazilian lead exposure that occurs mainly in battery plants, and some concern about lead in pigments, ceramics plastics, and from rubber industry.[119]

Usually, lead co-exists in the environment with cadmium and zinc, and are widely used in industry. In literature, it is reported that they affect the renal functions, alone or in combination, although, when together, the tubular renal dysfunction is propagated.[120] The disturbed hemoglobin % was also observed for adolescents and adult workers from battery recycling and welding workshops that are exposed to Cd and Pb in their workplace.[121]

Such pollutants can also be removed from solution using the ionic exchange property in addition to the adsorption. This feature is inherent of zeolite structure and arise from the isomorphous positioning of aluminium in tetrahedral coordination within their Si/A1 frameworks that imposes a net negative charge on the framework counterbalanced by cations held within the cavities and channels. This ionic exchange is studied in zeolites for over 150 years and it depends on the cationic species nature, temperature, solution concentration, solvent, anion species associated to the cations in solution, and the zeolite particular structure.[13; 122]

3.3 Characterization techniques

The regular structure of the zeolite crystals allows their development and applications. Although, the structure determination should be done by different techniques to enable the right determination of the properties. Among the main characterization techniques, it is possible to highlight the diffraction-based techniques and spectroscopic methods, that combined to electron microscopy, solve or stablish structural details.[12; 123] Below, the basics for the characterization techniques used in this work are presented.

3.3.1 XRD

X-rays are the most common radiation used to determine the crystalline structure of any material. Beyond them, neutrons, and electrons can also be used. This happens due to the diffraction phenomenon whose wavelength is at the same magnitude order than the interatomic distances in the structures, in the range of 0.1 and 100 Å (in the electromagnetic spectrum, they are located between γ and the ultraviolet radiation), in crystallography, they are in the range 0.5 and 2.5 Å.[124; 125]

The conventional X-rays source comes from an X-ray tube, where high-energy electrons collide with a target metal, generating electromagnetic waves. Their brightness is limited by the thermal properties of the target material, that must be cooled continuously because all kinetic energy of the accelerated electrons is converted into heat with the rapid deceleration. A much more advanced source of such radiation is the synchrotron, but due to its cost of both construction and maintenance, this is usually used in more advanced applications than only phase identification or structure refinement.[124]

Among the information that an XRD experiment can provide for zeolites, it is common to identify the unit cell size, the space group (which gives information on the lattice type and symmetry in the structure), and the atom coordinates for the asymmetric unit of the structure.[125] Research papers and databases provide tables with such descriptors. Table 2 brings the information for unit cell and space group of dehydrated zeolite A, LTA, as informed on the IZA website and Atlas of Zeolite Framework Types.[126]

Table 2 - Unit cell and space group information for dehydrated zeolite A

Crystal system	Cubic
Space group	Pm-3m
Space group number	#221
a (Å)	11.9190
b (Å)	11.9190
c (Å)	11.9190
α (º)	90.0
β (º)	90.0
γ (º)	90.0

Source: IZA.

Mesoporous solids in general, present a regular structure of pores and pore walls with poor crystallinity, which means, atoms are not positioned in each unit cell. Although, each mesoporous structure gives a characteristic X-ray diffraction pattern that comprises in each case, a small number of diffraction maxima at low scattering angles with an absence of high-angle reflections. These patterns possess insufficient information to allow structure solution as it happens for zeolites, even that they can be indexed to a space group symmetry.[44; 123]

One of the concepts to be reviewed with the diffraction effect is to consider crystalline planes represented as lattice points. Integrals h, k and l, called Miller indices, that are used to describe such planes and they can be better studied/explored in crystallography studies. The importance of those plans to diffraction relies on the diffraction of a set of points is equivalent to the reflex of themselves. Each set of planes leads to a possible diffraction maximum in a θ angle, as defined by the Bragg's law. This law, presented in (5) equation, stablishes the relation between the diffraction angle (Bragg's angle), wavelength, and interplanar spacing.[124; 125; 127]

$$n\lambda = 2d \sin\theta \qquad (5)$$

Among the experimental arrays to a XRD analysis, the powder measurement is one of the most common ones for zeolites, since they are notoriously difficult to grow as crystals large enough for a single crystal experiment, and commonly obtained as polycrystals.[12; 125] Those measurements are function of only one independent variable, the Bragg angle, literally

with the simplest possible design. For zeolites, it is used mainly for: identify the phases purity, refine structural models through the Rietveld refinement and completely determine the structures.[124; 125]

In a typical experiment, the intensity diffracted by a polycrystalline sample is measured as a function of Bragg angle 2θ. Thus, the patterns are usually plotted in the form of the measured intensity (as the independent variable) versus the Bragg angle. To understand the structural information is vital to consider it as a set of discrete diffraction peaks superimposed over a continuous background.[124]

The background may be used to extract information mainly about crystallinity, although it is usually treated as an inconvenience, and it should be minimized during the experiment. Apart from it, the structure of a typical powder diffraction pattern may be described by the following components: positions, intensities, and shapes of the Bragg reflections. Each of these components contains information about the crystal structure of the material, properties of the sample, and instrumental parameters: for example, the peak position is influenced mainly by the unit cell parameters of the crystals, and the radiation used in the measurement, but also by the absorption and porosity of the sample; the peak intensities on the other hand, are affected by the atomic parameters and polarization of the radiation, or preferred orientation of the sample; finally, instrumental parameters like radiation, geometry and beam conditioning are crucial for the peak shape, but the crystallinity and grain size can also be observed.[12; 124]

To perform phase identification with the powder diffraction data acquired, it possible to use specific programs provided by the diffractometer's manufactures, like the X´Pert High Score Plus for P'Analytical instruments,[6] usually loaded with information from the Powder Diffraction File (PDF) of the International Centre for Diffraction Data (ICDD)[12] or their own search/match program, and another option is to load the results on the IZA website if the researcher knows the structure that should be obtained.[128] At the end, it is important to mention that the comparison of patterns may be not straightforward as it is for other types of materials, and some practical considerations should be taken during this analysis: different synthesis conditions or post-syntheses treatments can cause subtle distortions, like reduced symmetry and indexing the pattern can facilitate identification; the low angle reflections are the one most strongly affected by non-framework species and calcined material usually presents them more intense, for example.[12; 125]

3.3.2 SEM

When an electron beam reaches a sample, a lot of elastic and inelastic collisions happen between the incident electrons and the ones forming the sample. This results in different signals emitted bringing information about the sample. The most important and widely studied are the transmitted, backscattered, and secondary electrons, as well as the X-rays. X-rays and transmitted electrons will be discussed in later sections.

Backscattered electrons reverse completely their path and contribute to an imaging signal rich in information on specimen characteristics such as composition, mass thickness, texture, grain size, defects, and crystallography. It can be analysed using the Scanning electron microscope with a detector coupled on the bottom of the column. Its use for the materials proposed in this work is minimum and a good example for this application can be heterogeneity studies in geological samples.[129]

The operational principle of a SEM lies on emission of a finely focused beam with energy E_0 typically selected in the range from 0.1 to 30 keV. Figure 5 presents a brief scheme of its operation: after emission from the source and acceleration to high energy, the electron beam is modified by apertures, magnetic and/or electrostatic lenses, and electromagnetic coils which act to successively reduce the beam diameter and to scan in a regular pattern across the sample surface.

Secondary electrons are commonly used in the image formation giving information essentially about the surface. They have a low energy and are captured by an Everhart–Thornley detector in one of the sides in the chamber. The image produced by this signal is an image that can be magnified to high values getting a resolution of around 5-10 nm. This brings advantage over the optical microscope, with resolution around 200 nm in its best condition. Topographical details (three-dimensional appearance of the specimen image) are another desired feature when analysing something by SEM.

The emitter or electron gun is the top region of the machine, and it is responsible for generating the electron beam. It can be classified as thermionic or field emission source. The thermionic emitters are a tungsten wire and a LaB_6 crystal where the electrons are ejected into the surrounding vacuum by a direct current that heats the filament to about 2700 K. Above the filament there is the Wehnelt cylinder that normally surrounds the filament, except for a small hole, to control the emission current from the gun. For the field-emission gun, a single crystal tungsten filament from which the electrons are pulled off by a strong extraction voltage, without heating. The disadvantage about the FEG is that it requires stable operation with an elaborate vacuum system resulting in substantially greater cost of the instrument. The gains to

the analysis, on the other side, justify its use since it presents a much smaller electron virtual source size, high current, high brightness, low energy spread and a long life.[130]

Figure 5 - SEM layout and function scheme presenting the electron gun emitting electrons that go through electromagnetic lens and apertures before reaching and scanning the sample. The final image is built in a screen after being detected and amplified

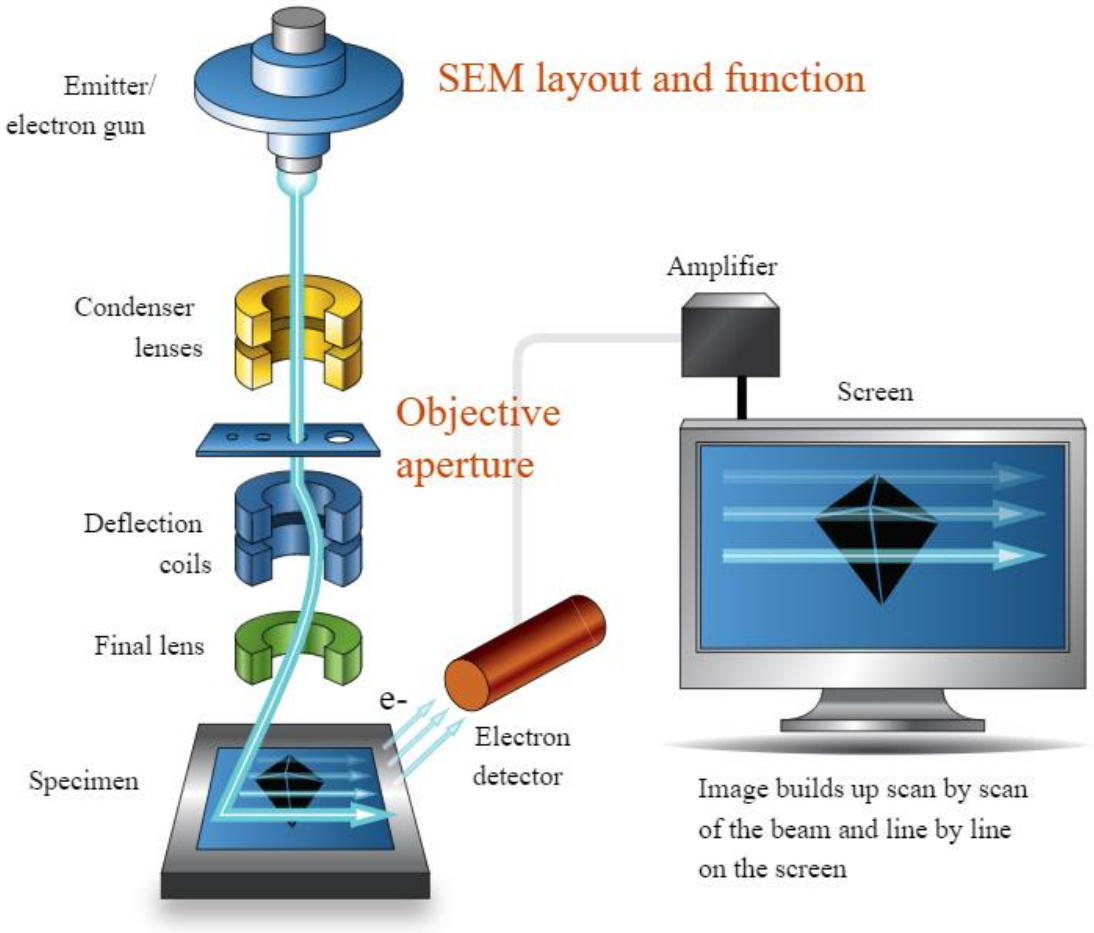

Source: Available at: < https://myscope.training/#/SEMlevel_2_3>. Access in 26 Feb. 2020.

When performing an analysis, some SEM parameters must be adjusted to obtain a good image. The choice depends on the sample and information that is required from that. The voltage, working distance or even the aperture size to the objective lens are examples of decision to be made before turning the beam on.

The accelerating voltage defines the beam penetration in the sample and an increase in accelerating voltage will result in higher signal and lower noise in final image, but some disadvantages can be faced like reduction in resolution of structural details from the specimen surface, since it will cause a greater penetration and other signals are recorded in the detector;

charging artifacts; and increased heating that can damage some specimens. In general, delicate or uncoated specimens use a very low energy (1-5 kV), physical science samples require a higher voltage (10-30 kV) and the coated biological samples lie on the intermediary range (5-10 kV). Working distance (WD) is the height from the bottom of the column and the top of the sample. It has influence on the diameter of the beam that reaches the sample and on the depth of field. If microanalysis will be performed, it should be the analytical WD (defined by the manufacturer to have the perfect angle to the EDS detector, commonly 10 mm).

To be analysed in a SEM, the sample needs to be dry (water can damage the sample and the microscope when the vacuum pulls it out) and conductive (to allow interaction with the incident beam as well as its outflow). Even though, some specialized techniques help such samples to be analysed under this microscope. For zeolites and related materials, they need to be covered with a thin layer of metal or carbon to make them conductive before imaging. This is done in vacuum, using the evaporation or sublimation technique. Films of thickness 10-20 nm conduct sufficiently to prevent charging of most specimens.

Initially, the sample needs to be attached to a support, the stub. The part of the sample of interest must be uppermost on the stub with a continuous electrical connection between them to allow the electron flow that can be done using conductive tapes or glues in combination with a conductive coating.

Nowadays, this is a powerful technique commonly seen and required in materials development or even assessment of their activity in aerospace, electronics, energy, catalysis, environmental, photonics, chemistry, etc. Changing operational parameters or sample preparation it is possible to analyse a wide range of samples and get especially morphological and surface information that can explain some chemical or physical behaviour from the specimens.

3.3.3 EDS

SEM and TEM machines usually present more than one detector that give different information about the sample, among them, chemical composition, and structure. The most common microanalysis technique is the Energy Dispersive Spectroscopy (sometimes called X-ray energy dispersive spectroscopy XEDS or EDX). It is a qualitative and quantitative X-ray microanalytical technique that can provide information on the chemical composition of a sample for elements with atomic number (Z) >3.[131]

The electron beam penetrates the sample, and it interacts with the atoms from which it is made, generating a few different signals, amongst them, the X-rays. The x-ray spectrum is composed by two types: characteristic or continuum x-rays. This X-ray spectrum can be used to identify and quantify the specific elements, except H and He that do not produce this signal.[129]

The spectrometer can detect photons from a threshold of approximately 40 eV to E_0 (which can be as high as 30 keV) with a detection limit of 0.1-0.5 wt%. The energies of the characteristic X-rays allow the elements making up the sample to be identified, while the intensities, allow the concentrations of the elements to be quantified using peak fitting procedures, such as the multiple linear least squares method.

This is a non-destructive analytical technique with the same preparation method and requirements as for the SEM, being desirable bulk, flat and polished for a very precise result. It is also important that the sample is stable under the electron beam. In SEM, the electrons from the primary beam spread out in the sample to form the interaction volume that depends on the accelerating voltage beam and the mean atomic number for each sample.

The interaction volume will be larger for a larger accelerating voltage, but smaller for samples with a higher mean atomic number. Typically, the spatial resolution for X-ray microanalysis is a few microns. To achieve a good interaction volume, parameters like voltage and spot size are usually higher than the ones used in imaging mode, and they are chosen depending on the signal reaching the detector.

Compositional mapping by spectrum imaging collects a full EDS spectrum at each pixel of an x-y array, and after applying the quantitative analysis procedure at each pixel, images are created for each element where the color level is assigned based on the measured concentration.[129]

Thus, qualitative, and quantitative results for the elements can be obtained as well as their precise location in a sample. The applications range is as wide as the SEM and the TEM

and it is a quite common and powerful tool to complement the images acquired in the microscope.

3.3.4 TEM

Transmission electron microscopy or simply TEM is a technique that uses an electron source to analyse specimens in nanoscale revealing details inaccessible by light microscopy. It is possible to investigate crystal structures and specimen orientations as well as the chemical compositions. In comparison to the light microscopy, it presents higher resolution, around 1 nm, and gives information about periodicity of a structure with symmetry and orientation for crystal structures.

Differently from SEM, this electronic microscopy uses a higher acceleration energy and works with thin or nanometric samples that allow the electrons to pass through them to be collected in a phosphorescent screen or camera while the detector for SEM is located on top of sample stage collecting electrons. This difference in electrons energy causes a big change in imaging and resolution that goes from 50 nm in SEM to 0.2 nm in a TEM machine working with 200 kV.[130]

It is also important to mention that the vacuum system is much more efficient for this column what increases the costs and the time to set up the instrument. Another point that should bring problems to the analysis and instrument is the electron-beam contamination that can occur both on the top and on the bottom surfaces of the specimen, causing additional scattering of electrons and reducing the contrast on the final image due to organic vapours that can enter the vacuum from components as rubber o-ring seals. To avoid this process, liquid nitrogen is added to a decontamination trap attached to the side of the TEM column.[130]

Figure 6 presents a scheme of a common TEM machine with the components pointed in the image, that can be divided in three sections:

a) Electron gun = It is usually positioned on the top of the instrument column and it generates the electron beam. Usually, it is formed by an emitter (the filament in figure), the Wehnelt cylinder and anode with a central role. Together with the condenser lens, the electron gun focuses the electrons onto the specimen and the operation of these components determine the diameter of the electron beam at the specimen and intensity level in final TEM image;

b) Specimen stage = It allows specimens to be inserted in the TEM as well as keep them stationary or intentionally moved. The grids must be well secured on the sample holder since the mechanical stability of the specimen stage is an important factor that determines the spatial resolution of the TEM image;

c) Imaging system = It is formed by the objective lens and the projector lens together with the CCD camera or viewing screen. The operation of these components determines the spatial resolution that can be obtained from the microscope.

Figure 6 - TEM scheme and function scheme

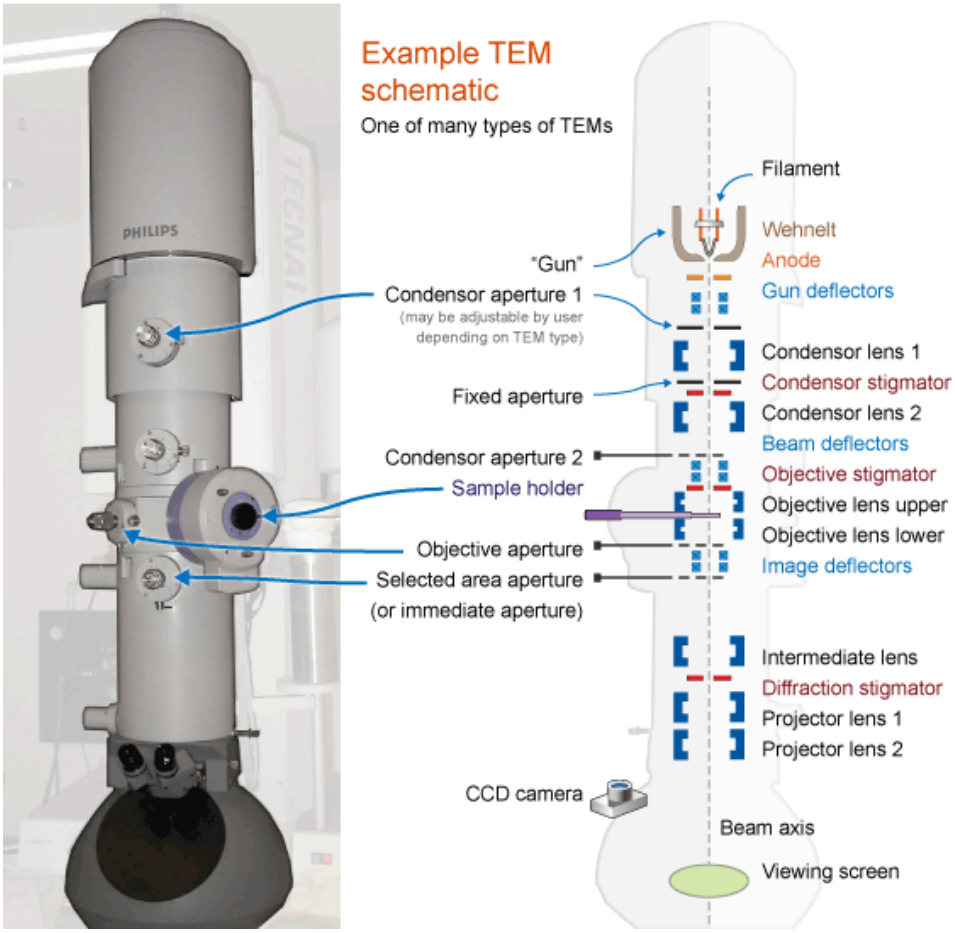

Source: Available at: <https://myscope.training/legacy/tem/introduction/>. Access in 26 Feb. 2020.

The thickness of a TEM specimen must be exceedingly small: usually in the range 10 nm to 1 µm. TEM specimen preparation involves ensuring that the thickness of at least some regions of the specimen is within this thickness range. Some methods to analyse bulky samples are mechanical grinding or cutting in tiny slices like the commonly known ultramicrotomy.

Although, some artifacts can be introduced to some samples using those, like defects dislocations or surface layer damaged.[130]

The chosen preparation method will depend on the information you need, time constrains, equipment and the material by itself. What you see or measure should not be affected by the technique or if it does, you must know how. The final sample must be electron transparent and representative of the material you want to study. Mostly, it should also be stable under the electron beam and in the laboratory environment, conducting, and non-magnetic (with just a few exceptions depending on the preparation).[132]

Commonly in materials sciences, especially for powder samples, the sample should be disposed in a 3 mm grid supported in a thin film, with the holey carbon film as the classical example for that, Figure 7 presents an image of such grids, as well as the sample holder used to insert the sample on the microscope. Some of the particles of the material of interest will be located partially over a hole so that they do not overlap anything else. Other procedures can also be used, but it should be known that the preparation method can be a long work or the focus in a work, having an extent bibliography about this to be explored.

Figure 7 - Copper grid (a) and sample holder (b) for TEM machine

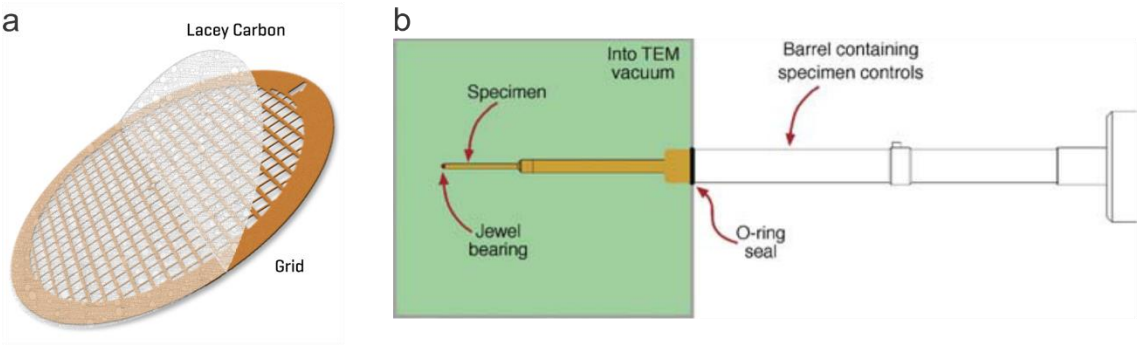

Source: Author (2021).

The ability of investigating small particles and structures allowed great advances in medical and materials sciences, including formation mechanisms or crystalline structures. The TEM technique is developing over the years, and it is very promising to future research in different fields, especially in nanoscience allowing that materials hard to be seen on it now, can be further studied.

3.3.5 IR

Spectroscopic methods bring complementary information to the diffraction techniques bringing information about the bonds between the atoms.[123; 133] Spectroscopy is the study of the interaction between light/electromagnetic radiation and matter. Independently of the energy or wavelength shined in a sample as a beam of a particular electromagnetic radiation, it is common among the spectroscopic techniques, observation of how the sample responds to it. Radio waves can cause changes in the magnetic orientation in some atoms, and this is the basis for the nuclear magnetic resonance (NMR) spectroscopy, better detailed in the next section. For the infrared spectroscopy, as briefly presented below, the information is provided stimulating vibration or rotation of two or more atoms in the sample.[134]

Either organic or inorganic compounds absorb various frequencies of electromagnetic radiation in the infrared region that correspond to the frequency of the bond's natural vibration, which results in resonance. There are several types of vibrations that cause it, like bend, stretch (both symmetric and asymmetric), and rotations (in three axis, x, y, and z). The unit usually used by chemists to refer to this radiation is called wavenumber and are expressed as reciprocal centimetres (cm^{-1}). This unit is used since it is directly proportional to energy. An IR spectrometer detects how the absorption of a sample varies with the wavenumber and the spectrum is displayed as a plot of the energy of this radiation versus the percentage of light transmitted by the compound.[134-136]

The energy absorbed by the molecules are affected by the type of vibration, strength of the bonds, and the mass of atoms. As a consequence, bending vibrations are of lower energy than stretching vibrations for the same bond, stronger bonds absorb at higher wavenumbers, and heavier atoms vibrate at a lower frequency than lighter ones.[134]

To determine the absorption spectrum for a compound, the instrument used is an infrared spectrometer, and two types of instruments can be used for this purpose: dispersive or Fourier transform spectrometers. The two provide nearly identical spectra for a given compound, but for the last ones, the spectrum is much more rapidly than the first ones. Therefore, a Fourier transform is performed on a sum of dozens of accumulated interferograms, giving a spectrum with a better signal-to-noise ratio, and greater sensitivity than a dispersion instrument.[135]

In general, any sample can be analysed by IR due to the preparation that can form a thin film of liquid between two plates, a solution held in special cells, a paste between two plates or a solid mixed with potassium bromide and compressed into a disk. For the nanoporous materials or the cellulose used for this work, the most common method is the last one, mixing

the solids with dried powdered potassium bromide and then pressing the mixture under high pressure. This substance is used for not being able to absorb the IR radiation, and under pressure, it melts and seals the compound into a matrix, resulting in a KBr pellet that can be inserted into a holder in the spectrometer. The main disadvantage is that KBr absorbs water and this may interfere with the spectrum.[134; 135]

This technique is widely available and applied extensively in the study of microporous solids for giving some structural insights about the zeolite framework. This information is provided by stimulating the vibration or rotation of two or more atoms in the probed matter and a typical spectrum is collected between 400 and 4000 cm^{-1}, also called the mid-IR, but it is also possible to find works exploring the near-IR (> 3000 cm) and the far-IR (< 300 cm^{-1}). This enables most of the fundamental bands from framework and hydroxyls to be measured. Also, it may be possible to deduce some structural information on a new zeolite for which X-rays diffraction data does provide enough information for analysing it.[13; 123; 133; 136] In adsorption, the knowledge about the structure of the adsorbent and their functional groups may help to elucidate the adsorption mechanism.[6]

The zeolite framework vibrations bands depend on both the structure type and the composition. However, for qualitative interpretation of the IR spectrum, it is traditionally separated into regions characteristic for classes of vibrations: 3200-3800 cm^{-1} for fundamental hydroxyl stretches, adsorbed water in the region of 3600 and around 1600 cm^{-1}, and framework vibrations from 400 to 1200 cm^{-1}. In the last region, it is also possible to make more detailed assumptions about the structure, with asymmetrical and symmetrical stretching, and T–O–T bending for the internal tetrahedra in the regions 950-1250, 650-720 and 420-500 cm^{-1}, respectively. And for the zeolite external linkages, double ring, symmetrical and asymmetrical stretching in 500-650, 750-820, and 1050-1150 cm^{-1}, respectively.[13; 123]

3.3.6 NMR

Nuclear magnetic resonance is a spectroscopic method as the IR, that interacting with radio frequencies, provides information on the environment of the atoms, their coordination geometry, and relevant internuclear distances and molecular motion. Whilst the IR reveals only the types of functional groups present. This technique stands out as an indispensable structural tool for zeolites and related materials. Furthermore, it is complimentary to XRD and a very versatile technique, allowing many types of measurements, coupled with a large number of elements that can be studied.[123; 134; 135]

The background for this technique relies on the nuclei for atoms behaving like magnetic bars aligning with the field. To make the nucleus change to higher energy alignment, energy must be supplied in the radio frequencies region of the electromagnetic spectrum. The precise frequencies depend on the environment of that nucleus, that is on the other nuclei and electrons in the neighbourhood. Thus, when a sample is placed in a strong magnetic field and the frequencies of radiation that it absorbs are measured, information about the nuclei in the molecule can be obtained.[134]

For solid materials like the nanoporous materials used in this work, the solid-state approach is the one used. This is because interactions that can be neglected in liquids and solutions, are very dependent on the spatial orientation of the sample, and considerably affect and broaden the NMR spectral lines. These effects can be removed by sample spinning to give a higher-resolution spectroscopy, from Magic Angle Spinning (MAS) experiments. In MAS NMR, the sample is typically spin at 10-30 kHz about an axis that makes an angle of 54°44' to the magnetic field. The samples can also be analysed using a wide range of approaches mainly to enhance resolution of the spectra for different atoms, like the Double Rotation (DOR), the Dynamic Angle Spinning (DAS), or the Multiple Quantum MAS (MQ MAS) NMR.[123; 137]

A wide range of atoms is available to be studied using NMR, and the main condition for this is that the nucleus possesses a non-zero spin value, like ^{17}O, ^{29}Si, and ^{13}C. Some of these nuclei have a low natural abundance and takes more time to get a good signal, whilst others are 100% abundant.[137] The aluminosilicate structure of zeolites has a strong effect on the spectra acquired, especially for ^{29}Si. Even at low framework Al concentrations, the Si resonances are broadened, and it is common that Q^4 silicon sign is overlapped. Another effect is that different Q^4 silicon environments are produced with different numbers of silicon and aluminium atoms in the second coordination shell. The number of aluminium tetrahedra sharing oxygens with the SiO_4 tetrahedron under consideration is indicated in brackets and it is possible to define five different units: Si(0Al), Si(1Al), Si(2Al), Si(3Al) and Si(4Al). The increase of aluminium concentration results in the characteristic Si shifting to about 5-10 ppm low field.[123; 138]

3.3.7 Textural properties

In general, the internal void volume is an important characteristic of microporous materials, especially for zeolites and hierarchical materials study since it will be crucial to properties like permeability or adsorption capacity. For this, characterizing pore volumes is

usually critical to understand the material main properties.[139] Physical adsorption of gases is one of the main experimental methods available to this purpose, assessing a wide range of pore sizes (0.35 to 100 nm) with low cost.[140; 141]

With such a wide range of pore sizes that can be studied with this technique, it is important to understand how the sorption behaviour happens in each case. In micropores, i.e. pores with widths not exceeding ca. 2 nm, the process is almost entirely connected to the interactions between fluid molecules and pore walls and they fill through a continuous process. To mesopores, pores of widths between 2 nm and 50 nm, not only the fluid-walls attraction rules the process, but also attractive interactions between the fluid molecules, which leads to a multilayer adsorption and pore condensation. Nevertheless, the macropores, pores with widths exceeding about 50 nm, are so wide that they can be considered as nearly flat surfaces.[85; 140]

Physisorption occurs whenever a gas, adsorptive, is brought into contact with the surface of a solid, adsorbent. The intermolecular forces among them usually occur as a result of geometric and electronic properties of both. Adsorption is used to denote the onward process of physisorption while its counterpart is desorption in which the amount adsorbed progressively decreases. Those terms are then used adjectivally to indicate the direction from which experimentally determines amounts adsorbed have been approached. Another detail to be observed with the physisorption is the adsorption hysteresis that arises when the adsorption and desorption curves do not coincide.[85; 141]

The physisorption process occurs as micropore filling, a primary physisorption process, while in mesopores, three distinct stages are observed: monolayer adsorption, all the adsorbed molecules are in contact with the surface layer of the adsorbent, multilayer adsorption, the adsorption space accommodates more than one layer of molecules, and the pore condensation following multilayer adsorption. This is a phenomenon that reflects a vapor-liquid phase transition in a finite-volume system.[85]

The strength of the fluid-fluid and fluid-wall interactions and geometry effects coupled with the pore state and bulk fluid define the adsorption isotherm shape and characteristics.[140] Over the past 35 years, IUPAC released some updates with the last document published by Thommes *et al*., 2015 [85] regarding the evaluation of surface area and pore size distribution. There, we can find among other important aspects that have to be considered during and post-analysis, as well as an accurate classification for the physisorption isotherms, as presented in Figure 8.

Type I isotherms are reversible and characteristic from microporous solids having relatively small external surfaces, like activated carbons, zeolites, and certain porous oxides, for

example. Those isotherms are concave to the p/p^0 axis with the adsorbed amount approaching a limiting value that is defined by the accessible micropore volume. In extremely low p/p^0, there is the micropore filling that appears in the graph as a steep uptake. Considering N_2 as adsorbent, type I(a) and type I(b) are different from each other depending on the size of the micropores: ultramicropores (pores of width < 0.7 nm) and supermicropores (0.7 nm < pore width < 2 nm), respectively.[85; 140; 142]

Type II and type VI isotherms are observed for non-porous or macroporous materials where mono and then multilayer formation occurs on the surface. Type VI isotherms although, are rare to be found and occur by adsorption on a highly uniform nonporous surface e.g.: argon adsorption on graphitized carbon blacks. Types III and V isotherms are related to weak adsorbate-adsorbent interactions with very small adsorbed amounts at low pressures: type III indicates that the adsorbed molecules are clustered around the most favourable sites on the surface whilst in type V, the molecular clustering is followed by pore filling (e.g.: water adsorption on hydrophobic micro or mesoporous adsorbents).[85; 140; 142]

Type IV isotherms are given by mesoporous adsorbents and the initial monolayer-multilayer adsorption on the mesopores walls is followed by pore condensation. A typical feature of those is a final saturation plateau that sometimes can be a mere inflexion point. The main difference between types IV(a) and IV(b) is the width for the pore diameter, that in case of N_2 as adsorbent, is 4 nm: pores wider than this critical value, present type a; pores with smaller width, the isotherm is completely reversible as in b.[85; 140]

Figure 8 - IUPAC classification of physisorption isotherms with the types of materials that present each isotherm in red

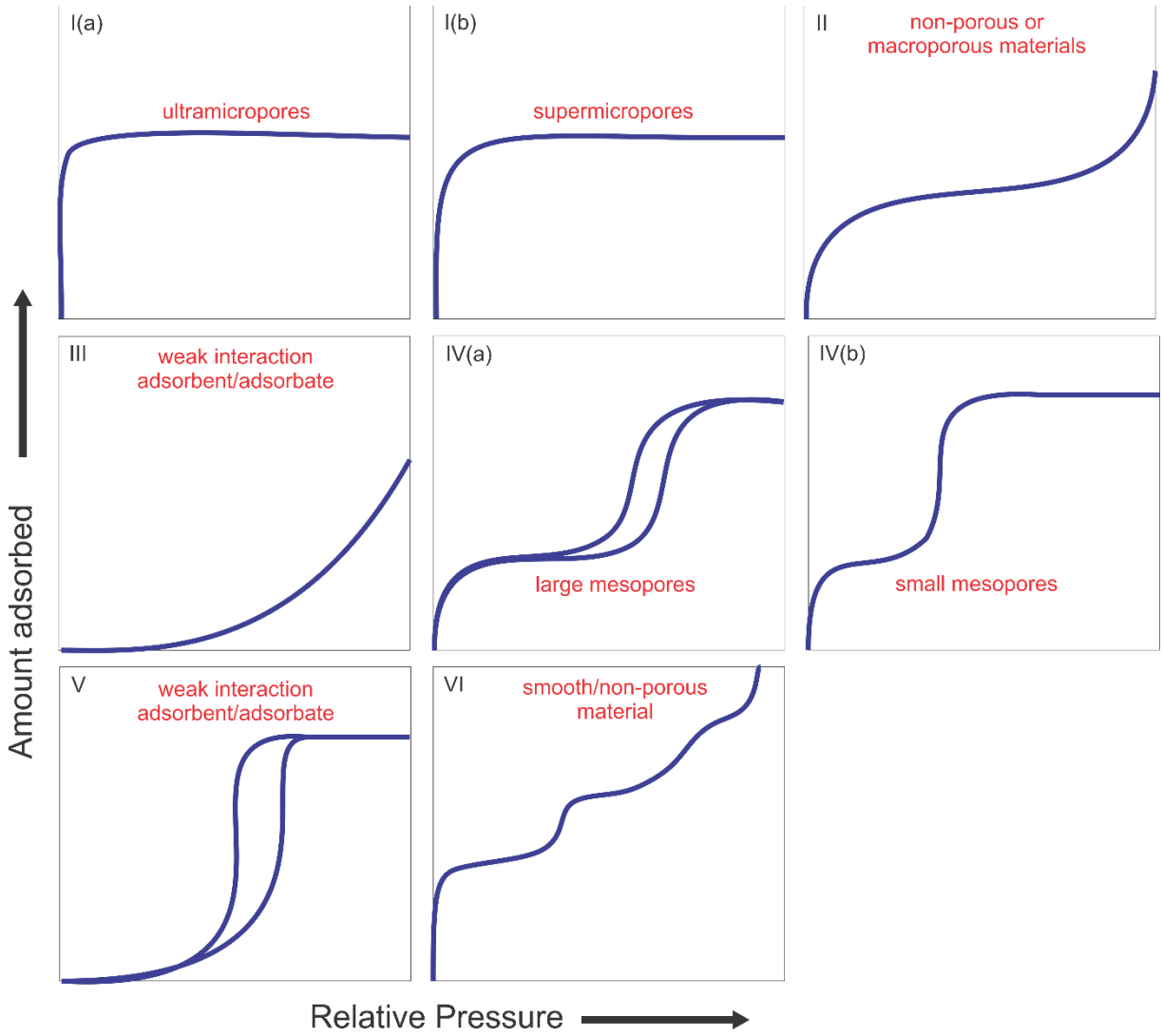

Source: Author (2021).

The pore condensation is often accompanied graphically by hysteresis loop with the desorption path different from that of adsorption. The type of loop is associated to the pore shape as presented in Figure 9.

Type H1 hysteresis loop presents a steep narrow loop on the adsorption branch, and it is dominant for materials with uniform distribution of spherical and cylindrical narrow mesopores as for templated silicas and ordered carbons, for example. In some other disordered materials represented by type H2, in addition to the steep adsorption loop, the desorption branch does not follow a similar path as observed for type H1. Materials with pores connected by necks present those isotherms and the desorption loops are caused by either pore-blocking/percolation or to cavitation-induced evaporation. The difference between types is that type H2(a) presents

the size distribution of pore cavities relatively wide compared to the distribution of neck sizes, whilst for type H2(b), the necks are wider. To present difference for the desorption branch, the neck should present diameter higher than the critical diameter for the adsorptive molecule (around 5 nm for N_2 at 77 K).[85; 140-142]

Figure 9 – IUPAC classification of hysteresis loops and their correlation with pore structure

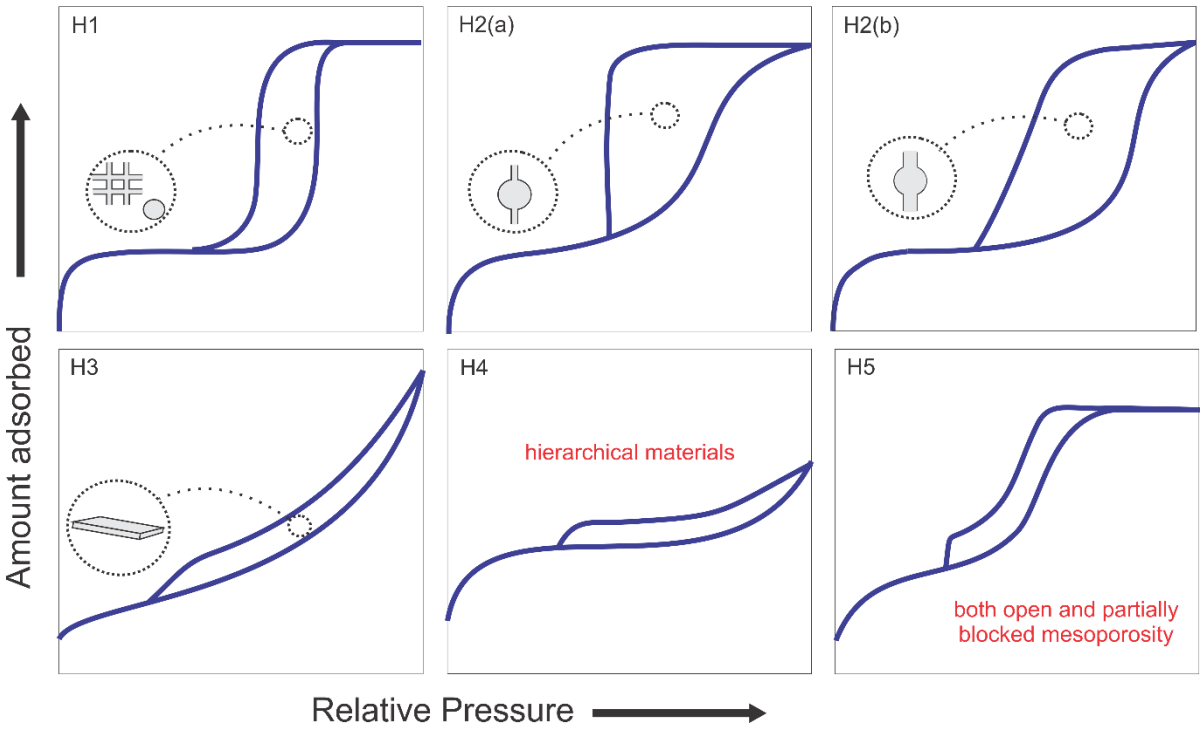

Source: Author (2021).

Type H3 hysteresis loop resembles a type II isotherm and cavitation also affects the desorption branch, as it does for the previous hysteresis types. This is typical for aggregates of plate-like particles and systems consisting of macropores not filled completely with adsorbate at atmospheric pressure. Type H4 is similar but the adsorption branch is a composite of types I and II and it is caused by materials containing micro- and meso- or macroporosity such as hierarchical carbons or mesoporous zeolites. Type H5 is unusual and it is commonly associated with pore structures containing both open and partially blocked mesopores.[85; 140]

To determine the physisorption isotherms, different apparatus can be used using static or dynamic techniques. The manometric method is the most suitable technique and the official recommendation according to IUPAC to surface area and pore size characterization.[85]

Prior to the adsorption experiment, it is required to remove all physically adsorbed material from the adsorbent surface while avoiding irreversible changes. Outgassing with

vacuum allows to prepare the surface under the same conditions that are required to start the experiment and many outgas protocols have been developed over the last decade for various types of adsorbents. Some pressure-controlled heating procedures can be applied for samples where the fragile structure can be damaged. Mostly, water is removed during degassing process. In mesopores or nonporous materials, it can be easily removed at low temperatures under influence of vacuum (<100°C), but in narrow micropores, high temperatures and long periods are often required.[85; 140]

For pore size analysis of nanoporous adsorbents ranging the complete micropore and mesopore region, the experiments should span a broad spectrum of pressures starting at ultralow pressures (0.01 mbar) which requires the use of special equipment which ensures the evacuation with a highly efficient turbomolecular vacuum pumping system as well as a combination of different pressure transducers.[85; 140]

The BET method is the most widely used procedure for evaluating the surface area of porous materials. Nitrogen was the adsorptive used traditionally and most analyses are due to the liquid nitrogen be readily available as well as the isotherms present a well-defined Point B. Although, the quadrupole of the nitrogen molecule is largely responsible for interaction with the surface functional groups, what affects not only the orientation of the adsorbate on the adsorbent surface, but also the micropore filling pressure.[85; 140]

The theory assumes that the adsorption energy is independent of the adsorption sites and gas molecules interact and under certain, carefully controlled conditions, the BET area of a mesoporous solid having types II or IV(a) isotherms can be considered to the effective area available for the adsorption. It can be applied over a relative pressure range from 0.05-0.35 in the adsorption branch of the isotherm, where monolayer adsorption takes place. For micropores, extreme caution is needed since it will be impossible to separate the process of monolayer-multilayer adsorption and micropore filling. Thus, the BET equation should be restricted to a smaller range. It must be emphasized although that the result in this case represents an apparent surface area.[85; 140; 142]

The BJH theory implements some assumptions to be used: the shape of pore is cylindrical, and the adsorbed amount results from both physical adsorption on the pore walls and capillary condensation in mesopores. Thus, it calculates the change in the thickness of adsorbed film from the decrease of relative pressure in the desorption branch and each of those decrements are result from evacuation of the largest pore from the capillary condensate and reduction in thickness of physically adsorbed water. It fails to describe both the micropore diameter and the narrow mesopores. This method is now recommended as useful only for

routine work and for an accurate pore size distribution, the Density Functional Theory (DFT).[140; 142]

This way, this work studies the formation of novel aerogel-like cartridges to be used in adsorptive systems, by combination of bacterial cellulose nanofibrils and nanoporous materials that can be either microporous, mesoporous or hybrid porous materials. The final cartridges should present improved diffusion due to the presence of hierarchical pore system and consequently, enhancing not only the removal from the medium but also the accessibility to the active sites. For this, the before mentioned characterization techniques were used, assessing the interaction between the materials, and influence of cellulose structure oxidation for the final piece.

4 EXPERIMENTAL

In this work, BC and nanoporous materials were produced individually and in composites forming cartridges being characterized by different techniques and tested in some applications as described below. The experiments were divided in 6 sections: bacterial cellulose, zeolites, PCH, multiporous zeolite, cartridges, characterization, and application tests.

4.1 Bacterial Cellulose

BC pellicles were produced at Food Microbiology Laboratory from Embrapa Brazilian Agricultural Research Corporation, using the bacterium strain *Komagataeibacter hansenii* ATCC 53582 in a culture medium described by Hestrin and Schram (HS)[143] with composition presented in Table 3:

Table 3 - Composition for the HS culture medium

Component	Concentration (g L^{-1})
Sugar	20.0
Yeast extract	5.0
Peptone	5.0
Citric acid	1.5
Sodium phosphate	2.7

Source: Author (2021).

The microorganisms were activated in sterilized HS solution at 121 °C for 15 minutes and incubated for 72 h at 30 °C in static cultivation. For production of the BC pellicles, 3% (v/v) of that inoculum were added to 70 mL of the culture medium in plastic trays. Then it was fermented statically in oven with biologic oxygen demand for 10 days at 30 °C (Figure 10a).

For purification step, the pellicles were taken out from the culture medium, washed with water flow, and kept at 70 °C for 1 h. The second purification step consisted of NaOH 2% (m/v) washing at 70 °C/1 h, followed by the pellicles' neutralization using tap water continuously and then, soaked with 2 L of DI water for 1 day.

For the disassembly step, three pellicles were cut in stripes with around 5 × 15 cm and processed with around 1 L of DI water in a high-performance blender, (Vitaprep 3, Vitamix) followed by centrifugation in an ultracentrifuge (Hitachi, CR22GIII) to 13000 rpm for 10 min at ambient temperature (Figure 10b). Humidity was measured in the resulting solid using an infrared balance (Marte, ID50) heating at 170 °C. The process was carried out at Biomass Technology Laboratory from Embrapa Brazilian Agricultural Research Corporation.

Then, part of the disassembled cellulose was oxidized by TEMPO (2,2,6,6-tetramethylpiperidine-1-oxyl) radical mediation for 2.5 h, using NaBr and NaClO. The amounts of each substance used is detailed in Table 4. At the end of the reaction, 50 mL of ethanol and HCl 0.5 mol L^{-1} were added to the system, followed by centrifugation (13000 rpm/10 min) at ambient temperature in an ultracentrifuge, resuspended in DI water, and washed with DI water for 2 times more (Figure 10c).

Table 4 - Relation between sample amount and reactants used for cellulose TEMPO oxidation

Substance	**Amount**
Sample	1.000 g
TEMPO (Sigma)	0.048 g
NaBr (Dinâmica)	0.300 g
NaClO (5% Solution, Dinâmica)	9.235 mL
H_2O	300 mL

Source: Author (2021).

By the end, the oxidized and the non-oxidized cellulose portions were nanofibrilated with concentrations adjusted by water addition (0.5 wt.% . for C0.5 and C_0, and 1.0%wt. for C1.0), using the high-performance blender in maximum rotation for 30 minutes (Figure 10d). The main steps (cultivation, purification and disassembly, oxidation and nanofibrilation) and conditions to obtain BC suspension are illustrated in Figure 10 with a scheme of the possible structure to the cartridges, on the bottom.

Figure 10 - Illustration showing the main steps and conditions to obtaining BC suspensions used in this work where the (a) cultivation, (b) purification and disassembly, (c) oxidation, and (d) nanofibrilation steps are illustrated. On the bottom, there is a scheme for the cellulose cartridges microscopically

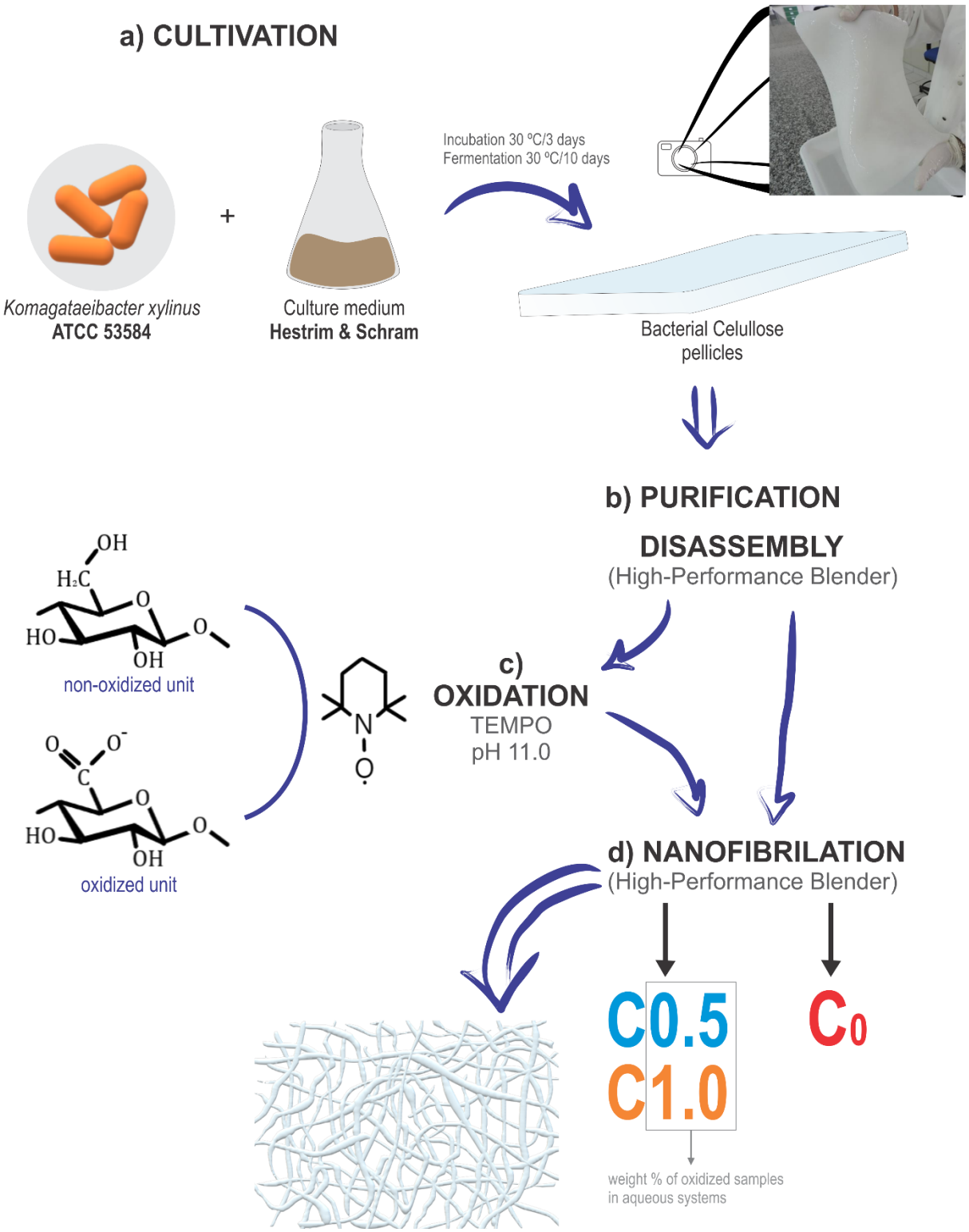

Source: Author (2021).

4.2 Zeolites

Two conventional zeolites (zeolites with only micropores in their crystals) were synthesized to this work, zeolite A and zeolite X, which present different pore structures. These are zeolites obtained easily, that have low Si/Al ratio and their synthesis can be performed without the use of organic molecules. When used for either adsorption or ionic exchange test, it is possible to compare their efficiency, as well as the difference on crystal shape and size, it will be observed the influence when interacting with the BC in the composite samples.

4.2.1 Zeolite A

The proposed micron-sized zeolite crystal was zeolite A, synthesised by hydrothermal route where the synthesis gel was prepared mixing a silicate solution, obtained from dissolving 7.16 g of sodium metasilicate ($NaSiO_3$, Sigma) in 35 mL of sodium hydroxide (NaOH, Vetec) 0.21 mol L^{-1}, to an aluminate solution obtained similarly to the previous one, dissolving 5.00 g of sodium aluminate ($NaAlO_2$, Sigma) in 35 mL of NaOH 0.21 mol L^{-1}.

This mixture formed a thick-white gel that was homogenised and transferred to a Teflon vessel (72 mL maximum volume) coupled to a stainless-steel autoclave. The autoclave was kept at room temperature for 24 h for ageing and then, heated at oven to 100 °C for 4 h. The solid obtained was centrifuged at 4000 rpm for 5 minutes, 8 times until reaching a pH lower than 11. The material was then dried at 110 °C and granulometry measured at 200 mesh (75 µm aperture).

Figure 11 presents in short, the procedure used to this synthesis, including the oxides ratio, as described by Thompson and Huber,[12; 144] that resulted in the weight amounts reported.

Figure 11 - Scheme presenting in summary the zeolite A synthesis procedure

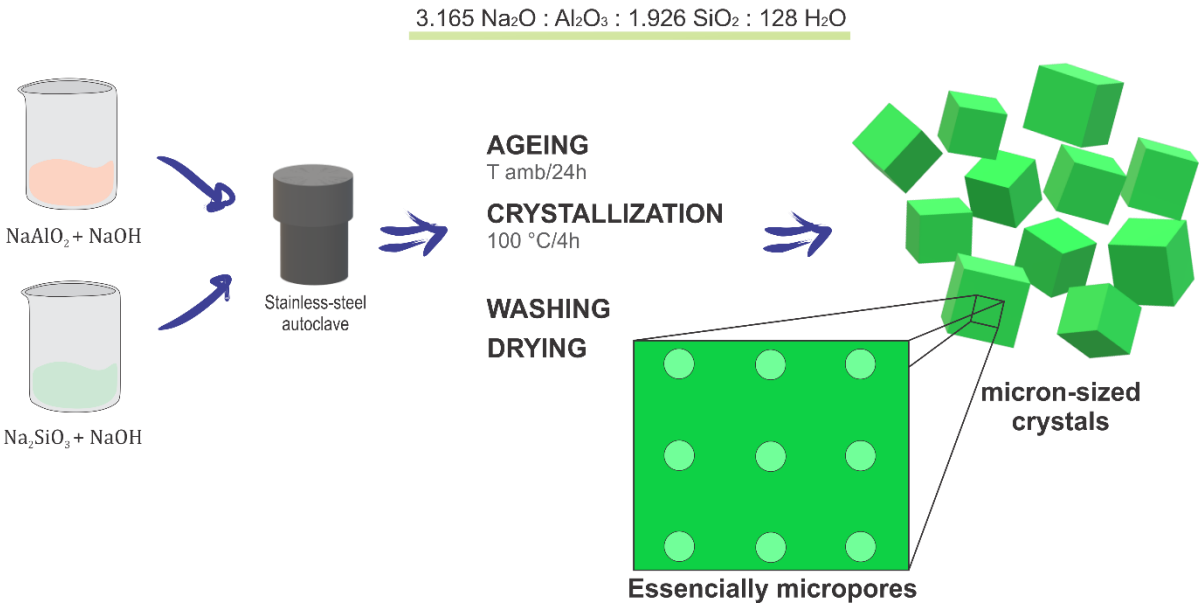

Source: Author (2021).

4.2.2 Zeolite X

In order to obtain a nanometric faujasite structure, a two-step methodology was used with the oxides ratio for each of them as described by Ginter, Bell and Radke,[145] presented in Figure 12 along with a general scheme for the process.

For seeding step (A), a silicate solution, prepared by dissolving 6.52 g of Na2SiO$_3$ in 16 mL of distilled water, was added under magnetic stirring to an aluminate solution, prepared by mixing 2.09 g of $NaAlO_2$ and 4.07 g of NaOH in 20 mL of distilled water until dissolution. This mixture was left at room temperature for 24 h.

For growing the seeds, a silicate solution (10.22 g of $NaSiO_3$ dissolved in 25 mL of distilled water) was added under magnetic stirring to the aluminate solution (formed with 35 mg of NaOH and 3.27 g of $NaAlO_2$ in 33 mL of distilled water). For the global synthesis gel, 4 mL of seeding solution was mixed to the growing solution dropwise while homogenization. The resulting gel was transferred to a Teflon vessel coupled to a stainless-steel autoclave to an induction cycle at room temperature following by crystallisation for 7 h in an oven at 100 °C. The solid obtained was centrifuged at 4000 rpm for 5 minutes for 8 times until pH lower than 11. The material was then dried at 110 °C and granulometry measured at 200 mesh (75 µm aperture).

Figure 12 - Scheme presenting in summary the zeolite X synthesis procedure

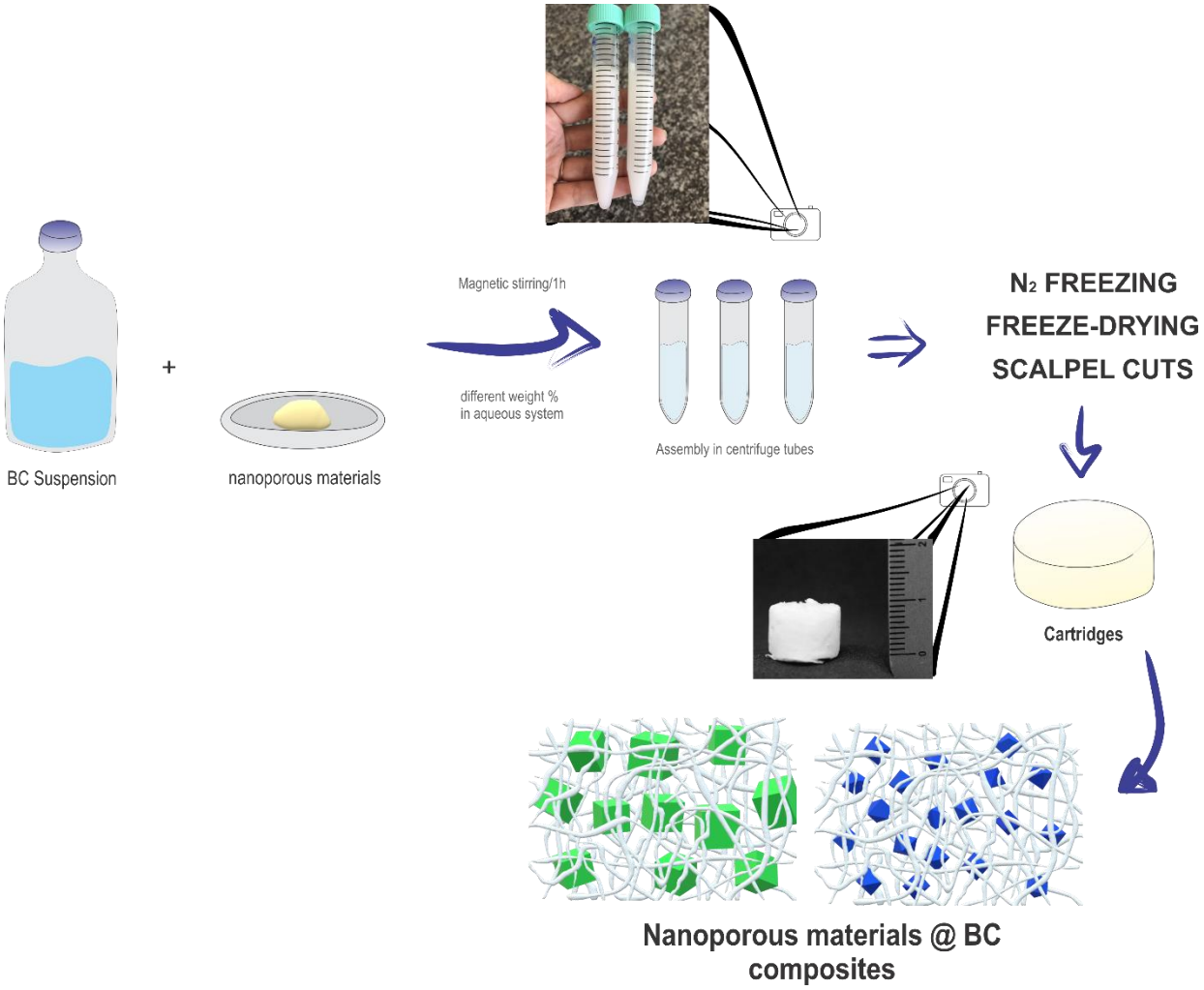

Source: Author (2021).

4.3 Mesoporous aluminosilicate

Kaolin was used as raw material for the mesoporous clay, provided by Rocha minérios - PB and its characteristics are described elsewhere.[146; 147] Prior to the synthesis, the clay was calcined and dealuminated partially. The calcination step was performed in a furnace forming metakaolin, at 600 °C/2 h, with heating rate of 10 °C min^{-1}. For dealumination, 10 g of the sample was transferred to a round flask with 100 mL of H_2SO_4 2.5 mol L^{-1}, heated for 90 °C/2 h under reflux. The solid was centrifuged, washed with diluted acid and water until pH 7.

The mesoporous aluminosilicate was formed in a gel with 1.00 g of dealuminated metakaolin mixed with 40 mL of NaOH 0.1 mol L^{-1} and 0.48 g of CTAB ($C_{19}H_{42}BrN$, cetyltrimethylammonium bromide, Vetec) stirring magnetically for 24 h, followed by an ageing time of 24 h and crystallization by hydrothermal treatment in a Teflon-lined stainless-steel autoclave at 110 °C/24 h. The solid was washed five times with DI water, dried overnight at 110 °C, and calcined at 550 °C/4 h, with heating rate of 1 °C min^{-1}. This sample was named M.

4.4 Multiporous zeolite

To obtain a hierarchical zeolite with mesopores in the formed crystal, TPOAC was used in a conventional gel synthesis as presented below. With these experiments it was possible to identify the influence on the external surface to the effective cartridges' formation, as well as to evaluate the activity for zeolite A in two different forms (either micropores or micro-mesoporous sample).

4.4.1 Zeolite A

The synthesis gel was prepared mixing a silicate solution containing the organosilane, obtained from dissolving 1.71 g of sodium metasilicate into 25 mL of sodium hydroxide 0.81 mol L^{-1} and 1.5 mL of TPOAC ($[(CH_3O)_3Si(CH_2)_3N(CH_3)_2(CH_2)_{17}CH_3]Cl$, [3-(trimethoxysilyl) propyl] dimethyloctadecyl ammonium chloride solution 42 wt.% in methanol, Sigma), to an aluminate solution, obtained by dissolving 1.91 g of sodium aluminate in 25 mL of NaOH 0.81 mol L^{-1}. This mixture formed a thick white gel that was homogenised for 10 minutes under magnetic stirring, and it was transferred to a Teflon vessel (42 mL maximum volume) coupled to a stainless-steel autoclave.

The autoclave was kept at room temperature for 24 h for ageing and then, heated in an oven to 100 °C for 4 h. The solid obtained was filtered until pH < 11. The material was then dried at 70 °C and calcined at 550 °C for 6 h using a heating rate of 2 °C min^{-1}.

Figure 13 presents in short, the procedure used for this synthesis, including the oxides ratio, as described by Cho *et. al*.[89] that resulted in the weight amounts reported previously.

Figure 13 - Scheme presenting in summary the multiporous zeolite A synthesis procedure

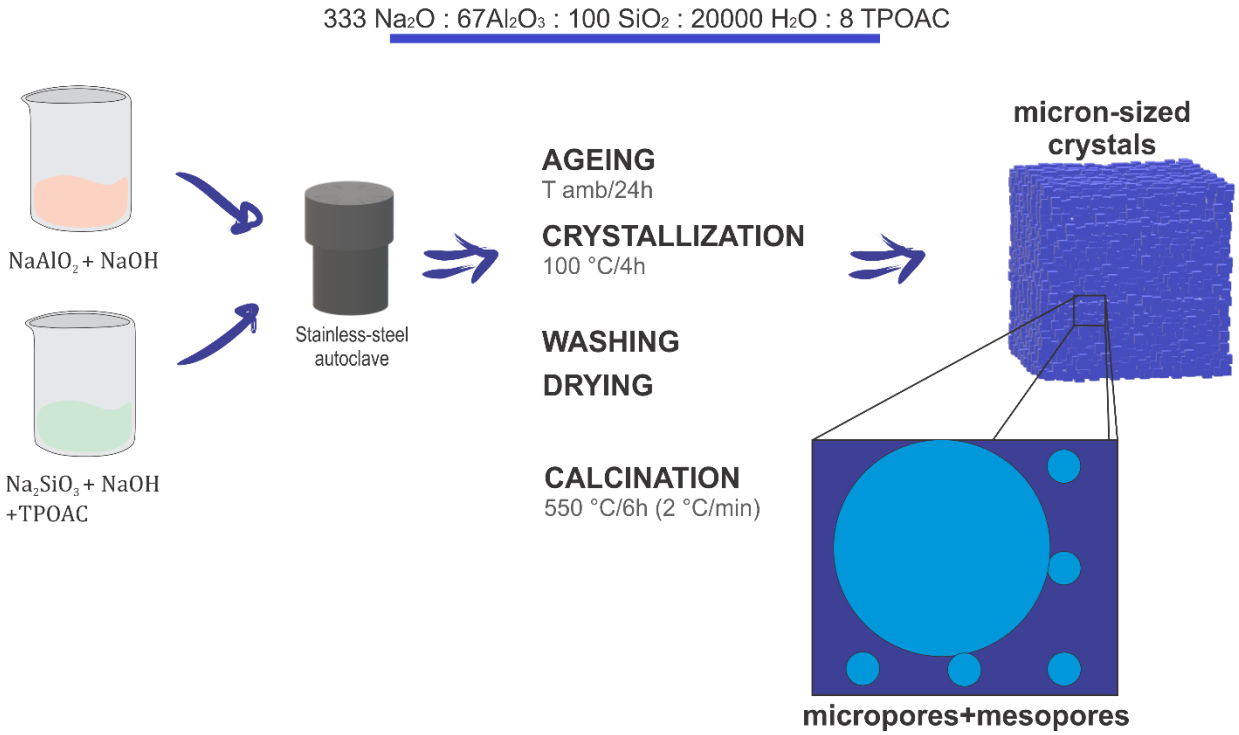

Source: Author (2021).

4.5 Cartridges

The cartridges with hierarchical structure were produced using oxidised and non-oxidised cellulose for two main different studies: composites mass study and oxidation influence study. For that, cartridges containing just cellulose, both oxidised, and non-oxidised, were formed, as well as cartridges adding the nanoporous materials reported above. Table 5 presents the materials formed and their names.

Table 5 - Summary on the names and compositions to the composite samples formed for this work

	Cellulose		
Nanoporous Material	**Non-oxidised (C_0) 0.5 wt.% .**	**Oxidised (C_{oxi}) 0.5 wt.% .**	**Oxidised 1.0 wt.% .**
Zeolite A	C_0A	C0.5-A0.5, C0.5-A1.0 (or $C_{oxi}A$)	C1.0-A0.5, C1.0-A1.0
Zeolite X	C_0X	C0.5-X0.5, C0.5-X1.0 (or $C_{oxi}X$)	C1.0-X0.5, C1.0-X1.0
Mesoporous clay	C_0M	C0.5-M0.5, C0.5-M1.0 (or $C_{oxi}M$)	C1.0-M0.5, C1.0-M1.0
Multiporous Zeolite A	-	$C\text{-}A_b$	-

Source: Author (2021).

For the composites mass studies, the weight composition was calculated in the wet system, changing from 0.5% and 1.0% for cellulose and zeolites A, X and M samples. These nanoporous materials were also used for the oxidation influence studies. The cartridges formed with zeolite A multiporous used 0.5% of oxidised cellulose and 1.0% of each porous material.

Figure 14 presents briefly, the methodology where the BC suspension and the nanoporous materials described previously are mixed with distilled water in different weight compositions to obtain the materials in Table 5. Homogeneous dispersions of the composites were obtained with magnetic stirring for 1 h. 10 mL of BC or composite suspension were added to a 15 mL falcon tube (conical bottom, cylinder body with 12 cm height and 14.5 mm diameter), followed by liquid N_2 freezing and stored in ultra-freezer -80 °C to freeze-drying (Labconco FreeZone 4.5). After freeze-drying, the cartridges were taken out from the tubes and

cut in smaller parts using scalpel, producing cartridges with a few millimetres, which were used in most of the characterisation essays, and ca. 10 cm for application tests.

Figure 14 - Scheme presenting the cartridges formation for the composite samples, showing initially the mixture, then, their aspect in the tubes, and the final cartridges after the freezing, freeze-drying, and scalpel cuts

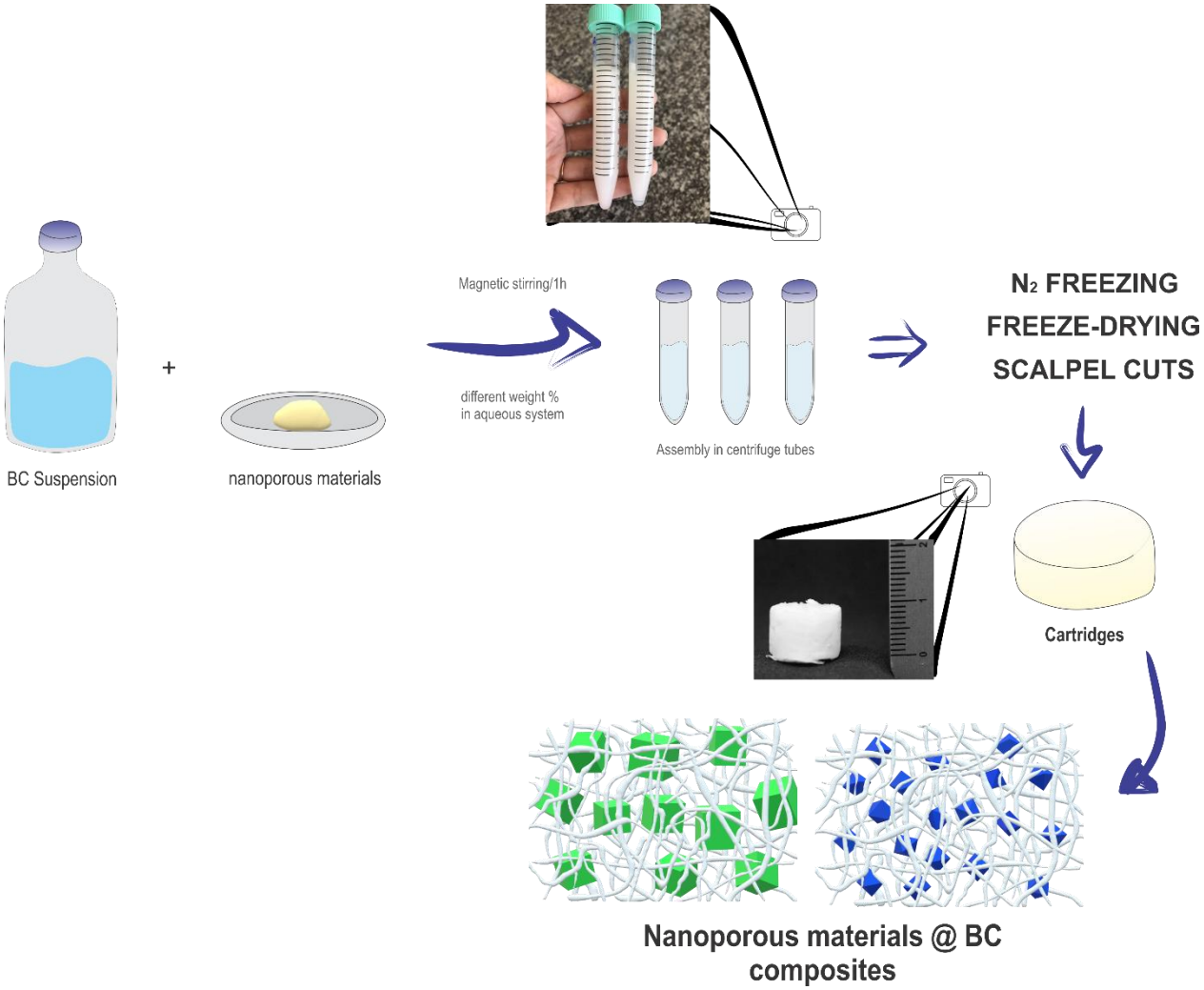

Source: Author (2021). Cellulose cartridges are prepared with the steps presented after assembly in centrifuge tubes.

4.6 Characterization

The obtained materials were characterised using different techniques that helped to identify the formed materials, their interactions, morphologies, and differences in their main properties.

4.6.1 X-ray diffraction

XRD measurements were carried out in a polycrystalline diffractometer model X-Pert PRO MPD-Panalytical, with spinner and Bragg-Bretano geometry, working in continuous mode and CoKα radiation with a linear focus at 40 kV and 40 mA. The diffractograms were obtained in the range from 5 to 50 °2θ and 67 count s^{-1}, at X-Rays Laboratory, Federal University of Ceará.

The crystalline phases identification was performed with the X-Pert HighScore Plus (Panalytical).

4.6.2 Scanning electron microscopy

SEM images were acquired using two tungsten filament electron beam microscopes, Inspect S50 (FEI) and Quanta 200 (FEI), and one Field-emission gun equipment, Quanta FEG 450 (FEI), with magnification up to 200,000 ×. The voltage acceleration was from 5.0 to 20.0 kV. Everhart-Thornley for secondary electrons and energy-dispersive X-ray detectors were used during the analysis. The samples were placed in aluminium stubs using carbon tape or Ag glue and metallized with 10 nm Platinum layer or 20 nm Gold layer.

The microscopes used were part of Analytical Central at Federal University of Ceará and School of Materials, The University of Manchester.

4.6.3 Transmission electron microscopy

TEM analyses were performed using a few milligrams from the solid zeolite X sample, dispersed in isopropylic alcohol, and treated in an ultrasonic bath for 20 min. Two droplets of this dispersion were added to a copper grid (300 mesh) recovered by a thin carbon layer (5 nm). This grid was then dried at room temperature overnight and analyzed in

TEM/HRTEM mode using a JEOL microscope, model JEM 2100 FEG-TEM operating at 200 kV at CNPEM, National Research Centre for Energy and Materials, LNNano, National Nanotechnology Laboratory. The acquired images were analysed in ImageJ Open source software.

4.6.4 Infrared spectroscopy

Infrared spectroscopy analyses were performed with the powder and cartridges samples. A small portion of sample was dispersed in KBr, forming pastilles analysed from 4000 to 400 cm^{-1} wavenumber range and a 2 cm^{-1} resolution in % Transmission using a Shimadzu equipment, model IRTracer-100 at the Analytical Central from the Chemistry Graduate program, Federal University of Ceará.

4.6.5 Carboxylate groups determination

The carboxylate content of the oxidized cellulose was determined using an electric conductivity titration method, where NaCl 0.01 mol L^{-1} (16,67 mL) was added to the cellulose (1.0 g) in water (183.3 mL) and then, the mixture was sufficiently stirred to obtain a well-dispersed slurry. Then, 0.1 mol L^{-1} HCl was added to set the pH value in the range of 2.5-3.0. This mixture was titrated using NaOH 0.04 mol L^{-1} to pH 11 (around 50 mL).

The carboxylate content was determined using the volumes V_0 and V_1 (NaOH volumes for the strong acid, HCl, and weak acid, -COOH, neutralization, respectively) at the conductimetry curve obtained.[148-151] To obtain the carboxylate content per cellulose gram and the degree of oxidation, equations (6) and (7), were used respectively.

$$C = \frac{(V_1 - V_0) \cdot C_{NaOH}}{m} \quad (6)$$

$$D.O.(\%) = \frac{162 \cdot mol_{acid}}{C - 14 \cdot mol_{acid}} \times 100 \quad (7)$$

Where: C = carboxylate content;

C_{NaOH} = NaOH concentration used on the titration;

m = dry cellulose weight;

mol_{acid} = C × m

162 = molecular weight to anhydrous-glucose units;

14 = molecular weight referent to the difference between C_{oxi} and C_0.

4.6.6 Nuclear magnetic resonance

Solid-state nuclear magnetic resonance spectroscopy was performed on a Bruker Advance 400 MHz spectrometer using a 4 mm probe, at a spin rate of 12000 Hz using a 90° pulse tip angle. ^{29}Si spectra were recorded with a 10 s recycle delay, while the ^{13}C and ^{27}Al, with 5 s.

For calculation of Si/Al ratio to zeolite X sample, with the relative intensities/areas to the Q_4 peaks, using Lowenstein's rule[123; 152] presented in equation (8):

$$Si/Al_{framework} = \frac{\sum_{n=0}^{4} I_{Si(nAl)}}{\sum_{n=0}^{4} \frac{n}{4} I_{Si(nAl)}} \quad (8)$$

Where: $I_{Si(nAl)}$ is the intensity (or area) of the NMR signal to Si(nAl) units

4.6.7 Thermogravimetric analyses

Thermal analysis measurements for the powders and the cartridges were performed in STA 6000 analyzer (PerkinElmer Instruments) using a heating rate of 10 °C min^{-1}, with a temperature range from 25 to 800 °C in synthetic air, 50 mL min^{-1} flow with around 8 mg of each material at Biomass Technology Laboratory from Embrapa Brazilian Agricultural Research Corporation.

Samples containing Zeolite A multiporous were performed in TGA Q50 (TA instruments) with the same parameters at the Analytical Central from the Chemistry Graduate program, Federal University of Ceará.

4.6.8 Textural Properties

The textural properties were determined by N_2 adsorption/desorption isotherms measurements obtained at -196 °C in relative pressure range from 0.01 to 0.995 with 50 points in adsorption and 50 points to desorption in a volumetric adsorption equipment Micromeritics ASAP 2020 at the Chemical Engineering and Analytical Sciences (CEAS), The University of Manchester.

For degassing, two temperatures were studied using 90 °C for 12 hours to the cellulose samples and composites as suggested in Zhang *et al.*[153] (C_0, C_{oxi}, C_0A, $C_{oxi}A$, C_0X, $C_{oxi}X$, C_0M, $C_{oxi}M$, $C\text{-}A_b$). The powder samples analysed were degassed using the 90 °C program as well at 350 °C to evaluate how the surface area can be related to the real ones (zeolite X, M sample and multiporous zeolite, A_b).

The specific surface area was calculated using the Brunauer-Emmett-Teller (BET) method considering the linear portion to the graphs ($P/P_0 = 0.05 – 0.35$), equation (9); the pore distribution graphs were obtained by the Barret-Joyner-Halenda (BJH) method using the desorption isotherm to the Kelvin model of pore filling, equation (10); and the total pore volume for each sample used the Gurvich rule, equation(11), measuring the nitrogen uptake just before it starts to condense outside the material.

$$\frac{{}^{P}/_{P_0}}{V \cdot \left(1 - {}^{P}/_{P_0}\right)} = \frac{1}{V_m \cdot C} + \frac{C - 1}{V_m \cdot C} \cdot \left({}^{P}/_{P_0}\right) \tag{9}$$

Where: S = specific surface area (m^2/g);

V_m = (cm^3 STP adsorbate/ g adsorbent);

N = Avogrado number (6.0221367×10^{23});

A_m = Adsorbate transversal area ($Å^2$).

$$\ln \frac{P}{P_0} = \frac{2\gamma V_M}{rRT} \tag{10}$$

Where: γ = surface tension of the adsorbate in the liquid form;

V_M = molar volume of the liquid;

R = universal gas constant;

r = radius of the meniscus formed in the mesopore;

T = temperature.

$$V_{pore} = \frac{n_{N_2}}{\rho_{N_2}} \tag{11}$$

Where: n_{N2} = specific amount of nitrogen adsorbed (g of nitrogen/g of crystal);

ρ_{N2} = density for liquid N_2.

4.7 Preliminary tests as adsorbents in aqueous medium

The materials were tested preliminary as adsorbents in aqueous medium initially to identify their ionic exchange for Ca^{2+} and then in a kinetic study surrounding Pb^{2+} over the multiporous zeolite.

4.7.1 Ca^{2+} ionic exchange experiments

The Ca^{2+} ionic exchange experiments were performed in triplicate with conical flaks containing 25 mL of a 3 mmol L^{-1} Ca^{2+} solution (prepared using $CaCl_2 \cdot 2H_2O$ in deionized water) stirring at 250 rpm for 30 minutes in an orbital shaker. At the end, the samples were centrifuged for 3800 rpm/2 min and analysed using flame photometry in an Analyser 910M equipment at Trace Analysis Laboratory, Federal University of Ceará.

The materials used for this step were the pure cellulose samples: C_0 and C_{oxi} (5 mg); the zeolite powders: A, X and A_b (10 mg each); and their respective composites: C_0A, C_0X, $C_{oxi}A$, $C_{oxi}X$ and C-A_b (15 mg each). These weights were defined considering that the composites used have C_{oxi} with 0.5 wt.% . in aqueous medium with 1.0 wt.% . for the nanoporous materials, and when dried, they possess a 1:2 cellulose:zeolite weight ratio. Figure 15 presents the steps used for this, including the weights used for each type of sample during the experiments.

Figure 15 - Scheme representing the Ca^{2+} ionic exchange experiments performed for the samples C_0, C_{oxi}, C_0A, C_0X, $C_{oxi}A$, $C_{oxi}X$, C-A_b and the zeolites A, X and A_b

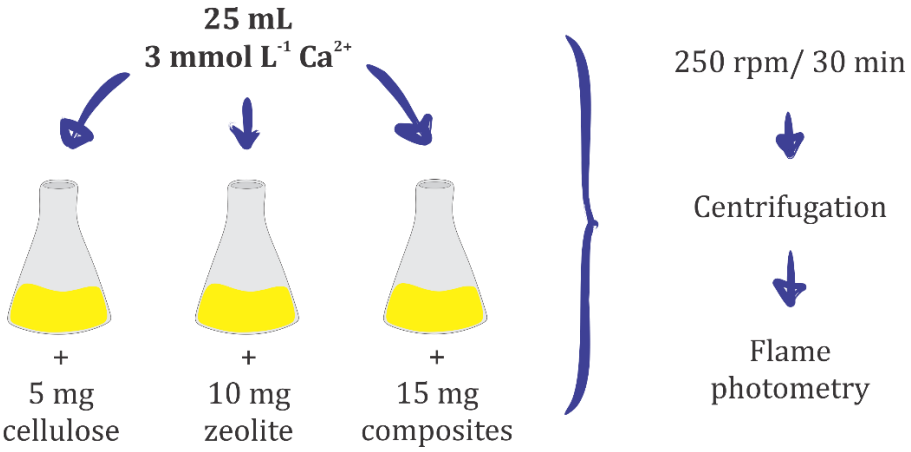

Source: Author (2021).

The results were expressed as Removal % for Ca^{2+} in both expected (calculated using the EDS values for Na^{+} in each sample, considering complete exchange by the structures) and real conditions. Equation (12) presents the calculation for this value:

$$Removal\% = \frac{(C_0 - C_e)}{C_0} \cdot 100 \qquad (12)$$

Where: C_0 = adsorbate initial concentration at equilibrium (mg g^{-1});

C_e = adsorbate concentration at equilibrium (mg g^{-1}).

4.7.2 Pb^{2+} adsorption studies

Two studies were performed regarding Pb^{2+} adsorption over the multiporous zeolite and three answers were obtained: selectivity in a multi-component solution with Cd^{2+} and for mono-component solutions, contact time and kinetic curves were studied. Figure 16 presents the schemes that summarize those steps.

Figure 16 – Scheme representing the Pb^{2+} adsorption studies of selectivity in a multi-component solution with Cd^{2+} by zeolite A_b related samples

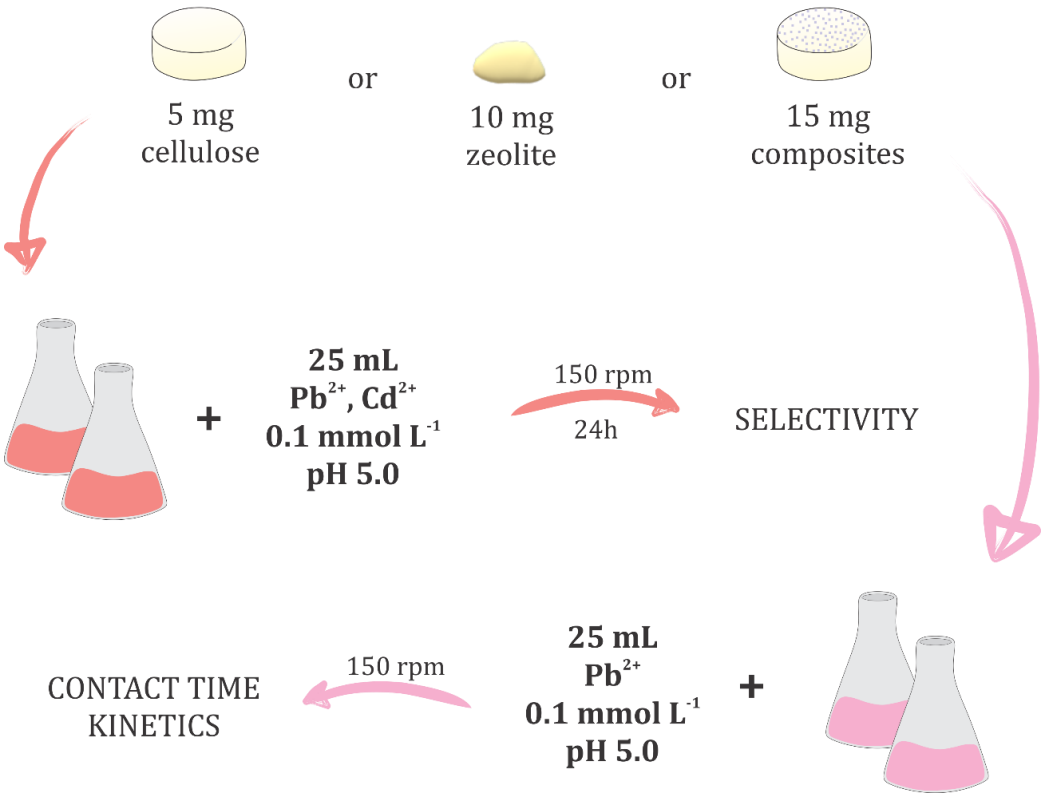

Source: Author (2021).

Selectivity studies were performed in triplicate with conical flasks containing 25 mL of a multi-component solution with 0.1 mmol L^{-1} for both Cd^{2+} and Pb^{2+} (prepared using their nitrate salts in CH_3COOH/CH_3COO^- buffer pH 5.0: $Pb(NO_3)_2$ and $Cd(NO_3)_2{\cdot}4H_2O$, Vetec) stirring at 150 rpm for 24 h in an orbital shaker. The samples weights were the same as reported previously for Ca^{2+} ionic exchange experiments: 5 mg for the cellulose sample, 10 mg for the zeolite samples (zeolite A was used to be compared to the multiporous zeolite A, A_b, and thus, allow the observation of mesoporous influence on the adsorption process) and 15 mg for the composite samples (C-A and C-A_b).

After 24 h, samples were centrifuged for 3800 rpm/2 min and analysed using flame atomic absorption spectrophotometry (FAAS) in a GBC 933 Plus equipment at Trace Analysis Laboratory, Federal University of Ceará.

The results were expressed as Removal %, adsorption capacity (q_e, mmol g^{-1}), expressed in equation (13), and ratio among q_e for Pb^{2+} and Cd^{2+}, expressed in equation (14),[154] to observe the selectivity calculation.

$$q_e = \frac{\left[\frac{(C_0 - C_e)}{m} \cdot V\right]}{MW} \tag{13}$$

Where: q_e = adsorption capacity at equilibrium (mmol g^{-1})

C_0 = adsorbate initial concentration at equilibrium (mg g^{-1});

C_e = adsorbate concentration at equilibrium (mg g^{-1});

m = sample weight (g);

V = adsorbate volume added (25 mL);

MW = molecular weight (for Pb, 207.2 g mol^{-1}; Cd, 112.4 g mol^{-1}).

$$S = \frac{q_e(Pb)}{q_e(Cd)} \tag{14}$$

Where: q_e(X) = adsorption capacity at equilibrium for X metal (mmol g^{-1}).

The contact time studies were performed in duplicate with conical flasks containing 25 mL of a mono-component solution with 0.1 mmol L^{-1} Pb^{2+} pH 5.0 solution stirring at 150 rpm for pre-determined time intervals (1, 3, 5, 10, 20, 30, 60, 120, 180, 240 and 300 min) in an orbital shaker. The weights for the samples were the same as reported previously for Ca^{2+}– ionic exchange and selectivity experiments: 5 mg for C, 10 mg for zeolite powders, A and A_b, and 15 mg for the composite samples, C-A and C-A_b. The results were expressed as

Removal %, adsorption capacity (q_e, mmol g^{-1}) and the data for C was used as a blank and subtracted from C_0 on the calculations for the composites.

The adsorption kinetics studies were performed using the contact time experiment data for the zeolites and their composites. The data for C was used as a blank and subtracted from C_0 on the calculations for the composites. Using the linear form for the pseudo-first order, described below by equation (15), and pseudo-second order, equation (16), models the data was adjusted and analysed.[155; 156] Using the intercept and slop from the linear fitting of each model, it was possible to obtain velocity constants and q_{calc} for the samples, presented together to the R^2 and error obtained.

$$\log(q_e - q_t) = \log q_e - \left(\frac{k_1}{2.303}\right) t \quad (15)$$

Where: q_e = adsorption capacity at equilibrium (mg g^{-1});
q_t = adsorption capacity at time *t* (mg g^{-1});
k_1 = pseudo-first order adsorption velocity constant (min^{-1});
t = time interval (min).

$$\frac{t}{q_t} = \frac{1}{k_2 q_e^2} + \frac{1}{q_e} t \quad (16)$$

Where: q_t = adsorption capacity at time *t* (mg g^{-1});
q_e = adsorption capacity at equilibrium (mg g^{-1});
k_2 = pseudo-second order adsorption velocity constant (g mg^{-1} min^{-1});
t = time interval (min).

Intraparticle diffusion investigation was performed for multiporous zeolite A_b and its composite with oxidized cellulose, C-A_b, using the contact time experimental data to obtain plots from $t^{1/2} \times q_t$ as described by equation (17). Two regions were identified to the graphs and from the slope in each independent linear fitting, the diffusion coefficients were obtained.

$$q_t = K_D t^{1/2} + C \quad (17)$$

Where: q_t = adsorption capacity at time *t* (mg g^{-1});
t = time interval;
K_D = intraparticle diffusion coefficient (mmol g^{-1} $min^{-1/2}$);
C = diffusion constant.

5 RESULTS AND DISCUSSION

The results and discussion for this work were divided by chapters, allowing the organization of the information acquired in groups of samples.

Chapter 6 deals about cartridges formed by pure cellulose nanofibrils, assessing both the partial oxidation of the structure and the concentration on the precursor hydrogel, in a way that the main properties for the neat samples can be inferred before the addition of any nanoporous material.

Chapters 7 8 and 9 present the results for the materials prepared from the cellulose aerogels structure with zeolites A and X, and the mesoporous aluminosilicate, respectively. Different weight compositions of 0.5% or 1.0% were analysed for both oxidized cellulose and nanoporous material, and using some characterization techniques, it was able to identify the main features for the materials and suggest their interactions.

In chapter 10 the influence for the cellulose oxidation is evaluated over the preparation of the cartridges with the materials studied previously (using the composition: 0.5% cellulose: 1.0% nanoporous material, resulting in a 1:2 ratio to the dried samples). Performing some characterization and ionic exchange experiments, it was possible to identify details and features that differentiate them and suggest the best choice to obtain such materials.

And finally, chapter 11 brings the results for hierarchical materials prepared from the cellulose aerogel structure with multiporous zeolite A. Due to the novelty and the promising properties that could be observed to this kind of materials, they were fully characterized and tested in aqueous adsorption systems. Most of the results discussed in there are published in Microporous and Mesoporous Materials, 312, Bessa, França, Pereira, Alexandre, Pérez-Page, Holmes, Nascimento, Rosa, Anderson and Loiola, Hierarchical zeolite based on multiporous zeolite A and bacterial cellulose: An efficient adsorbent of Pb^{2+}, 110752, Copyright Elsevier (2021).[157]

To conclude, the main findings of the work are organized in the General Conclusions chapter, and the last chapters present some suggestions for future works in this field and the Resulting papers and presentations.

6 CELLULOSE

In this chapter, the cartridges are formed by pure cellulose nanofibrils (without zeolite-like particles addition) and both the partial oxidation of the structure and the concentration in the precursor hydrogel are analysed allowing the main properties for the neat samples to be inferred before the addition of any nanoporous material.

6.1 XRD

The XRD results were used primarily to identify the main phases for the crystalline materials and how they behave when the composites are formed. Figure 17 presents the XRD patterns to the cellulose samples: C1.0 (Figure 17a), C0.5 (Figure 17b) and C_0 (Figure 17c). The blue squares point to the main peaks for cellulose Iα.

Figure 17 – Co-Kα XRD patterns to the cellulose samples: (a) C1.0, (b) C0.5, and (c) C_0

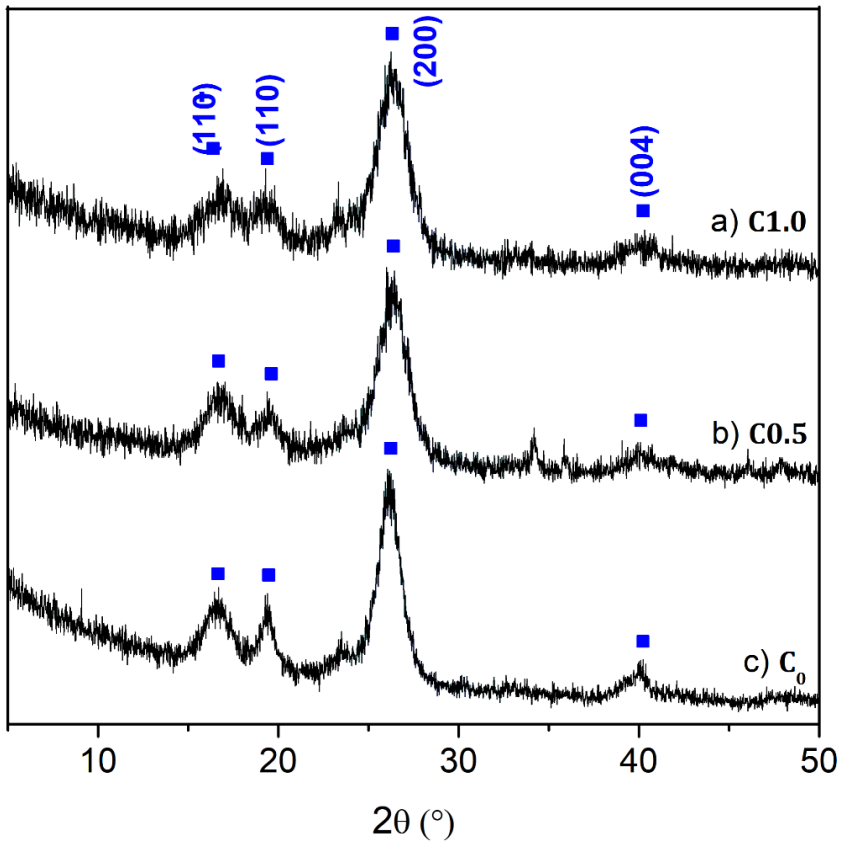

Source: Author (2021). The blue squares point to the Iα cellulose main peaks. Y axis = Intensity (a.u.).

All the cellulose samples used to this work present the main peaks referent to Iα cellulose in 2θ angles 16.5, 19.5, 26.1 and 40.0 °, related to the crystallographic planes ($1\bar{1}0$), (110), (200) and (004), respectively.[58; 66; 158; 159] This phase is registered on the Cambridge Structural Database System (CSDS) with the code 792796.[54] The structure oxidation keeps the plans in the same positions and relative intensities. The exception is only for the (004) peak, that becomes a shoulder in same 2θ value to C0.5 (Figure 17b) and C1.0 (Figure 17c). This is an indication that the oxidation does not change the crystallinity to the cellulose, as reported in other works.[148; 150; 160]

6.2 SEM

Figure 18 presents the scanning electron microscopy images for cellulose samples as stamped in each of them as it follows: BC (Figure 18a), C_0 (Figure 18b), C0.5 (Figure 18c) and C1.0 (Figure 18d). All the images bring the same scale bar.

Figure 18 – Scanning electron microscopy images for cellulose samples as stamped in each: (a) BC, (b) C_0, (c) C0.5 and (d) C1.0

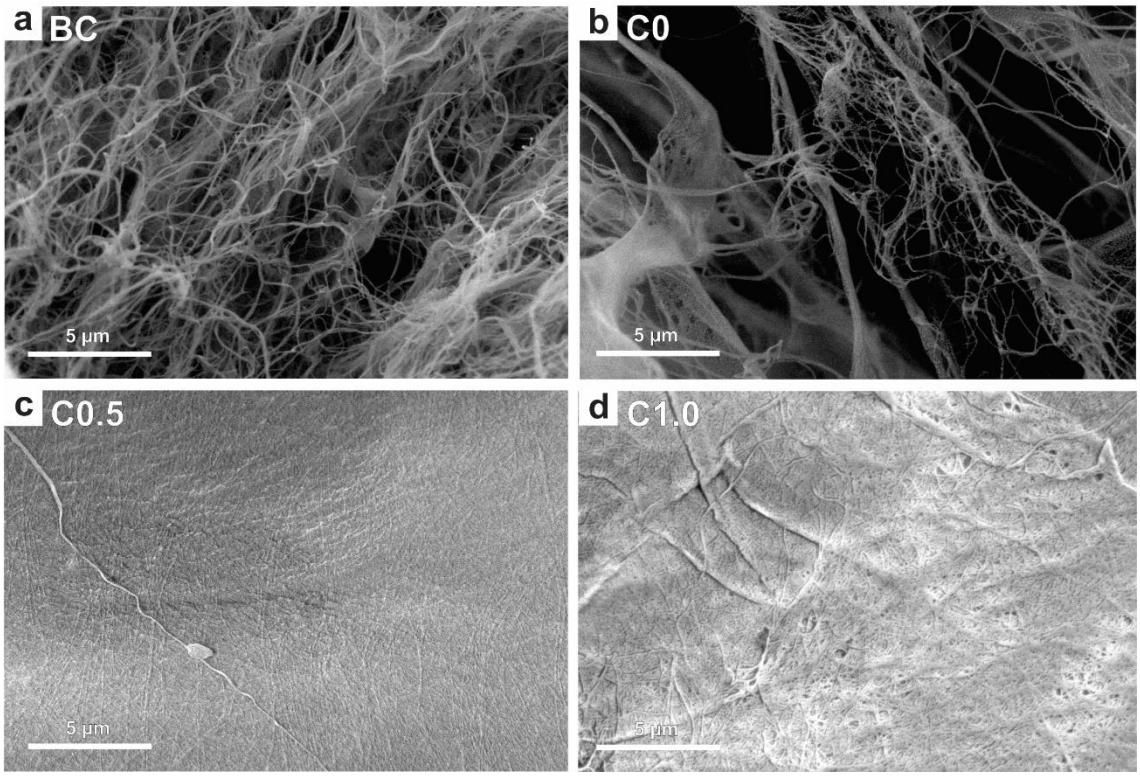

Source: Author (2021). All the images present the same scale bar of 5 µm.

The BC pellicle (Figure 18a) is essentially homogeneous nanofibrils forming a web, with diameters ranging from 50 to 100 nm as reported in previous works.[58; 158; 161] The disassembling step and adjustment in the cellulose content promotes some fibres to connect each other in thin sheets for the C_0 sample (Figure 18b) although most of it remains as nanofibrils connecting these sheets and loose through the cartridges structure while to oxidized samples the fibres are mainly forming bigger sheets.

Regarding to the samples changing the mass composition in the composite, it is possible to see an opened structure produced when the cartridges are formed in a way that the cellulose nanofibers are organized in irregular thin sheets with a few dozens in micrometre for the length and those are linked to other similar ones. This feature is forced during the freezing step, when the water nucleation and crystallization in ice crystals through the suspension pushes the fibres to interstitial regions forming this honeycomb structure with big voids.[162-166] For this reason, the cartridges present very low density, 10-20 kg m^{-3}, and high porosity, since the spaces where the water filled the suspensions were replaced by air, compatible to the characteristics for aerogels as described previously.[167; 168]

The sample with higher cellulose content, C1.0, Figure 18d, presents decrease for the cells size (voids between the sheets) that form the macropores in that structure as well as increase for the nanofibers' aggregation in the walls.[169; 170] As consequence, this sample should have better mechanical stability in comparison to the other oxidized cellulose sample.[171]

Table 6 presents the results obtained for SEM analyses coupled to EDS detector for the cellulose samples presented in Figure 18, highlighting with bold the elements in higher concentration in each sample.

Table 6 - Weight composition for elements C, O, Na and Cl to the cellulose samples (C_0, C0.5 and C1.0) using EDS detector in SEM analysis

Sample	**Weight %**			
	C	**O**	**Na**	**Cl**
C_0	**47.8**	43.8	4.4	4.1
C0.5	**51.8**	42.0	4.6	1.5
C1.0	**50.4**	43.3	5.1	1.1

Source: Author (2021).

The % weight is similar among the cellulose samples, having a slightly higher carbon concentration to oxidized samples, that cannot be completely considered, since carbon

tape was used in the sample preparation. The main difference is that the sodium content for the non-oxidized sample is closer to the chloride content, while for the oxidized samples, there are just around 1% of Cl, suggesting that the Na present in the samples as Na^+, 5 times higher than Cl^-, is neutralized by the carboxylate groups now present in the cellulose structure.

It is worthy to keep in mind that the interaction volume for the EDS signal generation is high and can present influence from the stub (aluminium piece) or the carbon tape used usually to fixate the sample. And how the equipment is set, it is not common to get a quantitative measure from the instruments, only semi-quantitative results.

6.3 FTIR

Figure 19 presents the FTIR spectra in KBr to the cellulose samples: C1.0 (Figure 19a), C0.5 (Figure 19b) and C_0 (Figure 19c), highlighting the 1800-1500 cm^{-1} region in blue and the main bands pointed. Table 7 is presented with the bands, their respective assignments, and references.

The cellulose spectra present the same wavenumbers to the bands related to the glycosidic structure and the main changes rely on the bands located on the blue region of Figure 19. The 1640 cm^{-1} band to the non-oxidized sample is related to deformation of OH groups in cellulose structure and interlayer stretching.[94; 172] When the sample is oxidized, this band is changed to bands related to the C=O stretching in carboxylate groups[173-175] (1610 and 1612 cm^{-1} in C0.5 and C1.0, respectively) and C=O ester linkages stretching for the acid form[151; 176-178] (1708 and 1712 cm^{-1}, respectively).

Figure 19 - FTIR spectra for (a) C1.0, (b) C0.5, and (c) C_0 in KBr with the main bands described on the image

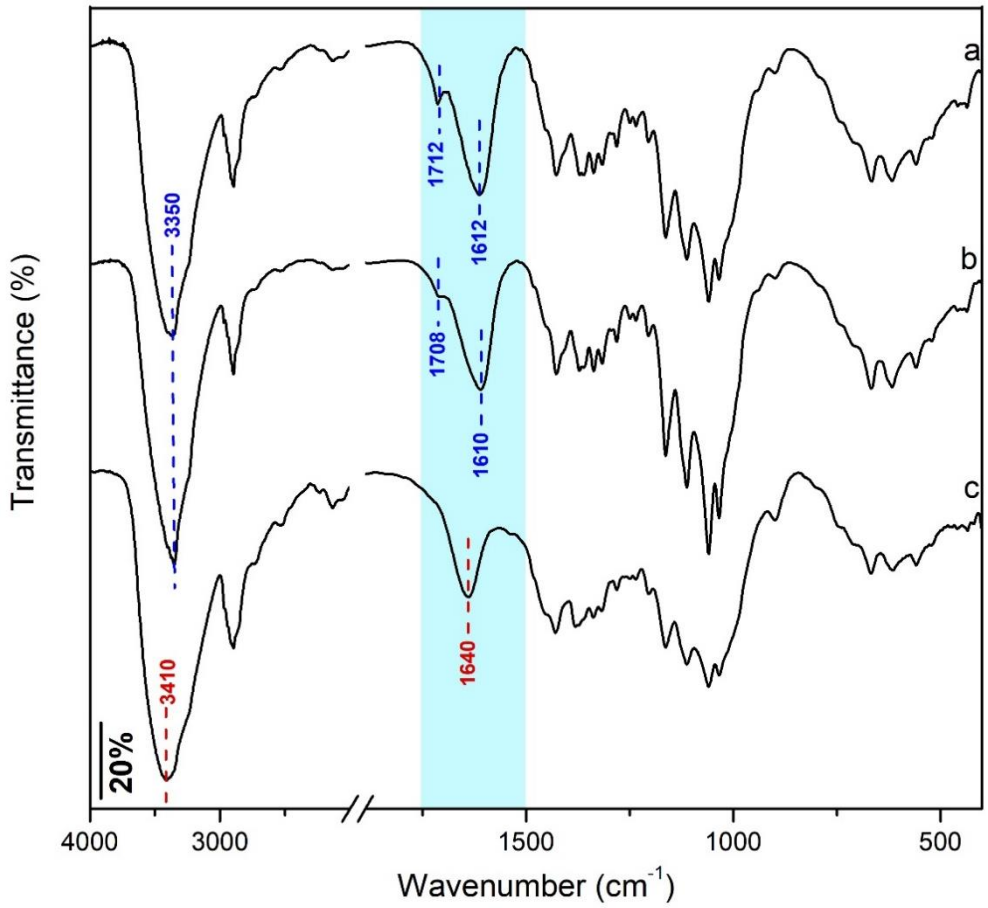

Source: Author (2021).

Table 7 – Main FTIR bands assignments to non-oxidized, C_0, and oxidized, C0.5 and C1.0, cellulose samples in KBr

Assignment	Wavenumber (cm^{-1})			References
	C_0	C0.5	C1.0	
Stretching of O–H bonds	3410	3350	3350	60; 160; 176; 179-183
C–H stretching vibrations	2895-2793	2895-2793	2895-2793	60; 160; 176; 179; 180; 182-184
Stretching of C=O in the ester bonds on carboxylic acid	-	1708	1712	173; 176; 185
O–H deformation in cellulose structure and interlayer stretching	1640	-	-	94; 160; 172
Stretching of C=O in the ester bonds on sodium carboxylate	-	1610	1612	160; 173; 174; 186

Assignment	Wavenumber (cm^{-1})			References
	C_0	C0.5	C1.0	
CH bending vibrations	1520-1262	1520-1262	1520-1262	30; 60; 172; 176; 179
C–O vibrations, characteristic from saccharide cellulose structure	1260-1010	1260-1010	1260-1010	30; 160; 176; 179; 187; 188
β-1,4-glucose bonds	898	898	898	60; 160; 176; 183
C–O–H bonds outside the plane	666	666	666	30; 60; 174; 183

Source: Author (2021).

TEMPO is a nitroxyl radical used as catalyst to selective oxidation to the primary OH groups in the cellulose structure. This process happens in situ, using hypobromite ions to oxidize this radical to nitrozone ion (19). When the oxidation happens to cellulose, this radical goes to the reduced form of TEMPO, N-hydroxy-2,2,6,6-tetramethylpiperidine (20). This method is largely used due to its high selectivity to the primary groups.[189; 190] Non-stoichiometric equations (18) to (21) present the reactions during this process:

$$2\,Br^- + 2\,OCl^- \rightarrow 2\,OBr^- + 2\,Cl^- \quad (18)$$

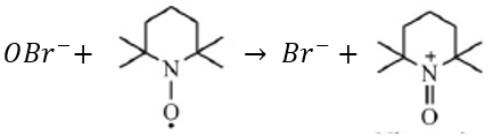

(19)

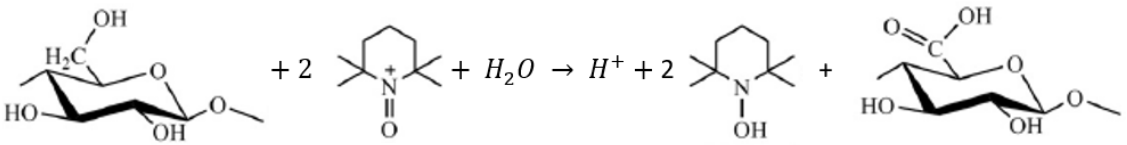

(20)

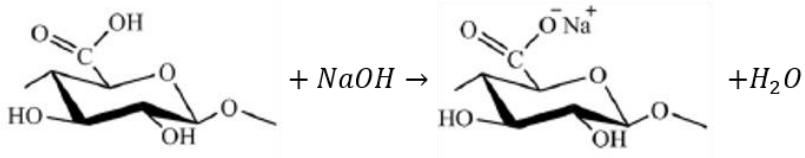

(21)

The cellulose oxidation can also be evidenced by the conductimetry titration presented in Figure 20. The intersection from the red lines results on the required volumes to neutralize the strong acid (HCl, added at the beginning of titration), V_0 = 12.8 mL, and the weak

acid (–COOH, present on the oxidized cellulose structure), V_1 = 25.75 mL. Thus, the resulting sample presents 0.52 mmol g^{-1} that is formed on the structure, like values reported in literature to different cellulose samples.[150; 151; 191] As reported by Saito and Isogai,[192] this is an indicative of an effective oxidation treatment, since the original cellulose samples present a very low carboxylate content. In a similar measurement, the non-oxidized sample would present essentially a strong acid neutralization.

Figure 20 - Conductimetry titration to the oxidized cellulose using 0.04 mol L^{-1} NaOH and 0.1 mol L^{-1} HCl

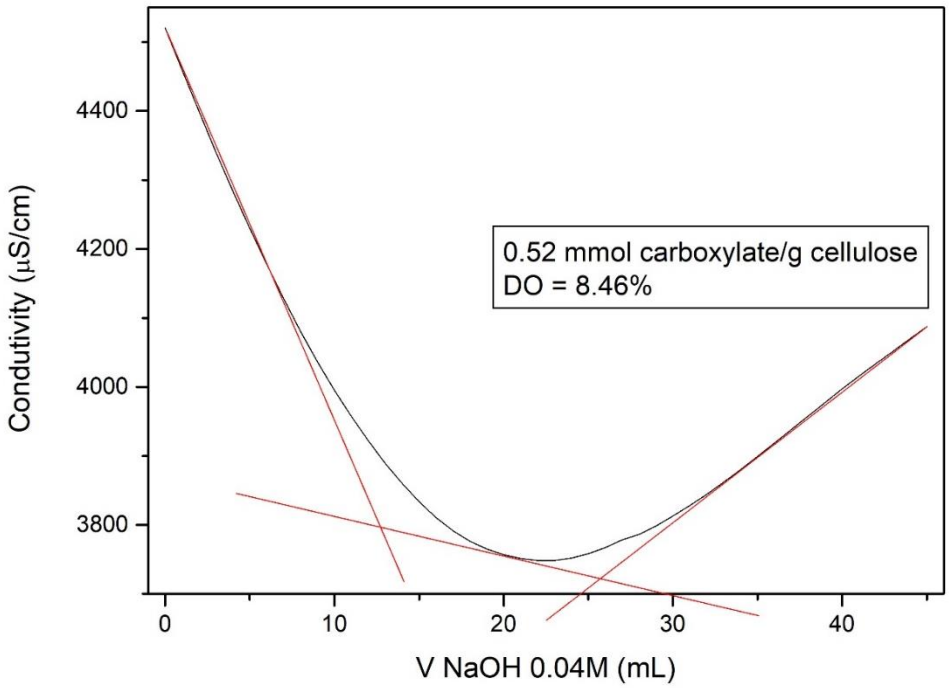

Source: Author (2021).

In addition, the partial oxidation promotes the narrowing of the bands on the region around 3400 cm^{-1}, as well as their shift to lower frequencies. This is especially due to changes in the intra and intermolecular hydrogen bonds caused by presence of carboxyl group that weakens them.[30; 151; 181; 185]

6.4 TGA

Figure 21 presents the thermal analyses for cellulose samples, C_0, C0.5 and C1.0, and their differentiate graphs on the right side of the figure. From these results, the events were identified and presented in Table 8 pointing initial and final temperature, as well as maximum loss temperature to each event and the partial and total loss to the sample.

The cellulose samples present similar behaviour with almost 100% weight loss at the end. Parameters as crystallinity or orientation of the fibres have influence on the thermal degradation and the presence of TEMPO oxidation salts increased slightly the ash content of functionalized samples.[66; 159; 160]

The first event (I) in both the samples is related to water evaporation that was physically adsorbed at the material with maximum temperature at 60 °C. The second event (II) is more intense with around 69% loss and is related to cellulose degradation reactions as dehydration, decomposition and depolymerization of glycosidic units. This event shows difference between the non-oxidized to the oxidized samples in a way that the oxidation promotes the degradation starting in lower temperatures since it goes from 217 to 172 °C, what leads to a 45 °C difference in the starting temperature. This can be attributed to the weakening of the hydrogen bonds on the cellulose chains due to the exchange of the primary hydroxyl for the polar carboxylate or carboxylic groups.[193; 194] The last events can be related to oxidation and break of carbonaceous residues producing gaseous compounds with low molecular mass.[67; 94; 179; 186; 195-197]

Figure 21 - Thermograms acquired in synthetic air at 50 mL min^{-1} flow and heating rate of 10 °C min^{-1} for cellulose samples and their respective differentiate graphs

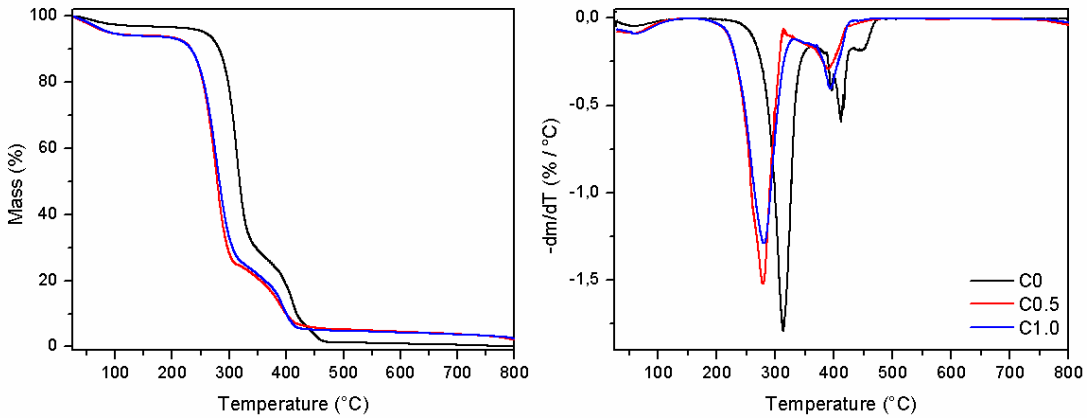

Source: Author (2021).

Table 8 - Thermal events observed in cellulose samples using synthetic air at 50 mL min^{-1} and heating rate of 10 °C min^{-1}

Sample	T_i / ºC	T_f / ºC	T_{max} / ºC	Event	Partial loss / %	Total loss / %
C_0	25	106	58	(I)	2.89	**99.8**
	217	**360**	**313**	**(II)**	**68.2**	
	386	400	396	(III)	4.0	
	400	430	412	(IV)	11.6	
	430	475	450	(V)	5.7	
C0.5	25	137	57	(I)	5.9	**98.0**
	172	**315**	**260**	**(II)**	**69.1**	
			280			
	315	485	390	(III)	19.7	
C1.0	25	137	61	(I)	6.1	**97.6**
	172	**329**	**280**	**(II)**	**69.2**	
	329	468	394	(III)	19.9	

Source: Author (2021). Where: T_x are the temperatures for each thermal event and "i" represents the starting temperature, "f", the final and "max", the maximum, according to the derivative graph for each thermogram.

6.5 Conclusions

Cartridges formed only by cellulose fibrils were analysed, assessing the partial oxidation of structure, as well as the concentration. This allow us to infer some properties or particularities when the nanoporous materials are added to the samples.

Independently of the oxidation degree or concentration, the low crystallinity is maintained for cellulose Iα crystalline phase. Their morphology studies show that the BC pellicles are essentially nanofibers forming a net and when the aerogels are formed, they are pushed together in laminae, in higher extent, when the cellulose was oxidized.

The oxidation step is evidenced by the carboxylate bands in 1610 and 1710 cm^{-1} in the Infrared spectra with degree of oxidation around 8.5% to the structure. From the TGA measurements, the samples are almost completely lost in the temperature interval studied and the event with maximum of degradation can be highlighted since it is related to dehydration,

decomposition and depolymerization reactions and to the oxidized samples, it is shifted to lower temperatures due to the weakening of hydrogen bonds for the cellulose structure.

Thus, since the cellulose forms used in this study revealed similar characteristics, initially a weight composition will be analysed with 3 different nanoporous materials and oxidized sample, and further, the oxidation influence over such materials is discussed to define the best possibility for the cartridges formation with zeolites and mesoporous materials for different applications.

7 HIERARCHICAL COMPOSITE MATERIALS WITH ZEOLITE A

In this chapter, it is presented the hierarchical materials in form of cartridges, prepared from the cellulose aerogels structure with microporous zeolite A with different weight composition. Using some characterization techniques, it was able to identify the main features from the materials and suggest their interaction.

7.1 XRD

Weight composition between the two components (nanoporous materials and oxidized cellulose) were changed in the range of 0.5% and 1.0% in aqueous systems and Figure 22 presents the XRD patterns to the zeolite A sample (Figure 22e) and its composites samples with oxidized cellulose 1.0%, C1.0-A1.0 (Figure 22a) and C1.0-A0.5 (Figure 22b), and 0.5%, C0.5-A1.0 (Figure 22c) and C0.5-A0.5 (Figure 22d). The blue squares point the main peaks to the cellulose phase and the green triangles, zeolite A.

The zeolite A pattern presented thin peaks with high intensity, an indication of well-structured crystals with a high growth rate. The identified phase is referent to LTA structure,[198] with a cubic crystal system and *Pm-3m* space group. This phase is registered on Inorganic Crystal Structure Database (ICSD) with the code 86644.[199]

The zeolite A composite samples on Figure 22 show the positions to the main peaks remaining the same and the differences are the relative intensities between the materials. The background is more visible to those samples, since they are immersed in a more amorphous matrix, the cellulose. Observing the $(01\bar{1})$ plan, around 26 °2θ, it decreases with the increment of the zeolite content in the sample, in a point that when there is the higher cellulose percentage, the peaks related to plans (442) and (622) from zeolite (on the left and right, respectively) are hidden by the cellulose peak.

Figure 22 – Co-Kα XRD patterns to the zeolite A sample (e) and its composites samples with oxidized cellulose 1.0%, (a) C1.0-A1.0 and (b) C1.0-A0.5, and 0.5%, (c) C0.5-A1.0 and (d) C0.5-A0.5

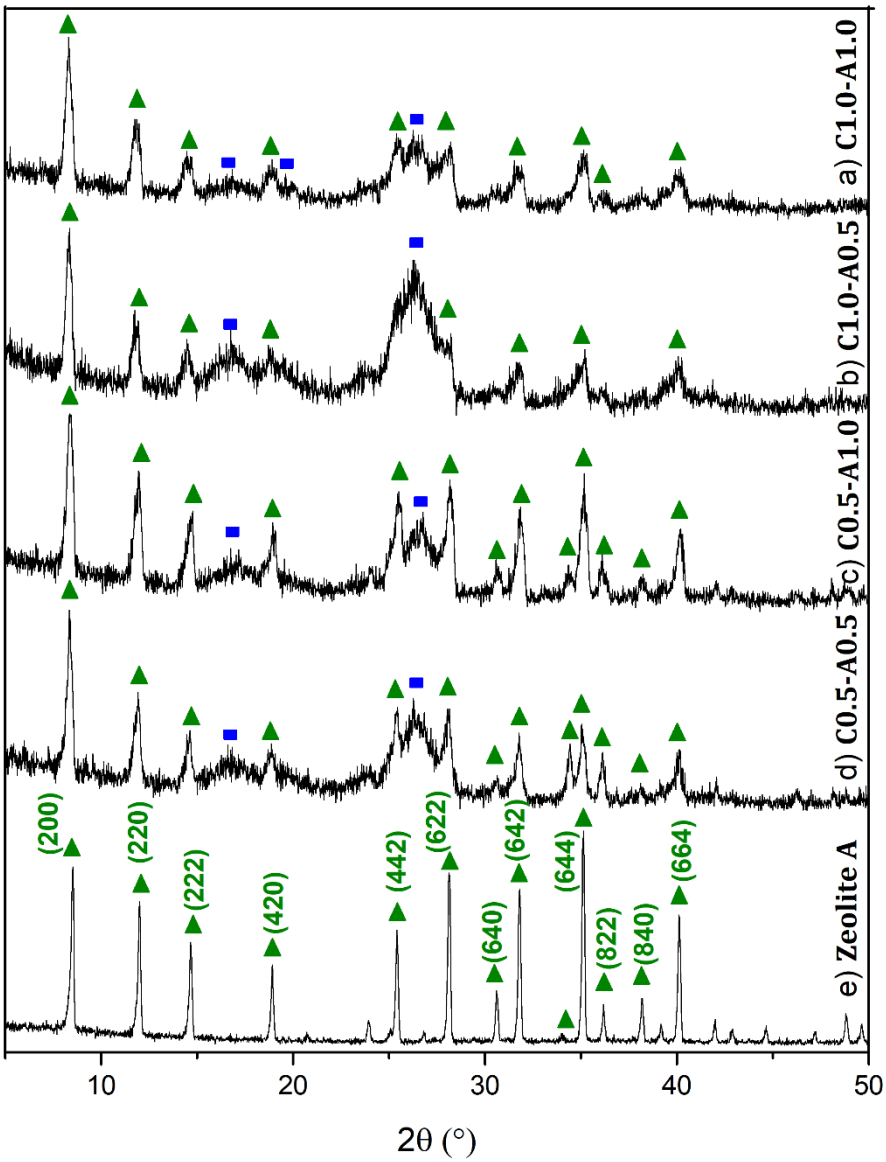

Source: Author (2021). The blue squares point the main peaks to the cellulose phase and the green triangles, zeolite A. Y axis = Intensity (a.u.).

7.2 SEM

Figure 23 presents scanning electron microscopy images for zeolite A. From the images is possible to identify that zeolite A is formed by homogeneous cubic crystals of ca. 1 µm, characteristics of this zeolite type.[13; 146; 200] The presence of truncated edges on the cubes instead of a perfect shaped cube, is due to high content of Na ions of the starting hydrogel.[201]

Figure 23 - Scanning electron micrography images for zeolite A

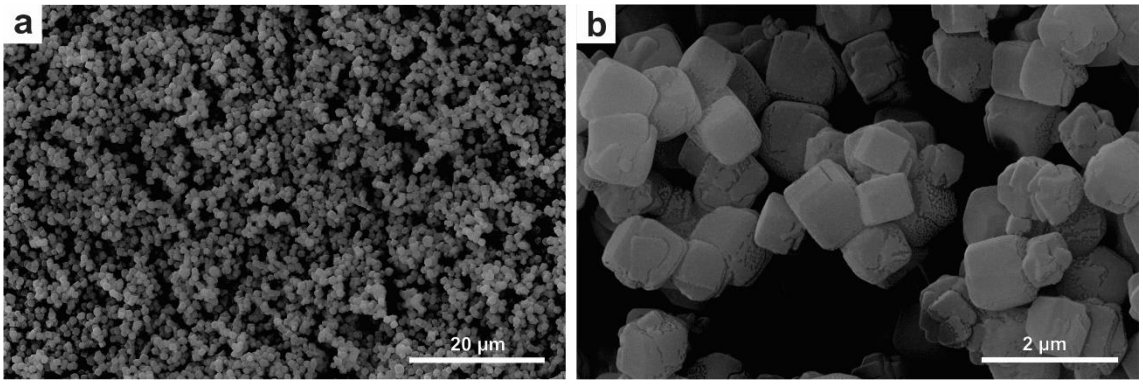

Source: Author (2021).

Figure 24 presents scanning electron microscopy images for zeolite A composite cartridges with different weight composition as stamped in each of them as it follows: C0.5-A0.5 (Figure 24a-b), C0.5-A1.0 (Figure 24c-d), C1.0-A0.5 (Figure 24e-f) and C1.0-A1.0 (Figure 24g-h). The left images present a scale bar of 20 µm and the right ones a detailed view with increased magnification and scale bar of 4 µm.

Samples containing only 0.5% in wet weight for zeolite, C0.5-A0.5 (Figure 24a-b) and C1.0-A0.5 (Figure 24c-d), show well-formed sheets with few loosen fibrils over the surface or between them and the zeolite crystals are apparently mainly dispersed inside the sheets. Meanwhile the cartridges with higher zeolite concentration, C0.5-A1.0 (Figure 24e-f) and C1.0-A1.0 (Figure 24g-h), were well-formed, presenting crystals dispersed in most part of the layers area both inside and on their surface, fixed by fibrils as it is observed more clearly in Figure 24d.

Table 9 presents the results obtained for SEM analyses coupled to EDS detector for the zeolites A presented in Figure 24, highlighting with bold the elements in higher concentration in each sample and the last column presents the Si/Al molar ratio.

Figure 24 - Scanning electron micrography images for zeolite A + BC composites ranging the weight composition between 0.5% and 1.0% before freeze-drying as stamp in each: (a-b) C0.5-A0.5, (c-d) C0.5-A1.0, (e-f) C1.0-A0.5 and (g-h) C1.0-A1.0

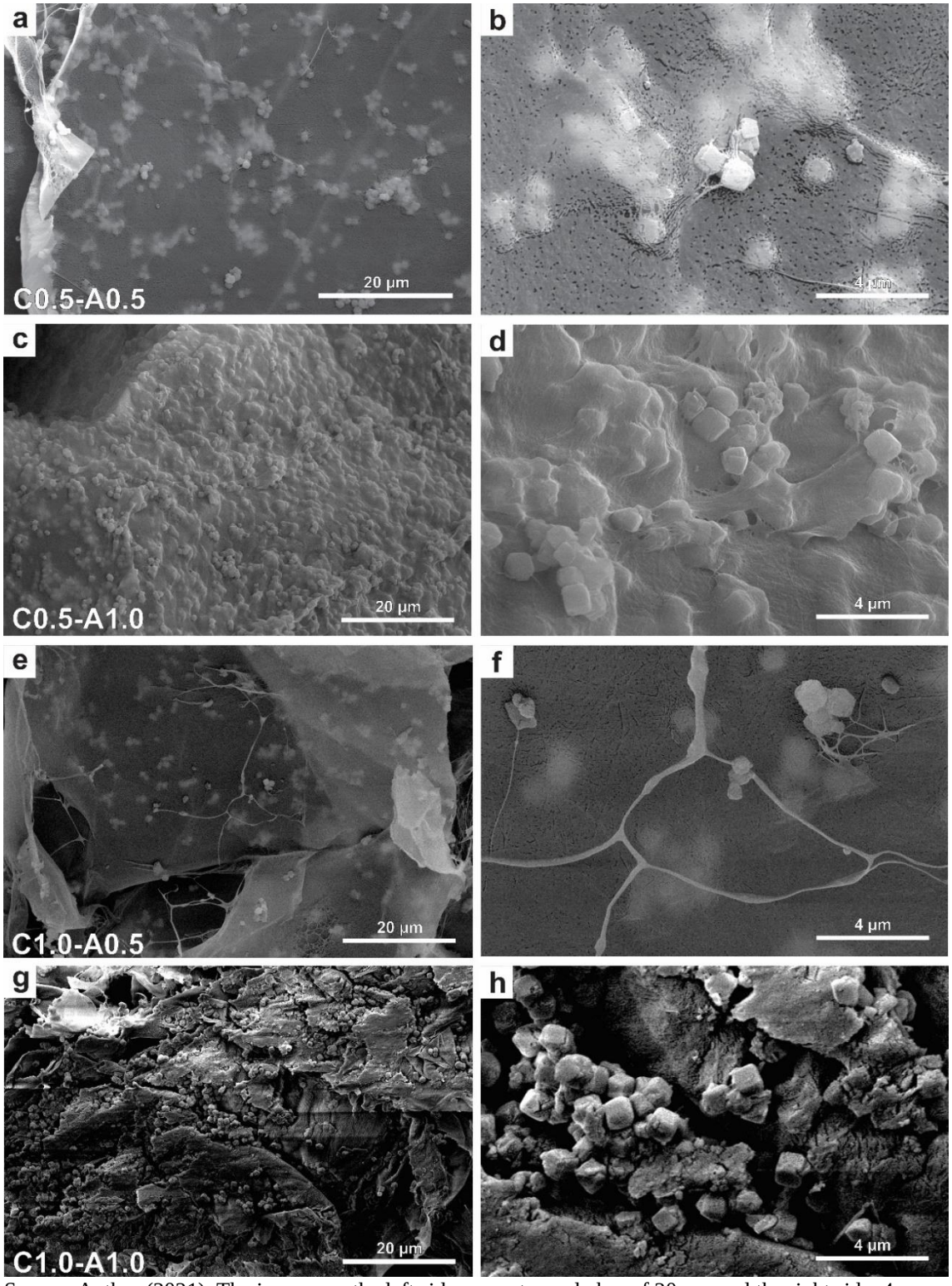

Source: Author (2021). The images on the left side present a scale bar of 20 µm and the right side, 4 µm.

Table 9 - Weight composition for elements C, O, Al, Si, Na and Cl, as well as the Si/Al molar ratio, to zeolites A and X and their composites with BC using EDS detector in SEM analysis

Sample	% Weight						Si/Al
	C	O	Al	Si	Na	Cl	
Zeolite A	3.3	33.2	**23.0**	**26.0**	14.5	-	1.09
C0.5-A0.5	38.2	43.8	**5.4**	**5.4**	7.2	-	0.96
C0.5-A1.0	22.4	35.0	**14.5**	**16.7**	11.4	-	1.11
C1.0-A0.5	41.1	44.1	**4.2**	**4.4**	6.2	-	1.01
C1.0-A1.0	38.3	36.1	**7.5**	**8.1**	9.2	0.8	1.04

Source: Author (2021).

In zeolite-related materials, the Si/Al molar ratio is a piece of information of great importance, as well as Na content since the ion inside the zeolite pores is responsible for many adsorption processes. The synthesised zeolite A presents a Si/Al from 1.09, compatible values found both in Rietveld refinement presented previously and in other works.[13; 202] To the related composites, the values remain close to that, changing the zeolite content. From the XRD, it is suggested that the zeolite structure is maintained. To check if the zeolite structure was changed or if it is only an interference from the sample preparation, other techniques can help to answer this question, like the NMR, better discussed in later sections.

7.3 FTIR

Figure 25 presents the FTIR spectra in KBr to the zeolite A sample (Figure 25e) and its respective composites samples with oxidized cellulose 1.0%, C1.0-A1.0 (Figure 25a) and C1.0-A0.5 (Figure 25b), and 0.5%, C0.5-A1.0 (Figure 25c) and C0.5-A0.5 (Figure 25d). The 1800-1500 cm^{-1} region is highlighted in blue and the main bands are pointed. Table 10 is presented with the bands, their respective assignments, and references.

Figure 25 - FTIR spectra for (e) zeolite A and its respective composites samples with oxidized cellulose 1.0%, (a) C1.0-A1.0 and (b) C1.0-A0.5, and 0.5%, (c) C0.5-A1.0 and (d) C0.5-A0.5, in KBr with the main bands described on the image

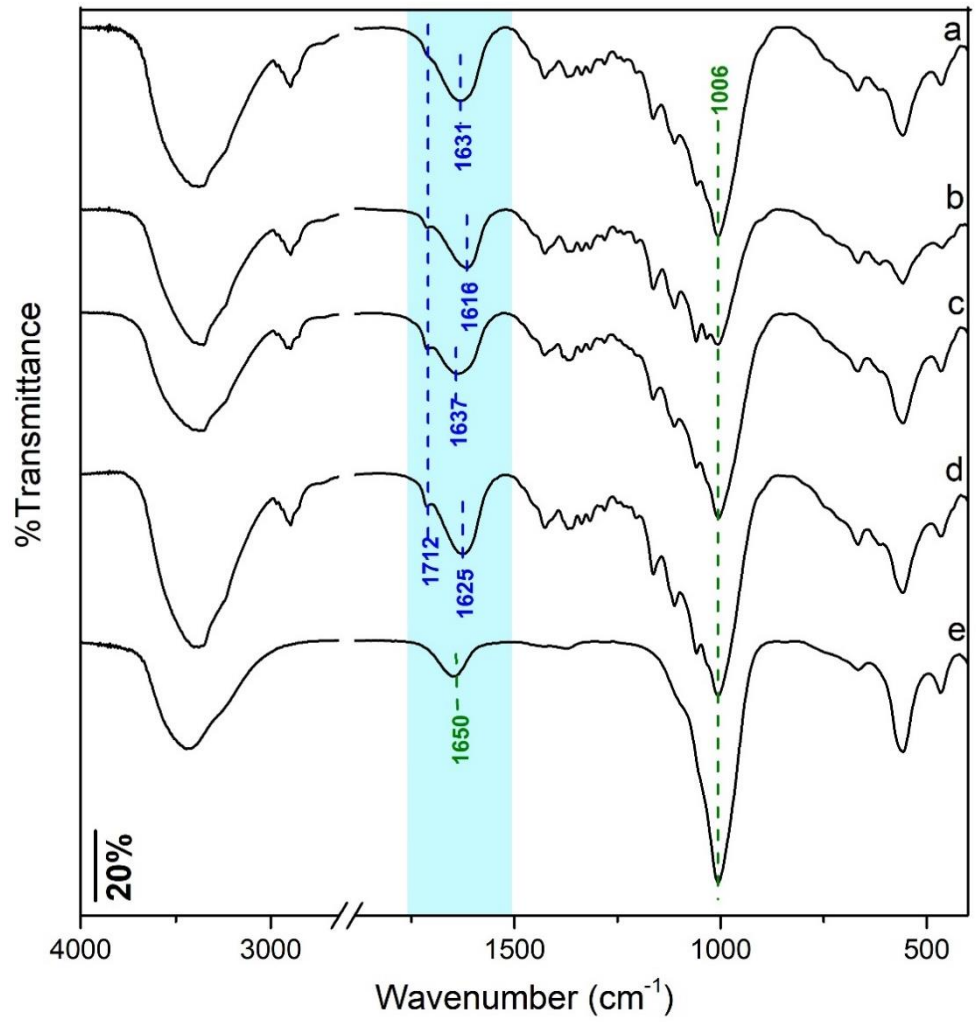

Source: Author (2021).

Table 10 – Main FTIR bands assignments to zeolite A and its respective composites samples with oxidized cellulose 1.0%, C1.0-A1.0 and C1.0-A0.5, and 0.5%, C0.5-A1.0 and C0.5-A0.5, in KBr

Assignment	**Wavenumber (cm^{-1})**							**References**
	ZeoA	**C0.5**	**C0.5-A0.5**	**C0.5-A1.0**	**C1.0**	**C1.0-A0.5**	**C1.0-A1.0**	
Stretching of O–H bonds	3435	3350	3350	3350	3350	3350	3350	60; 146; 160; 176; 179-183
Stretching of C=O in the ester bonds on carboxylic acid	-	1708	1712	1712	1712	1712	1712	173; 176; 185
Stretching of C=O in the ester bonds on sodium carboxylate	-	1610	1625	1637	1612	1616	1631	173; 174; 186
Vibrations of O–H coming from adsorbed water on the zeolite structure	1650	-	-	-	-	-	-	146; 184; 203; 204
Stretching of Si–O bonds in SiO_2	1006	-	1006	1006	-	1006	1006	146; 203-205
Symmetric stretching of T–O (T = Si or Al) bonds in internal tetrahedra	668	-	668	668	-	668	668	146; 183; 205; 206
Characteristic double four member rings (d4r)	558	-	558	558	-	558	558	146; 183; 203; 206
Internal T–O bending in double-ring (d4r)	465	-	465	465	-	465	465	146; 183; 206

Source: Author (2021).

Zeolite A presents broad bands that are characteristic to the LTA structure[13] in a way that the 1006 cm^{-1} stretching is related to the internal vibrations to the T–O (T=Si, Al) bonds, the zeolites primary building unit.[146; 203; 204] This band is not present to C0.5 (Figure 19b) or C1.0 (Figure 19a), but it is clear to all the composite samples. To those samples with higher zeolite content (C0.5-A1.0, Figure 25c, and C1.0-A1.0, Figure 25a), higher intensity can be noticed, as expected.

The other zeolite A structure bands can be found at 668, 558 and 465 cm^{-1}, related to tetrahedra T–O internal stretching, d4r stretching and internal tetrahedra on the d4r ring, respectively.[146; 183; 203; 204] The same wavenumbers are observed to the composite samples without any shifts, which suggests that the internal structure is not modified with the cartridge's formation.

The blue region in Figure 25, 1800-1500 cm^{-1}, highlights the main features to the presented spectra, since the composites formation promotes shifts to the bands related to cellulose oxidation and adsorbed water on the structure. The composites present higher frequencies, which means, a better interaction among the two substances. This shift is also more pronounced with higher zeolite content on the sample.

7.4 TGA

Figure 26 presents the thermal analyses for zeolite A and its composite samples varying the weight composition, C0.5-A0.5, C0.5-A1.0, C1.0-A0.5, C1.0-A1.0, and their differentiate graphs on the right side of the figure. From these results, the events were identified and presented in Table 11 pointing initial and final temperature, as well as maximum loss temperature to each event and the partial and total loss to the sample.

The zeolite A sample by itself presents high thermal stability with approximately 25% total weight loss happening in two main events that are related to water desorption: (I) the first event releases molecules that are weakly bonded to the structure and it is the most prominent one; (II) the second is related to molecules that are strongly attached to the internal channels cavities.[207; 208] This is a group 3 zeolite, as classified in Breck, 1984[13] and it does not have significant changes for the structure after being dehydrated until 800 °C.

Figure 26 - Thermograms acquired in synthetic air with 50 mL min⁻¹ flow and heating rate of 10 °C min⁻¹ for zeolite A composite samples with different weight composition and their respective differentiate graphs

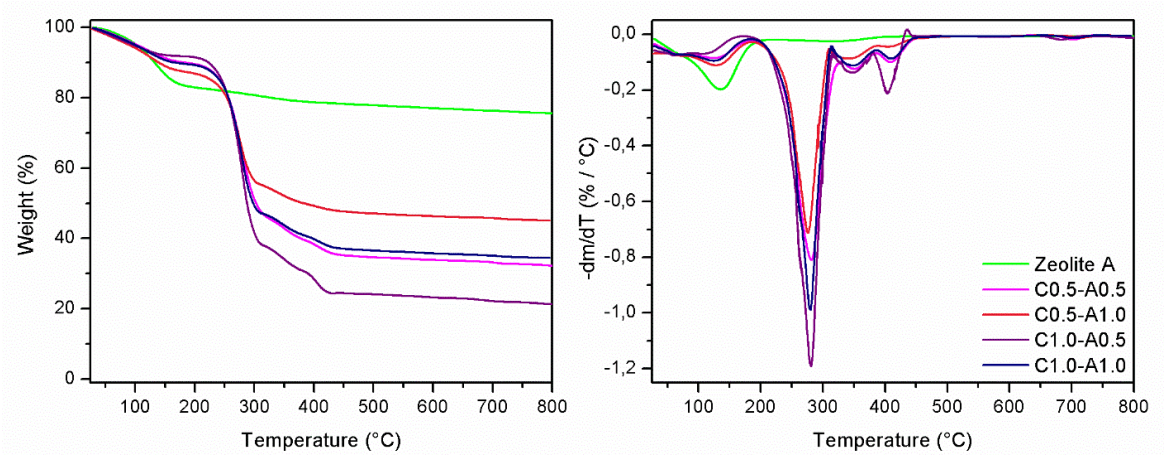

Source: Author (2021).

For the composites, the zeolite addition to the cartridges promotes decrease in the material weight loss, so that the sample with higher zeolite content C0.5-A1.0 has 45% resulting mass, while the sample containing just cellulose presents 2%. This behaviour is expected, since there is a thermally stable material in the cellulosic matrix, the zeolite, that changes not only the total loss but also the identified events, as observed by displacement at initial temperature for event II to higher temperatures (except for the sample with higher cellulose content, C1.0-A0.5).

Table 11 - Thermal events observed to zeolite A composite samples with different weight compositions using synthetic air at 50 mL min⁻¹ and heating rate of 10 °C min⁻¹

Sample	T_i / ºC	T_f / ºC	T_{max} / ºC	Event	Partial loss / %	Total loss / %
Zeolite A	**25**	**215**	**65**	**(I)**	**17.5**	**24.6**
			135			
	215	400	318	(II)	1.6	
C0.5-A0.5	25	187	66	(I)	10.0	**67.7**
			124			
	187	**330**	**281**	(II)	**50.0**	
	330	385	350	(III)	5.5	
	385	453	408	(IV)	4.5	
	665	736	700	(V)	2.4	
C0.5-A1.0	25	185	128	(I)	12.8	**55.1**
	185	**310**	**260**	(II)	**32.0**	

Sample	T_i / ºC	T_f / ºC	T_{max} / ºC	Event	Partial loss / %	Total loss / %
			276			
	310	386	342	(III)	5.4	
	386	451	408	(IV)	2.3	
	689	755	717	(V)	2.5	
C1.0-A0.5	25	174	62	(I)	8.0	**78.9**
			111			
	174	**316**	**260**	(II)	**54.2**	
			280			
	316	381	347	(III)	7.0	
	381	436	403	(IV)	6.6	
	646	715	684	(V)	2.1	
C1.0-A1.0	25	186	67	(I)	10.5	**65.8**
			126			
	186	**314**	**260**	(II)	**42.5**	
			280			
	314	386	350	(III)	6.3	
	386	450	409	(IV)	3.7	
	668	738	704	(V)	2.3	

Source: Author (2021). Where: T_x are the temperatures for each thermal event and "i" represents the starting temperature, "f", the final and "max", the maximum, according to the derivative graph for each thermogram.

The first event (I) also presents changes being extended for 50 °C above the observed for pure cellulose samples with higher weight loss due to the water release from the zeolite structure in addition to the cellulose degradation reactions. A higher number of thermal events is observed to the composites with low weight loss in each of them that can be related to the capture by the porous structure from compounds produced in cellulose degradation. This hypothesis, in addition to the thermal insulating effect produced by the zeolite crystals well-dispersed in the polymeric matrix, can explain the residues production at the end of the analysis that does not present a direct relation with the zeolite content in the cartridges.[184]

7.5 Conclusions

Hierarchical materials were formed using bacterial cellulose nanofibrils and a microporous zeolite A in an aerogel-like material with different weight compositions. By using different characterization techniques, some features were observed suggesting their main properties.

From the XRD, the main peaks are maintained for zeolite LTA and cellulose and the relative intensities change accordingly to the weight composition in the cartridge. The cubic crystals of zeolite A are distributed over the cellulose structure and for the sample with higher zeolite content, the crystals are inside and outside the laminae. Their basic structure remains the same except for the bands related to the cellulose oxidation, that are shifted to higher wavenumbers, indicating better chemical interaction from that group.

The use of zeolite A crystals in this composite promotes a better thermal stabilization observing not only lower weight loss for such samples, but also moving the main event for cellulose degradation for higher temperatures. Thus, we can conclude that the insertion of well-defined particles as zeolite A in a cellulose matrix can be an interesting approach for the formation of hierarchical cartridges to be used in aqueous or gaseous separations systems.

8 HIERARCHICAL COMPOSITE MATERIALS WITH ZEOLITE X

In this chapter, it is presented the hierarchical materials in form of cartridges, prepared from the cellulose aerogels structure with zeolite X nanometric particles with different weight composition. Using some characterization techniques, it was able to identify the main features for the materials and suggest their interaction.

8.1 XRD

Figure 27 presents the XRD patterns to the zeolite X sample (Figure 27e) and its composites samples with oxidized cellulose 1.0%, C1.0-X1.0 (Figure 27a) and C1.0-X0.5 (Figure 27b), and 0.5%, C0.5-X1.0 (Figure 27c) and C0.5-X0.5 (Figure 27d). The blue squares point the main peaks to the cellulose phase and the light green hexagons, zeolite X.

The diffractogram to zeolite X indicates only one crystalline phase referent to the Faujasite structure, ICSD code 31541.[209] Most of the peaks present a broad "full-width at half maximum" (FWHM) and low intensity, that can be related to nanometric crystals. Nevertheless, the diffraction plans (220), 11.8 °2θ, and (440), 23.5 °2θ, present thinner peaks that can be an indication of preferred growth for those plans during crystallization.

The observation on the background for the composite cartridges shows that the peaks position also remains unchanged, as observed for zeolite A samples, and the main difference is just the intensity for zeolite peaks. That decreases when added to the cellulosic matrix in comparison to the pure zeolite, and the (111) plan is the most likely to identify changes to the relative intensity among the two samples. For example, samples C0.5-X0.5 (Figure 27d) and C1.0-X1.0 (Figure 27a) show similar intensities for the two main peaks (7.2 and 26.4 °2θ), whilst the sample with higher zeolite content, C0.5-X1.0 (Figure 27c), presents the zeolite peak more prominent than the cellulose one.

Figure 27 – Co-Kα XRD patterns to the zeolite X sample (e) and its composites samples with oxidized cellulose 1.0%, (a) C1.0-X1.0 and (b) C1.0-X0.5, and 0.5%, (c) C0.5-X1.0 and (d) C0.5-X0.5

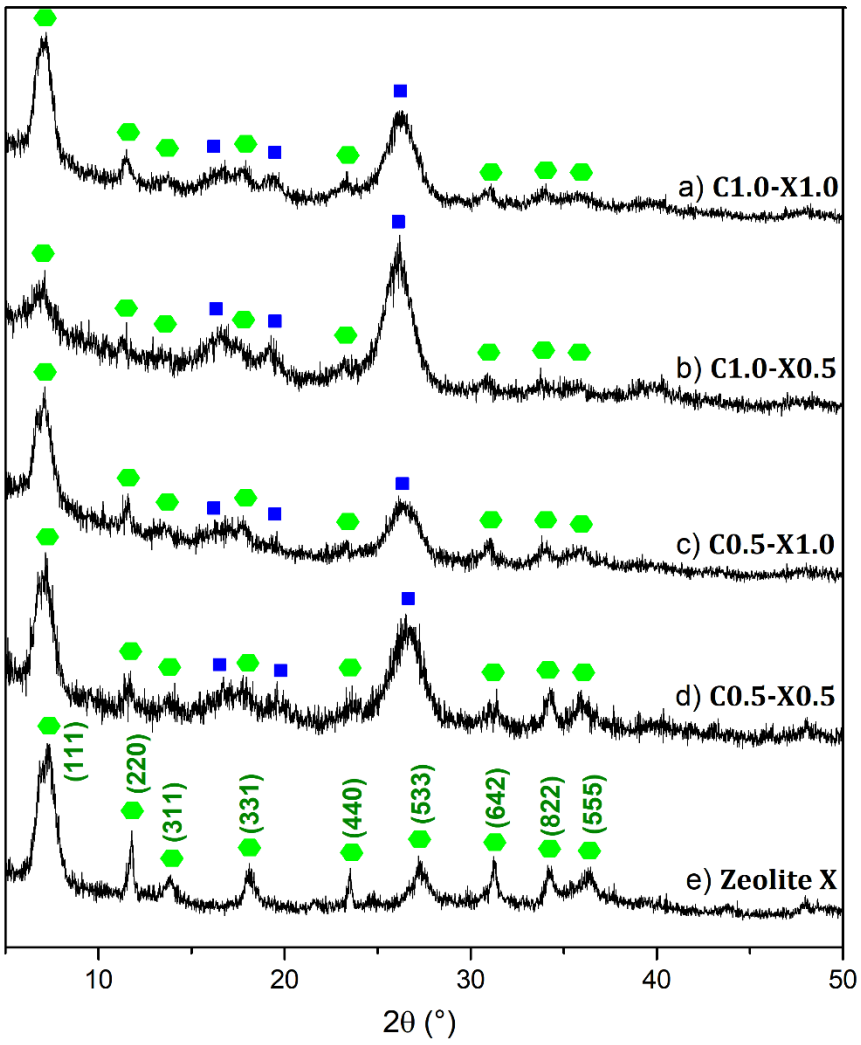

Source: Author (2021). The blue squares point the main peaks to the cellulose phase and the light green hexagons, zeolite X. Y axis = Intensity (a.u.).

8.2 SEM

Zeolite X presents small size in the range of nanometres. Thus, it is possible to verify agglomeration of small particles, but it is not accurate to describe its size and shape. Figure 28 presents scanning electron microscopy images for zeolite X composite cartridges with different weight composition as stamped in each of them as it follows: C0.5-X0.5 (Figure 28a-b), C0.5-X1.0 (Figure 28c-d), C1.0-X0.5 (Figure 28e-f) and C1.0-X1.0 (Figure 28g-h). The left images present a scale bar of 20 µm and the right ones, present a detailed view with increased magnification and scale bar of 4 µm.

The cartridges formed with zeolite X have in general, similar aspect to the ones formed with zeolite A. With zeolite X smaller particles, it is possible to observe a better distribution over the cellulose sheets, as well as less roughness on the surface for the sample with lower zeolite content, C1.0-X0.5 (Figure 28e-f), such feature indicates the zeolite presence in the layers.

As observed in both composites set of samples, the interaction that occurs between cellulose-zeolite is a surface mechanism that seems to have a better effect over the particles with smaller sizer, allowing their good distribution and avoiding agglomeration between them.

Table 12 presents the results obtained for SEM analyses coupled to EDS detector for the zeolite X samples presented in Figure 28, highlighting with bold the elements in higher concentration in each sample and the last column presents the Si/Al molar ratio.

Table 12 - Weight composition for elements C, O, Al, Si, Na and Cl, as well as the Si/Al molar ratio, to zeolites A and X and their composites with BC using EDS detector in SEM analysis

SAMPLE	**% WEIGHT**						**Si/Al**
	C	**O**	**Al**	**Si**	**Na**	**Cl**	
Zeolite X	6.3	28.9	**21.5**	**30.2**	12.7	0.4	1.35
C0.5-X0.5	42.5	46.2	**3.2**	**3.4**	4.3	0.4	1.02
C0.5-X1.0	36.9	44.4	**5.6**	**6.2**	6.5	0.3	1.07
C1.0-X0.5	44.0	46.9	**2.1**	**2.3**	4.4	0.4	1.06
C1.0-X1.0	39.9	43.9	**4.6**	**5.6**	5.6	0.5	1.17

Source: Author (2021).

Zeolite X, in the other hand, presents Si/Al = 1.35, and the composites diverge from that, being closer to 1. This is probably due to the stub influence over the aluminium %. From the XRD, it is suggested that the zeolite structure is maintained. To check if the zeolite structure was changed or if it is only an interference from the sample preparation, other techniques can help to answer this question, like the NMR, better discussed in later sections.

Figure 28 - Scanning electron microscopy images for zeolite X + BC composites ranging the weight composition between 0.5% and 1.0% before freeze-drying as stamp in each: (a-b) C0.5-X0.5, (c-d) C0.5-X1.0, (e-f) C1.0-X0.5 and (g-h) C1.0-X1.0

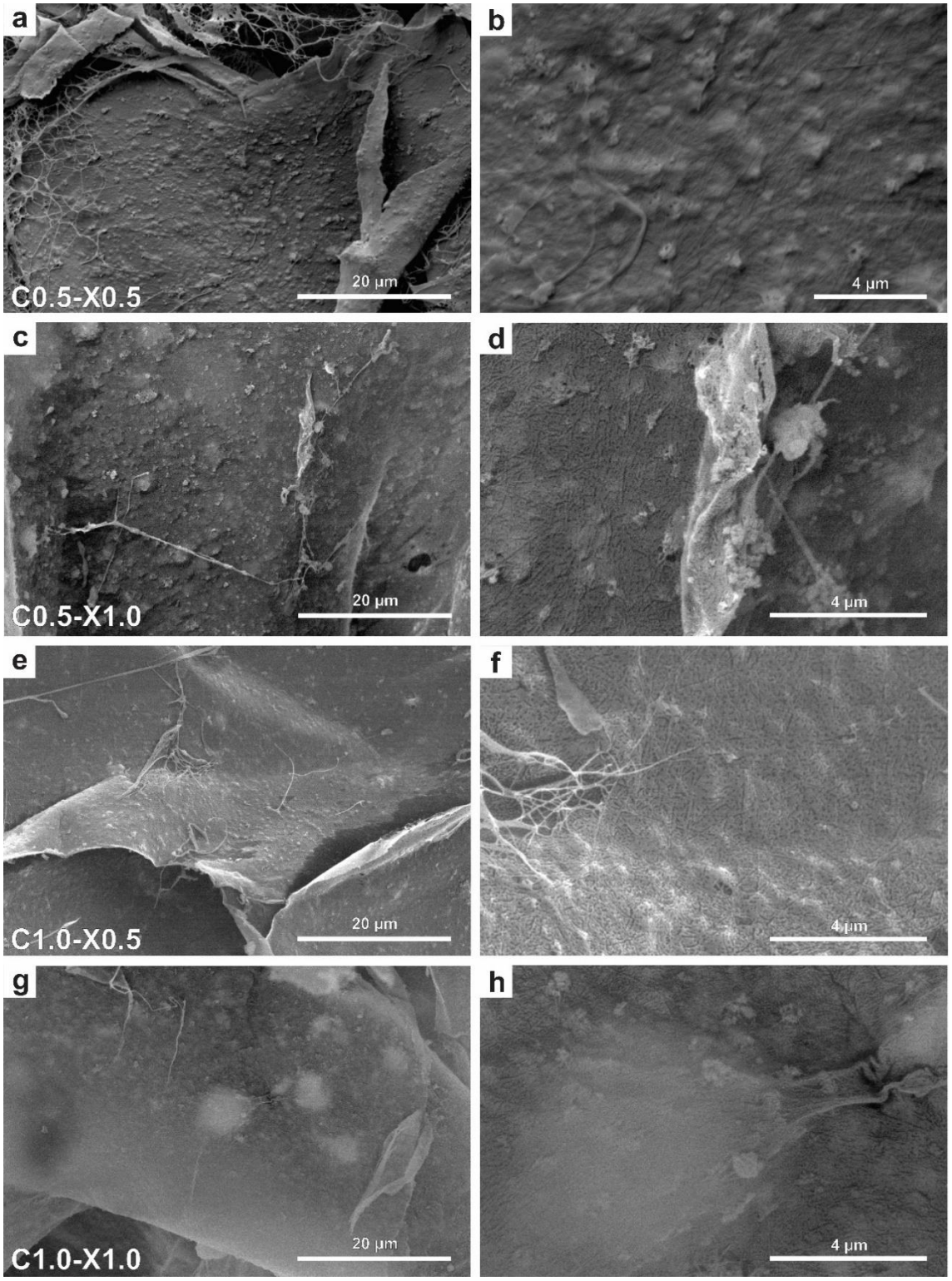

Source: Author (2021). The images on the left side present a scale bar of 20 µm and the right side, 4 µm.

8.3 TEM

Figure 29 presents transmission electron microscopy images for zeolite X using different magnifications highlighting two different particles shapes by pink arrows (Figure 29b) and in pink lines, their channels (Figure 29c) by high-resolution transmission electron microscopy.

Figure 29 - Transmission electron microscopy images for zeolite X using different magnifications

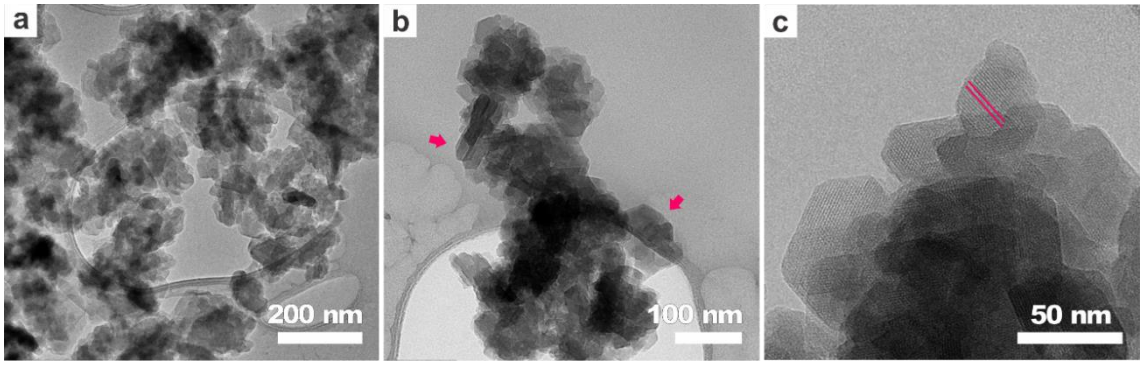

Source: Author (2021). Where the arrows point to particles with different shapes and lines present the channel systems for the zeolite.

From images presented in Figure 29 for zeolite X, it is found the hexagonal plates shape to the particles with around 50 nm diameter and agglomeration, as observed for the SEM images and expected for nanometric samples synthesized in absence of organic directing structure agents.[210; 211]

In Figure 29b, the pink arrows point to some of these particles where it is possible to see the presence of some crystals having one of the axes increased, that indicates preferential growth for some of the crystalline planes as suggested in XRD analysis. It is still possible in Figure 29c, to observe the internal channels for this zeolite using the high-resolution apparatus. They can be described as stacking of packed tubes that are intercepted with equidimensional and parallel in [110] direction.[13]

8.4 FTIR

Figure 30 presents the FTIR spectra in KBr to the zeolite X sample (Figure 30e) and its respective composites samples with oxidized cellulose 1.0%, C1.0-X1.0 (Figure 30a) and C1.0-X0.5 (Figure 30b), and 0.5%, C0.5-X1.0 (Figure 30c) and C0.5-X0.5 (Figure 30d).

The 1800-1500 cm^{-1} region is highlighted in blue and the main bands are pointed. Table 13 is presented with the bands, their respective assignments, and references.

Figure 30 - FTIR spectra for (e) zeolite X and its respective composites samples with oxidized cellulose 1.0%, (a) C1.0-X1.0 and (b) C1.0-X0.5, and 0.5%, (c) C0.5-X1.0 and (d) C0.5-X0.5, in KBr with the main bands described on the image

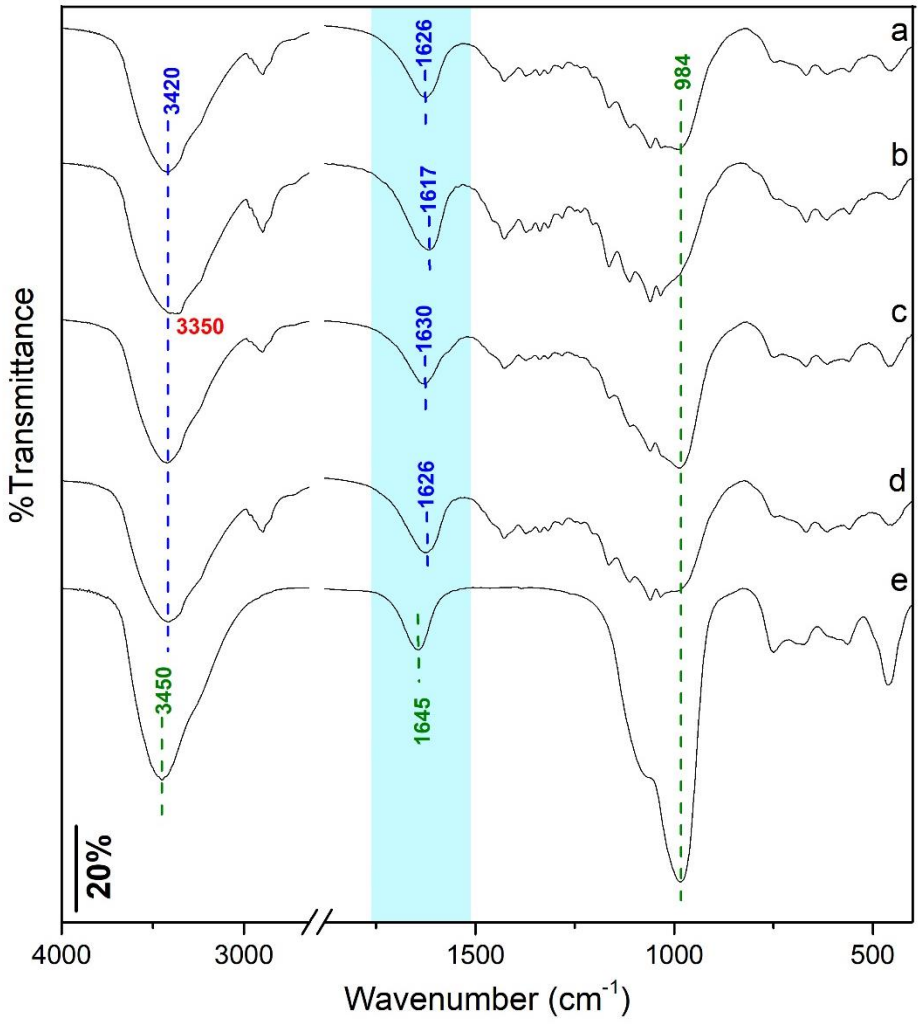

Source: Author (2021).

Table 13 – Main FTIR bands assignments to zeolite X and its respective composites samples with oxidized cellulose 1.0%, C1.0-X1.0 and C1.0-X0.5, and 0.5%, C0.5-X1.0 and C0.5-X0.5, in KBr

Assignment	**Wavenumber (cm^{-1})**							**References**
	ZeoX	**C0.5**	**C0.5-X0.5**	**C0.5-X1.0**	**C1.0**	**C1.0-X0.5**	**C1.0-X1.0**	
Stretching of O–H bonds	3450	3350	3420	3420	3350	3350	3420	60; 180; 181; 183; 212
Stretching of C=O in the ester bonds on carboxylic acid	-	1708	-	-	1712	-	-	173; 176; 185
Stretching of C=O in the ester bonds on sodium carboxylate	-	1610	1626	1630	1612	1617	1626	173; 174; 186
Vibrations of O–H coming from adsorbed water on the zeolite structure	1645	-	-	-	-	-	-	212-216
Asymmetric stretching of T–O (T = Si or Al) bonds in external tetrahedra	1073	-	-	-	-	-	-	210; 213-215; 217
Asymmetric stretching of T–O bonds in internal tetrahedra	984	-	984	984	-	984	984	210; 212-217
Symmetric stretching of T–O bonds in internal tetrahedra	750	-	750	750	-	745	750	210; 213-217
Symmetric stretching of T–O bonds in external tetrahedra	675	-	668	668	-	668	668	210; 212-217
Characteristic double six member rings (d6r)	565	-	559	559	-	559	559	210; 212-217
Internal T–O bending in double-ring	460	-	460	460	-	460	460	210; 212; 213; 217

Source: Author (2021).

Zeolite X spectrum (Figure 30e) presents broad bands typical from FAU structure with the T–O (T = Si, Al) bonds at 1073 and 984 cm^{-1} and the other less intense bands at 750, 675, 565 and 460 cm^{-1}. When the composites are formed, the only zeolite band that changes its position is the band at 675 cm^{-1}, due to some cellulose bands with similar intensities present in the same region. In summary, the overall zeolite structure does not change with the addition to cellulose matrix.

The main differences to be observed to the spectra are related to hydroxyl groups and the signal referent to sodium carboxylate in oxidized cellulose. The band at 3350 cm^{-1} for cellulose shifts to 3420 cm^{-1} (the only exception is sample C1.0-X0.5, Figure 30b, for having the higher cellulose amount among the composites); This is an indication of cellulose interacting with the zeolites using hydrogen bonds. The other feature is highlighted in the blue region on Figure 30 with shifts to higher wavenumbers when zeolite is added. As stated to zeolite A samples, this is a strong evidence of better interaction between both cellulose and zeolite X.

8.5 NMR

For zeolites, the NMR brings interesting results, not only related to the identification of their chemical environment, but also to do an accurate quantification of Si/Al. Figure 31 presents the ^{29}Si MAS-NMR fitted spectrum and deconvolution of the five Q^4 main peaks for zeolite X. The discrimination of those is also presented in Table 14 together with relative peak area and peak width, parameters obtained with the fitting.

The shape for the zeolite X spectrum matches to previous works[138; 218; 219] and considering the relative areas from the deconvolution fitting to the signal, the Si/Al ratio was 1.3, close to the value obtained from EDS measurements.

Figure 31 - ^{29}Si MAS-NMR fitted spectra and deconvolution of main peaks for zeolite X

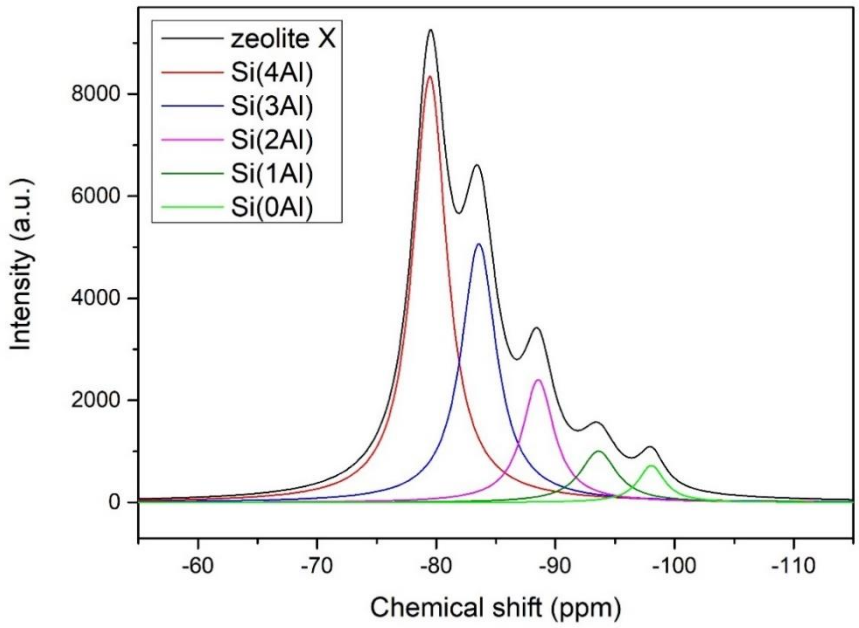

Source: Author (2021).

Table 14 - ^{29}Si MAS-NMR Q_4 peaks fitted for zeolite X as well as parameters obtained during the fitting: relative peak area and peak width

Chemical shift (ppm)	Q-type	Relative peak area	Peak width (ppm)
-79.4	Q^4(4Al)	47.68	3.52
-83.5	Q^4(3Al)	30.15	3.52
-88.5	Q^4(2Al)	12.78	3.52
-93.6	Q^4(1Al)	6.17	3.52
-98.0	Q^4(0Al)	3.22	3.52

Source: Author (2021).

8.6 TGA

Figure 32 presents the thermal analyses for zeolite X and its composite samples varying the weight composition, C0.5-X0.5, C0.5-X1.0, C1.0-X0.5, C1.0-X1.0, and their differentiate graphs on the right side of the figure. From these results, the events were identified and presented in Table 15 pointing initial and final temperature, as well as maximum loss temperature to each event and the partial and total loss to the sample.

Figure 32 - Thermograms acquired in synthetic air with 50 mL min⁻¹ flow and heating rate of 10 °C min⁻¹ for zeolite X composite samples with different weight composition and their respective differentiate graphs

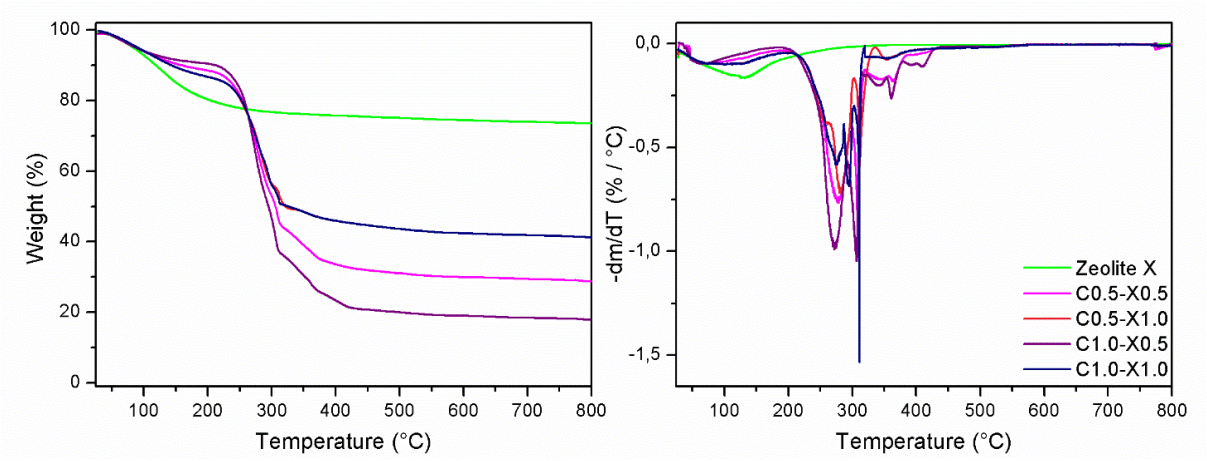

Source: Author (2021).

Zeolite X presented similar weight loss as zeolite A (Figure 26 and Table 15), due to the water desorption from the channels. The low Si/Al promotes water molecules to be located inside the voids, next to cations. This is a group 4 zeolite, as classified in Breck, 1984[13] and structural changes will happen only after 750 °C.

For the composites, the zeolite addition promotes decrease in the material weight loss and as expected and observed for zeolite A, the samples with higher zeolite content, C0.5-X1.0 has 41% resulting mass. The observations for first event being extended and the second event happening in a higher temperature are also present to this set of samples, as well as the higher number of thermal events when the zeolite is added. Those are all evidence of how the zeolite improves the thermal behaviour in the cartridges.

Table 15 - Thermal events observed to zeolite X composite samples with different weight compositions using synthetic air at 50 mL min⁻¹ and heating rate of 10 °C min⁻¹

Sample	T_i / °C	T_f / °C	T_{max} / °C	Event	Partial loss / %	Total loss / %
Zeolite X	**25**	**350**	**130**	**(I)**	**24.1**	**26.2**
C0.5-X0.5	25	196	72	(I)	11.7	**71.3**
	196	**298**	**277**	**(II)**	**34.6**	
	298	319	309	(III)	9.8	
	319	384	344	(IV)	9.3	
			364			
	384	444	410	(V)	2.6	

C0.5-X1.0	25	200	126	(I)	13.1	**58.8**
	200	**302**	**256**	**(II)**	**31.1**	
			282			
	302	335	311	(III)	6.6	
	335	399	354	(IV)	3.0	
C1.0-X0.5	25	189	67	(I)	9.4	**82.1**
	189	**291**	**272**	**(II)**	**39.1**	
	291	315	307	(III)	15.4	
	315	378	341	(IV)	10.8	
			361			
	378	432	392	(V)	4.7	
			410			
C1.0-X1.0	25	203	102	(I)	13.4	**65.9**
	203	**302**	**274**	**(II)**	**31.3**	
			294			
	302	319	311	(III)	4.7	
	319	394	355	(IV)	4.6	

Source: Author (2021). Where: T_x are the temperatures for each thermal event and "i" represents the starting temperature, "f", the final and "max", the maximum, according to the derivative graph for each thermogram.

8.7 Conclusions

Hierarchical materials were formed using bacterial cellulose nanofibrils and zeolite X nanometric crystals with different weight compositions. By using different characterization techniques, some features were observed suggesting their main properties.

From the XRD, a faujasite phase is identified and the formation of the composites with cellulose the crystalline phase is maintained, and the relative intensities change accordingly, as observed for zeolite A composites. The crystals are found as nanometric hexagonal plates with some agglomeration and from the SEM analysis, their distribution throughout the cartridges was observed, being better distributed over the laminae that form the aerogels.

The FTIR spectrum presents the bands from the faujasite structure in both the powder and the composite samples with shifts observed to higher wavenumbers to carboxylate

groups, indicating better chemical interaction from that. The NMR results confirm the zeolite X in the sample.

Thermal stabilization is also observed to the composites extending the first event and for the second event, higher temperatures are observed. Thus, as for zeolite A, the presence of zeolites in the cellulose matrix are interesting for the formation of hierarchical cartridges.

9 HIERARCHICAL COMPOSITE MATERIALS WITH MESOPOROUS ALUMINOSILICATE

In this chapter, it is presented the hierarchical materials in form of cartridges, prepared from the cellulose aerogels structure with a mesoporous aluminosilicate derived from clay, with different weight composition. Using some characterization techniques, it was able to identify the main features from the materials and suggest interactions or improvements when compared to the other materials.

For this set of samples, the XRD experiments could not be performed for this set of samples, since in the studied range, the mesoporous materials are amorphous and present only a broad band composed by the background.

9.1 SEM

The sample M presents similar morphology to kaolin used for the synthesis, with thin, flat, and non-shaped particles that look more transparent to the electron beam. Figure 33 presents scanning electron micrography images for sample M composite cartridges with different weight composition as stamped in each of them as it follows: C0.5-M0.5 (Figure 33a-b), C0.5-M1.0 (Figure 33c-d), C1.0-M0.5 (Figure 33e-f) and C1.0-M1.0 (Figure 33g-h). The left images present a scale bar of 20 µm and the right ones, present a detailed view with increased magnification and scale bar of 4 µm.

Like the composites formed with zeolite A and zeolite X, the composites containing sample M and cellulose are formed by sheets where the inorganic material particles are dispersed in a tangle of cellulose fibrils. In lower concentrations, C0.5-M0.5 (Figure 33a-b) and C1.0-M0.5 (Figure 33e-f), although the particles do not present a well-defined shape as for zeolite A, they can be seen immersed in the cellulose sheets, whilst for the samples with just 1.0 wt.% ., C0.5-M1.0 (Figure 33c-d) and C1.0-M1.0 (Figure 33g-h), the particles can also be seen at the surface with the fibrils more evident over the sheets and between them too.

It was important to evaluate the effect of the cartridges formation over this mesoporous aluminosilicate since it does not have a defined shape or pore system as the zeolites discussed previously. Differently from the zeolites, especially zeolite X, sample M presents agglomeration even to the composites with low content and shows that other materials can be

used to obtain aerogel cartridges, but it might not interact as well as the zeolites to be dispersed throughout the structure.

Figure 33 - Scanning electron microscopy images for M sample+ BC composites ranging the weight composition between 0.5% and 1.0% before freeze-drying as stamp in each: (a-b) C0.5-M0.5, (c-d) C0.5-M1.0, (e-f) C1.0-M0.5 and (g-h) C1.0-M1.0

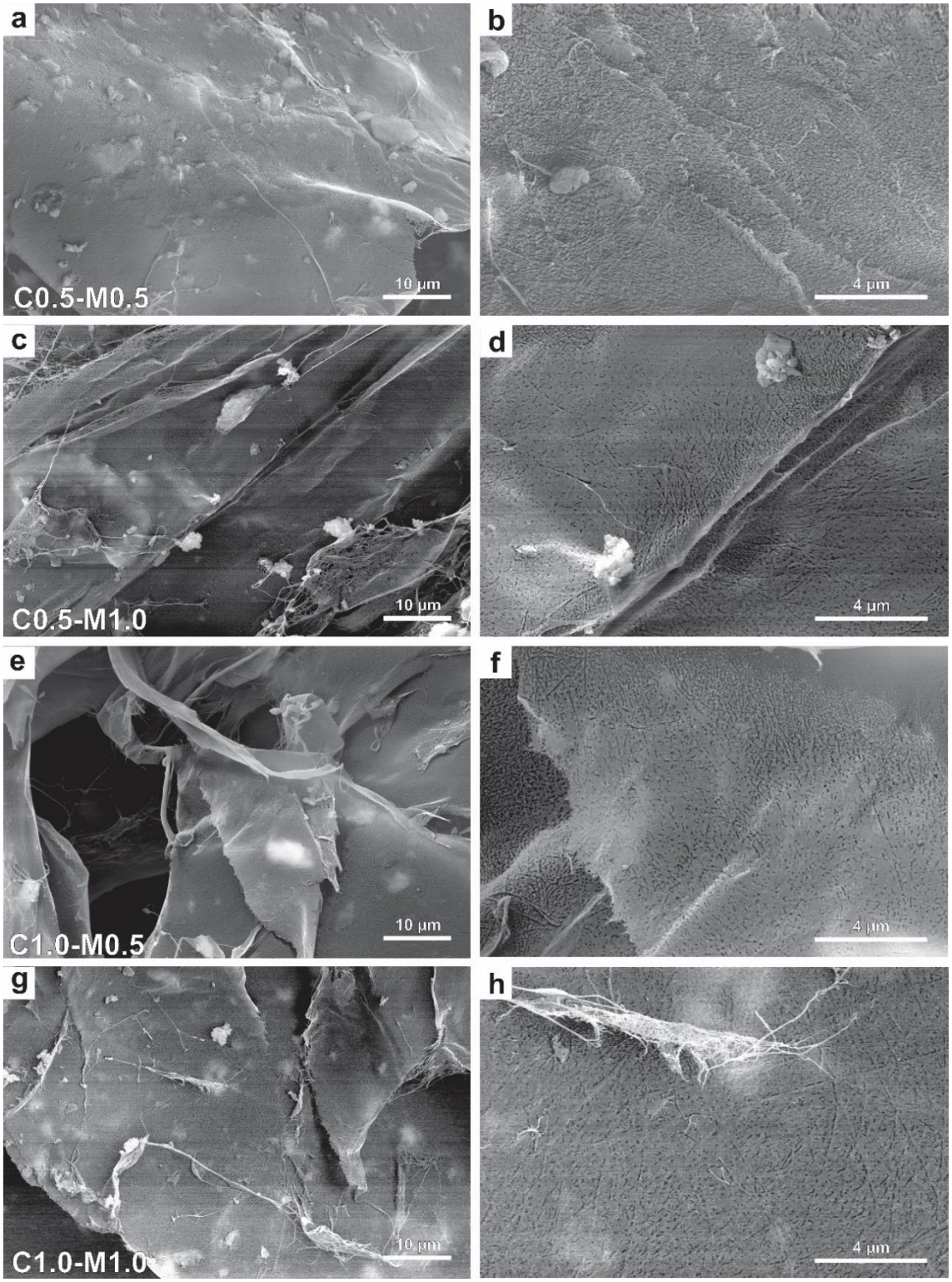

Source: Author (2021). The images on the left side present a scale bar of 20 µm and the right side, 4 µm.

9.2 FTIR

Figure 34 presents the FTIR spectra in KBr to the sample M (Figure 34e) and its respective composites samples with oxidized cellulose 1.0%, C1.0-M1.0 (Figure 34a) and C1.0-M0.5 (Figure 34b), and 0.5%, C0.5-M1.0 (Figure 34c) and C0.5-M0.5 (Figure 34d). The 1800-1500 cm^{-1} region is highlighted in blue and the main bands are indicated. Table 16 is presented with the bands, their respective assignments, and references.

Figure 34 - FTIR spectra for (e) sample M and its respective composites samples with oxidized cellulose 1.0%, (a) C1.0-M1.0 and (b) C1.0-M0.5, and 0.5%, (c) C0.5-M1.0 and (d) C0.5-M0.5, in KBr with the main bands described on the image

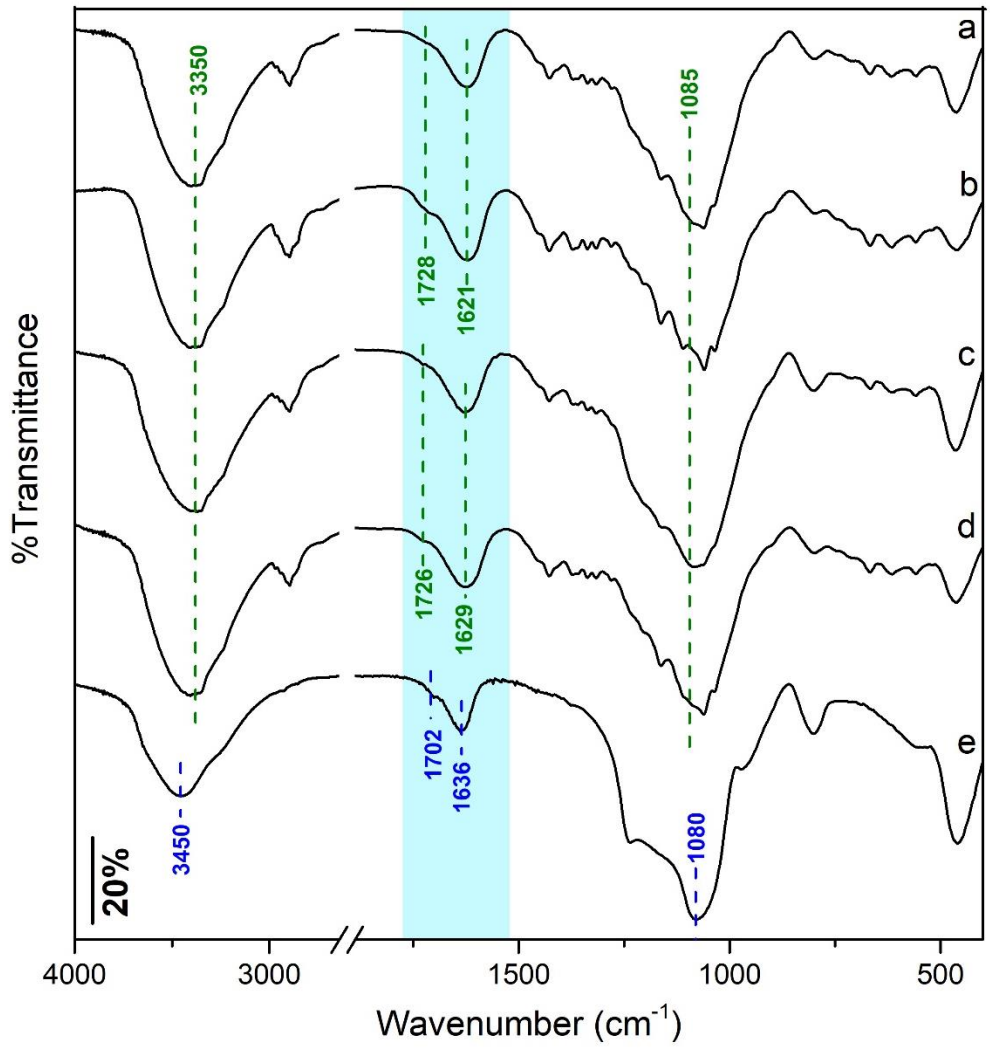

Source: Author (2021).

Table 16 – Main FTIR bands assignments to sample M and its respective composites samples with oxidized cellulose 1.0%, C1.0-M1.0 and C1.0-M0.5, and 0.5%, C0.5-M1.0 and C0.5-M0.5, in KBr

Assignment	**Wavenumber (cm^{-1})**							**References**
	Sample M	**C0.5**	**C0.5-M0.5**	**C0.5-M1.0**	**C1.0**	**C1.0-M0.5**	**C1.0-M1.0**	
Stretching of O–H bonds	3450	3350	3350	3350	3350	3350	3350	147; 160; 180; 183; 220-222
Stretching of C=O in the ester bonds on carboxylic acid	-	1708	1726	1726	1712	1712	1719	173; 176; 185
Stretching of C=O in the ester bonds on sodium carboxylate	-	1610	1629	1629	1612	1621	1621	173; 174; 186
Vibrations of O–H coming from adsorbed water on the structure	1636	-	-	-	-	-	-	147; 220-223
Asymmetrical stretching vibrations of Si–O–Si surface groups	1237	-	-	-	-	-	-	147; 220; 222; 223
Asymmetrical stretching vibrations of Si–O–Si groups	1080	-	1085	1085	-	1085	1085	147; 220-223
Si–OH stretching	970	-	970	970	-	970	970	147; 220-223
Si–O–Si stretching of silica	802	-	802	802	-	797	802	147; 220-223
Si–O–Si deformation	460	-	465	465	-	462	462	147; 220-223

Source: Author (2021).

For the sample M spectrum (Figure 34e) the broad bands specially on 1300-400 cm^{-1} region are typical to bands observed for mesoporous clay-derived materials, as PCH's[220-222; 224] and Al-MCM-41.[147; 223; 225] When the composites are formed, the most prominent change for the sample happens to the main band at 1080 cm^{-1}, asymmetrical stretching vibrations of Si-O-Si groups, change to higher wavenumber in all the samples.

To the cellulose bands, the ones on the blue region for the image present the main difference, showing the carboxylate either in salt or acid form have influence over the cartridge stabilization. The stretching of C=O in the ester bonds on sodium carboxylate goes from 1610 and 1612 cm^{-1} in cellulose samples C0.5 and C1.0, to 1629 and 1621 cm^{-1}, respectively. This indicates stronger interaction with the inorganic material using the carboxylate groups in cellulose structure, highlighting the samples formed with lower cellulose content.

The stretching of C=O in the ester bonds on carboxylic acid that remains the same to zeolite A samples (Figure 25) and it is not visible to zeolite X samples (Figure 25), is shifted on this set of samples to higher wavenumbers, observing a bigger difference for C0.5 samples, as it is in sodium carboxylate group. The bands around 3400 cm^{-1} follow the same trend as zeolite A samples and the cellulose is dominant to the hydrogen bonds.

9.3 TGA

Figure 35 presents the thermal analyses for sample M and its composite samples varying the weight composition, C0.5-M0.5, C0.5-M1.0, C1.0-M0.5, C1.0-M1.0, and their differentiate graphs on the right side of the figure. From these results, the events were identified and presented in Table 17 pointing initial and final temperature, as well as maximum loss temperature to each event and the partial and total loss to the sample.

Figure 35 - Thermograms acquired in synthetic air with 50 mL min^{-1} flow and heating rate of 10 °C min^{-1} for sample M composite samples with different weight composition and their respective differentiate graphs

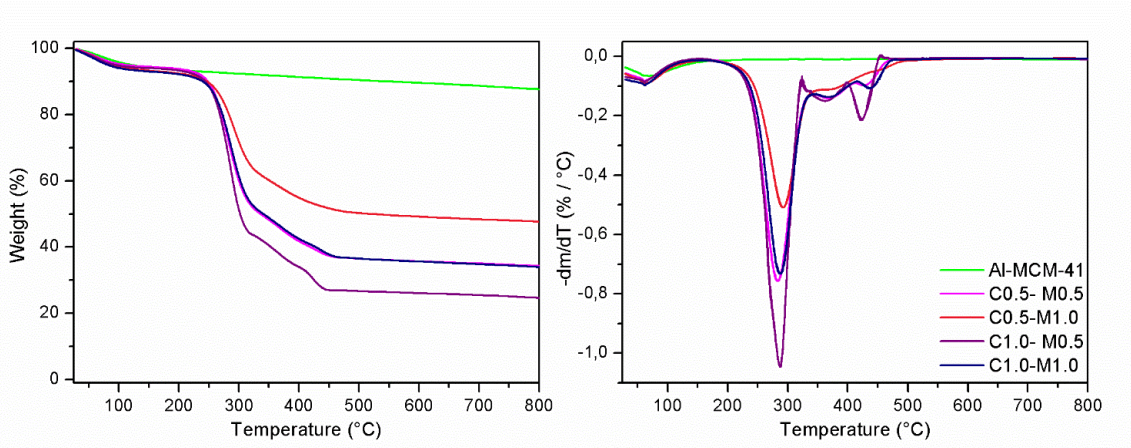

Source: Author (2021).

Sample M presented maximum weight loss of 12.5% essentially in a thermal event between 25 and 250°C related to adsorbed water loss in the structure in a lower extent when compared to the previous materials, zeolites A and X. However, this value is compatible to similar mesoporous and clay materials. Above this temperature, the low water loss for the material can be attributed to water elimination from adjacent silanol groups condensation forming siloxane linkages.[226; 227]

To the composites, it is noticed that the addition of the mesoporous material to the cartridges promotes the decrease in weight loss for the resulting material, as observed to the samples containing zeolites presenting around 47% in final weight to the sample with higher M sample relative quantity, C0.5-M1.0. That is also the sample with higher difference in maximum temperature to the main event, since it changes from 280 °C in pure cellulose to 292 °C. Besides that, the first thermal event presents modifications, being extended to temperatures superior to the samples containing just cellulose.

Like what happens to zeolites composites, the second main event after 300 °C, related to oxidation and carbonaceous waste breakdown, happens in two smaller events when the composites are formed that are also attenuated; the increment on porous materials added to the system promotes them to appear in higher temperatures.

Table 17 - Thermal events observed to sample M composites with different weight compositions using synthetic air at 50 mL min^{-1} and heating rate of 10 °C min^{-1}

Sample	T_i / ºC	T_f / ºC	T_{max} / ºC	Event	Partial loss / %	Total loss / %
M sample	**25**	**250**	**67**	**(I)**	**7.0**	**12.5**
			200			
C0.5-M0.5	25	167	62	(I)	5.7	**65.7**
	167	**342**	**283**	**(II)**	**44.9**	
	342	411	370	(III)	8.7	
	411	469	430	(IV)	3.9	
C0.5-M1.0	25	160	63	(I)	6.8	**52.4**
	160	**350**	**292**	**(II)**	**33.0**	
	350	435	376	(III)	7.6	
	435	485	457	(IV)	2.1	
C1.0-M0.5	25	160	63	(I)	6.2	**75.4**
	160	**324**	**268**	**(II)**	**50.4**	
			287			
	324	399	330	(III)	9.6	
			364			
	399	455	422	(IV)	7.0	
C1.0-M1.0	25	160	63	(I)	7.2	**65.9**
	160	**342**	**287**	**(II)**	**43.0**	
	342	415	369	(III)	8.5	
	415	475	437	(IV)	4.5	

Source: Author (2021). Where: T_x are the temperatures for each thermal event and "i" represents the starting temperature, "f", the final and "max", the maximum, according to the derivative graph for each thermogram.

9.4 Textural properties

Figure 36 presents the N_2 adsorption/desorption isotherms for sample M. The detail in the graph presents the pore distribution curve for this material from the BJH plots.

Figure 36 - N_2 adsorption/desorption isotherms for sample M; the detail in the graph presents the BJH plots with the pore distribution curve for this material

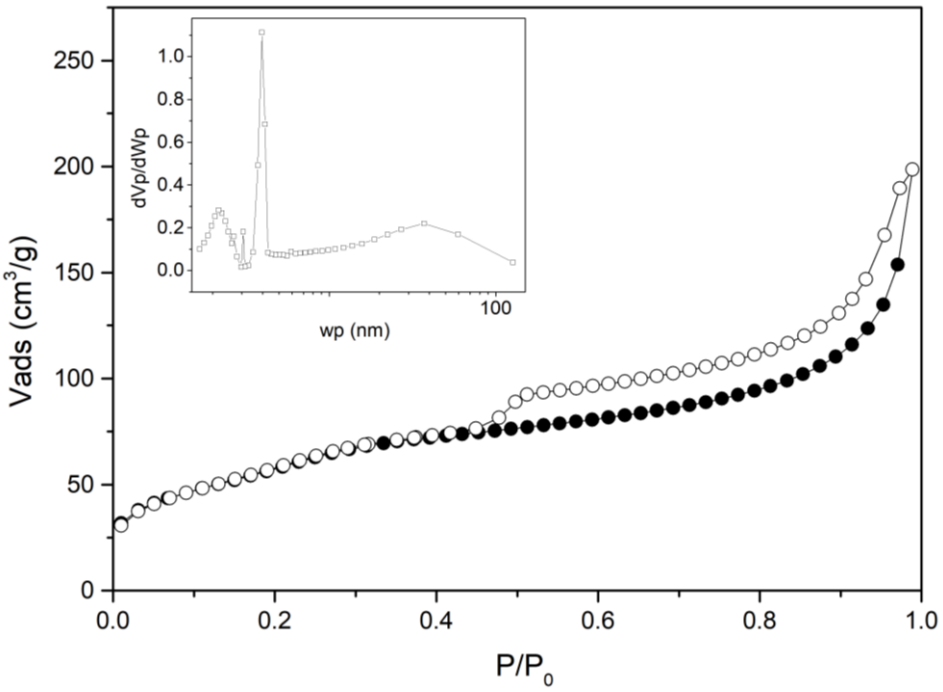

Source: Author (2021). The filled symbols are referent to the adsorption branch and the blank ones, desorption.

The sample M presented type IV(a) isotherm with H4 hysteresis indicating the presence of a mesoporous structure with interlayer pores, typical for clay materials.[224; 228] The pore size distribution observed from the BJH plots on the inset of the figure suggests that a wide range of mesopores is formed with peaks centred at 2.3, 3.1, 3.9 and 38.0 nm. The latter is presented as a broad peak and in addition to the high uptake at relative pressures above 0.95, it can be attributed to the clay particles agglomeration.

Using the BET equation, the surface area was calculated as 208 m^2 g^{-1} higher than pristine clays.[46; 229; 230] Together with NMR data presented in the following chapter, it is possible to infer that the acid treatment for this work exposed Si atoms on the kaolin's lamellae but it also deposited some amorphous Al on the surface, making the clay more rigid to the formation of a defined mesoporous structure as reported by Santos *et al.*,[147; 225] or other structures like Al-MCM-41 or PCH's.[223; 231] This causes irregular distribution for the surfactant on the synthesis and giving rise to pores with different sizes as well as formed between the particles.

9.5 Conclusions

Cartridges possibly with a hierarchical structure were formed using bacterial cellulose nanofibrils and the mesoporous aluminosilicate in an aerogel-like material with different weight compositions. By using different characterization techniques, some features were observed that distinguished or confirmed properties already discussed in the previous chapters.

When analysing their dispersion over the aerogel structure, this study had shown that the particles throughout the aerogels' thin sheets with some agglomeration over the sheets. In the FTIR results, the interaction between the two components indicates stronger interaction with lower cellulose content, and as discussed previously, using the sodium carboxylate groups in the cellulose structure.

The addition of nanoporous materials to the cellulosic matrix also allows a better thermal behaviour for the composites, putting the cellulose degradation event to higher temperatures. By the end, textural analysis for the mesoporous clay suggests effectiveness in the mesopores formation, since the surface area obtained is higher than the values obtained for the pristine samples, reported in literature.

Taken together, these results point to the possibility of obtaining hierarchical cartridges using other non-zeolitic materials in addition to the bacterial cellulose hydrogel.

10 CELLULOSE OXIDATION INFLUENCE OVER THE CARTRIDGES

In this chapter, it is presented the influence that the oxidation step plays over the preparation of the hierarchical cartridges. Performing some characterization and ionic exchange experiments, it was possible to identify details and features that differentiate them and suggest the best choice to obtain such materials.

10.1 XRD

Figure 37 presents the XRD patterns for composites containing C_0 and C_{oxi} and the nanoporous materials: C_{oxi}A (Figure 37a), C_0A (Figure 37b), C_{oxi}X (Figure 37c) and C_0X (Figure 37d). The blue squares point the main peaks to the cellulose phase, green triangles, zeolite A and light green hexagons, zeolite X. As stated in the last chapter, the XRD is not presented for sample M composites since they present only a broad peak in the studied range, without any crystallinity.

The crystalline structures remain the same comparing the oxidation effect to the cartridges' formation, although, to this set of samples, zeolite A presents much intense peaks to the non-oxidized composite (Figure 37b). It can be explained for having more crystals available to the X-rays on the surface of the cellulose sheets,[184] as it will be shown and better discussed to the SEM analyses. This feature is not observed to zeolite X composite samples mainly due to its nanometric size in the same range that the cellulose, so the interaction with the energy is similar, even changing their dispersion on the cartridges.

Figure 37 - Co-Kα XRD patterns for composites containing C_0 and C_{oxi} and the nanoporous materials: (a) $C_{oxi}A$, (b) C_0A, (c) $C_{oxi}X$ and (d) C_0X

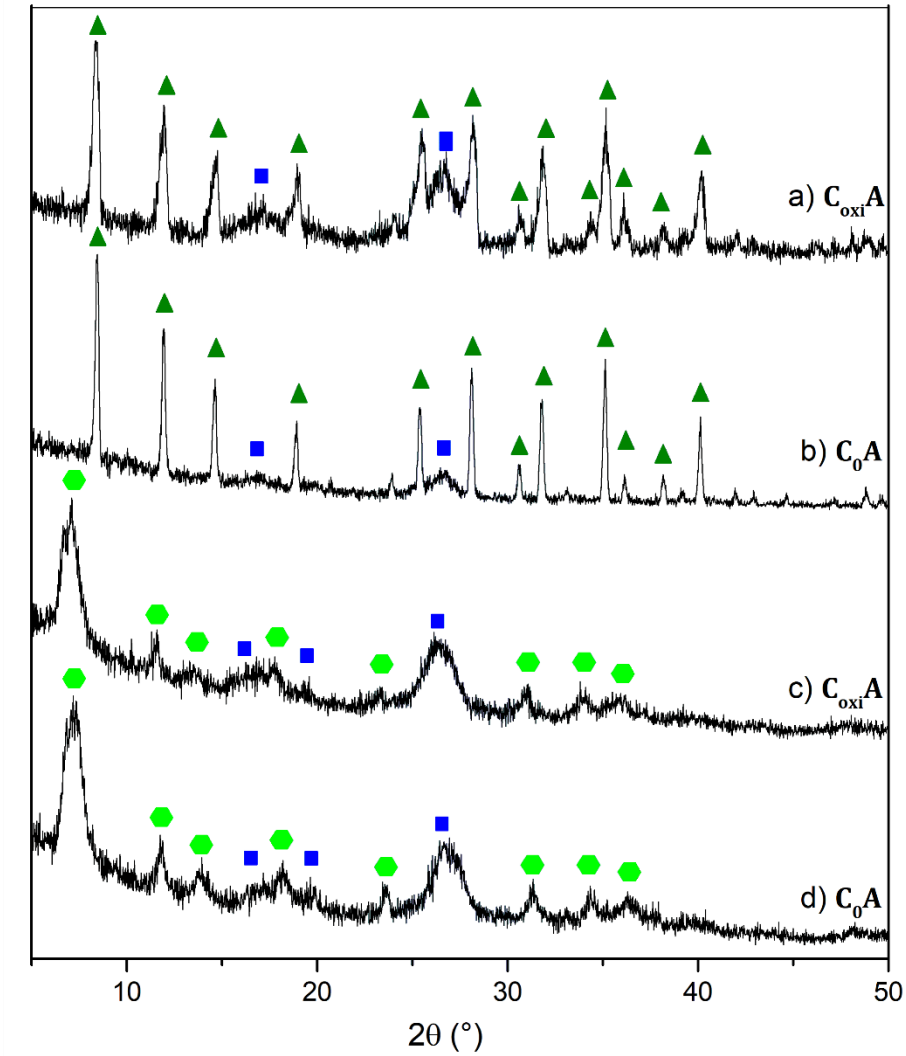

Source: Author (2021). The blue squares point the main peaks to the cellulose phase, green triangles, zeolite A and light green hexagons, zeolite X. Y axis = Intensity (a.u.).

10.2 SEM

Figure 38 presents scanning electron micrography images for the composite cartridges with non-oxidized cellulose and the insets are referent to the respective oxidized ones: C_0A (Figure 38a), $C_{oxi}A$ (Figure 38b), C_0X (Figure 38c), $C_{oxi}X$ (Figure 38d), C_0M (Figure 38e) and $C_{oxi}M$ (Figure 38f). All the images bring the same scale bar making comparison easier.

Figure 38 - Scanning electron microscopy images for composites formed with non-oxidized cellulose: (a) C_0A, (c) C_0X and (e) C_0M; the small images are referent to the respective oxidized samples: (b) $C_{oxi}A$, (d) $C_{oxi}X$ and (f) $C_{oxi}M$

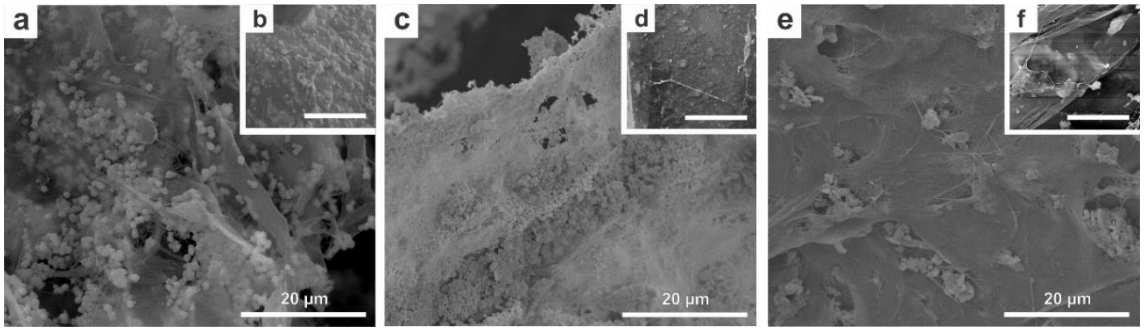

Source: Author (2021). All the images present the same scale bar of 20 µm.

All the small images were presented previously in normal size ($C_{oxi}A$, Figure 24c; $C_{oxi}X$, Figure 28c; $C_{oxi}M$, Figure 33c) and are repeated here as insets just to make the comparison easier. A huge difference is observed to those cartridges, since the sheets are much better assembled when the nanoporous materials are added than what it was to the pure-cellulose cartridges (Figure 18b), although the inorganic particles get agglomerated and mostly accessible to the surface. This is a macroscopic evidence about the weak interaction when there are no carboxylate groups in the cellulose structure. This hypothesis will be discussed further in coming sections to evaluate an explanation for that.

Table 18 presents the results obtained for SEM analyses coupled to EDS detector for the non-oxidized composite samples presented in Figure 38, highlighting with bold the elements in higher concentration in each sample and the last column presents the Si/Al molar ratio.

Table 18 - Weight composition for elements C, O, Al, Si, Na and Cl, as well as the Si/Al molar ratio, to non-oxidized cellulose composites with zeolites A (C_0A) and X (C_0X) using EDS detector in SEM analysis

SAMPLE	**% WEIGHT**						**Si/Al**
	C	**O**	**Al**	**Si**	**Na**	**Cl**	
C_0A	29.7	44.7	**8.5**	**8.8**	8.4	-	1.00
C_0X	24.1	27.9	**15.8**	**20.9**	11.4	-	1.27

Source: Author (2021).

The Si/Al molar ratio for this set of non-oxidized samples is closer to the values in the pure zeolites and once again, the results can be confirmed by the NMR studies presented in later sections.

10.3 FTIR

Figure 39 presents the FTIR spectra in KBr to the composite cartridges with oxidized and non-oxidized celluloses with zeolite A, $C_{oxi}A$ (Figure 39a) and C_0A (Figure 39b), zeolite X, $C_{oxi}X$ (Figure 39c) and C_0X (Figure 39d), and M sample, $C_{oxi}M$ (Figure 39e) and C_0M (Figure 39f) with the main bands pointed.

Figure 39 - FTIR spectra for composites containing C_0 and C_{oxi} and the nanoporous materials: (a) $C_{oxi}A$, (b) C_0A, (c) $C_{oxi}X$, (d) C_0X, (e) $C_{oxi}M$ and (f) C_0M in KBr with the main bands described on the image

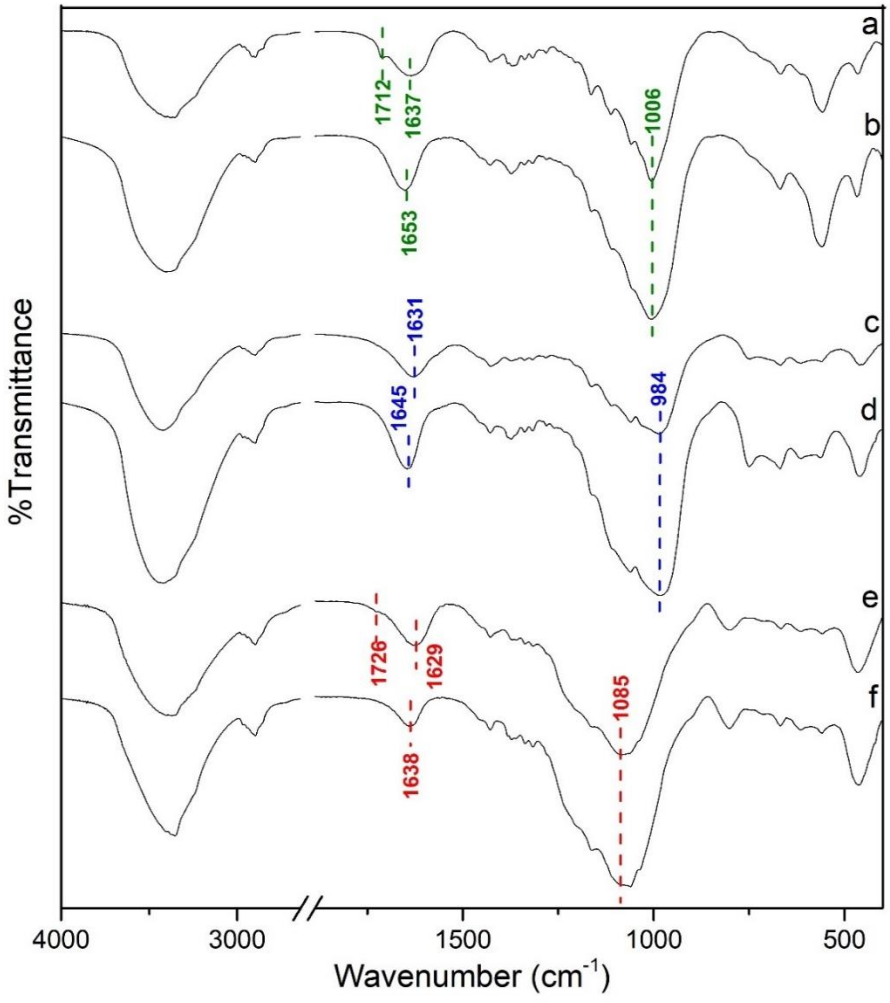

Source: Author (2021).

The composite samples containing the zeolites A and X keep the bands related to the zeolitic structure, as pointed by bands 1006 cm^{-1} ($C_{oxi}A$, Figure 39a, and C_0A, Figure 39b) and 984 cm^{-1} ($C_{oxi}X$, Figure 39c, and C_0X, Figure 39d). The M sample, although, shifts its main

band at 1080 cm^{-1} to higher wavenumbers in both composites, $C_{oxi}M$ (Figure 39e) and C_0M (Figure 39f). Such materials, with a layered shape as presented in SEM, may have more O–T–O exposed groups on the surface, allowing the interaction with the cellulose fibrils. In next section, NMR, there will be an attempt of observing this relation.

The bands present on the 1800-1500 cm^{-1} region show shifting to higher wavenumbers in all the composite samples in Figure 39 (except for C_0M), in a way that interaction seems to be markedly important using carboxylate groups from cellulose structure.

10.4 NMR

Figure 40 presents the ^{13}C MAS-NMR spectra to oxidized and non-oxidized celluloses and the composites formed with zeolite A (C_0A and $C_{oxi}A$), zeolite X (C_0X and $C_{oxi}X$) and M sample (C_0M and $C_{oxi}M$). On top of the left and right sides, the non-oxidized and oxidized units, respectively, are presented with the carbon atoms numbered as the signals in the spectra.

On the left side of Figure 40, the non-oxidized cellulose (C_0) and composites are presented, and on the right side, the oxidized samples (C_{oxi}). Comparing them, no differences can be seen related to the structure oxidation and the peaks positions to all the samples: C1 = 105 ppm, C4 = 89 and surface atom = 85 ppm, C2, C3 and C5 = 75-72 ppm, C6 = 65 ppm and the surface atom=62 ppm.[65; 232; 233] The major changes are related to the relative intensities that become more prominent to the composites. This is an indication of surface interaction as suggested for the IR results, using hydrogen bonds and carboxylate groups.

Figure 41 presents the ^{29}Si MAS-NMR spectra for zeolite A related samples on the left side, zeolite X related samples on the centre and M sample and its composites on the right side of the figure. ^{27}Al MAS-NMR spectra are also presented in Figure 42, following the same organizing parameters. Peaks with changes in chemical shift are presented in red.

Figure 40 - ^{13}C MAS-NMR spectra for oxidized and non-oxidized celluloses and their composites with zeolites A and X and M sample

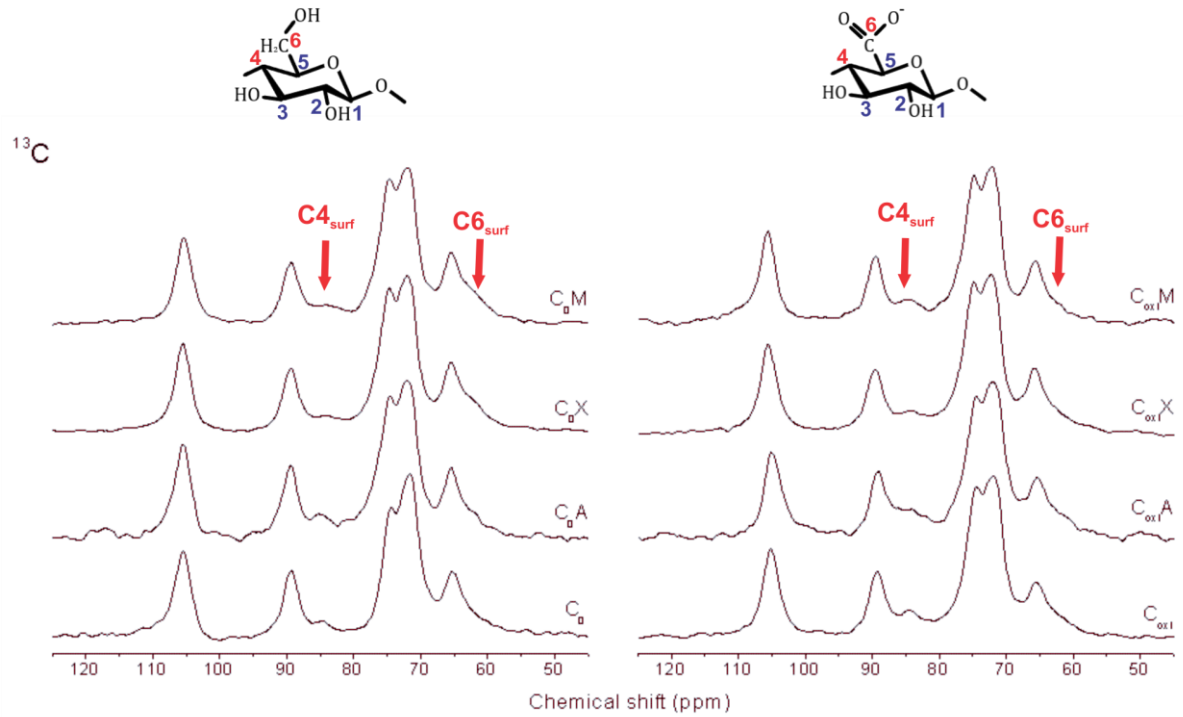

Source: Author (2021).

Figure 41 - ^{29}Si MAS-NMR spectra for the zeolites A and X and M sample with their composites related to the oxidation effect studies. Peaks with changes to the chemical shift are presented in red

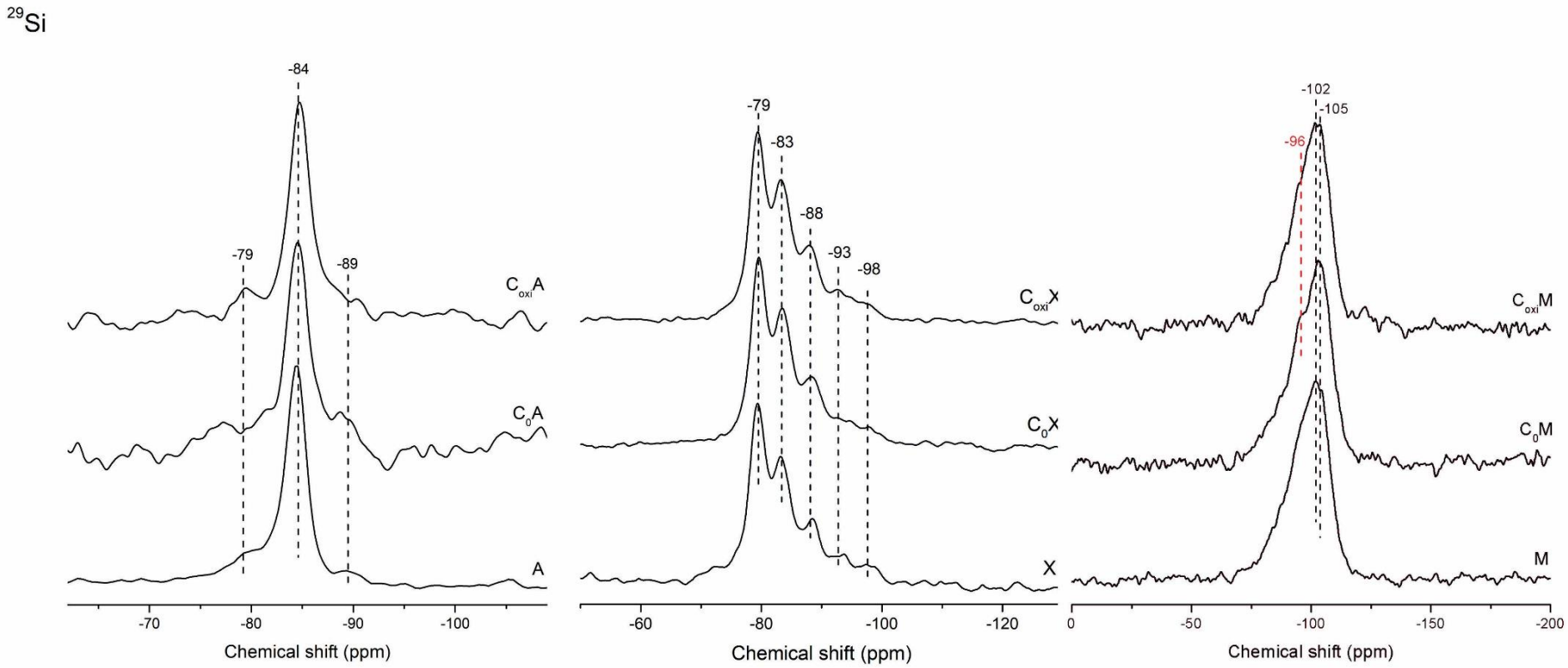

Source: Author (2021).

Figure 42 - ^{27}Al MAS-NMR spectra for the zeolites A and X and M sample with their composites related to the oxidation effect studies. Peaks with changes to the chemical shift are presented in red

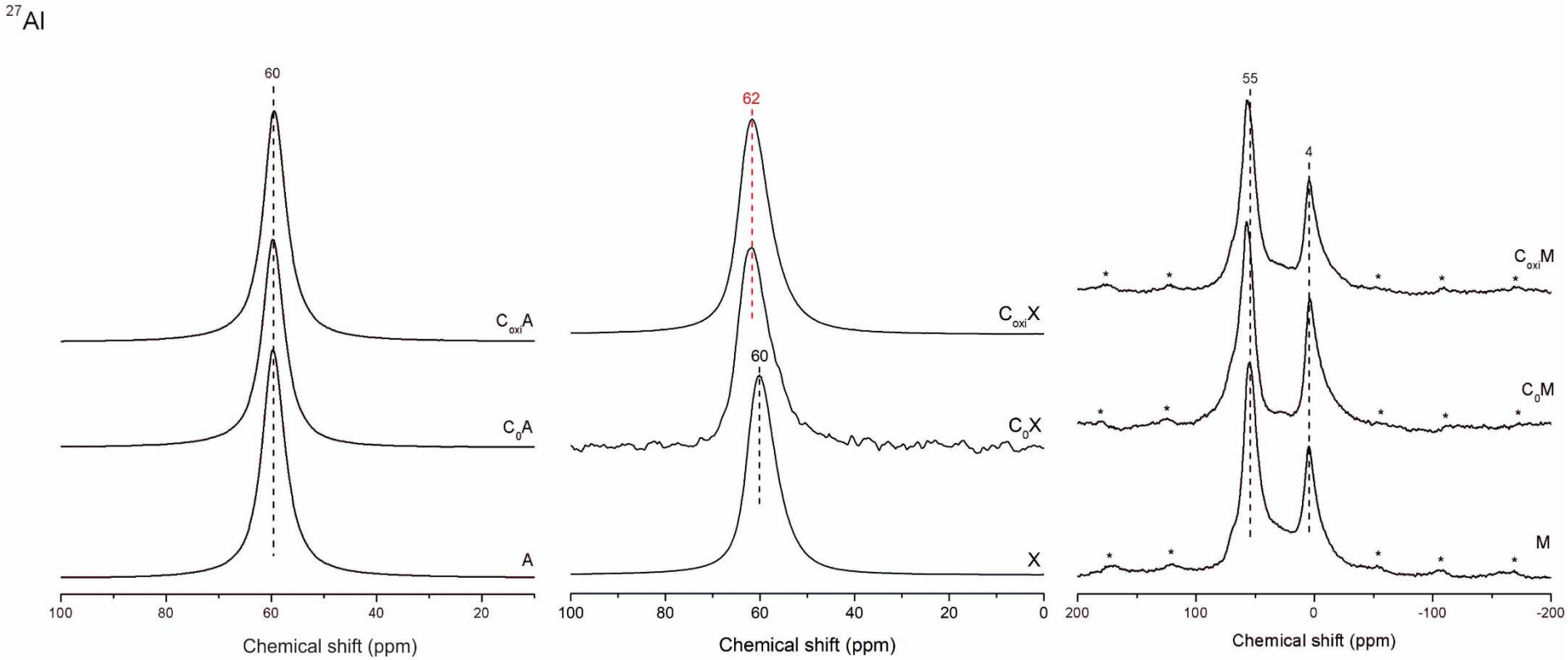

Source: Author (2021). Side bands are pointed with *.

The ^{29}Si MAS-NMR spectra for C_{oxi}X and C_0X show the same positions for the observed peaks and changes in the relative intensity to the last peaks. It is known that the groups Q^4 (4Al) and Q^4 (3Al) are present mainly on the bulk for the zeolite X crystals and the Q^4 (2Al) and Q^4 (1Al) groups also present the surface silanol groups contribution.[219] In both the samples, the peaks Q^4 (1Al) and Q^4 (0Al) decrease slightly their relative intensities indicating such surface silanol groups taking part on the interaction with both cellulose samples.

For zeolite A, the main peak corresponds to Q^4 (4Al) and since the Si/Al ratio > 1.0 (obtained previously from XRD Rietveld refinement and EDS), a small amount of Q^4 (3Al) can be observed at -89 ppm.[234; 235] The signal on the left side can be attributed to the surface silanol groups to this zeolite. Both the signals move slightly on the composites spectra strongly indicating the interaction to the cellulose fibres through such groups.

The ^{29}Si MAS-NMR spectrum for sample M shows a main signal at -102 ppm related to Q^4 Si species on the sample and when the composites spectra are compared to it, other peaks are distinguished. This can indicate that either the composites promote the emergence of other groups on the sample or the peaks referent to those were overlapped by the Q^4 signal and become visible due to the interaction with the cellulose. For some asymmetry on the peak observed for M, the later seems to be a more reasonable option. Thus, the peak in -96 ppm decreases slightly for C_{oxi}M and more pronouncedly to C_0M, being the main interaction force used with the cellulose structure.

The ^{27}Al MAS-NMR spectra to the samples show the presence of tetracoordinated aluminium for all the samples: zeolite A and composites (60 ppm), zeolite X and composites (60 and 62 ppm), sample M and composites (55 ppm). The zeolites do not present peaks or signals in any other region for the spectra, whilst M sample also presents a peak in 4 ppm referent to octahedral Al extra-framework and between those, the broad peak around 30 ppm that indicates the presence of pentacoordinated/amorphous Al.[46; 218; 234; 236; 237] This is a strong evidence about the partially inefficient acid treatment to the kaolin, making the clay more rigid to the formation of a defined mesoporous structure due to the deposition of Al on the surface and the presence of high amount of octacoordinated Aluminium.

Zeolite A and its composites with the different celluloses do not present any shift to the peak. The minor changes that occur for the Si environment are mostly on the surface and not enough to promote visible changes to the zeolite A bulk. Zeolite X on its turn, for being a nanometric particle, presents a slight shift to lower fields from 60 to 62 ppm, since the interactions happen using the silanol groups on the surface, the angle for the Al–O–Si bonds will also present changes causing a higher chemical shift to the composite samples.

Sample M and its composites present the same positions for the two main Al peaks, keeping the intensity ratio for the tetrahedral and octahedral species, which indicates that Al is mainly incorporated to the structure and the composites formation does not change this feature. The broad peak around 30 ppm can be related to the presence of unreacted metakaolin and decreases on the composite samples, showing that the cartridges allow the not-amorphous parts to be better entangled by the cellulose nanofibers.

10.5 TGA

Figure 43 presents the thermal analyses for zeolite A and its composites formed with non-oxidized and oxidized cellulose, C_0A and C_{oxi}A respectively; Figure 44 presents the same for zeolite X, C_0X and C_{oxi}X, and Figure 45, for M sample, C_0M and C_{oxi}M. The main thermal events for the non-oxidized samples are presented in Table 19 pointing initial, final, and maximum loss temperature as well as the partial and total loss. The same parameters are presented in the table for samples discussed on the previous chapters (C_0, C_{oxi}, C_{oxi}A, C_{oxi}X and C_{oxi}M) to ease the comparison.

Comparing these results to C_0 (Figure 21) degradation and to the composites formed with the same nanoporous materials and oxidized cellulose (c, for all the Figures), it can be noticed that the same feature is presented to the samples, where in general, the oxidation promotes the cellulose degradation reactions happening in lower temperatures and the addition of inorganic materials to the cellulose matrix shows lower weight loss.

An interesting thing to be observed to the samples is that the weight loss to the non-oxidized samples is ca. 10% lower than the ones containing oxidized cellulose and observations to T_i, T_f and T_{max} of the main event indicate signal broadening for C_0A with anticipation to T_i and delay to T_f, whilst for C_0X and C_0M, the event starts in higher temperatures. This effect is very prominent to M sample presenting almost 100 °C difference. The shape of the particles as plates/layers is effective enabling interaction with the cellulose fibrils and leverages the insulating properties over the sample.[108; 184]

Figure 43 - Thermograms acquired in synthetic air with 50 mL min^{-1} flow and heating rate of 10 °C min^{-1} with the respective differentiate graphs for zeolite A, C_0A and $C_{oxi}A$

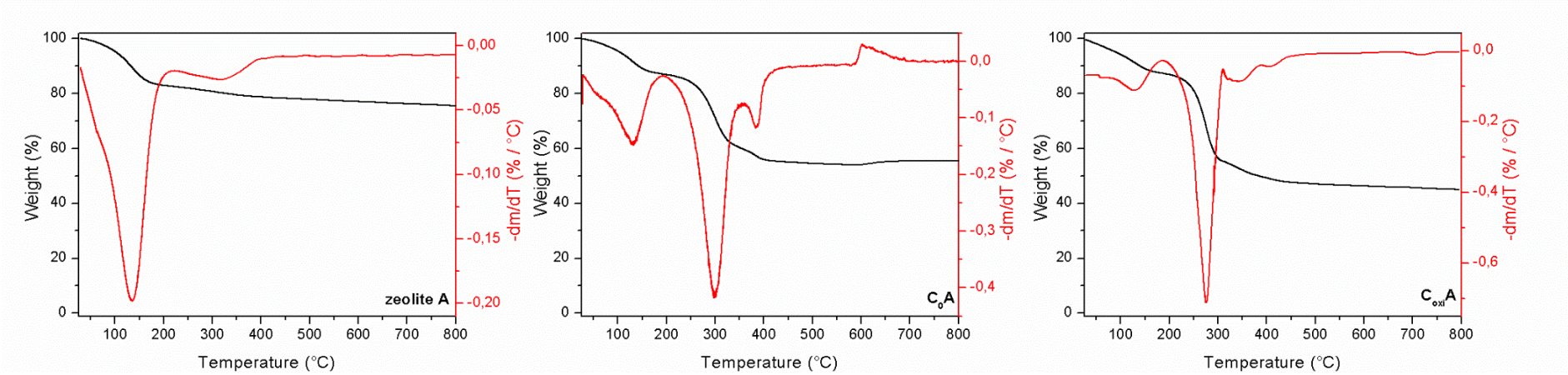

Source: Author (2021).

Figure 44 - Thermograms acquired in synthetic air with 50 mL min^{-1} flow and heating rate of 10 °C min^{-1} with the respective differentiate graphs for zeolite X, C_0X and $C_{oxi}X$

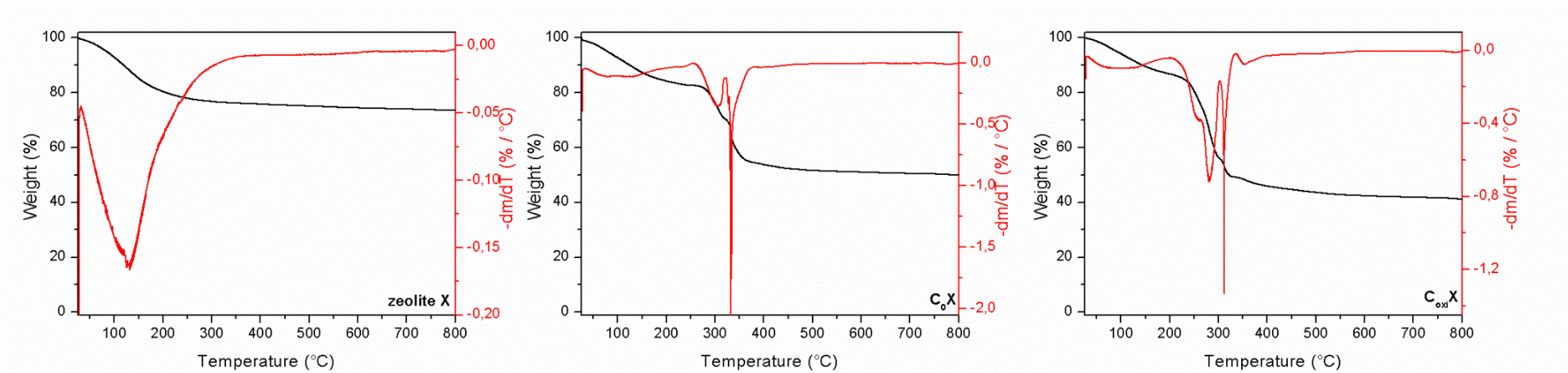

Source: Author (2021).

Figure 45 - Thermograms acquired in synthetic air with 50 mL min^{-1} flow and heating rate of 10 °C min^{-1} with the respective differentiate graphs for M sample, C_0M and $C_{oxi}M$

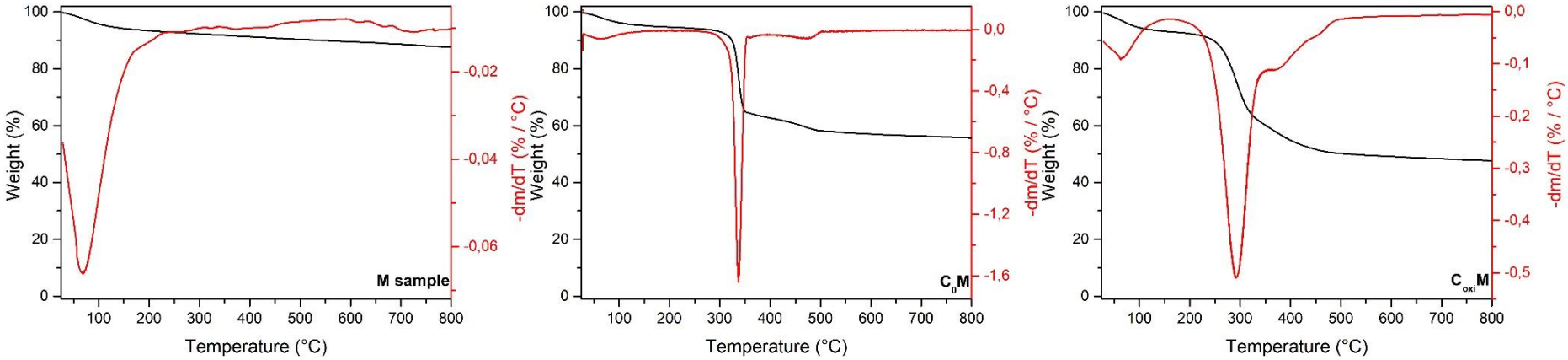

Source: Author (2021).

Table 19 - Thermal events observed to non-oxidized cellulose composites, C_0A, C_0X and C_0M, using synthetic air at 50 mL min^{-1} and heating rate of 10 °C min^{-1}. The data for the main degradation event for samples C_0, C_{oxi}, $C_{oxi}A$, $C_{oxi}X$ and $C_{oxi}M$ already discussed on the previous chapter are also presented to ease the comparison

Sample	T_i / ºC	T_f / ºC	T_{max} / ºC	Event	Partial loss / %	Total loss / %
C_0	**217**	**360**	**313**	**(II)**	**68.2**	**99.8**
C_{oxi}	**172**	**315**	**260**	**(II)**	**69.1**	**98.0**
			280			
C_0A	25	192	61	(I)	12.7	**44.7**
			131			
	192	**357**	**300**	**(II)**	**27.6**	
	357	422	386	(III)	4.1	
$C_{oxi}A$	**185**	**310**	**260**	**(II)**	**32.0**	**55.1**
			276			
C_0X	**25**	**256**	**133**	**(I)**	**17.3**	**49.8**
	256	321	307	(II)	12.2	
	321	374	331	(III)	15.9	
$C_{oxi}X$	**200**	**302**	**256**	**(II)**	**31.1**	**58.8**
			282			
C_0M	25	135	64	(I)	4.6	**44.9**
	274	**354**	**337**	**(II)**	**29.5**	
	418	503	474	(III)	4.4	
$C_{oxi}M$	**160**	**350**	**292**	**(II)**	**33.0**	**52.4**

Source: Author (2021). Where: T_x are the temperatures for each thermal event and "i" represents the starting temperature, "f", the final and "max", the maximum, according to the derivative graph for each thermogram.

It is important to summarize that all the composites present a better thermal behaviour influenced by the addition of nanoporous materials to cellulose, indicating that the formed materials are more stable due to the changes over their intermolecular bonds. Even though the cellulose oxidation does not cause a big issue to the required applications and the lowest temperature observed is high enough to allow their use in many adsorption experiments.

10.6 Ionic exchange

Figure 46 presents the removal results for ionic exchange with Ca^{2+} comparing cellulose samples (C_0 and C_{oxi}) to zeolite A and its composites (C_0A and $C_{oxi}A$) on the left side and to zeolite X and its composites (C_0X and $C_{oxi}X$) on the right side. Table 20 presents the expected values for Ca^{2+} removal according to Na^+ EDX results and the measured values.

Figure 46 - Removal results for ionic exchange with a 3 mmol L^{-1} Ca^{2+} for 30 minutes at 250 rpm in ambient conditions comparing cellulose samples (C_0 and C_{oxi}) to zeolite A and its composites (C_0A and $C_{oxi}A$) on the left side and to zeolite X and its composites (C_0X and $C_{oxi}X$) on the right side

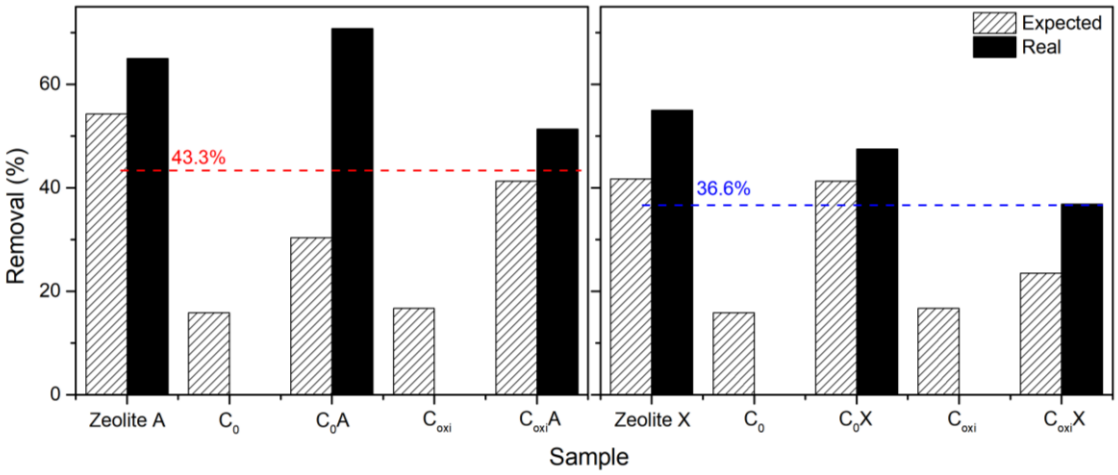

Source: Author (2021). The red signs present the expected removal values to the composites considering the zeolite A weight content in the cartridges, and in blue, to zeolite X.

Only the zeolite samples were tested for ionic exchange experiments since they are most used for this purpose industrially. The calculated Ca^{2+} removal from the Na^+ EDX results for the samples considers that all the sodium is exchanged for calcium during the experiments. From the data, it is visible that the zeolites and the composites present a better removal behaviour for Ca^{2+} than it was expected, whilst the cellulose cartridges did not exhibit any removal, even that they have some sodium content (around 16%).

Usually, nanocellulose-based materials present functional groups or molecules grafted to surface hydroxyl groups, improving the adsorptive properties for several pollutants.[238] Mautner *et al.*, 2019[239] performed some studies using nanopapers formed by oxidized cellulose nanofibrils functionalized with phosphoric groups to act as ionic exchange membranes and they found good adsorption capacities due to the presence of H_2PO_3 linked through carboxylate groups. Although, they suggest that adsorption preferably takes place on the surface and is less favoured within the nanopaper bulk. Thus, the sodium not exchanged for

this process can be attributed to their encapsulation inside the cellulose sheets, not on the surface.

Table 20 – Calculated and measured removal results for ionic exchange with a 3 mmol L^{-1} Ca^{2+} for 30 minutes at 250 rpm in ambient conditions to zeolite A and zeolite X-related samples.

Sample	**Calculates Ca^{2+} removal (%)**	**Measured Ca^{2+} removal (%)**
Zeo A	54.3	65.0
Zeo X	41.7	55.0
C_0	15.9	0
C_0A	30.4	70.8
C_0X	41.3	47.5
C_{oxi}	16.7	0
$C_{oxi}A$	41.3	51.4
$C_{oxi}X$	23.5	36.9

Source: Author (2021).

Zeolites X presents a lower exchange capacity, since it has a higher Si/Al and consequently, lower cations presence in its framework.[240] Zeolites ionic exchange properties are known since the XIX century[241] and zeolite A, for having the lowest possible Si/Al ratio is the most used material for this purpose.[146; 242]

When compared to their respective composites, the measured values were also higher than expected. The red and blue lines point to the amount that should be exchanged considering the real value obtained for the zeolite; for example, zeolite A showed 65% removal which means that considering its weight% in the composite sample and that the cellulose would not have effect on it, the cartridges should have 43% removal equally. The observation for this trend then, can clearly show the positive effect that the cellulose had to the Ca^{2+} removal, more pronouncedly to the non-oxidized cellulose.

Figure 47 brings SEM images to the samples with zeolite A and both non-oxidized, C_0A (Figure 47a-b), and oxidized cellulose, $C_{oxi}A$ (Figure 47c-d), before (left side) and after (right side) the ionic exchange experiments.

Figure 47 - SEM images to the samples (a-b) C_0A and (c-d) $C_{oxi}A$ before (left side) and after (right side) the ionic exchange experiments

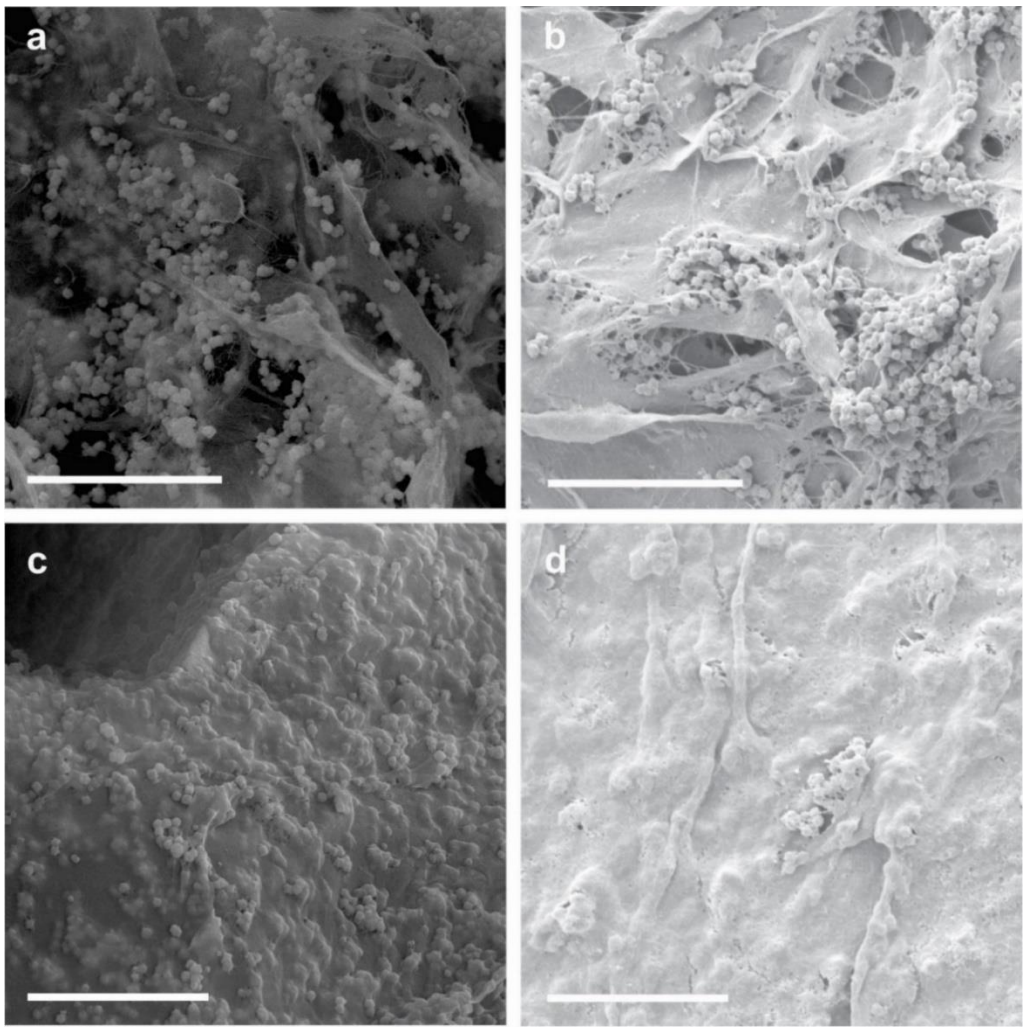

Source: Author (2021). The images present a scale bar of 20 µm.

The SEM study comparing the morphology to the cartridges before and after the ionic exchange experiments allows assessing leaching of the zeolites from the cartridges or even some changes to the nanofibers' organization. The results suggest that the structure is not changed after some time in aqueous medium at neutral pH and the proposed materials are stable. Some experiments regarding their reusability would be helpful to identify if the exchanged capacity presents any changes.

10.7 Conclusions

Hierarchical materials were formed by bacterial cellulose in both oxidized and non-oxidized forms with three nanoporous materials: zeolites A and X, and mesoporous aluminosilicate. By using different characterization techniques and ionic exchange experiments, the main differences and features observed to the cartridges were analysed. From the studies, the oxidation step was determined as important to form the cartridges allowing not only an effective interaction between the materials, but also for stabilization of the cellulose suspensions.

The XRD shows that there is not difference to the crystallinity of such materials, but a higher amount available to interaction with the X-ray beam. Analysing their morphology, the non-oxidized cartridges present the particles agglomerated and mainly on the surface of the aerogel's sheets.

From the FTIR, the cartridges with zeolites present only shifts on 1800-1500 cm^{-1} region and with the mesoporous clay, also to the main structural band. From the NMR, the use of hydrogen bonding plus the interaction with carboxylate groups are suggested to stabilize the composite structure and thus, the oxidation step is important for the hierarchization.

The thermal behaviour for all the samples is improved with the addition of nanoporous materials causing changes over the intermolecular bonds, and even though the cellulose oxidation promotes degradation in lower temperatures, it is high enough to allow their application in many adsorption systems. From the ionic exchange experiments, both the zeolites and their composites had the measured removal for Ca^{2+} higher than calculated as well as a positive effect for the cellulose on the cartridges.

Taken together, these results show that hierarchical cartridges can be formed with bacterial cellulose and three different nanoporous materials, suggesting that the oxidation step allows better interaction between the materials independently of the shape or pore system.

11 HIERARCHICAL COMPOSITE MATERIALS WITH MULTIPOROUS ZEOLITE A

In this chapter, it is presented the hierarchical materials in form of cartridges prepared from the cellulose aerogels structure with the zeolites that already present hierarchical structure, so called multiporous zeolite A. Due to the novelty and all the promising properties that could be observed in this type of materials, it was fully characterized as well as tested in adsorption systems. The main part of this chapter was published in Microporous and Mesoporous Materials, 312, Bessa, França, Pereira, Alexandre, Pérez-Page, Holmes, Nascimento, Rosa, Anderson and Loiola, Hierarchical zeolite based on multiporous zeolite A and bacterial cellulose: An efficient adsorbent of Pb^{2+}, 110752, Copyright Elsevier (2021).[157]

11.1 XRD

Figure 48 presents the XRD patterns to zeolite A_b as synthesised (Figure 48a) and calcined (Figure 48b). It is also presented the composite formed with oxidized cellulose, C-A_b (Figure 48c). The blue squares point the main peaks to the cellulose phase and the green triangles, zeolite A. The red circles highlight the peak that was not noticed before the composite is formed.

Both zeolite A_b as-synthesized (Figure 48a) and calcined (Figure 48b) present peaks in the same positions as zeolite A (Figure 22e), referent to LTA structure hydrated in a cubic system and *Pm-3m* space group.[198] The composite formed with oxidized cellulose, C-A_b (Figure 48c) show the main peaks slightly shifted to higher angles and a peak that was not present in cellulose or zeolite graphs appear with around 80% relative intensity (marked with a red circle in Figure 48).

Rietveld refinements for the zeolites A (Figure 49) and A_b (Figure 50) calcined show the difference among those samples. Their cell parameters are very similar keeping the angles, α, β and γ, at 90 ° for being a cubic cell whilst a = b = c = 24.61 Å for zeolite A suggested at IZA[198] and for zeolites A and A_b = 24.56 and 24.62 Å, respectively. The Si/Al content to each zeolite was 1.00 for the IZA-zeolite A, and 1.06 and 1.02 for zeolites A and A_b.

Figure 48 – Co-Kα XRD patterns to (a) zeolite A_b as-synthesized, (b) zeolite A_b calcined and (c) its composite with oxidized cellulose, C-A_b

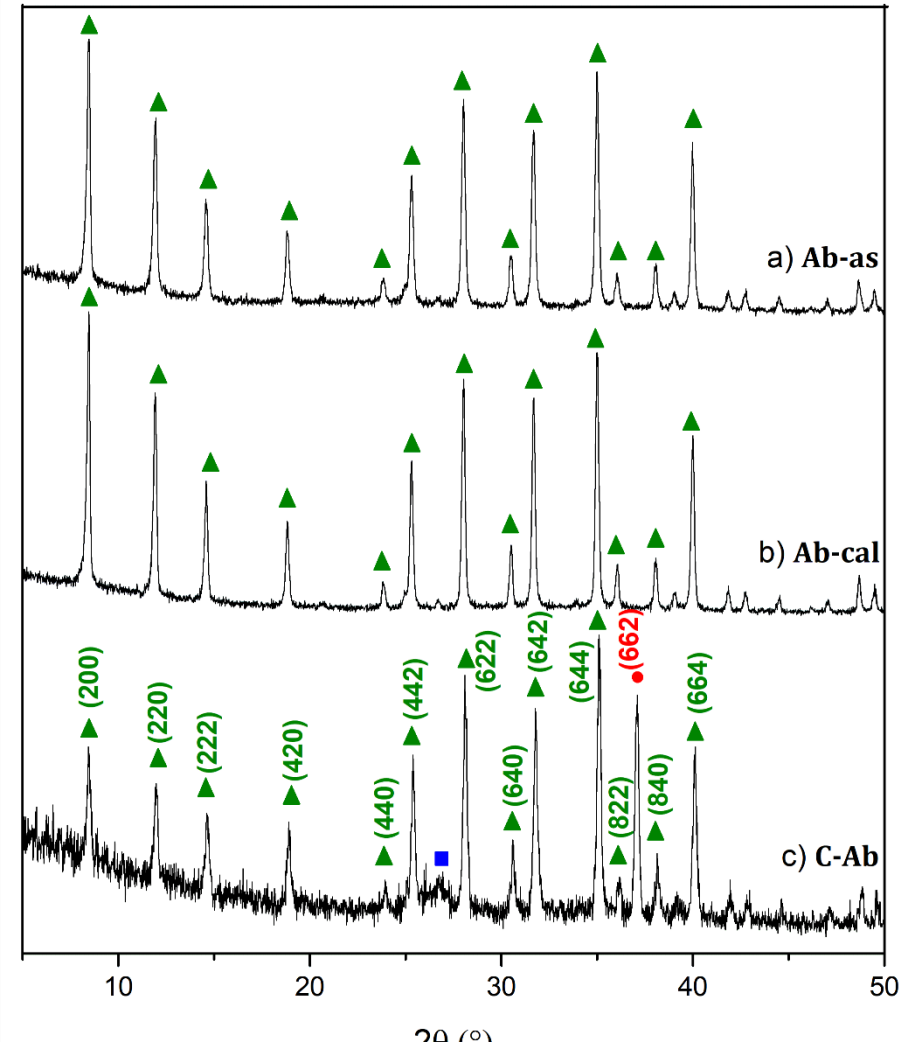

Source: Author (2021). The blue squares point the main peaks to the cellulose phase and the green triangles, zeolite A. The red circles highlight the peak that was not present before the composite be formed. Y axis = Intensity (a.u.).

Like zeolite A composites, the background gets more visible due to the cellulose fibrils (low crystallinity and nanosize) and it is possible to identify mainly the (200) cellulose plan at 26 °2θ. The strong signal at 37 °2θ is referent to (662) plane in zeolite A and together with the intensity decrease observed for the initial peaks, (200), (220), (222) and (420), is an evidence of changes in the location of Na^+ inside the pores as well as water molecules, due to the rehydration of the zeolite structure when interacting to the cellulose nanofibers.[243; 244]

Figure 49 - Rietveld refinement for zeolite A, with the quality parameters presented in the box

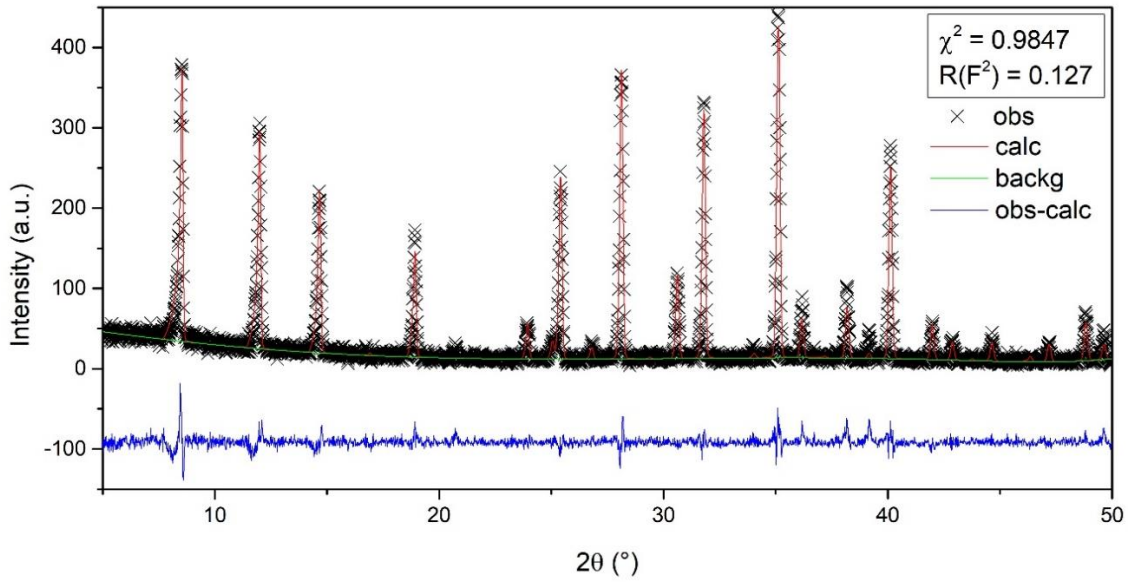

Source: Bessa (2021).[157] Where the black X points are the observed pattern, the red line, the calculated one, the green one, background, and the blue, the difference.

Figure 50 - Rietveld refinement for zeolite A_b, with the quality parameters presented in the box

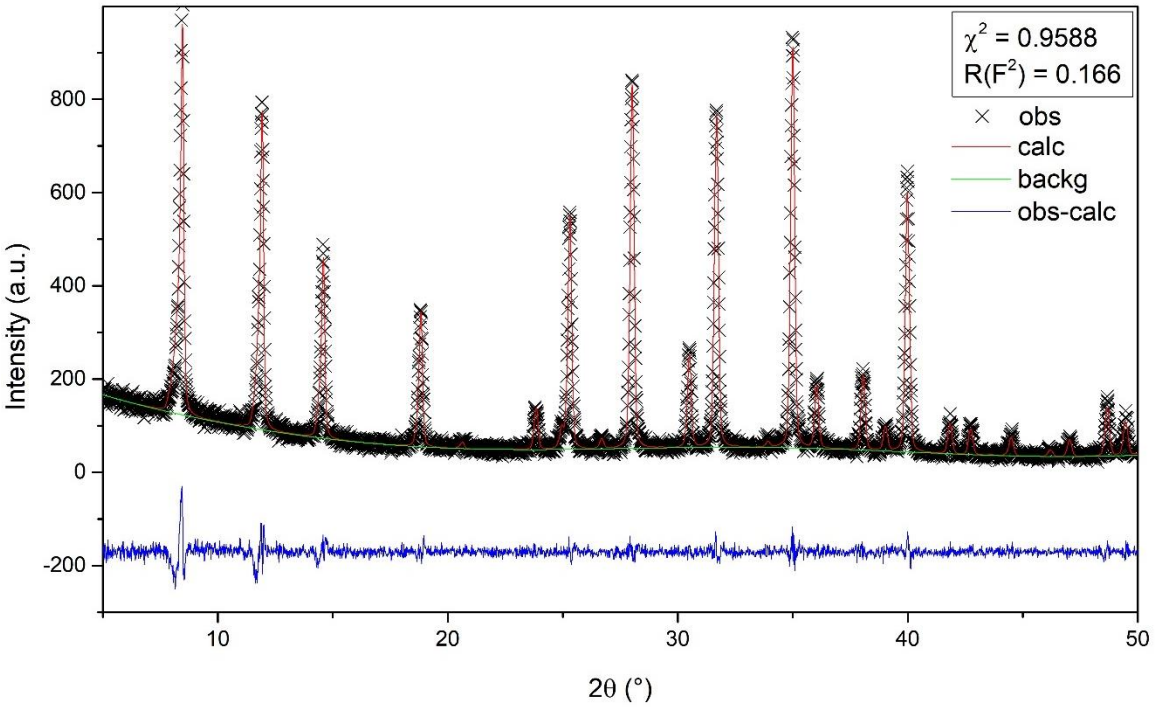

Source: Bessa (2021).[157] Where the black X points are the observed pattern, the red line, the calculated one, the green one, background, and the blue, the difference.

11.2 SEM

Figure 51 presents scanning electron micrography images for as-synthesized zeolite A multiporous (Figure 51a-b), calcined (Figure 51c-d) and the composite formed with BC (Figure 51e-f). The left images present a scale bar of 20 µm and the right ones, present a detailed view with increased magnification and scale bar of 2 µm.

Figure 51 - Scanning electron microscopy images for zeolite A_b (a-b) as-synthesized, (c-d) calcined and (e-f) the composite formed with BC

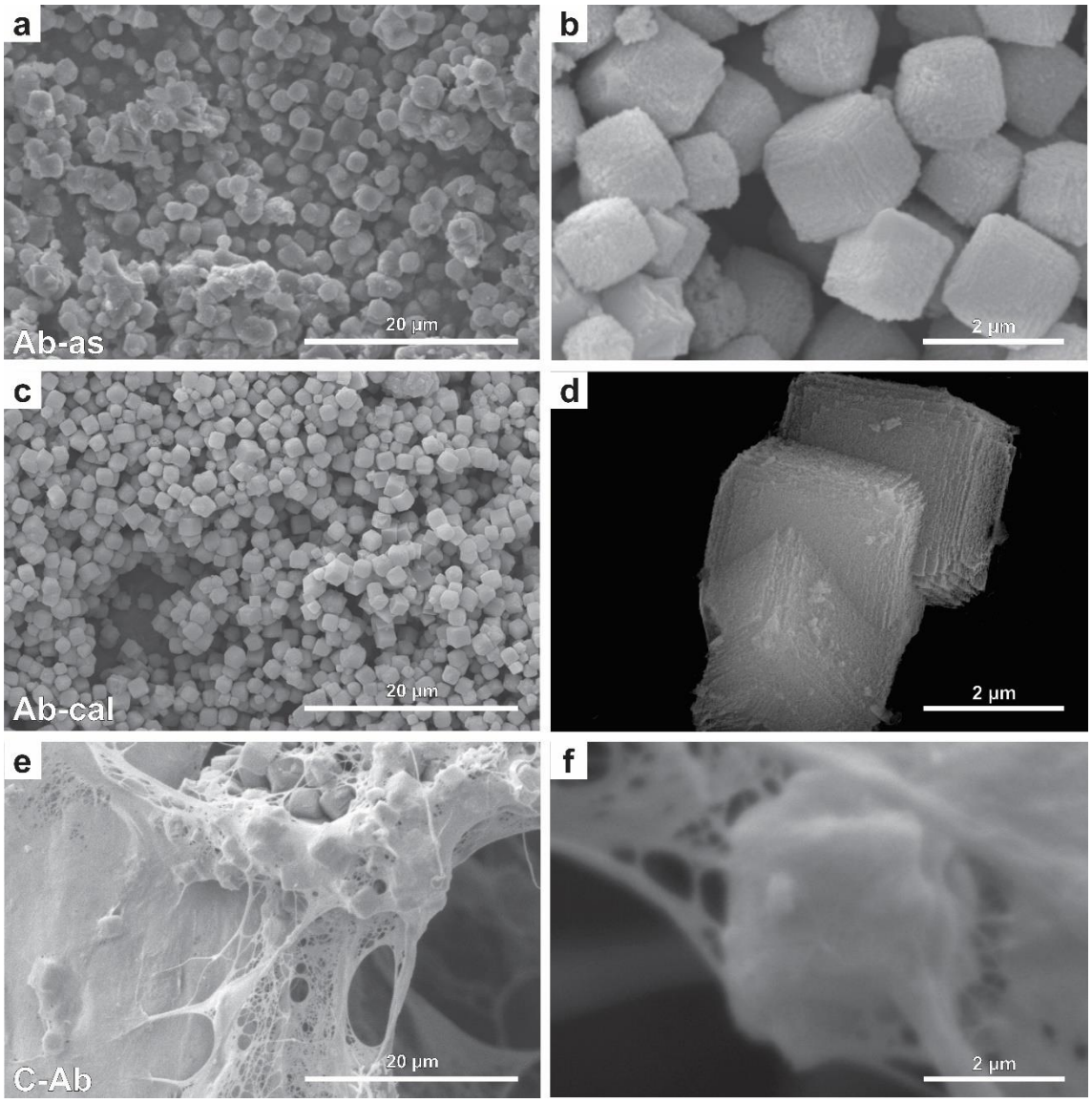

Source: Author (2021).

The multiporous zeolite obtained using organosilane presents morphology similar to the microporous zeolite A formed by conventional method or even other aluminosilicate

materials.[146; 245-247] One difference is the surface aspect formed by small particles that is maintained after calcination and the size ca. 2 µm. This characteristic was reported in other works with organosilanes to mesopore formation.[89; 214; 248] Such molecules are used before the hydrothermal treatment in the synthesis gel: silane quantity is crucial not only to the mesopores sizes, but also to define nanocrystals dimensions.[86]

Xu *et al*., 2016[249] reported works where the ramifications in triply branched molecules may not be part at the micropores' formation but contribute to stabilize the zeolitic structure. And Cho *et al*., 2009[89] present both the zeolite synthesis with TPHAC, and the pore expansion studies with polymers. Considering some of their findings, we can attribute the increased crystal size observed in this sample to the volume of the TPOAC molecule used to form the mesopores by itself together with the possibility of expansion happening by the same organic.

When forming the composite with oxidized cellulose, the agglomeration is not avoided, possibly due to high interaction that the crystal establishes to each other with this increased surface area. The crystals show particle morphologies composed by numerous domains of interconnected crystals, so it can be easily imagined that the multiporous zeolite has good properties related to the nanometric particles (large external surface area and fast diffusion, for example[250]), in a bulky crystal. Thus, as nanometric particles, agglomeration among them is quite common.

The cartridges also show more clearly the entangling from the fibres with the voids on the crystals' surface. Such agglomeration is an improvement, when compared to a powder sample with the crystals very compacted. In different points to the cartridges images, it is possible to see spaces between the fibres enabling the adsorbents to easily access the zeolite pores.

Table 21 presents the results obtained for SEM analyses coupled to an EDS detector for the multiporous zeolite samples presented in Figure 51, highlighting with bold the elements in higher concentration in each sample and the last column presents the Si/Al molar ratio.

The multiporous zeolite A obtained in this work presented a Si/Al molar ratio compatible to the values obtained by Rietveld refinement presented previously and to the expected for zeolite A that is maintained for its composite. This agrees to the results suggested in other techniques related to a good interaction keeping the structure and main properties from both the materials.

Table 21 - Weight composition for elements C, O, Al, Si, Na and Cl, as well as the Si/Al molar ratio, to zeolite A_b after calcination and its composite with BC (C-A_b) using EDS detector in SEM analysis

SAMPLE	% WEIGHT						Si/Al
	C	O	Al	Si	Na	Cl	
A_b	-	45.1	**19.8**	**21.3**	13.7	-	1.04
C-A_b	15.6	25.8	**15.2**	**14.8**	15.2	13.4	0.95

Source: Author (2021).

11.3 FTIR

Figure 52 presents the FTIR spectra in KBr to zeolite A (Figure 52a) for better comparison with the zeolite A_b as synthesised (Figure 52b) and calcined (Figure 52c). It is also presented the composite formed with oxidized cellulose, C-A_b (Figure 52d). The region with changes from the as synthesised to the calcined sample is highlighted in blue and the main bands are pointed. Table 22 is presented with the bands, their respective assignments, and references.

The spectra to zeolites A (Figure 52a) and A_b (Figure 52b-c) are similar to each other, presenting the bands related to zeolite A structure on the same wavenumbers. The difference is just for zeolite A_b as-synthesized (Figure 52b) that still has the TPOAC molecule on the structure and thus, the bands related specifically to C-H vibrations derived from CH_3– and CH_2– groups at 2850 and 2925 cm^{-1}, respectively. The absence of those bands to the calcined spectrum (Figure 52c) and further to the composite samples (Figure 52d), proves that the organosilane was removed successfully during the calcination process.[213; 214]

Another observation from the spectra is the broadening of signal around 1000 cm^{-1} for the calcined sample (Figure 52c). It is suggested in literature[89; 214; 251] that when this type of molecules is used to promote the mesopore formation throughout the crystals, during synthesis, they link to the zeolite structure by Si–O–Si bonds, and thus, this band gets broader when the organic moiety is removed, leaving only the Si–O part connected to the zeolite.

When the composite is formed, the cellulose characteristic bands become shorter in form of small shoulders, as observed on the region 1250-1000 cm^{-1}, Figure 52d. The band related to C=O in sodium carboxylate changes from 1610 cm^{-1}, in pure cellulose, to 1650 cm^{-1}. This shift to higher wavenumber is even more pronounced than the observed to zeolite A

(Figure 25d), suggesting that the presence of the mesopores in the crystal promotes a better interaction with the cellulose nanofibrils.

Figure 52 - FTIR spectra for (a) zeolite A, for comparison, (b) zeolite A_b as-synthesized, (c) zeolite A_b calcined and (d) C-A_b in KBr with the main bands described on the image

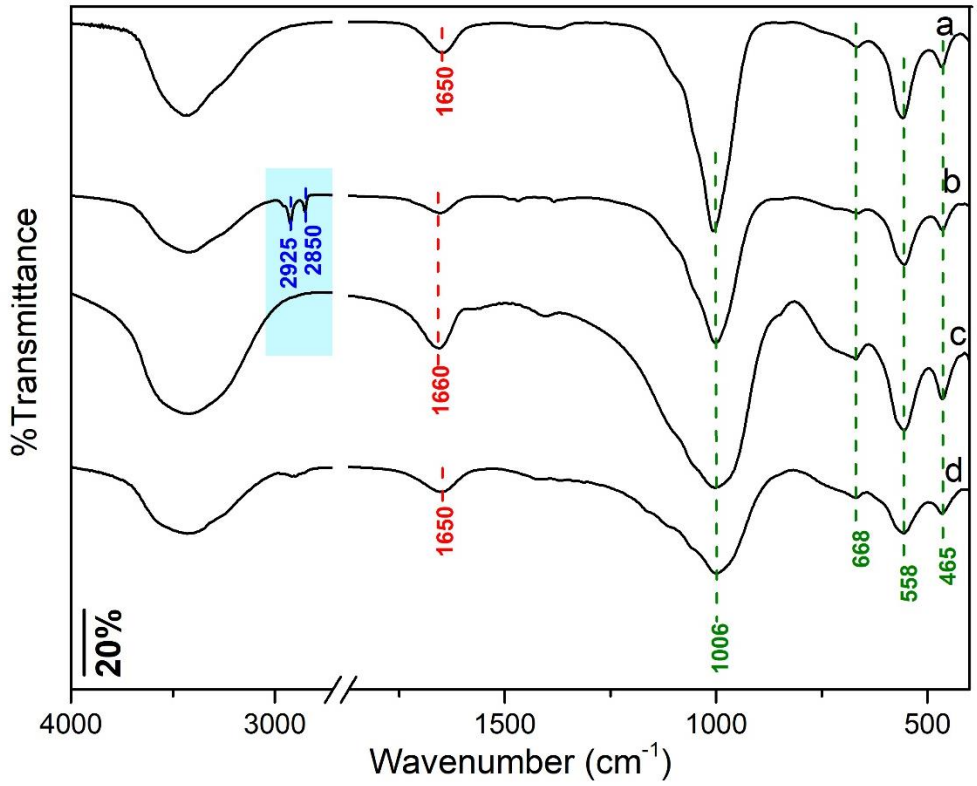

Source: Bessa (2021).[157]

Table 22 – Main FTIR bands assignments to zeolites A_b-as and A_b-cal as well as the composite formed with oxidized cellulose, C-A_b, in KBr

Assignment	Wavenumber (cm^{-1})			References
	A_b-as	**A_b-cal**	**C-A_b**	
Stretching of O–H bonds	3420	3420	3420	146; 183; 203; 204
C–H vibration derived from CH_2– group	2925	-	-	213; 214
C–H vibration derived from CH_3– group	2850	-	-	213; 214
Vibrations of O–H coming from adsorbed water on the zeolite structure	1660	1660		145; 201; 202

Assignment	Wavenumber (cm^{-1})			References
	A_b-as	A_b-cal	C-A_b	
Stretching of C=O in the ester bonds on sodium carboxylate on the cellulose structure			1650	173; 174; 184; 186
Stretching of Si–O bonds in SiO_2	1006	1006	1006	146; 203-205
Symmetric stretching of T–O (T = Si or Al) bonds in internal tetrahedra	668	668	668	146; 183; 205; 206
Characteristic double four member rings (d4r)	558	558	558	146; 183; 203; 206
Internal T–O bending in double-ring (d4r)	465	465	465	146; 183; 206

Source: Author (2021).

11.4 TGA

Figure 53 presents the thermal analyses for zeolites A_b as synthesised and calcined with their differentiate graphs on the right side of the figure.

The thermograms present the thermal events related to the zeolite structure in the presence of the organosilane used (A_b-as) and after its removal using calcination (A_b-cal). The organic molecule is evidenced on the event between 250 and 450 °C with circa 15.8% loss.[91; 213; 248; 252] The first event for both the samples is related to water loss (up until 210 °C) presenting 17.5 and 24% in A_b-as and A_b-cal, respectively. Thus, the water content on the zeolite structure is higher when the organosilane is removed showing that this molecule was occupying pores. For A_b-cal, this is the main event, and it is comparable to the weight loss observed for conventional zeolite, although the total weight loss (28.4%) is bigger due to the mesopores silanol dehydration in higher temperatures.

Figure 54 presents the thermograms on the left side and the differentiate graphs on the right side for the composites formed with zeolites A (C-A) and A_b (C-A_b), to observe the effect that the mesopores had over the thermal stability.

The better interaction that the cellulose plays on the multiporous zeolite crystals is also observed from these results. Comparing the two TGA curves, the total loss for both the composites is quite different, even though, both uses oxidized bacterial cellulose and the same concentrations. The C-A_b cartridge presents 41.4% loss at 800 °C, while the C-A has 55.1%. More differences are also identified from the differentiate graphs, where for the first event, both

T_f and T_{MAX} are lower than the C-A, and the weight loss is slightly higher than the other one. This can be attributed to the slightly higher water content on this zeolite from the sylanols.

Figure 53 - Thermograms acquired in synthetic air with 50 mL min^{-1} flow and heating rate of 10 °C min^{-1} with the differentiate graphs for zeolites A_b as synthesised and calcined

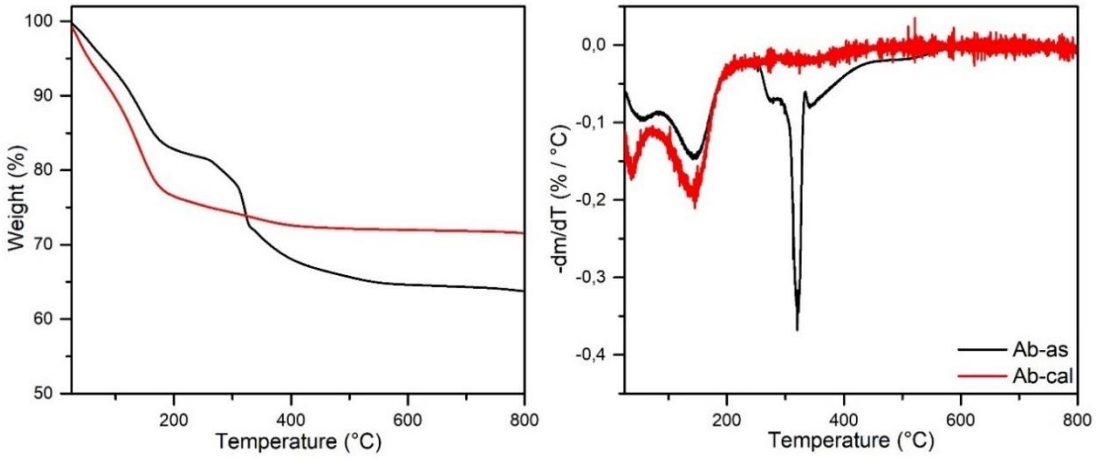

Source: Author (2021).

Figure 54 - Thermograms acquired in synthetic air with 50 mL min^{-1} flow and heating rate of 10 °C min^{-1} with the differentiate graphs for the cartridges with zeolites A (C-A) and A_b (C-A_b)

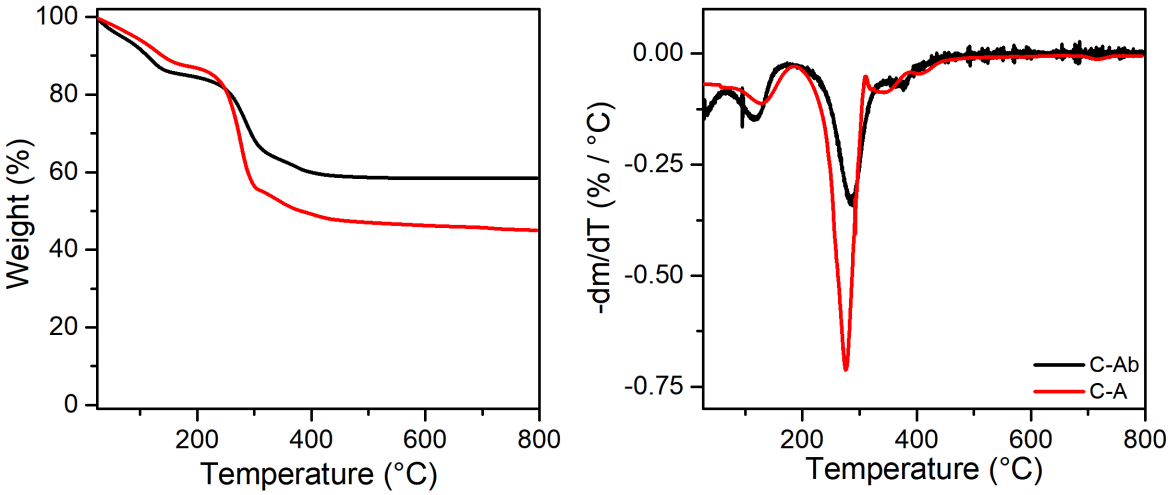

Source: Author (2021).

The second event for C-A_b, related to cellulose degradation reactions, starts in a lower temperature than C-A, but the T_{MAX} is 10 °C higher, as well as T_f, almost 40 °C more. The weight loss for this event is also much lower. Such evidence shows the main improvements

to the use of multiporous zeolite in the cartridges that allow a better heat distribution avoiding the cellulose degradation.

11.5 Textural properties

Figure 55 presents the N_2 adsorption/desorption isotherms for zeolite A_b in different degassing temperatures, 90 °C (A_b-90) and 350 °C (A_b-350).

Figure 55 - N_2 Adsorption/desorption isotherms for zeolite A_b in two different degassing temperatures

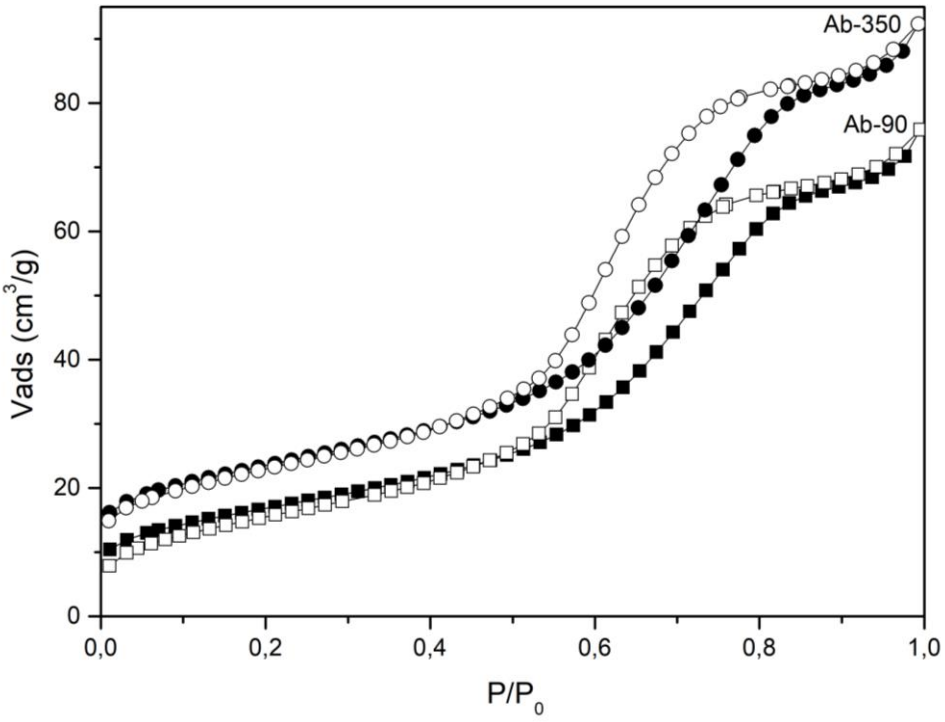

Source: Author (2021). The filled symbols are the adsorption curve, and the blank ones are the desorption.

The isotherms present type IV(a) with H2(b) hysteresis indicating the presence of 'ink-bottle' mesopores in the samples, where there is a lower aperture and higher internal volume. The pronounced hysteresis is a typical observation for micro-mesoporous materials.[214] In such analysis conditions, zeolite A does not present any adsorption with very low surface area since its small apertures (4 Å) do not allow the N_2 molecules to diffuse into the ultramicropores.[85; 89; 253]

This fact also explains the small difference among the different degassing temperatures. For a microporous sample, this difference is approximately 50%. In a higher degassing temperature, the water molecules that are mainly located in the micropores, are removed and a higher amount of N_2 can be adsorbed. For this molecule, even removing the water molecules from the micropores, this area is still inaccessible to the process and only sites on the mesopores are available. Thus, the 34% more observed when degassing at 350 °C can be attributed only to the increased surface area from the water loss or dehydration of silanol groups from the mesopores.

Figure 56 presents the N_2 adsorption/desorption isotherms for zeolite A_b and its composite sample formed with oxidized cellulose on the left side and on the right side, the respective pore distribution curves. The BET surface area, pore size and total pore volume to each sample is presented on Table 23.

The cellulose sample also shows low adsorbed volume with increase to higher relative pressure from the macropores in the sample. When the composite C-A_b is analysed, the shape for the isotherm is the same as the zeolite powder and only decrease to S_{BET} (from 59 to 39 $m^2\ g^{-1}$) and V_T (0.11 to 0.07 $cm^3\ g^{-1}$) are observed. Such values are compatible to the amount of zeolite present in the sample, and this is a clear evidence about the cellulose role as mainly a physical support to the zeolite without damaging their surface properties.

Figure 56 - N_2 Adsorption/desorption isotherms for zeolite A_b and its composite, C-A_b, using a 90 °C degassing temperature on the left side and on the right side, the respective pore distribution curves

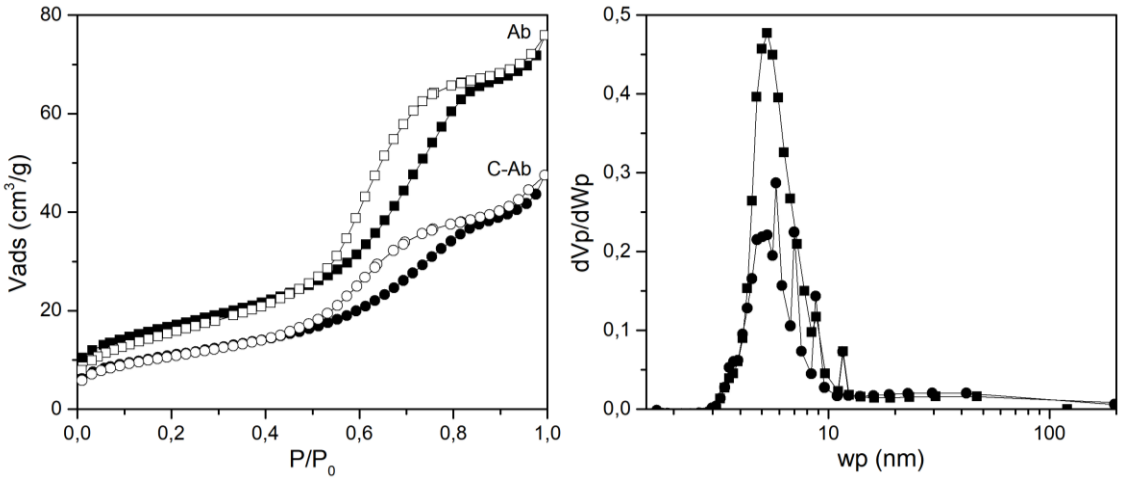

Source: Author (2021). The filled symbols are the adsorption curve, and the blank ones are the desorption.

Table 23 - Main surface properties for cellulose sample (C_{oxi}), zeolite A_b in two different degassing temperatures and the composite (C-A_b). All the samples were degassed at 90 °C, except for the A_b-350, at 350 °C

Sample	Surface area ($m^2\ g^{-1}$)	Mean pore size (nm)	Total pore volume ($cm^3\ g^{-1}$)
C_{oxi}	20	8.8	0.04
A_b-90	59	7.6	0.11
A_b-350	79	7.0	0.14
C-A_b	38	7.2	0.07

Source: Author (2021).

From BJH plots (Figure 56b), the pores apertures are observed and a main peak at 5.3 nm along to another one around 11.7 nm are observed for A_b. Although, to C-A_b, this distribution is not more centred in one of the peaks, but at least 5 pore sizes can be distinguished ranging from 5.0 to 12.0 nm. The observation of the graph shows that there is a strong decrease to peaks related to the smaller pores (5.0 and 5.8 nm) while for 11.7 nm for example, the peak remains the same from the zeolite to the composite. This is an evidence that the pores with smaller apertures are hindered by the cellulose nanofibers during their interaction, along to the decrease for pore size presented in Table 23.

11.6 Ionic Exchange

Figure 57 presents the removal results for ionic exchange with Ca^{2+} comparing zeolites A and A_b, as well as C-A_b to identify changes that happen when the composite is formed with the multiporous zeolite. Table 24 presents the expected values for Ca^{2+} removal according to Na^+ EDX results and the measured values.

As observed to the previous results, the measured Ca^{2+} removal was higher than the expected getting almost 1/3 more to the zeolite A_b powder. Together to the fact that according to EDX, zeolite A_b presents a lower Na^+ content, this can be an evidence of the exchange sites not only related to this cation. In this sample, the evidence is more pronounced due to the use of organosilane molecule, that acts together to the sodium tailoring and stabilizing the zeolite structure. Thus, two mechanisms are probably involved in this removal studies: ionic exchange with Na^+ inside the micropores and adsorption on the mesopores.

Table 24 – Expected and measured removal results for ionic exchange with a 3 mmol L^{-1} Ca^{2+} for 30 minutes at 250 rpm in ambient conditions to zeolite A_b-related samples

Sample	Expected Ca^{2+} removal (%)	Measured Ca^{2+} removal (%)
Zeo A	54.3	65.0
Zeo A_b	49.6	73.3
C_{oxi}	16.7	0
C-A_b	55.1	64.2

Source: Author (2021).

Figure 57 - Removal results for ionic exchange with a 3 mmol L^{-1} Ca^{2+} for 30 minutes at 250 rpm in ambient conditions comparing zeolite A, zeolite A_b, C_{oxi} and C-A_b

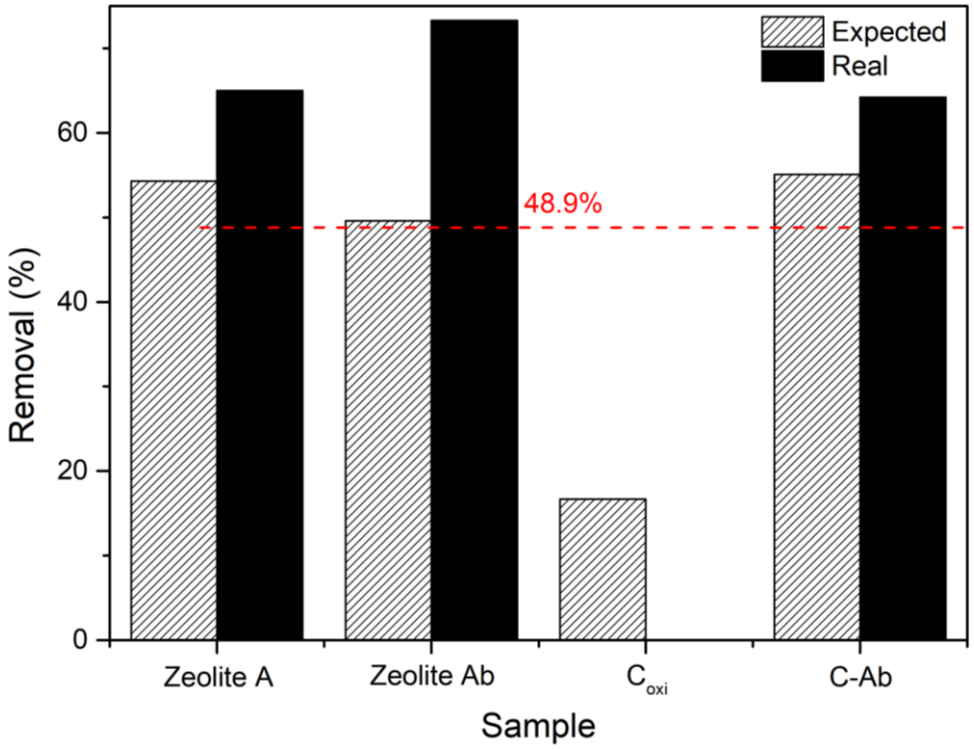

Source: Author (2021). The red signs present the expected removal values to the composites considering the zeolite A_b weight content in the cartridge.

Comparing the samples C-A_b and C_{oxi}A, the same trend of improving the removal when added to oxidized cellulose is observed and in addition, the composite with zeolite A_b presents higher values, confirming the improvement achieved when a multiporous zeolite is used for this purpose.

11.7 Adsorption

Figure 58 presents removal results for selectivity between Pb^{2+} and Cd^{2+} to zeolites A and A_b, cellulose and their respective composites, C-A and C-A_b. Table 25 brings the removal %, q_e and Selectivity values for the samples that allow to evaluate better their selectivity behaviour to these ions.

Figure 58 - Selectivity studies for samples C, A, C-A, A_b and C-A_b using Cd^{2+} and Pb^{2+} 0.1 mmol L^{-1} pH 5.0 solution at room temperature and 150 rpm in orbital shaker for 24 h

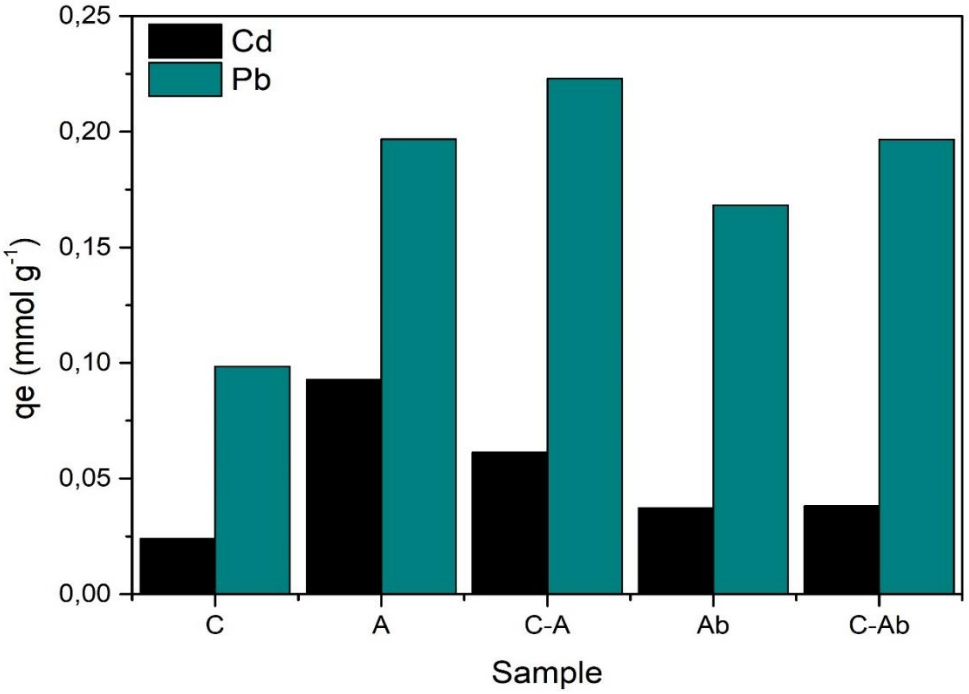

Source: Author (2021).

Table 25 – Removal%, q_e and Selectivity values for the samples C, A, C-A, A_b and C-A_b obtained from kinetic studies performed with Cd^{2+} and Pb^{2+} 0.1 mmol L^{-1} pH 5.0 solution at room temperature and 150 rpm in orbital shaker

Sample	Removal (%)		q_e (mmol g^{-1})		S
	Pb^{2+}	Cd^{2+}	Pb^{2+}	Cd^{2+}	
C	23.2	5.0	0.098	0.024	4.1
A	97.8	40.6	0.197	0.093	2.1
C-A	85.0	21.2	0.223	0.061	3.5
A_b	91.4	17.9	0.168	0.037	4.5
C-A_b	70.7	11.1	0.197	0.038	5.6

Source: Author (2021).

From this study, some important features can be inferred initially regarding the adsorption process from the materials. Firstly, the Pb^{2+} selectivity over Cd^{2+} to all the tested materials is not unusual, since many works in literature report that multicomponent systems with this cation present a higher adsorption capacity for it.[212; 254; 255] This can be attributed to its smaller hydrated radius (4.01 Å for Pb^{2+} compared to 4.26 Å for Cd^{2+}) allowing it to pass through the micropores and channels easily, especially for zeolite A with 4Å micropore aperture.[256; 257] Other factors can also influence the selectivity of zeolites, where not only the charge and radius for the cations, but a combination of interactions are involved i.e. electrostatic forces and hydrogen bonding between the metal and zeolite framework.[255]

Zeolites are highly selective for polarizable ions such Pb^{2+} and Cd^{2+} and when Si/Al ratio is lower, higher is the selectivity. Usually, ionic exchange is the governing process.[240] Regarding nanocellulose materials, the pathways may involve adsorption on surface and pores or even entrapment in inter/intrafibrillar capillaries and spaces for the framework, in addition to the ionic exchange process.[258]

The ionic exchange results for Ca^{2+} presented in the previous section show 0% removal for the cellulose sample and in the current adsorption study, even for Cd^{2+}, it presents some removal (5%). Comparing their radium (4.12 Å for Ca^{2+}), a different trend should be expected. Thus, for the cellulose cartridges, some hypotheses can be suggested: (a) the sizes for the cations do not present influence over the process; (b) probably this is not an ionic exchange governed process.

Observing results for zeolites samples, Zeolite A presents a better removal for the ions than its multiporous version, A_b, although, the selectivity measure is much better for the last one. This makes zeolite A_b more useful for multicomponent systems since the removal% is around 90% in the used conditions. Both the composites with cellulose also present improvements surrounding the selectivity, reaching the maximum for C-A_b. The q_e obtained for the composites is also higher than the pure zeolites proving the enhancement to lead uptake from the medium. For C-A_b, this effect looks better, so $q_{e(Cd)}$ is kept at the same level as A_b and just Pb^{2+} capacity has a positive effect.

This is a strong justification for its use as column materials to be used in Pb^{2+} fixed-bed adsorption processes. Such differences can be explained by the presence of pores bigger than the zeolite micropores by themselves, favouring accessibility to the active sites of the zeolite.[256] Specifically related to the zeolite A_b, the mesopores seem to have adsorptive behaviour as observed for the studies presented previously.

Figure 59 presents the contact time studies to Pb^{2+} adsorption comparing zeolites A and A_b, as well as their composites with oxidized cellulose, C-A and C-A_b, and the sample containing just cellulose. For composite samples, the q_e values plotted on the graph are considering just the zeolite content. Table 26 presents the maximum removal values obtained after 300 min and q_e values obtained to the whole cartridge and considering just the zeolite content in the composite samples.

The analysis for the data considering the contact time allows the observation of a quick process happening, for all the samples, with equilibrium reached before 300 min. Specially for zeolite A and C, the first minutes are enough to reach a high adsorption capacity and then a slight decrease is observed, reaching the equilibrium. This feature can be explained for the high amount of adsorption sites due to the adsorbent excess. Also, comparing the zeolites/composites to the cellulose data, their higher adsorption capacities and removal are related to the increased surface area and adsorption sites available.[259; 260]

The profiles for zeolite A and its composite are different, observing equilibrium reached in a further time for the C-A sample (5 min × 30 min). Nakamoto *et al*., 2017[261] observed the same trend when studying composites with Mordenite in a polymeric fibre suggesting that there is a slowdown due to the polymers overlaying the zeolite particles that are the active adsorbents. For zeolite A_b and C-A_b, the profile is the same and thus, it is suggested that the presence of the mesopores on the crystals does not damage the path that the adsorbate should follow when reaching the micropores.

Figure 59 – Contact time studies for samples C, A, C-A, A_b and C-A_b using a Pb^{2+} 0.1 mmol L^{-1} pH 5.0 solution at room temperature and 150 rpm in orbital shaker

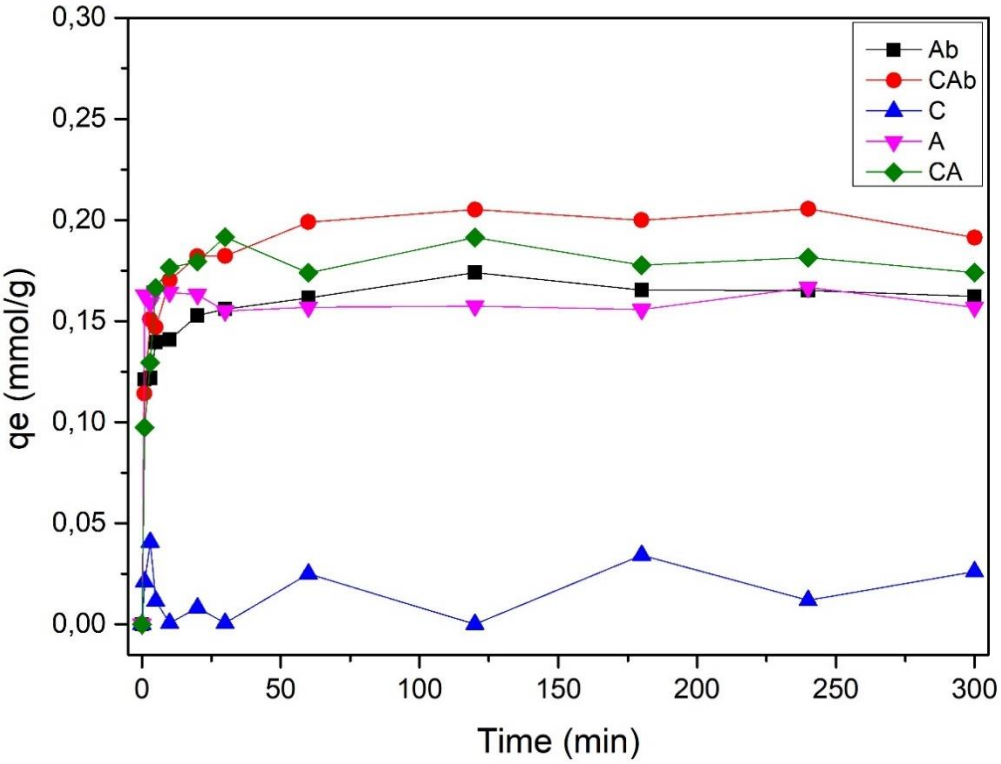

Source: Author (2021).

Table 26 - Removal and q_e values for the samples C, A, C-A, A_b and C-A_b obtained from contact time studies performed with Pb^{2+} 0.1 mmol L^{-1} pH 5.0 solution at room temperature and 150 rpm in orbital shaker

Sample	Removal (%)	q_e (mmol g^{-1}) [a]	q_e (mmol g^{-1}) [b]
C	9.2	0.041	-
A	96.0	0.167	-
C-A	100.0	0.128	0.191
A_b	95.2	0.174	-
C-A_b	88.5	0.137	0.205

Source: Author (2021). Where column a presents the qe values for the whole sample and b, considering just the zeolite content for the composites.

The behaviour for zeolite A_b is also indicative for the presence of active sites over the mesopores and not only ionic exchange from the micropores have effect on the adsorption process. If the mesopores act solely for the improvement on mass transference properties, the species would quickly reach the internal micropores and equilibrium would be similar or even better than achieved for microporous zeolite A.[260] Then, the intracrystalline mesopores affect

not only the pore architecture, but also the functional surface groups in a way that the Al–OH and Si–OH groups will be present and active for Pb^{2+} adsorption in the structure instead of the Al–O–Si on the essentially microporous structure.[262] In addition, their adsorption capacities are similar even that its Na^{+} content is lower, so if the ionic exchange were the governing process, it would be expected lower adsorption.[263]

The values in column b for Table 26 show that correcting the cellulose effect to the composite samples, an improvement to the adsorptive behaviour can be observed for both the zeolites and in higher extent to the multiporous zeolite A_b. In literature, it is suggested that the presence of carboxylate groups on cellulosic materials improves the heavy metals uptake. In those cases, the adsorption happens from chelating formation using the pair of electrons in this group and the vacant electron orbitals for Pb^{2+}. Zeolite A_b having a higher amount of hydroxyl groups, can interact trough them to the cellulose structure and here, the chelating reaction occurs more pronounced.[264-266]

Figure 60 and Figure 61 present the linear fitting for zeolites A and A_b and their composites with oxidized cellulose using respectively, the pseudo-first order and pseudo-second order kinetic models. On Table 27, the parameters obtained from the fitting can be observed, as well as the experimental q_e to each sample.

Kinetic studies allow to describe the adsorption velocity for the ions onto the adsorbent material that have influence not only to the equilibrium achievement, but also to the mechanism involved. Comparison for the correlation coefficient, R^2, and the q_e values (experimental × calculated) for both pseudo-first order and pseudo-second order models shows that the data is better fitted to the pseudo-second order model. In literature, it is common to identify this kinetic model governing the adsorption process for both cellulosic materials,[265] aerogels[254] and zeolites that can present some mesoporosity[260; 262] or not.[267]

For this model, adsorbent and adsorbate contribute to velocity rates and consequently, to the mechanism. This fitting indicates chemisorption as the main factor influencing the adsorption. The K_2 values obtained from the intercept of (16) are influenced by the presence of mesopores with higher values for zeolite A_b and it decreases slightly indicating that the process is slowed down when the cellulose is present with the multiporous zeolite.

Figure 60 – Linear fitting using pseudo-first order kinetic model for zeolites A and A_b and their respective composites with oxidized cellulose, C-A and C-A_b, to a Pb^{2+} 0.1 mmol L^{-1} pH 5.0 solution at room temperature and 150 rpm in orbital shaker

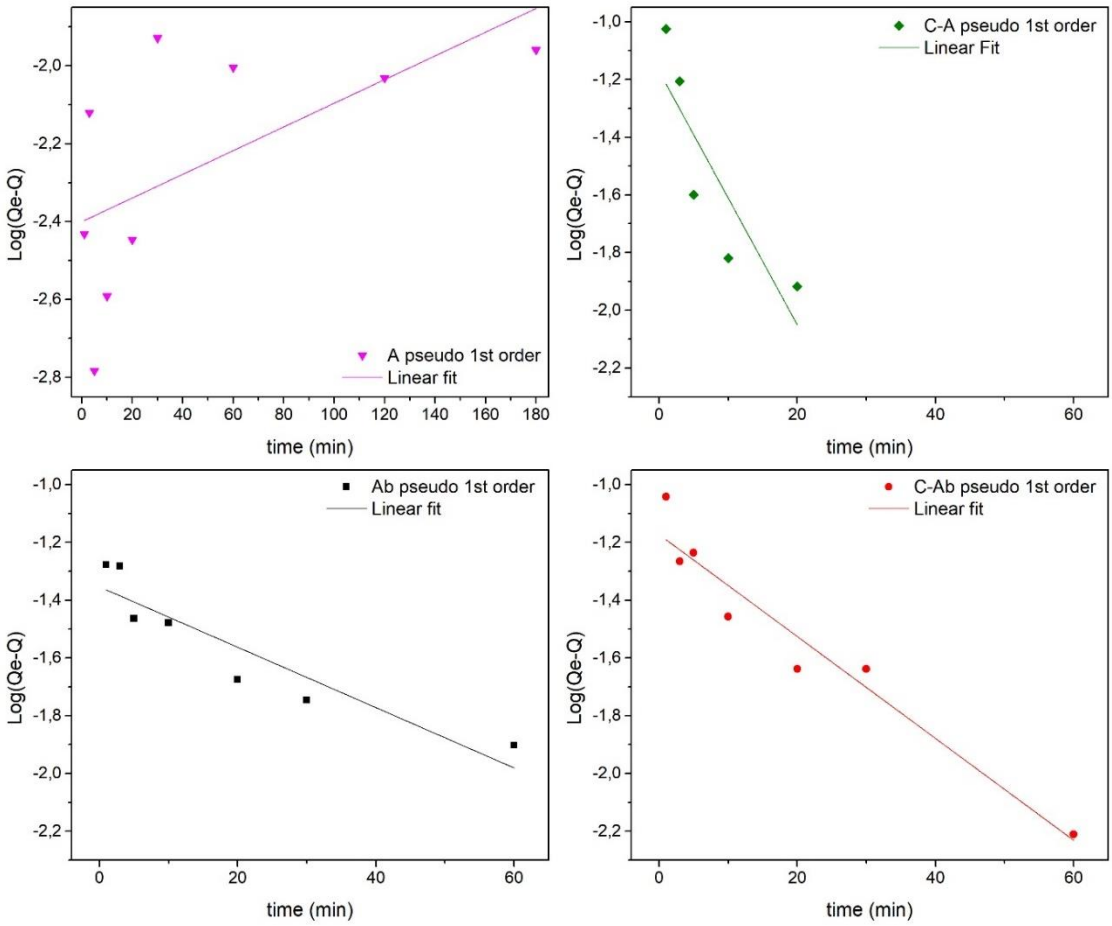

Source: Bessa (2021).[157]

Figure 61 – Linear fitting using pseudo-second order kinetic model for zeolites A and A_b and their respective composites with oxidized cellulose, C-A and C-A_b, to a Pb^{2+} 0.1 mmol L^{-1} pH 5.0 solution at room temperature and 150 rpm in orbital shaker

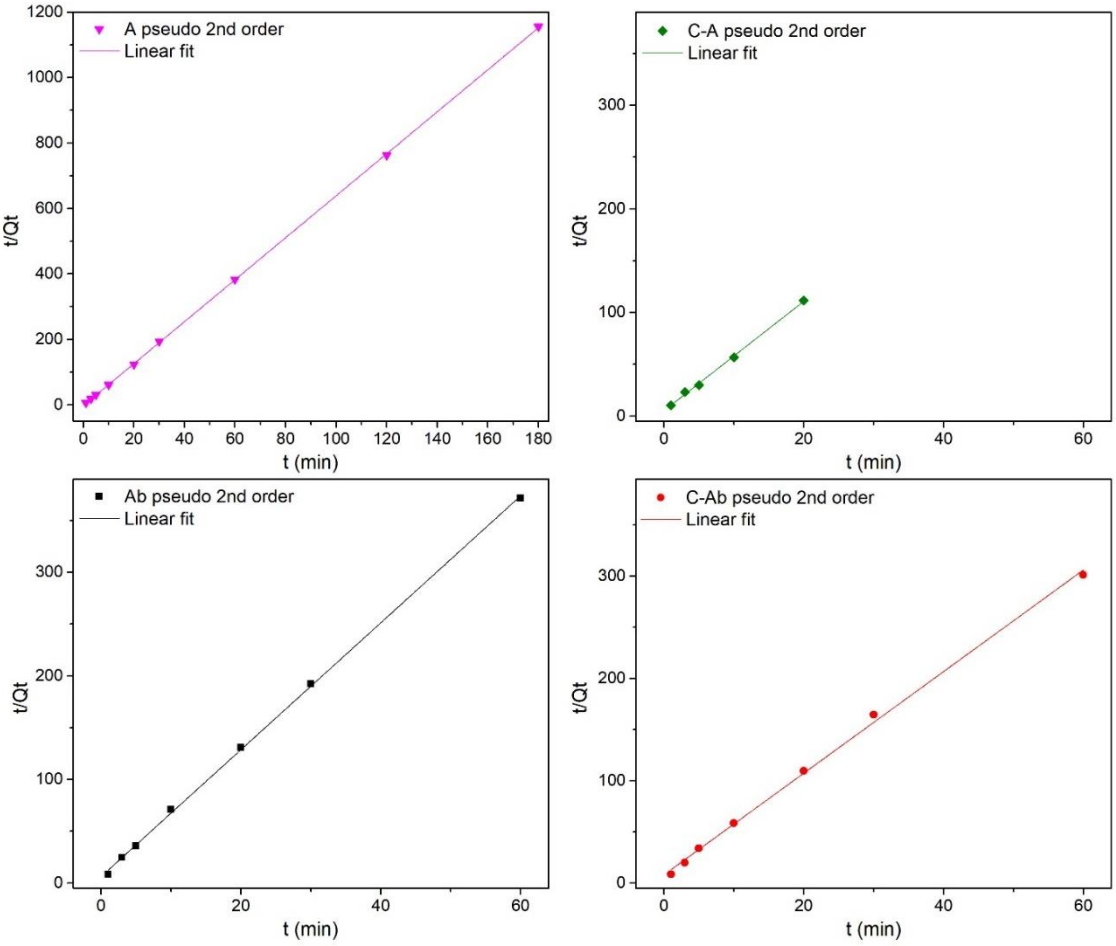

Source: Bessa (2021).[157]

Table 27 - Parameters obtained from linear fitting using both pseudo-first order and pseudo-second order kinetic models for Pb^{2+} adsorption to a 0.1 mmol L^{-1} pH 5.0 solution at room temperature and 150 rpm in orbital shaker

Sample	q_{exp} **(A)**	**Kinetic models**							
		Pseudo-first order				**Pseudo-second order**			
		q_{calc} **(A)**	k_1 **(B)**	R^2	**RSS**	q_{calc} **(A)**	k_2 **(C)**	R^2	**RSS**
A	0.167	0.004	-0.007	0.280	0.228	0.167	-17.812	0.999	0.004
C-A	0.191	0.067	0.101	0.664	0.552	0.191	5.320	0.998	0.001
A_b	0.174	0.044	0.024	0.834	0.241	0.174	5.192	0.999	0.002
C-A_b	0.205	0.067	0.040	0.928	0.108	0.205	2.934	0.998	.002

Source: Bessa (2021).[157] A: mmol g^{-1}; B: min^{-1}; C: g $mmol^{-1}$ min^{-1}.

Figure 62 presents the intraparticle diffusion plots for Pb^{2+} adsorption over zeolite A_b and its composite C-A_b with the diffusion coefficients expressed for each fitted section.

Figure 62 - Intraparticle diffusion plots for Pb^{2+} adsorption over zeolite A_b and its composite C-A_b with diffusion coefficients for each section in the respective samples

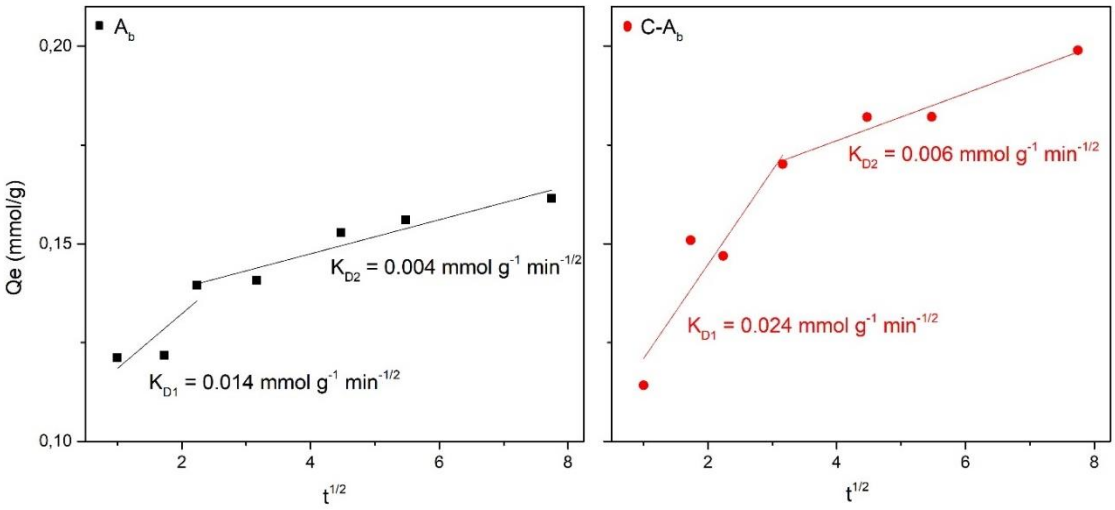

Source: Bessa (2021).[157]

From the plots presented in Figure 62, it is possible to distinguish two different regions and not a straight line passing through the graph origin which means that the intraparticle diffusion is not the only limiting process on the process. The first section represents the ions diffusion on the adsorbent surface, whilst the second is the diffusion to the inner pores. The observation of K_{D1} and K_{D2} for both the samples shows that the second part presents a lower coefficient due to the increased mass transference on the micropores, although this is improved in the composite sample.

The comparison for the coefficients between the samples indicates that the presence of the zeolite dispersed in the cellulosic matrix improves the diffusion process because of the bigger pores insertion to the structure, helping the ions to move to the inner pores on the zeolite structure, as observed by other authors in literature. [260-262]

11.8 Conclusions

In this chapter, it is presented hierarchical materials in form of cartridges, prepared from bacterial cellulose aerogels structure with multiporous zeolite A. By using different characterization techniques as well as some ionic exchange and adsorption experiments, the main properties of such materials were observed and compared with cartridges containing microporous zeolite A.

From the XRD, a new peak is observed as well as some relative intensities variations due to Na^+ and H_2O inside the pores changing their locations when the composites are formed. Their interaction is also evidenced by Infrared and their morphology, that even with some agglomeration, the presence of smaller particles forming the cubic crystals allow the cellulose nanofibers to entangle them. This feature is also suggested from the N_2 isotherms pore distribution plots, where the smaller pores observed to the crystals are probably hindered by the cellulose nanofibers.

From the N_2 adsorption/desorption isotherms, the presence of the mesopores to the zeolite crystal is also evidenced with 'ink-bottle' shape that is maintained to the cartridges. The positive interaction between the two materials is also observed from the improvement in their thermal stability.

Although, when the experiments with the bivalent metallic cations were performed, the improvements were even more evident and the mesopores act not only allowing better accessibility to the zeolite micropore active sites, but also in their removal. The selectivity experiments with Pb^{2+} and Cd^{2+} show: $A < A_b < C\text{-}A_b$ to Pb^{2+} with more than 90% removal to the last one. The equilibrium is reached quickly (less than 300 min) and chemisorption is the main adsorption process involved, from the best fitting for the linear form of the pseudo-second order kinetic model. At the end, the intraparticle diffusion is observed and the cartridges show improved behaviour, showing that the cellulose has an important role in the hierarchization process.

This way, these cartridges stand out as adsorptive materials for Pb^{2+} in both batch and flow experiments, with good interaction between zeolite and cellulose and hierarchical structure that allow them to present better selectivity and intraparticle diffusion process.

12 GENERAL CONCLUSIONS

This work was undertaken to design hierarchical cartridges with nanoporous materials to be used in adsorption systems and evaluate the interaction between bacterial cellulose nanofibrils and the inorganic compounds by means of different characterization techniques.

The investigation of cellulose cartridges has shown the basic characteristics for such materials and independently of the oxidation or concentration, crystallinity was the same, observing for the oxidized sample that the fibrils were better assembled in thin sheets in the aerogel structure as well as their main degradation event identified in lower temperatures.

When the different nanoporous materials are added to the oxidized cellulose, there are improvements in thermal stabilization moving the main degradation event for higher temperatures. The positive interaction is also observed from the FTIR results that shift the bands for carboxylate group to higher wavenumbers.

Comparing the samples with the same amounts for both non-oxidized and oxidized cartridges, it is found that the particles are more agglomerated and the nanofibrils are more loosen for the composites containing the non-oxidized cellulose, suggesting that the presence of carboxylate groups to the cellulose structure allows interactions between surface groups present on the zeolites and clay surface. The lower degradation temperature observed to the cartridges with oxidized cellulose, it can still allow their use in many adsorption systems.

A superior cartridge is then proposed using oxidized bacterial cellulose and a zeolite with a hierarchical porous structure; thus, the hierarchy would be achieved with the three pore types interconnected and not only the macropores from the cellulose aerogels and the micro or mesopores from the zeolites and clay. Thus, the positive interaction is suggested from the infrared results, as well as the improvements in thermal stability, diminishing not only the weight loss, but also the main thermal event.

This material keeps the porous structure and even that it is suggested the smaller mesopores hindered by the cellulose nanofibrils, the adsorption studies prove that both the cellulosic structure and the mesopores promote upgrading to the cartridges allowing better removal for both Ca^{2+} and Pb^{2+}, accessibility to the active sites and this way, improving selectivity and intraparticle diffusion for Pb^{2+} with chemisorption as the main adsorption process involved, from the linear form to the pseudo-second order kinetic model.

Overall, this study strengthens the idea that hierarchical cartridges can be formed from the combination of bacterial cellulose with zeolites or other different inorganic nanoporous materials, for adsorption processes.

13 IDEAS FOR FUTURE WORKS

During the development of this work different ideas and possibilities arise regarding the bacterial cellulose and nanoporous materials, showing the great perspectives for future research projects in this area. About the topics studied and discussed in this work, other tests could be performed for future works using the same materials:

- ✓ Adsorption tests for other metallic cations that are well-known to be used in zeolites, with the C-A_b cartridge;
- ✓ Test efficiency in continuous flow experiments for cation and gas adsorption;
- ✓ Test the cartridges as analytical devices for pre-concentration experiments.

14 RESULTING PAPERS AND PRESENTATIONS

R. A. Bessa, A. L. P. Castro, A. L. S. Pereira, M. F. Rosa and A. R. Loiola. Hierarchical structured materials formed by combination of zeolite crystals and bacterial cellulose fibers. 41ª Reunião Anual da Sociedade Brasileira de Química, Foz do Iguaçu, 2018. Poster presentation.

R. A. Bessa, A. L. P. Castro, A. L. S. Pereira, A. R. Loiola and M. F. Rosa. Materiais hierarquicamente estruturados formados pela combinação de cristais de zeólita A e fibras de celulose bacteriana. XVI Encontro de graduação e V Encontro de pós-graduação da Embrapa Agroindústria Tropical. Fortaleza, 2018. Oral presentation.

A. L. P. Castro, R. A. Bessa, A. L. S. Pereira, M. F. Rosa and A. R. Loiola. Bacterial Cellulose impregnation with Al-MCM-41 forming hierarchical cartridges. XIX Brazilian Meeting on Inorganic Chemistry | VI Latin American Meeting on Biological Inorganic Chemistry | VII Brazilian Meeting on Rare Earths, Fortaleza, 2018. Poster presentation.

R. A. Bessa, A. L. P. Castro, A. L. S. Pereira, M. F. Rosa and A. R. Loiola. Influence of Bacterial Cellulose oxidation in hierarchical cartridges containing zeolite A. XIX Brazilian Meeting on Inorganic Chemistry | VI Latin American Meeting on Biological Inorganic Chemistry | VII Brazilian Meeting on Rare Earths, Fortaleza, 2018. Poster presentation.

R. A. Bessa, A. L. P. Castro, A. L. S. Pereira, M. F. Rosa, M. W. Anderson, A. R. Loiola. Hierarchical Cartridges Formed Combining Bacterial Cellulose Nanofibrils And Zeolite Y Nanocrystals. 42th Annual Meeting of the British Zeolite Association (BZA meeting), Birmingham, 2019. Oral presentation.

R. A. Bessa, A. L. P. Castro, A. L. S. Pereira, M. F. Rosa, M. W. Anderson, A. R. Loiola. Hierarchical Cartridges Formed Combining Bacterial Cellulose Nanofibrils And Zeolite Y Nanocrystals. 19th International Zeolite Conference, Perth, 2019. Oral presentation. Granted with travel grant.

R. A. Bessa, A. R. Loiola, M. F. Rosa and M. W. Anderson. Cubos em teia. III Exposição Arte sob o microscópio, Fortaleza, 2019. Image exibition.

R. A. Bessa, A. L. S. Pereira, M. F. Rosa, M. W. Anderson and A. R. Loiola. Formação de zeólitas hierárquicas pela adição de zeólita multiporosa com celulose bacteriana. XI Semana da Química e IV Workshop da Pós-graduação em Química, Fortaleza (online), 2020. Oral presentation.

R. A. Bessa, A. M. M. França, A. L. S. Pereira, N. P. Alexandre, M. Pérez-Page, S. M. Holmes, R. F. Nascimento, M. F. Rosa, M. W. Anderson and A. R. Loiola. Bacterial cellulose and zeolite as hierarchical system for adsorption. #LatinXChem Twitter Conference 2020. Poster presentation.

R. A. Bessa, A. R. Loiola, M. R. Freitas, A. L. S. Pereira and M. W. Anderson. Trimodal hierarchical zeolite LTA for adsorption: a preliminary characterization study. 13th Brazilian Meeting on Adsorption, Fortaleza (online), 2020. Oral presentation.

R. A. Bessa, A. M. M. França, A. L. S. Pereira, N. P. Alexandre, M. Pérez-Page, S. M. Holmes, R. F. Nascimento, M. F. Rosa, M. W. Anderson, A. R. Loiola. Hierarchical zeolite based on multiporous zeolite A and bacterial cellulose: An efficient adsorbent of Pb^{2+}. Microporous and Mesoporous Materials 312, 110752, 2021.

R. A. Bessa, A. L. S. Pereira, M. F. Rosa, M. W. Anderson and A. R. Loiola. Hierarchization of zeolites A and X using Bacterial Cellulose as macroporous support. Journal of the Brazilian Chemical Society. Submitted.

R. A. Bessa, A. L. S. Pereira, M. Perez-Page, S. Holmes, M. F. Rosa, A. R. Loiola, and M. W. Anderson. Macro-meso-microporous materials formed by hierarchical zeolite A impregnation in Bacterial cellulose aerogels. 8th Conference of the Federation of European Zeolite Associations (FEZA2020), Brighton. Poster presentation.

REFERENCES

1 DEIERLEIN, A. L., *et al.* Lead exposure during childhood and subsequent anthropometry through adolescence in girls. **Environment International,** v. 122, p. 310-315, 2019/01/01/ 2019. ISSN 0160-4120. Available at: http://www.sciencedirect.com/science/article/pii/S0160412018318488. Access at: 4th june 2020.

2 ZENG, X., *et al.* Heavy metal exposure has adverse effects on the growth and development of preschool children. **Environmental Geochemistry and Health,** v. 41, n. 1, p. 309-321, 2019/02/01 2019. ISSN 1573-2983. Available at: https://doi.org/10.1007/s10653-018-0114-z. Access at: 4th june 2020.

3 SARIGIANNIS, D. A. Indoor Air Quality Indicators. In: ARMON, R. H. and HÄNNINEN, O. (Ed.). **Environmental Indicators**. Dordrecht: Springer Netherlands, 2015. p.827-841. ISBN 978-94-017-9499-2.

4 CAROLIN, C. F., *et al.* Efficient techniques for the removal of toxic heavy metals from aquatic environment: A review. **Journal of Environmental Chemical Engineering,** v. 5, n. 3, p. 2782-2799, 2017/06/01/ 2017. ISSN 2213-3437. Available at: http://www.sciencedirect.com/science/article/pii/S2213343717302208. Access at: 4th june 2020.

5 FU, F.;WANG, Q. Removal of heavy metal ions from wastewaters: A review. **Journal of Environmental Management,** v. 92, n. 3, p. 407-418, 2011/03/01/ 2011. ISSN 0301-4797. Available at: http://www.sciencedirect.com/science/article/pii/S0301479710004147. Access at: 4th june 2020.

6 NASCIMENTO, R. F., *et al.* **Adsorção: aspectos teóricos e aplicações ambientais**. 2. Fortaleza-CE: Imprensa Universitária da Universidade Federal do Ceará (UFC), 2020. ISBN 978-65-990722-7-7.

7 ZHAO, S., *et al.* Methyl mercaptan removal from gas streams using metal-modified activated carbon. **Journal of Cleaner Production,** v. 87, p. 856-861, 2015/01/15/ 2015. ISSN 0959-6526. Available at: http://www.sciencedirect.com/science/article/pii/S0959652614010415. Access at: 18th april 2016.

8 LIU, Q., *et al.* High-performance removal of methyl mercaptan by nitrogen-rich coconut shell activated carbon. **RSC Advances,** v. 7, n. 37, p. 22892-22899, 2017. Available at: http://dx.doi.org/10.1039/C7RA03227G. Access at: 4th june 2017.

9 MA, X., *et al.* Reactive adsorption of low concentration methyl mercaptan on a Cu-based MOF with controllable size and shape. **RSC Advances,** v. 6, n. 99, p. 96997-97003, 2016. Available at: http://dx.doi.org/10.1039/C6RA18593B. Access at: 4th june 2017.

10 PEREGO, C., *et al.* Zeolites and related mesoporous materials for multi-talented environmental solutions. **Microporous and Mesoporous Materials,** v. 166, p. 37-49,

2013/01/15/ 2013. ISSN 1387-1811. Available at: http://www.sciencedirect.com/science/article/pii/S1387181112002740. Access at: 17th april 2016.

11 AIN, Q.-U.;FAROOQ, M. U.;JALEES, M. I. Application of Magnetic Graphene Oxide for Water Purification: Heavy Metals Removal and Disinfection. **Journal of Water Process Engineering,** v. 33, p. 101044, 2020/02/01/ 2020. ISSN 2214-7144. Available at: http://www.sciencedirect.com/science/article/pii/S2214714419309602. Access at: 29th august 2020.

12 MINTOVA, S.;BARRIER, N. **Verified Syntheses of Zeolitic Materials**. 3rd edition. [*s.l.*]: Elsevier, 2016.

13 BRECK, D. W. **Zeolite molecular sieves**. New York: Wiley, 1984. 771

14 SERRANO, D. P.;ESCOLA, J. M.;PIZARRO, P. Synthesis strategies in the search for hierarchical zeolites. **Chemical Society Reviews,** v. 42, n. 9, p. 4004-4035, 2013. ISSN 0306-0012. Available at: http://dx.doi.org/10.1039/C2CS35330J. Access at: 19th june 2016.

15 DAVIS, M. E. Zeolites and molecular sieves: not just ordinary catalysts. **Industrial & Engineering Chemistry Research,** v. 30, n. 8, p. 1675-1683, 1991/08/01 1991. ISSN 0888-5885. Available at: https://doi.org/10.1021/ie00056a001. Access at: 2nd july 2016.

16 LIANG, J., *et al.* Heterogeneous Catalysis in Zeolites, Mesoporous Silica, and Metal–Organic Frameworks. **Advanced Materials,** v. 29, n. 30, p. 1701139, 2017. ISSN 0935-9648. Available at: https://onlinelibrary.wiley.com/doi/abs/10.1002/adma.201701139. Access at: 13rd september 2020.

17 BECK, J. S., *et al.* A new family of mesoporous molecular sieves prepared with liquid crystal templates. **Journal of the American Chemical Society,** v. 114, n. 27, p. 10834-10843, 1992/12/01 1992. ISSN 0002-7863. Available at: https://doi.org/10.1021/ja00053a020. Access at: 13rd september 2020.

18 GALARNEAU, A.;BARODAWALLA, A.;PINNAVAIA, T. J. Porous clay heterostructures formed by gallery-templated synthesis. **Nature,** v. 374, n. 6522, p. 529-531, 1995/04/01 1995. ISSN 1476-4687. Available at: https://doi.org/10.1038/374529a0. Access at: 20th april 2020.

19 SUN, M.-H., *et al.* Applications of hierarchically structured porous materials from energy storage and conversion, catalysis, photocatalysis, adsorption, separation, and sensing to biomedicine. **Chemical Society Reviews,** v. 45, n. 12, p. 3479-3563, 2016. ISSN 0306-0012. Available at: http://dx.doi.org/10.1039/C6CS00135A. Access at: 20th december 2018.

20 OLIVEIRA, F. F., *et al.* Reactive Adsorption of Parabens on Synthesized Micro- and Mesoporous Silica from Coal Fly Ash: pH Effect on the Modification Process. **ACS Omega,** v. 5, n. 7, p. 3346-3357, 2020/02/25 2020. ISSN 2470-1343. Available at: https://doi.org/10.1021/acsomega.9b03537. Access at: 25th june 2020.

21 RENU;AGARWAL, M.;SINGH, K. Heavy metal removal from wastewater using various adsorbents: a review. **Journal of Water Reuse and Desalination,** v. 7, n. 4, p. 387-419, 2016. ISSN 2220-1319. Available at: https://doi.org/10.2166/wrd.2016.104. Access at: 4th june 2020.

22 SHI, J., *et al.* Preparation and application of modified zeolites as adsorbents in wastewater treatment. **Water Science and Technology,** v. 2017, n. 3, p. 621-635, 2018. ISSN 0273-1223. Available at: https://doi.org/10.2166/wst.2018.249. Access at: 4th june 2020.

23 HARTMANN, M.;MACHOKE, A. G.;SCHWIEGER, W. Catalytic test reactions for the evaluation of hierarchical zeolites. **Chemical Society Reviews,** v. 45, n. 12, p. 3313-3330, 2016. ISSN 0306-0012. Available at: http://dx.doi.org/10.1039/C5CS00935A. Access at: 20th december 2018.

24 PÉREZ-RAMÍREZ, J., *et al.* Hierarchical zeolites: enhanced utilisation of microporous crystals in catalysis by advances in materials design. **Chemical Society Reviews,** v. 37, n. 11, p. 2530-2542, 2008. ISSN 0306-0012. Available at: http://dx.doi.org/10.1039/B809030K. Access at: 15th august 2019.

25 YANG, X.-Y., *et al.* Hierarchically porous materials: synthesis strategies and structure design. **Chemical Society Reviews,** v. 46, n. 2, p. 481-558, 2017. ISSN 0306-0012. Available at: http://dx.doi.org/10.1039/C6CS00829A. Access at: 20th december 2018.

26 SCHWIEGER, W., *et al.* Hierarchy concepts: classification and preparation strategies for zeolite containing materials with hierarchical porosity. **Chemical Society Reviews,** v. 45, n. 12, p. 3353-3376, 2016. ISSN 0306-0012. Available at: http://dx.doi.org/10.1039/C5CS00599J. Access at: 5th june 2018.

27 FU, J., *et al.* A thermally stable and hydrophobic composite aerogel made from cellulose nanofibril aerogel impregnated with silica particles. **Journal of Materials Science,** v. 53, n. 9, p. 7072-7082, 2018/05/01 2018. ISSN 1573-4803. Available at: https://doi.org/10.1007/s10853-018-2034-9. Access at: 27th may 2019.

28 VAN RIE, J.;THIELEMANS, W. Cellulose-gold nanoparticle hybrid materials. **Nanoscale,** v. 9, n. 25, p. 8525-8554, 2017. ISSN 2040-3364. Available at: http://dx.doi.org/10.1039/C7NR00400A. Access at: 5th december 2017.

29 MA, X., *et al.* Multifunctional flexible composite aerogels constructed through in-situ growth of metal-organic framework nanoparticles on bacterial cellulose. **Chemical Engineering Journal,** v. 356, p. 227-235, 2019/01/15/ 2019. ISSN 1385-8947. Available at: http://www.sciencedirect.com/science/article/pii/S138589471831756X. Access at: 18th december 2018.

30 DUARTE, E. B., *et al.* Production of hydroxyapatite–bacterial cellulose nanocomposites from agroindustrial wastes. **Cellulose,** v. 22, n. 5, p. 3177-3187, 2015/10/01 2015. ISSN 1572-882X. Available at: https://doi.org/10.1007/s10570-015-0734-8. Access at: 14th march 2016.

31 CHEN, X., *et al.* Zeolite Cotton in Tube: A Simple Robust Household Water Treatment Filter for Heavy Metal Removal. **Scientific Reports,** v. 10, n. 1, p. 4719, 2020/03/13 2020. ISSN 2045-2322. Available at: https://doi.org/10.1038/s41598-020-61776-8. Access at: 18th march 2020.

32 KESHAVARZI, N., *et al.* Nanocellulose–Zeolite Composite Films for Odor Elimination. **ACS Applied Materials & Interfaces,** v. 7, n. 26, p. 14254-14262, 2015/07/08 2015. ISSN 1944-8244. Available at: http://dx.doi.org/10.1021/acsami.5b02252. Access at: 29th august 2017.

33 RIEGER, K. A., *et al.* Antimicrobial Activity of Silver Ions Released from Zeolites Immobilized on Cellulose Nanofiber Mats. **ACS Applied Materials & Interfaces,** v. 8, n. 5, p. 3032-3040, 2016/02/10 2016. ISSN 1944-8244. Available at: http://dx.doi.org/10.1021/acsami.5b10130. Access at: 29th august 2017.

34 BRANDES, R., *et al.* A Mini-Review on the Progress of Spherical Bacterial Cellulose Production. **Journal of Nano Research,** v. 45, p. 142-154, 2017. Available at: https://www.scientific.net/JNanoR.45.142. Access at: 8th august 2017.

35 LEE, K.-Y., *et al.* More Than Meets the Eye in Bacterial Cellulose: Biosynthesis, Bioprocessing, and Applications in Advanced Fiber Composites. **Macromolecular Bioscience,** v. 14, n. 1, p. 10-32, 2014. ISSN 1616-5195. Available at: http://dx.doi.org/10.1002/mabi.201300298. Access at: 6th december 2017.

36 STUMPF, T. R., *et al.* In situ and ex situ modifications of bacterial cellulose for applications in tissue engineering. **Materials Science and Engineering: C,** v. 82, n. Supplement C, p. 372-383, 2018/01/01/ 2018. ISSN 0928-4931. Available at: http://www.sciencedirect.com/science/article/pii/S0928493116323748. Access at: 31st december 2017.

37 BAERLOCHER, C.;MCCUSKER, L. B.;OLSON, D. H. Introduction and explanatory notes. In: BAERLOCHER, C.;MCCUSKER, L. B., *et al.* (Ed.). **Atlas of Zeolite Framework Types (Sixth Edition)**. Amsterdam: Elsevier Science B.V., 2007. p.3-11. ISBN 978-0-444-53064-6.

38 MCCUSKER, L.;LIEBAU, F.;ENGELHARDT, G. Nomenclature of structural and compositional characteristics of ordered microporous and mesoporous materials with inorganic hosts (IUPAC Recommendations 2001). **Pure and Applied Chemistry,** v. 73, n. 2, p. 381-394, 2001. ISSN 0033-4545. Access at: 18th september 2020.

39 Framework Type Codes. Available at: http://www.iza-structure.org/IZA-SC_FTC_list.htm. Access at: 17th january 2021.

40 LI, J.;CORMA, A.;YU, J. Synthesis of new zeolite structures. **Chemical Society Reviews,** v. 44, n. 20, p. 7112-7127, 2015. ISSN 0306-0012. Available at: http://dx.doi.org/10.1039/C5CS00023H. Access at: 19th june 2016.

41 MAESEN, T. Chapter 1 - The Zeolite Scene – An Overview. In: ČEJKA, J.;VAN BEKKUM, H., *et al.* (Ed.). **Studies in Surface Science and Catalysis**. [*s.l.*]: Elsevier, v.168, 2007. p.1-12. ISBN 0167-2991.

42 COSTA, J. A. S., *et al.* Recent progresses in the adsorption of organic, inorganic, and gas compounds by MCM-41-based mesoporous materials. **Microporous and Mesoporous Materials,** v. 291, p. 109698, 2020/01/01/ 2020. ISSN 1387-1811. Available at: http://www.sciencedirect.com/science/article/pii/S1387181119305554. Access at: 30th june 2020.

43 ZHAO, D., *et al.* Triblock Copolymer Syntheses of Mesoporous Silica with Periodic 50 to 300 Angstrom Pores. **Science,** v. 279, n. 5350, p. 548-552, 1998. Available at: http://science.sciencemag.org/content/sci/279/5350/548.full.pdf. Access at: 18th september 2020.

44 SCHWANKE, A., *et al.* **Materiais Mesoporosos: um caminho acessível**. Natal, RN - Brasil: EDUFRN, 2016. 181

45 KANG, F.;WANG, Q.;XIANG, S. Synthesis of mesoporous Al-MCM-41 materials using metakaolin as aluminum source. **Materials Letters,** v. 59, n. 11, p. 1426-1429, 2005/05/01/ 2005. ISSN 0167-577X. Available at: http://www.sciencedirect.com/science/article/pii/S0167577X04010018. Access at: 5th april 2018.

46 DU, C.;YANG, H. Investigation of the physicochemical aspects from natural kaolin to Al-MCM-41 mesoporous materials. **Journal of Colloid and Interface Science,** v. 369, n. 1, p. 216-222, 2012/03/01/ 2012. ISSN 0021-9797. Available at: http://www.sciencedirect.com/science/article/pii/S002197971101530X. Access at: 19th march 2018.

47 OKADA, K., *et al.* Synthesis and characterization of mesoporous silica from selectively acid-treated saponite as the precursors. **Journal of Colloid and Interface Science,** v. 314, n. 1, p. 176-183, 2007/10/01/ 2007. ISSN 0021-9797. Available at: http://www.sciencedirect.com/science/article/pii/S0021979707007114. Access at: 25th june 2020.

48 CECILIA, J. A., *et al.* Synthesis, Characterization, Uses and Applications of Porous Clays Heterostructures: A Review. **The Chemical Record,** v. 18, n. 7-8, p. 1085-1104, 2018. ISSN 1527-8999. Available at: https://onlinelibrary.wiley.com/doi/abs/10.1002/tcr.201700107. Access at: 29th march 2020.

49 **Handbook of Clay Science**. [*s.l.*]: Elsevier, 2006. 1224 ISBN 1572-4352.

50 BERGAYA, F.;LAGALY, G. Chapter 1 General Introduction: Clays, Clay Minerals, and Clay Science. In: BERGAYA, F.;THENG, B. K. G., *et al.* (Ed.). **Developments in Clay Science**. [*s.l.*]: Elsevier, v.1, 2006. p.1-18. ISBN 1572-4352.

51 MOON, R. J., *et al.* Cellulose nanomaterials review: structure, properties and nanocomposites. **Chemical Society Reviews,** v. 40, n. 7, p. 3941-3994, 2011. ISSN 0306-0012. Available at: http://dx.doi.org/10.1039/C0CS00108B. Access at: 8th june 2020.

52 ESA, F.;TASIRIN, S. M.;RAHMAN, N. A. Overview of Bacterial Cellulose Production and Application. **Agriculture and Agricultural Science Procedia,** v. 2, n. Supplement C, p. 113-119, 2014/01/01/ 2014. ISSN 2210-7843. Available at: http://www.sciencedirect.com/science/article/pii/S2210784314000187. Access at: 6th december 2017.

53 ISLAM, M. U., *et al.* Strategies for cost-effective and enhanced production of bacterial cellulose. **International Journal of Biological Macromolecules,** v. 102, p. 1166-1173, 2017/09/01/ 2017. ISSN 0141-8130. Available at: http://www.sciencedirect.com/science/article/pii/S014181301730716X. Access at: 24th may 2017.

54 NISHIYAMA, Y., *et al.* Crystal Structure and Hydrogen Bonding System in Cellulose Iα from Synchrotron X-ray and Neutron Fiber Diffraction. **Journal of the American Chemical Society,** v. 125, n. 47, p. 14300-14306, 2003/11/01 2003. ISSN 0002-7863. Available at: http://dx.doi.org/10.1021/ja037055w. Access at: 5th december 2017.

55 ZHOU, S., *et al.* Cladophora Cellulose: Unique Biopolymer Nanofibrils for Emerging Energy, Environmental, and Life Science Applications. **Accounts of Chemical Research,** v. 52, n. 8, p. 2232-2243, 2019/08/20 2019. ISSN 0001-4842. Available at: https://doi.org/10.1021/acs.accounts.9b00215. Access at: 8th june 2020.

56 HUANG, S., *et al.* Correlation between crystalline cellulose structure and cellulose synthase complex shape: a spectroscopic study with unicellular freshwater alga Micrasterias. **Cellulose,** v. 27, n. 1, p. 57-69, 2020/01/01 2020. ISSN 1572-882X. Available at: https://doi.org/10.1007/s10570-019-02793-3. Access at: 8th june 2020.

57 IWAMOTO, S., *et al.* Elastic Modulus of Single Cellulose Microfibrils from Tunicate Measured by Atomic Force Microscopy. **Biomacromolecules,** v. 10, n. 9, p. 2571-2576, 2009/09/14 2009. ISSN 1525-7797. Available at: https://doi.org/10.1021/bm900520n. Access at: 8th june 2020.

58 NUMATA, Y., *et al.* Structural and rheological characterization of bacterial cellulose gels obtained from Gluconacetobacter genus. **Food Hydrocolloids,** v. 92, p. 233-239, 2019/07/01/ 2019. ISSN 0268-005X. Available at: http://www.sciencedirect.com/science/article/pii/S0268005X18316990. Access at: 31st march 2020.

59 THORAT, MEGHANA N.;DASTAGER, S. G. High yield production of cellulose by a Komagataeibacter rhaeticus PG2 strain isolated from pomegranate as a new host. **RSC Advances,** v. 8, n. 52, p. 29797-29805, 2018. Available at: http://dx.doi.org/10.1039/C8RA05295F. Access at: 8th june 2020.

60 WANG, S.-S., *et al.* Physicochemical characterization of high-quality bacterial cellulose produced by Komagataeibacter sp. strain W1 and identification of the associated genes in bacterial cellulose production. **RSC Advances,** v. 7, n. 71, p. 45145-45155, 2017. Available at: http://dx.doi.org/10.1039/C7RA08391B. Access at: 5th december 2017.

61 LI, J., *et al.* Production of high crystallinity type-I cellulose from Komagataeibacter hansenii JR-02 isolated from Kombucha tea. **Biotechnology and Applied Biochemistry,**

v. 66, n. 1, p. 108-118, 2019. ISSN 0885-4513. Available at: https://iubmb.onlinelibrary.wiley.com/doi/abs/10.1002/bab.1703. Access at: 8th june 2020.

62 LIU, L.-X., *et al.* Komagataeibacter cocois sp. nov., a novel cellulose-producing strain isolated from coconut milk. **International Journal of Systematic and Evolutionary Microbiology,** v. 68, n. 10, p. 3125-3131, 2018. ISSN 1466-5026. Available at: https://www.microbiologyresearch.org/content/journal/ijsem/10.1099/ijsem.0.002947. Access at: 8th june 2020.

63 DE OLIVEIRA BARUD, H. G., *et al.* A multipurpose natural and renewable polymer in medical applications: Bacterial cellulose. **Carbohydrate Polymers,** v. 153, p. 406-420, 2016/11/20/ 2016. ISSN 0144-8617. Available at: http://www.sciencedirect.com/science/article/pii/S0144861716308578. Access at: 10th may 2017.

64 CAMPANO, C., *et al.* Enhancement of the fermentation process and properties of bacterial cellulose: a review. **Cellulose,** v. 23, n. 1, p. 57-91, February 01 2016. ISSN 1572-882X. Available at: https://doi.org/10.1007/s10570-015-0802-0. Access at: 27th november 2017.

65 CASTRO, C., *et al.* Structural characterization of bacterial cellulose produced by Gluconacetobacter swingsii sp. from Colombian agroindustrial wastes. **Carbohydrate Polymers,** v. 84, n. 1, p. 96-102, 2011/02/11/ 2011. ISSN 0144-8617. Available at: http://www.sciencedirect.com/science/article/pii/S0144861710008854. Access at: 2nd november 2017.

66 PACHECO, G., *et al.* Development and characterization of bacterial cellulose produced by cashew tree residues as alternative carbon source. **Industrial Crops and Products,** v. 107, p. 13-19, 2017/11/15/ 2017. ISSN 0926-6690. Available at: http://www.sciencedirect.com/science/article/pii/S0926669017303394. Access at: 18th april 2020.

67 VAZQUEZ, A., *et al.* Bacterial Cellulose from Simple and Low Cost Production Media by Gluconacetobacter xylinus. **Journal of Polymers and the Environment,** v. 21, n. 2, p. 545-554, June 01 2013. ISSN 1572-8900. Available at: https://doi.org/10.1007/s10924-012-0541-3. Access at: 7th february 2018.

68 VELÁSQUEZ-RIAÑO, M.;BOJACÁ, V. Production of bacterial cellulose from alternative low-cost substrates. **Cellulose,** v. 24, n. 7, p. 2677-2698, July 01 2017. ISSN 1572-882X. Available at: https://doi.org/10.1007/s10570-017-1309-7. Access at: 27th november 2017.

69 GOMES, F. P., *et al.* Production of bacterial cellulose by Gluconacetobacter sacchari using dry olive mill residue. **Biomass and Bioenergy,** v. 55, p. 205-211, 2013/08/01/ 2013. ISSN 0961-9534. Available at: http://www.sciencedirect.com/science/article/pii/S0961953413000536. Access at: 1st june 2017.

70 HUANG, Y., *et al.* Recent advances in bacterial cellulose. **Cellulose,** v. 21, n. 1, p. 1-30, 2014/02/01 2014. ISSN 1572-882X. Available at: https://doi.org/10.1007/s10570-013-0088-z. Access at: 6th december 2017.

71 ISIK, Z.;UNYAYAR, A.;DIZGE, N. Filtration and Antibacterial Properties of Bacterial Cellulose Membranes for Textile Wastewater Treatment. **Avicenna J Environ Health Eng,** v. 5, n. 2, p. 106-114, 2018/12/1 2018. Available at: http://ajehe.umsha.ac.ir/Article/ajehe-4084. Access at: 15th june 2020.

72 ALVES, A. A., *et al.* Bacterial cellulose membranes for environmental water remediation and industrial wastewater treatment. **International Journal of Environmental Science and Technology**, 2020/05/03 2020. ISSN 1735-2630. Available at: https://doi.org/10.1007/s13762-020-02746-5. Access at: 15th june 2020.

73 ION, V. A.;PÂRVULESCU, O. C.;DOBRE, T. Volatile organic compounds adsorption onto neat and hybrid bacterial cellulose. **Applied Surface Science,** v. 335, n. Supplement C, p. 137-146, 2015/04/30/ 2015. ISSN 0169-4332. Available at: http://www.sciencedirect.com/science/article/pii/S0169433215003359. Access at: 27th november 2017.

74 SANTOSO, S. P., *et al.* Preparation of nanocrystalline cellulose-montmorillonite composite via thermal radiation for liquid-phase adsorption. **Journal of Molecular Liquids,** v. 233, p. 29-37, 2017/05/01/ 2017. ISSN 0167-7322. Available at: http://www.sciencedirect.com/science/article/pii/S0167732216340016. Access at: 29th january 2018.

75 WANG, Y., *et al.* Ultra-light nanocomposite aerogels of bacterial cellulose and reduced graphene oxide for specific absorption and separation of organic liquids. **RSC Advances,** v. 4, n. 41, p. 21553-21558, 2014. Available at: http://dx.doi.org/10.1039/C4RA02168A. Access at: 10th june 2020.

76 KAMAL, T., *et al.* Microwave Assisted Synthesis and Carboxymethyl Cellulose Stabilized Copper Nanoparticles on Bacterial Cellulose Nanofibers Support for Pollutants Degradation. **Journal of Polymers and the Environment,** v. 27, n. 12, p. 2867-2877, 2019/12/01 2019. ISSN 1572-8919. Available at: https://doi.org/10.1007/s10924-019-01565-1. Access at: 18th june 2020.

77 CHEN, Y., *et al.* TEMPO-oxidized bacterial cellulose nanofibers-supported gold nanoparticles with superior catalytic properties. **Carbohydrate Polymers,** v. 160, n. Supplement C, p. 34-42, 2017/03/15/ 2017. ISSN 0144-8617. Available at: http://www.sciencedirect.com/science/article/pii/S0144861716313893. Access at: 31st december 2017.

78 HUANG, C., *et al.* TEMPO-oxidized bacterial cellulose nanofiber membranes as high-performance separators for lithium-ion batteries. **Carbohydrate Polymers,** v. 230, p. 115570, 2020/02/15/ 2020. ISSN 0144-8617. Available at: http://www.sciencedirect.com/science/article/pii/S014486171931238X. Access at: 15th june 2020.

79 HUANG, C., *et al.* Composite nanofiber membranes of bacterial cellulose/halloysite nanotubes as lithium ion battery separators. **Cellulose,** v. 26, n. 11, p. 6669-6681, 2019/07/01 2019. ISSN 1572-882X. Available at: https://doi.org/10.1007/s10570-019-02558-y. Access at: 16th june 2020.

80 HARTMANN, M.;SCHWIEGER, W. Hierarchically-structured porous materials: from basic understanding to applications. **Chemical Society Reviews,** v. 45, n. 12, p. 3311-3312, 2016. ISSN 0306-0012. Available at: http://dx.doi.org/10.1039/C6CS90043G. Access at: 20th december 2018.

81 MINTOVA, S.;ČEJKA, J. Chapter 9 - Micro/Mesoporous Composites. In: ČEJKA, J.;VAN BEKKUM, H., *et al.* (Ed.). **Studies in Surface Science and Catalysis**. [*s.l.*]: Elsevier, v.168, 2007. p.301-VI. ISBN 0167-2991.

82 ČEJKA, J.;MINTOVA, S. Perspectives of Micro/Mesoporous Composites in Catalysis. **Catalysis Reviews,** v. 49, n. 4, p. 457-509, 2007/10/01 2007. ISSN 0161-4940. Available at: https://doi.org/10.1080/01614940701583240. Access at: 20th june 2020.

83 KERR, G. T. Chemistry of crystalline aluminosilicates. V. Preparation of aluminum-deficient faujasites. **The Journal of Physical Chemistry,** v. 72, n. 7, p. 2594-2596, 1968/07/01 1968. ISSN 0022-3654. Available at: https://doi.org/10.1021/j100853a058. Access at: 5th december 2020.

84 MASARU, O., *et al.* Formation of Uniform Mesopores in ZSM-5 Zeolite through Treatment in Alkaline Solution. **Chemistry Letters,** v. 29, n. 8, p. 882-883, 2000. Available at: https://www.journal.csj.jp/doi/abs/10.1246/cl.2000.882. Access at: 5th december 2020.

85 THOMMES, M., *et al.* Physisorption of gases, with special reference to the evaluation of surface area and pore size distribution (IUPAC technical report). **Pure and Applied Chemistry,** v. 87, p. 1051+, 2015 September-October// 2015. ISSN 00334545. Available at: https://link.gale.com/apps/doc/A479714017/AONE?u=capes&sid=AONE&xid=960cf3e0. Access at: 18th january 2020.

86 SACHSE, A.;GARCÍA-MARTÍNEZ, J. Surfactant-Templating of Zeolites: From Design to Application. **Chemistry of Materials,** v. 29, n. 9, p. 3827-3853, 2017/05/09 2017. ISSN 0897-4756. Available at: https://doi.org/10.1021/acs.chemmater.7b0059). Access at: 18th january 2020.

87 CHOI, M., *et al.* Amphiphilic organosilane-directed synthesis of crystalline zeolite with tunable mesoporosity. **Nature Materials,** v. 5, p. 718, 08/06/online 2006. Available at: http://dx.doi.org/10.1038/nmat1705. Access at: 14th february 2018.

88 CHOI, M., *et al.* Stable single-unit-cell nanosheets of zeolite MFI as active and long-lived catalysts. **Nature,** v. 461, p. 246, 09/10/online 2009. Available at: http://dx.doi.org/10.1038/nature08288. Access at: 14th february 2018.

89 CHO, K., *et al.* Generation of Mesoporosity in LTA Zeolites by Organosilane Surfactant for Rapid Molecular Transport in Catalytic Application. **Chemistry of Materials,** v. 21,

n. 23, p. 5664-5673, 2009/12/08 2009. ISSN 0897-4756. Available at: https://doi.org/10.1021/cm902861y. Access at: 23rd october 2020.

90 CARVALHO, K. T. G.;URQUIETA-GONZALEZ, E. A. Microporous–mesoporous ZSM-12 zeolites: Synthesis by using a soft template and textural, acid and catalytic properties. **Catalysis Today,** v. 243, p. 92-102, 2015/04/01/ 2015. ISSN 0920-5861. Available at: http://www.sciencedirect.com/science/article/pii/S0920586114006634. Access at: 17th october 2019.

91 JI, D., *et al*. Mesostructured Y zeolite from NaY with low Si/Al by one-step method based on bifunctional surfactant. **Materials Chemistry and Physics,** v. 196, p. 284-287, 2017/08/01/ 2017. ISSN 0254-0584. Available at: http://www.sciencedirect.com/science/article/pii/S0254058417303401. Access at: 25th january 2019.

92 KIM, J.;CHOI, M.;RYOO, R. Effect of mesoporosity against the deactivation of MFI zeolite catalyst during the methanol-to-hydrocarbon conversion process. **Journal of Catalysis,** v. 269, n. 1, p. 219-228, 2010/01/01/ 2010. ISSN 0021-9517. Available at: http://www.sciencedirect.com/science/article/pii/S0021951709003789. Access at: 18th january 2020.

93 LIU, S., *et al.* Enhancement of desalination performance of thin-film nanocomposite membrane by cellulose nanofibers. **Journal of Membrane Science,** v. 592, p. 117363, 2019/12/15/ 2019. ISSN 0376-7388. Available at: http://www.sciencedirect.com/science/article/pii/S0376738819314644. Access at: 14th september 2020.

94 ARAÚJO, I. M. S., *et al*. Hydrothermal synthesis of bacterial cellulose–copper oxide nanocomposites and evaluation of their antimicrobial activity. **Carbohydrate Polymers,** v. 179, p. 341-349, 2018/01/01/ 2018. ISSN 0144-8617. Available at: http://www.sciencedirect.com/science/article/pii/S0144861717311141. Access at: 5th december 2020.

95 FAN, X., *et al.* A Nanoprotein-Functionalized Hierarchical Composite Air Filter. **ACS Sustainable Chemistry & Engineering,** v. 6, n. 9, p. 11606-11613, 2018/09/04 2018. Available at: https://doi.org/10.1021/acssuschemeng.8b01827. Access at: 19th december 2018.

96 Author. **Antibacterial mask, antibacterial filter for the mask, and antibacterial method using the mask or the filter**.

97 Author. **X-TYPE ZEOLITE-HYDROPHILIC POLYMER COMPOSITE AND PRODUCTION METHOD FOR THE SAME**.

98 Author. **PROCESSO DE OBTENÇÃO DE FILMES ADSORVENTE, FILMES ADSORVENTE OBTIDOS E USO DOS MESMOS.** PAULO, U. D. S.

99 RECHBERGER, F.;NIEDERBERGER, M. Synthesis of aerogels: from molecular routes to 3-dimensional nanoparticle assembly. **Nanoscale Horizons,** v. 2, n. 1, p. 6-30, 2017.

ISSN 2055-6756. Available at: http://dx.doi.org/10.1039/C6NH00077K. Access at: 25th october 2019.

100 PIERRE, A. C.;PAJONK, G. M. Chemistry of Aerogels and Their Applications. **Chemical Reviews,** v. 102, n. 11, p. 4243-4266, 2002/11/01 2002. ISSN 0009-2665. Available at: https://doi.org/10.1021/cr0101306. Access at: 15th february 2018.

101 LONG, L.-Y.;WENG, Y.-X.;WANG, Y.-Z. Cellulose Aerogels: Synthesis, Applications, and Prospects. **Polymers,** v. 10, n. 6, p. 623, 2018. ISSN 2073-4360. Available at: https://www.mdpi.com/2073-4360/10/6/623. Access at: 14th september 2020.

102 BUCHTOVÁ, N.;BUDTOVA, T. Cellulose aero-, cryo- and xerogels: towards understanding of morphology control. **Cellulose,** v. 23, n. 4, p. 2585-2595, 2016/08/01 2016. ISSN 1572-882X. Available at: https://doi.org/10.1007/s10570-016-0960-8. Access at: 27th may 2019.

103 ZHANG, X., *et al.* The effect of freezing speed and hydrogel concentration on the microstructure and compressive performance of bamboo-based cellulose aerogel. **Journal of Wood Science,** v. 61, n. 6, p. 595-601, 2015/12/01 2015. ISSN 1611-4663. Available at: https://doi.org/10.1007/s10086-015-1514-7. Access at: 14th september 2020.

104 LAVOINE, N.;BERGSTROM, L. Nanocellulose-based foams and aerogels: processing, properties, and applications. **Journal of Materials Chemistry A,** v. 5, n. 31, p. 16105-16117, 2017. ISSN 2050-7488. Available at: http://dx.doi.org/10.1039/C7TA02807E. Access at: 28th october 2017.

105 **Aerogels Handbook**. New York, US: Springer, 2011. ISBN 978-1-4419-7589-8.

106 PEREIRA, A. L. S., *et al.* Bacterial cellulose aerogels: Influence of oxidation and silanization on mechanical and absorption properties. **Carbohydrate Polymers,** v. 250, p. 116927, 2020/12/15/ 2020. ISSN 0144-8617. Available at: http://www.sciencedirect.com/science/article/pii/S0144861720311000. Access at: 25th august 2020.

107 HE, J., *et al.* Superelastic and superhydrophobic bacterial cellulose/silica aerogels with hierarchical cellular structure for oil absorption and recovery. **Journal of Hazardous Materials,** v. 346, p. 199-207, 2018/03/15/ 2018. ISSN 0304-3894. Available at: http://www.sciencedirect.com/science/article/pii/S0304389417309457. Access at: 9th april 2019.

108 BENDAHOU, D., *et al.* Nano-fibrillated cellulose-zeolites based new hybrid composites aerogels with super thermal insulating properties. **Industrial Crops and Products,** v. 65, p. 374-382, 2015/03/01/ 2015. ISSN 0926-6690. Available at: http://www.sciencedirect.com/science/article/pii/S0926669014006992. Access at: 9th april 2019.

109 VALENCIA, L., *et al.* Bio-based Micro-/Meso-/Macroporous Hybrid Foams with Ultrahigh Zeolite Loadings for Selective Capture of Carbon Dioxide. **ACS Applied**

Materials & Interfaces, v. 11, n. 43, p. 40424-40431, 2019/10/30 2019. ISSN 1944-8244. Available at: https://doi.org/10.1021/acsami.9b11399. Access at: 13rd august 2020.

110 FECHINE, P. B. A. **Avanços no desenvolvimento de nanomateriais**. Fortaleza: Imprensa Universitária, 2020. ISBN 978-65-991493-7-5.

111 FURUKAWA, H., *et al.* The Chemistry and Applications of Metal-Organic Frameworks. **Science,** v. 341, n. 6149, p. 1230444, 2013. Available at: https://science.sciencemag.org/content/sci/341/6149/1230444.full.pdf. Access at: 18th january 2021.

112 WRIGHT, P. A. Chapter 7 Adsorption and Diffusion. In: (Ed.). **Microporous Framework Solids**. [*s.l.*]: The Royal Society of Chemistry, 2008. p.257-311. ISBN 978-0-85404-812-0.

113 FOO, K. Y.;HAMEED, B. H. Insights into the modeling of adsorption isotherm systems. **Chemical Engineering Journal,** v. 156, n. 1, p. 2-10, 2010/01/01/ 2010. ISSN 1385-8947. Available at: http://www.sciencedirect.com/science/article/pii/S1385894709006147. Access at: 18th january 2021.

114 NOROOZI, B.;SORIAL, G. A. Applicable models for multi-component adsorption of dyes: A review. **Journal of Environmental Sciences,** v. 25, n. 3, p. 419-429, 2013/03/01/ 2013. ISSN 1001-0742. Available at: http://www.sciencedirect.com/science/article/pii/S1001074212601946. Access at: 18th january 2021.

115 LARGITTE, L.;PASQUIER, R. A review of the kinetics adsorption models and their application to the adsorption of lead by an activated carbon. **Chemical Engineering Research and Design,** v. 109, p. 495-504, 2016/05/01/ 2016. ISSN 0263-8762. Available at: http://www.sciencedirect.com/science/article/pii/S0263876216000691. Access at: 21st january 2021.

116 CHANG, S.;LU, C.;LIN, K.-Y. A. Comparisons of kinetics, thermodynamics and regeneration of tetramethylammonium hydroxide adsorption in aqueous solution with graphene oxide, zeolite and activated carbon. **Applied Surface Science,** v. 326, p. 187-194, 2015/01/30/ 2015. ISSN 0169-4332. Available at: http://www.sciencedirect.com/science/article/pii/S0169433214026397. Access at: 22nd january 2018.

117 ARMON, R. H.;HÄNNINEN, O. **Environmental Indicators**. Dordrecht: Springer, 2015. 1068 ISBN 978-94-017-9499-2.

118 OBENG-GYASI, E. Sources of lead exposure in various countries. **Rev Environ Health,** v. 34, n. 1, p. 25-34, Mar 26 2019. ISSN 0048-7554. Access at: 21st january 2021.

119 PAOLIELLO, M. M. B.;DE CAPITANI, E. M. Occupational and environmental human lead exposure in Brazil. **Environmental Research,** v. 103, n. 2, p. 288-297, 2007/02/01/ 2007. ISSN 0013-9351. Available at:

http://www.sciencedirect.com/science/article/pii/S0013935106001502. Access at: 21st january 2021.

120 CHEN, X., *et al.* The association between lead and cadmium co-exposure and renal dysfunction. **Ecotoxicology and Environmental Safety,** v. 173, p. 429-435, 2019/05/30/ 2019. ISSN 0147-6513. Available at: http://www.sciencedirect.com/science/article/pii/S0147651319300983. Access at: 21th january 2021.

121 BALOCH, S., *et al.* Occupational exposure of lead and cadmium on adolescent and adult workers of battery recycling and welding workshops: Adverse impact on health. **Science of The Total Environment,** v. 720, n. 21 january 2021, p. 137549, 2020/06/10/ 2020. ISSN 0048-9697. Available at: http://www.sciencedirect.com/science/article/pii/S0048969720310603. Access at: 12nd november 2020.

122 DYER, A. Chapter 16 - Ion-Exchange Properties of Zeolites and Related Materials. In: ČEJKA, J.;VAN BEKKUM, H., *et al.* (Ed.). **Studies in Surface Science and Catalysis**. [*s.l.*]: Elsevier, v.168, 2007. p.525-553. ISBN 0167-2991.

123 WRIGHT, P. A. Chapter 3 Structure Determination: Experimental Techniques. In: (Ed.). **Microporous Framework Solids**. [*s.l.*]: The Royal Society of Chemistry, 2008. p.79-147. ISBN 978-0-85404-812-0.

124 PECHARSKY, V.;ZAVALIJ, P. **Fundamentals of Powder Diffraction and Structural Characterization of Materials**. 2. [*s.l.*]: Springer US, 2009. XXIV, 744 ISBN 978-0-387-09579-0.

125 MORRIS, R. E.;WHEATLEY, P. S. Chapter 11 - Diffraction Techniques Applied to Zeolites. In: ČEJKA, J.;VAN BEKKUM, H., *et al.* (Ed.). **Studies in Surface Science and Catalysis**. [*s.l.*]: Elsevier, v.168, 2007. p.375-IX. ISBN 0167-2991.

126 BAERLOCHER, C.;MCCUSKER, L. B.;OLSON, D. H. LTA - Pm3¯m. In: BAERLOCHER, C.;MCCUSKER, L. B., *et al.* (Ed.). **Atlas of Zeolite Framework Types (Sixth Edition)**. Amsterdam: Elsevier Science B.V., 2007. p.194-195. ISBN 978-0-444-53064-6.

127 DINNEBIER, R. E.;BILLINGE, S. J. L. Chapter 1 Principles of Powder Diffraction. In: (Ed.). **Powder Diffraction: Theory and Practice**. [*s.l.*]: The Royal Society of Chemistry, 2008. p.1-19. ISBN 978-0-85404-231-9.

128 BAERLOCHER, C.;MCCUSKER, L. Database of Zeolite Structures. Available at: http://www.iza-structure.org/databases. Access at: 23rd january 2021.

129 GOLDSTEIN, J. I., *et al.* **Scanning Electron Microscopy and X-Ray Microanalysis**. 4. New York: Springer-Verlag New York, 2018. XXIII, 550 ISBN 978-1-4939-6676-9.

130 EGERTON, R. F. **Physical Principles of Electron Microscopy: An Introduction to TEM, SEM, and AEM**. 2. Switzerland: Springer International Publishing, 2016. XI, 196 ISBN 978-3-319-39877-8.

131 Energy Dispersive Spectroscopy. Available at: https://myscope.training/index.html#/EDSlevel_2_1. Access at: 17th january 2021.

132 WILLIAMS, D. B.;CARTER, C. B. **Transmission Electron Microscopy: A Textbook for Materials Science**. 2. US: Springer US, 2009. LXII, 775 ISBN 978-0-387-76501-3.

133 LERCHER, J. A.;JENTYS, A. Chapter 13 - Infrared and Raman Spectroscopy for Characterizing Zeolites. In: ČEJKA, J.;VAN BEKKUM, H., *et al.* (Ed.). **Studies in Surface Science and Catalysis**. [*s.l.*]: Elsevier, v.168, 2007. p.435-476. ISBN 0167-2991.

134 Spectroscopy in a Suitcase. 2016. Available at: https://edu.rsc.org/download?ac=11383. Access at: 24th january 2021.

135 PAVIA, D. L., *et al.* **Introduction to Spectroscopy**. [*s.l.*]: Cengage Learning, 2008. ISBN 9780495114789.

136 DA SILVA FREITAS, C. M. A. **FTIR study of zeolites: the nature, concentration and accessibility of the acid sites**. 2020. 164 (Doctor of Philosophy). Keele University, Keele, 2020.

137 GEDEON, A.;FERNANDEZ, C. Chapter 12 - Solid-State NMR Spectroscopy in Zeolite Science. In: ČEJKA, J.;VAN BEKKUM, H., *et al.* (Ed.). **Studies in Surface Science and Catalysis**. [*s.l.*]: Elsevier, v.168, 2007. p.403-XII. ISBN 0167-2991.

138 LIPPMAA, E., *et al.* Investigation of the structure of zeolites by solid-state high-resolution silicon-29 NMR spectroscopy. **Journal of the American Chemical Society,** v. 103, n. 17, p. 4992-4996, 1981/08/01 1981. ISSN 0002-7863. Available at: https://doi.org/10.1021/ja00407a002. Access at: 12th may 2020.

139 ONGARI, D., *et al.* Accurate Characterization of the Pore Volume in Microporous Crystalline Materials. **Langmuir,** v. 33, n. 51, p. 14529-14538, 2017/12/26 2017. ISSN 0743-7463. Available at: https://doi.org/10.1021/acs.langmuir.7b01682. Access at: 1st march 2020.

140 CYCHOSZ, K. A., *et al.* Recent advances in the textural characterization of hierarchically structured nanoporous materials. **Chemical Society Reviews,** v. 46, n. 2, p. 389-414, 2017. ISSN 0306-0012. Available at: http://dx.doi.org/10.1039/C6CS00391E. Access at: 5th december 2020.

141 THOMMES, M. Chapter 15 - Textural Characterization of Zeolites and Ordered Mesoporous Materials by Physical Adsorption. In: ČEJKA, J.;VAN BEKKUM, H., *et al.* (Ed.). **Studies in Surface Science and Catalysis**. [*s.l.*]: Elsevier, v.168, 2007. p.495-XIII. ISBN 0167-2991.

142 BARDESTANI, R.;PATIENCE, G. S.;KALIAGUINE, S. Experimental methods in chemical engineering: specific surface area and pore size distribution measurements—BET, BJH, and DFT. **The Canadian Journal of Chemical Engineering,** v. 97, n. 11, p.

2781-2791, 2019. ISSN 0008-4034. Available at: https://onlinelibrary.wiley.com/doi/abs/10.1002/cjce.23632. Access at: 1st march 2020.

143 HESTRIN, S.;SCHRAMM, M. Synthesis of cellulose by Acetobacter xylinum. 2. Preparation of freeze-dried cells capable of polymerizing glucose to cellulose. **Biochemical Journal,** v. 58, n. 2, p. 345-352, 1954. ISSN 0264-6021 1470-8728. Available at: http://www.ncbi.nlm.nih.gov/pmc/articles/PMC1269899/. Access at: 1st november 2017.

144 THOMPSON, R. W.;HUBER, M. J. Chapter 55 - LTA Linde Type A Si(50), Al(50). In: ROBSON, H. and LILLERUD, K. P. (Ed.). **Verified Syntheses of Zeolitic Materials**. Amsterdam: Elsevier Science, 2001. p.179-181. ISBN 978-0-444-50703-7.

145 GINTER, D. M.;BELL, A. T.;RADKE, C. J. FAU Linde Type Y Si(71), Al(29). In: MINTOVA, S. and BARRIER, N. (Ed.). **Verified Syntheses of Zeolitic Materials**. 3rd edition. [*s.l.*]: Elsevier, 2016. ISBN 978-0-692-68539-6.

146 BESSA, R. A., *et al.* Kaolin-based magnetic zeolites A and P as water softeners. **Microporous and Mesoporous Materials,** v. 245, n. Supplement C, p. 64-72, 2017/06/01/ 2017. ISSN 1387-1811. Available at: http://www.sciencedirect.com/science/article/pii/S1387181117301610. Access at: 5th december 2020.

147 SANTOS, E. C., *et al.* Al-MCM-41 Synthesized from Kaolin via Hydrothermal Route: Structural Characterization and Use as an Efficient Adsorbent of Methylene Blue. **Journal of the Brazilian Chemical Society,** v. 29, p. 2378-2386, 2018. ISSN 0103-5053. Available at: http://www.scielo.br/scielo.php?script=sci_arttext&pid=S0103-50532018001102378&nrm=iso. Access at: 25th january 2019.

148 SAITO, T.;ISOGAI, A. TEMPO-Mediated Oxidation of Native Cellulose. The Effect of Oxidation Conditions on Chemical and Crystal Structures of the Water-Insoluble Fractions. **Biomacromolecules,** v. 5, n. 5, p. 1983-1989, 2004/09/01 2004. ISSN 1525-7797. Available at: https://doi.org/10.1021/bm0497769. Access at: 31st march 2020.

149 SAITO, T., *et al.* Cellulose Nanofibers Prepared by TEMPO-Mediated Oxidation of Native Cellulose. **Biomacromolecules,** v. 8, n. 8, p. 2485-2491, 2007/08/01 2007. ISSN 1525-7797. Available at: https://doi.org/10.1021/bm0703970. Access at: 24th may 2018.

150 PEREIRA, A. L. S. **Aerogéis de nanocelulose funcionalizados para absorção seletiva de solventes orgânicos** 2018. 118 (PhD). Programa de pós-graduação em Química, Universidade Federal do Ceará, Fortaleza-CE, 2018.

151 JIA, Y., *et al.* Surfactant-free emulsions stabilized by tempo-oxidized bacterial cellulose. **Carbohydrate Polymers,** v. 151, n. Supplement C, p. 907-915, 2016/10/20/ 2016. ISSN 0144-8617. Available at: http://www.sciencedirect.com/science/article/pii/S0144861716306439. Access at: 31st december 2017.

152 THOMAS, J. M.;KLINOWSKI, J. The Study of Aluminosilicate and Related Catalysts by High-Resolution Solid-State NMR Spectroscopy. In: ELEY, D. D.;PINES, H., *et al.*

(Ed.). **Advances in Catalysis**. [*s.l.*]: Academic Press, v.33, 1985. p.199-374. ISBN 0360-0564.

153 ZHANG, S., *et al.* Carbon aerogels by pyrolysis of TEMPO-oxidized cellulose. **Applied Surface Science,** v. 440, p. 873-879, 5/15/ 2018. ISSN 0169-4332. Available at: https://www.sciencedirect.com/science/article/pii/S0169433218302708. Access at: 20th june 2020.

154 INGLEZAKIS, V. J.;LOIZIDOU, M. D.;GRIGOROPOULOU, H. P. Ion exchange of Pb^{2+}, Cu^{2+}, Fe^{3+}, and Cr^{3+} on natural clinoptilolite: selectivity determination and influence of acidity on metal uptake. **Journal of Colloid and Interface Science,** v. 261, n. 1, p. 49-54, 2003/05/01/ 2003. ISSN 0021-9797. Available at: http://www.sciencedirect.com/science/article/pii/S0021979702002448. Access at: 4th may 2020.

155 LAGERGREN, S. K. About the Theory of So-called Adsorption of Soluble Substances. **Sven. Vetenskapsakad. Handingarl,** v. 24, p. 1-39, 1898 1898. Available at: https://ci.nii.ac.jp/naid/10016440244/en/. Access at: 4th may 2020.

156 HO, Y. S.;MCKAY, G. Pseudo-second order model for sorption processes. **Process Biochemistry,** v. 34, n. 5, p. 451-465, 1999/07/01/ 1999. ISSN 1359-5113. Available at: http://www.sciencedirect.com/science/article/pii/S0032959298001125. Access at: 4th may 2020.

157 BESSA, R. A., *et al.* Hierarchical zeolite based on multiporous zeolite A and bacterial cellulose: An efficient adsorbent of Pb^{2+}. **Microporous and Mesoporous Materials,** v. 312, 2021/01/01/ 2021. ISSN 1387-1811. Available at: http://www.sciencedirect.com/science/article/pii/S1387181120307526. Access at: 3rd december 2020.

158 YE, J., *et al.* Bacterial cellulose production by Acetobacter xylinum ATCC 23767 using tobacco waste extract as culture medium. **Bioresource Technology,** v. 274, p. 518-524, 2019/02/01/ 2019. ISSN 0960-8524. Available at: http://www.sciencedirect.com/science/article/pii/S0960852418316729. Access at: 31st march 2020.

159 DÓRAME-MIRANDA, R. F., *et al.* Bacterial cellulose production by Gluconacetobacter entanii using pecan nutshell as carbon source and its chemical functionalization. **Carbohydrate Polymers,** v. 207, p. 91-99, 2019/03/01/ 2019. ISSN 0144-8617. Available at: http://www.sciencedirect.com/science/article/pii/S0144861718314012. Access at: 31st march 2020.

160 NASCIMENTO, E. S., *et al.* TEMPO oxidation and high-speed blending as a combined approach to disassemble bacterial cellulose. **Cellulose,** v. 26, n. 4, p. 2291-2302, 2019/03/01 2019. ISSN 1572-882X. Available at: https://doi.org/10.1007/s10570-018-2208-2. Access at: 5th december 2020.

161 LI, Q., *et al.* Flexible cellulose nanofibrils as novel pickering stabilizers: The emulsifying property and packing behavior. **Food Hydrocolloids,** v. 88, p. 180-189, 2019/03/01/ 2019. ISSN 0268-005X. Available at:

http://www.sciencedirect.com/science/article/pii/S0268005X18314814. Access at: 20th december 2018.

162 DONIUS, A. E., *et al.* Superior mechanical performance of highly porous, anisotropic nanocellulose–montmorillonite aerogels prepared by freeze casting. **Journal of the Mechanical Behavior of Biomedical Materials,** v. 37, n. Supplement C, p. 88-99, 2014/09/01/ 2014. ISSN 1751-6161. Available at: http://www.sciencedirect.com/science/article/pii/S1751616114001374. Access at: 5th december 2020.

163 ALI, Z. M.;GIBSON, L. J. The structure and mechanics of nanofibrillar cellulose foams. **Soft Matter,** v. 9, n. 5, p. 1580-1588, 2013. ISSN 1744-683X. Available at: http://dx.doi.org/10.1039/C2SM27197D. Access at: 17th december 2017.

164 DONG, H., *et al.* Hydrogel, aerogel and film of cellulose nanofibrils functionalized with silver nanoparticles. **Carbohydrate Polymers,** v. 95, n. 2, p. 760-767, 2013/06/20/ 2013. ISSN 0144-8617. Available at: http://www.sciencedirect.com/science/article/pii/S0144861713002804. Access at: 17th december 2017.

165 KORHONEN, J. T., *et al.* Inorganic Hollow Nanotube Aerogels by Atomic Layer Deposition onto Native Nanocellulose Templates. **ACS Nano,** v. 5, n. 3, p. 1967-1974, 2011/03/22 2011. ISSN 1936-0851. Available at: http://dx.doi.org/10.1021/nn200108s. Access at: 16th december 2017.

166 HUANG, L., *et al.* Bacterial cellulose nanofibers promote stress and fidelity of 3D-printed silk based hydrogel scaffold with hierarchical pores. **Carbohydrate Polymers,** v. 221, p. 146-156, 2019/10/01/ 2019. ISSN 0144-8617. Available at: http://www.sciencedirect.com/science/article/pii/S0144861719305958. Access at: 17th october 2019.

167 SEHAQUI, H.;ZHOU, Q.;BERGLUND, L. A. High-porosity aerogels of high specific surface area prepared from nanofibrillated cellulose (NFC). **Composites Science and Technology,** v. 71, n. 13, p. 1593-1599, 2011/09/09/ 2011. ISSN 0266-3538. Available at: http://www.sciencedirect.com/science/article/pii/S026635381100234X. Access at: 15th march 2018.

168 KARADAGLI, I., *et al.* Production of porous cellulose aerogel fibers by an extrusion process. **The Journal of Supercritical Fluids,** v. 106, n. Supplement C, p. 105-114, 2015/11/01/ 2015. ISSN 0896-8446. Available at: http://www.sciencedirect.com/science/article/pii/S089684461530036X. Access at: 15th march 2018.

169 SEHAQUI, H., *et al.* Mechanical performance tailoring of tough ultra-high porosity foams prepared from cellulose I nanofiber suspensions. **Soft Matter,** v. 6, n. 8, p. 1824-1832, 2010. ISSN 1744-683X. Available at: http://dx.doi.org/10.1039/B927505C. Access at: 17th december 2017.

170 MARTOÏA, F., *et al.* Cellulose nanofibril foams: Links between ice-templating conditions, microstructures and mechanical properties. **Materials & Design,** v. 104, n.

Supplement C, p. 376-391, 2016/08/15/ 2016. ISSN 0264-1275. Available at: http://www.sciencedirect.com/science/article/pii/S026412751630572X. Access at: 28th october 2017.

171 KORHONEN, J. T., *et al.* Hydrophobic Nanocellulose Aerogels as Floating, Sustainable, Reusable, and Recyclable Oil Absorbents. **ACS Applied Materials & Interfaces,** v. 3, n. 6, p. 1813-1816, 2011/06/22 2011. ISSN 1944-8244. Available at: http://dx.doi.org/10.1021/am200475b. Access at: 16th december 2017.

172 SANAEEPUR, H., *et al.* A novel Co^{2+} exchanged zeolite Y/cellulose acetate mixed matrix membrane for CO_2/N_2 separation. **Journal of the Taiwan Institute of Chemical Engineers,** v. 60, p. 403-413, 2016/03/01/ 2016. ISSN 1876-1070. Available at: http://www.sciencedirect.com/science/article/pii/S1876107015004836. Access at: 25th may 2018.

173 JIANG, F.;DINH, D. M.;HSIEH, Y.-L. Adsorption and desorption of cationic malachite green dye on cellulose nanofibril aerogels. **Carbohydrate Polymers,** v. 173, p. 286-294, 2017/10/01/ 2017. ISSN 0144-8617. Available at: http://www.sciencedirect.com/science/article/pii/S0144861717306227. Access at: 19th march 2018.

174 KAMAL MOHAMED, S. M., *et al.* The effect of zinc oxide (ZnO) addition on the physical and morphological properties of cellulose aerogel beads. **RSC Advances,** v. 5, n. 109, p. 90193-90201, 2015. Available at: http://dx.doi.org/10.1039/C5RA17366C. Access at: 5th december 2020.

175 LI, Z., *et al.* Production of nano bacterial cellulose from waste water of candied jujube-processing industry using Acetobacter xylinum. **Carbohydrate Polymers,** v. 120, n. Supplement C, p. 115-119, 2015/04/20/ 2015. ISSN 0144-8617. Available at: http://www.sciencedirect.com/science/article/pii/S0144861714011746. Access at: 5th december 2020.

176 LU, Q.-L., *et al.* One-pot tandem reactions for the preparation of esterified cellulose nanocrystals with 4-dimethylaminopyridine as a catalyst. **RSC Advances,** v. 5, n. 69, p. 56198-56204, 2015. Available at: http://dx.doi.org/10.1039/C5RA08690F. Access at: 5th december 2020.

177 RUAN, C.-Q., *et al.* Favored surface-limited oxidation of cellulose with Oxone ® in water. **RSC Advances,** v. 7, n. 64, p. 40600-40607, 2017. Available at: http://dx.doi.org/10.1039/C7RA06141B. Access at: 5th december 2020.

178 LAVOINE, N., *et al.* Improvement of the Thermal Stability of TEMPO-Oxidized Cellulose Nanofibrils by Heat-Induced Conversion of Ionic Bonds to Amide Bonds. **Macromolecular Rapid Communications,** v. 37, n. 13, p. 1033-1039, 2016. Available at: https://onlinelibrary.wiley.com/doi/abs/10.1002/marc.201600186. Access at: 5th december 2020.

179 VASCONCELOS, N. F., *et al.* Bacterial cellulose nanocrystals produced under different hydrolysis conditions: Properties and morphological features. **Carbohydrate Polymers,** v. 155, p. 425-431, 2017/01/02/ 2017. ISSN 0144-8617. Available at:

http://www.sciencedirect.com/science/article/pii/S0144861716310396. Access at: 5th december 2020.

180 ANDRADE, F. K., *et al.* Stable microfluidized bacterial cellulose suspension. **Cellulose,** v. 26, n. 10, p. 5851-5864, July 01 2019. ISSN 1572-882X. Available at: https://doi.org/10.1007/s10570-019-02512-y. Access at: 5th december 2020.

181 XU, X., *et al.* Cellulose Nanocrystals vs. Cellulose Nanofibrils: A Comparative Study on Their Microstructures and Effects as Polymer Reinforcing Agents. **ACS Applied Materials & Interfaces,** v. 5, n. 8, p. 2999-3009, 2013/04/24 2013. ISSN 1944-8244. Available at: http://dx.doi.org/10.1021/am302624t. Access at: 16th december 2017.

182 ZHANG, B.-X.;AZUMA, J.-I.;UYAMA, H. Preparation and characterization of a transparent amorphous cellulose film. **RSC Advances,** v. 5, n. 4, p. 2900-2907, 2015. Available at: http://dx.doi.org/10.1039/C4RA14090G. Access at: 5th december 2017.

183 DOGAN, H.;HILMIOGLU, N. D. Zeolite-filled regenerated cellulose membranes for pervaporative dehydration of glycerol. **Vacuum,** v. 84, n. 9, p. 1123-1132, 2010/04/19/ 2010. ISSN 0042-207X. Available at: http://www.sciencedirect.com/science/article/pii/S0042207X10000679. Access at: 6th september 2017.

184 SOHEILMOGHADDAM, M., *et al.* Bionanocomposites of regenerated cellulose/zeolite prepared using environmentally benign ionic liquid solvent. **Carbohydrate Polymers,** v. 106, p. 326-334, 2014/06/15/ 2014. ISSN 0144-8617. Available at: http://www.sciencedirect.com/science/article/pii/S0144861714002161. Access at: 10th may 2017.

185 TSERKI, V., *et al.* A study of the effect of acetylation and propionylation surface treatments on natural fibres. **Composites Part A: Applied Science and Manufacturing,** v. 36, n. 8, p. 1110-1118, 2005/08/01/ 2005. ISSN 1359-835X. Available at: http://www.sciencedirect.com/science/article/pii/S1359835X05000345. Access at: 29th december 2017.

186 BARUD, H. S., *et al.* Thermal behavior of cellulose acetate produced from homogeneous acetylation of bacterial cellulose. **Thermochimica Acta,** v. 471, n. 1, p. 61-69, 2008/05/30/ 2008. ISSN 0040-6031. Available at: http://www.sciencedirect.com/science/article/pii/S0040603108000506. Access at: 6th december 2017.

187 MTIBE, A., *et al.* A comparative study on properties of micro and nanopapers produced from cellulose and cellulose nanofibres. **Carbohydrate Polymers,** v. 118, n. Supplement C, p. 1-8, 2015/03/15/ 2015. ISSN 0144-8617. Available at: http://www.sciencedirect.com/science/article/pii/S0144861714010078. Access at: 27th november 2017.

188 ULLAH, M. W., *et al.* In situ synthesis of a bio-cellulose/titanium dioxide nanocomposite by using a cell-free system. **RSC Advances,** v. 6, n. 27, p. 22424-22435, 2016. Available at: http://dx.doi.org/10.1039/C5RA26704H. Access at: 6th december 2017.

189 CHANG, P. S.;ROBYT, J. F. Oxidation of Primary Alcohol Groups of Naturally Occurring Polysaccharides with 2,2,6,6-Tetramethyl-1-Piperidine Oxoammonium Ion. **Journal of Carbohydrate Chemistry,** v. 15, n. 7, p. 819-830, 1996/09/01 1996. ISSN 0732-8303. Available at: https://doi.org/10.1080/07328309608005694. Access at: 14th february 2018.

190 COSERI, S. Cellulose: To depolymerize… or not to? **Biotechnology Advances,** v. 35, n. 2, p. 251-266, 2017/03/01/ 2017. ISSN 0734-9750. Available at: http://www.sciencedirect.com/science/article/pii/S0734975017300022. Access at: 6th september 2017.

191 BESBES, I.;ALILA, S.;BOUFI, S. Nanofibrillated cellulose from TEMPO-oxidized eucalyptus fibres: Effect of the carboxyl content. **Carbohydrate Polymers,** v. 84, n. 3, p. 975-983, 2011/03/17/ 2011. ISSN 0144-8617. Available at: http://www.sciencedirect.com/science/article/pii/S0144861710010398. Access at: 31st march 2020.

192 SAITO, T.;ISOGAI, A. Ion-exchange behavior of carboxylate groups in fibrous cellulose oxidized by the TEMPO-mediated system. **Carbohydrate Polymers,** v. 61, n. 2, p. 183-190, 2005/08/04/ 2005. ISSN 0144-8617. Available at: http://www.sciencedirect.com/science/article/pii/S0144861705001542. Access at: 31st march 2020.

193 ISOGAI, A.;SAITO, T.;FUKUZUMI, H. TEMPO-oxidized cellulose nanofibers. **Nanoscale,** v. 3, n. 1, p. 71-85, 2011. ISSN 2040-3364. Available at: http://dx.doi.org/10.1039/C0NR00583E. Access at: 5th february 2019.

194 LAI, C., *et al.* Surface characterization of TEMPO-oxidized bacterial cellulose. **Surface and Interface Analysis,** v. 45, n. 11-12, p. 1673-1679, 2013. ISSN 0142-2421. Available at: https://onlinelibrary.wiley.com/doi/abs/10.1002/sia.5306. Access at: 5th february 2019.

195 BARUD, H. S., *et al.* Thermal characterization of bacterial cellulose–phosphate composite membranes. **Journal of Thermal Analysis and Calorimetry,** v. 87, n. 3, p. 815-818, March 01 2007. ISSN 1572-8943. Available at: https://doi.org/10.1007/s10973-006-8170-5. Access at: 10th may 2017.

196 MOHAMMADKAZEMI, F.;AZIN, M.;ASHORI, A. Production of bacterial cellulose using different carbon sources and culture media. **Carbohydrate Polymers,** v. 117, n. Supplement C, p. 518-523, 2015/03/06/ 2015. ISSN 0144-8617. Available at: http://www.sciencedirect.com/science/article/pii/S014486171401011X. Access at: 5th december 2020.

197 COSTA, A. F. S., *et al.* Production of Bacterial Cellulose by Gluconacetobacter hansenii Using Corn Steep Liquor As Nutrient Sources. **Frontiers in Microbiology,** v. 8, n. 2027, 2017-October-17 2017. ISSN 1664-302X. Available at: https://www.frontiersin.org/article/10.3389/fmicb.2017.02027. Access at: 27th november 2017.

198 GRAMLICH, V.;MEIER, W. M. The crystal structure of hydrated NaA: A detailed refinement of a pseudosymmetric zeolite structure. **Zeitschrift fur Kristallographie - New Crystal Structures,** v. 133, n. 133, p. 134-149, 1971. Available at: https://www.scopus.com/inward/record.uri?eid=2-s2.0-84864163984&doi=10.1524%2fzkri.1971.133.133.134&partnerID=40&md5=f68d22fcb76f5490dca599ecc6952616. Access at: 14th april 2020.

199 IKEDA, T., *et al.* Structural Study of Sodium-Type Zeolite LTA by Combination of Rietveld and Maximum-Entropy Methods. **Chemistry of Materials,** v. 10, n. 12, p. 3996-4004, 1998/12/01 1998. ISSN 0897-4756. Available at: https://doi.org/10.1021/cm980442y. Access at: 5th december 2020.

200 CARDOSO, A. M., *et al.* Integrated synthesis of zeolites 4A and Na-P1 using coal fly ash for application in the formulation of detergents and swine wastewater treatment. **Journal of Hazardous Materials,** v. 287, p. 69-77, Apr 28 2015. ISSN 0304-3894.

201 BRONIĆ, J., *et al.* Influence of alkalinity of the starting system on size and morphology of the zeolite A crystals. **Materials Chemistry and Physics,** v. 132, n. 2, p. 973-976, 2012/02/15/ 2012. ISSN 0254-0584. Available at: http://www.sciencedirect.com/science/article/pii/S0254058411010716. Access at: 15th april 2020.

202 LOIOLA, A. R., *et al.* Structural analysis of zeolite NaA synthesized by a cost-effective hydrothermal method using kaolin and its use as water softener. **Journal of Colloid and Interface Science,** v. 367, p. 34-39, Feb 1 2012. ISSN 0021-9797.

203 YOUSSEF, H. F.;HEGAZY, W. H.;ABO-ALMAGED, H. H. Preparation and characterization of micronized zeolite Na-A: cytotoxic activity of silver exchanged form. **Journal of Porous Materials,** v. 22, n. 4, p. 1033-1041, August 01 2015. ISSN 1573-4854. Available at: https://doi.org/10.1007/s10934-015-9977-x. Access at: 5th december 2020.

204 FAGHIHIAN, H., *et al.* Synthesis of a novel magnetic zeolite nanocomposite for removal of Cs+ and Sr2+ from aqueous solution: Kinetic, equilibrium, and thermodynamic studies. **Journal of Colloid and Interface Science,** v. 393, n. 0, p. 445-451, 2013. ISSN 0021-9797. Available at: (http://www.sciencedirect.com/science/article/pii/S0021979712012970. Access at: 2nd september 2017.

205 HUANG, Y.;JIANG, Z. Vibrational spectra of completely siliceous zeolite A. **Microporous Materials,** v. 12, n. 4, p. 341-345, 1997/12/01/ 1997. ISSN 0927-6513. Available at: http://www.sciencedirect.com/science/article/pii/S0927651397000825). Access at: 29th december 2017.

206 TAO, Y.;KANOH, H.;KANEKO, K. Synthesis of Mesoporous Zeolite A by Resorcinol−Formaldehyde Aerogel Templating. **Langmuir,** v. 21, n. 2, p. 504-507, 2005/01/01 2005. ISSN 0743-7463. Available at: http://dx.doi.org/10.1021/la047686j. Access at: 31st december 2017.

207 LIN, G., *et al.* Synthesis and adsorption property of zeolite FAU/LTA from lithium slag with utilization of mother liquid. **Chinese Journal of Chemical Engineering,** v. 23, n. 11, p. 1768-1773, 2015/11/01/ 2015. ISSN 1004-9541. Available at: http://www.sciencedirect.com/science/article/pii/S1004954115003560. Access at: 5th december 2020.

208 TOUNSI, H.;MSEDDI, S.;DJEMEL, S. Preparation and characterization of Na-LTA zeolite from Tunisian sand and aluminum scrap. **Physics Procedia,** v. 2, n. 3, p. 1065-1074, 2009/11/01/ 2009. ISSN 1875-3892. Available at: http://www.sciencedirect.com/science/article/pii/S1875389209001473. Access at: 7th february 2018.

209 GALLEZOT, P.;BEAUMONT, R.;BARTHOMEUF, D. Crystal structure of a dealuminated Y-type zeolite. **The Journal of Physical Chemistry,** v. 78, n. 15, p. 1550-1553, 1974/07/01 1974. ISSN 0022-3654. Available at: https://doi.org/10.1021/j100608a018. Access at: 5th december 2020.

210 HOLMBERG, B. A., *et al.* Controlling size and yield of zeolite Y nanocrystals using tetramethylammonium bromide. **Microporous and Mesoporous Materials,** v. 59, n. 1, p. 13-28, 2003/04/18/ 2003. ISSN 1387-1811. Available at: http://www.sciencedirect.com/science/article/pii/S1387181103002713. Access at: 23rd january 2018.

211 AWALA, H., *et al.* Template-free nanosized faujasite-type zeolites. **Nature Materials,** v. 14, p. 447, 01/05/online 2015. Available at: http://dx.doi.org/10.1038/nmat4173. Access at: 24th may 2018.

212 SIVALINGAM, S.;SEN, S. Swift sono-hydrothermal synthesis of pure NaX nanocrystals with improved sorption capacity from industrial resources. **Applied Surface Science,** v. 463, p. 190-196, 2019/01/01/ 2019. ISSN 0169-4332. Available at: http://www.sciencedirect.com/science/article/pii/S016943321832138X. Access at: 15th april 2020.

213 JIAO, W. Q., *et al.* Preparation of hierarchically structured Y zeolite with low Si/Al ratio and its applications in acetalization reactions. **RSC Advances,** v. 4, n. 102, p. 58596-58607, 2014. Available at: http://dx.doi.org/10.1039/C4RA11042K. Access at: 10th april 2020.

214 ZHAO, X., *et al.* Efficient assembly of hierarchical NaY aggregates by using an organosilane modified SDA. **Microporous and Mesoporous Materials,** v. 264, p. 92-103, 2018/07/01/ 2018. ISSN 1387-1811. Available at: http://www.sciencedirect.com/science/article/pii/S138718111830009X. Access at: 5th december 2020.

215 SIVALINGAM, S.;SEN, S. An ultra-fast non-conventional waste management protocol to recycle of industrial fly ash into zeolite X. **Environmental Science and Pollution Research,** v. 26, n. 34, p. 34693-34701, 2019/12/01 2019. ISSN 1614-7499. Available at: https://doi.org/10.1007/s11356-018-3664-9. Access at: 15th april 2020.

216 WANG, Y., *et al.* Synthesis, characterization and CO2 adsorption of NaA, NaX and NaZSM-5 from rice husk ash. **Solid State Sciences,** v. 86, p. 24-33, 2018/12/01/ 2018. ISSN 1293-2558. Available at: http://www.sciencedirect.com/science/article/pii/S129325581830880X. Access at: 15th april 2020.

217 RASOULI, M., *et al.* Effect of nanocrystalline zeolite Na-Y on meta-xylene separation. **Microporous and Mesoporous Materials,** v. 152, p. 141-147, 2012/04/01/ 2012. ISSN 1387-1811. Available at: http://www.sciencedirect.com/science/article/pii/S1387181111005713. Access at: 5th december 2020.

218 MORALES-PACHECO, P., *et al.* Synthesis and Structural Properties of Zeolitic Nanocrystals II: FAU-Type Zeolites. **The Journal of Physical Chemistry C,** v. 113, n. 6, p. 2247-2255, 2009/02/12 2009. ISSN 1932-7447. Available at: https://doi.org/10.1021/jp8070713. Access at: 5th december 2020.

219 MEDEIROS-COSTA, I. C., *et al.* Characterization of hierarchical zeolites: Combining adsorption/intrusion, electron microscopy, diffraction and spectroscopic techniques. **Microporous and Mesoporous Materials,** v. 287, p. 167-176, 2019/10/01/ 2019. ISSN 1387-1811. Available at: http://www.sciencedirect.com/science/article/pii/S1387181119303695. Access at: 5th december 2020.

220 OLEJNICZAK, Z., *et al.* 29Si MAS NMR and FTIR study of inorganic–organic hybrid gels. **Journal of Molecular Structure,** v. 744-747, p. 465-471, 2005/06/03/ 2005. ISSN 0022-2860. Available at: http://www.sciencedirect.com/science/article/pii/S002228600400969X. Access at: 20th april 2020.

221 WANG, Y., *et al.* A new insight into the compositional and structural control of porous clay heterostructures from the perspective of NMR and TEM. **Microporous and Mesoporous Materials,** v. 224, p. 285-293, 2016/04/01/ 2016. ISSN 1387-1811. Available at: http://www.sciencedirect.com/science/article/pii/S1387181116000044. Access at: 29th march 2020.

222 PÁLKOVÁ, H., *et al.* Laponite-derived porous clay heterostructures: II. FTIR study of the structure evolution. **Microporous and Mesoporous Materials,** v. 127, n. 3, p. 237-244, 2010/02/01/ 2010. ISSN 1387-1811. Available at: http://www.sciencedirect.com/science/article/pii/S1387181109003539. Access at: 20th april 2020.

223 YANG, H., *et al.* Novel synthesis of ordered mesoporous materials Al-MCM-41 from bentonite. **Applied Clay Science,** v. 47, n. 3, p. 351-355, 2010/02/01/ 2010. ISSN 0169-1317. Available at: http://www.sciencedirect.com/science/article/pii/S0169131709003469. Access at: 24th february 2018.

224 ENOTIADIS, A., *et al.* Synthesis and characterization of porous clay-organic heterostructures. **Journal of Sol-Gel Science and Technology,** v. 91, n. 2, p. 295-301,

2019/08/01 2019. ISSN 1573-4846. Available at: https://doi.org/10.1007/s10971-019-05042-y. Access at: 29th march 2020.

225 SANTOS, E. C. D. **Síntese e caracterização de Al-MCM-41 a partir de caulim por rota hidrotérmica e avaliação de desempenho na adsorção de azul de metileno**. 2015. 81 (Masters degree). Departamento de Química Orgânica e Inorgânica, Universidade Federal do Ceará, Fortaleza-CE, Brasil, 2015.

226 BRAHMI, L., *et al.* Catalytic Performance of Al-MCM-41 Catalyst for the Allylation of Aromatic Aldehydes with Allyltrimethylsilane: Comparison with TiCl4 as Lewis acid. **Journal of Molecular Catalysis A: Chemical,** v. 423, p. 31-40, 2016/11/01/ 2016. ISSN 1381-1169. Available at: http://www.sciencedirect.com/science/article/pii/S1381116916302175. Access at: 24th february 2018.

227 DE MIRANDA, R. P. R., *et al.* New Routes Study for Synthesis of Molecular Sieves Type Al-MCM-41 and Al-SBA-15. **Materials Science Forum,** v. 727-728, p. 1222-1227, 2012. ISSN 1662-9752. Available at: http://www.scientific.net/MSF.727-728.1222. Access at: 24th february 2018.

228 HAO, Q.-Q., *et al.* Porous Montmorillonite Heterostructures Directed by a Single Alkyl Ammonium Template for Controlling the Product Distribution of Fischer–Tropsch Synthesis over Cobalt. **Chemistry of Materials,** v. 24, n. 6, p. 972-974, 2012/03/27 2012. ISSN 0897-4756. Available at: https://doi.org/10.1021/cm203872m. Access at: 29th march 2020.

229 BARAKAN, S.;AGHAZADEH, V. Synthesis and characterization of hierarchical porous clay heterostructure from Al, Fe -pillared nano-bentonite using microwave and ultrasonic techniques. **Microporous and Mesoporous Materials,** v. 278, p. 138-148, 2019/04/01/ 2019. ISSN 1387-1811. Available at: http://www.sciencedirect.com/science/article/pii/S1387181118306103. Access at: 16th june 2020.

230 KOOLI, F., *et al.* Preparation and catalytic activities of porous clay heterostructures from aluminium-intercalated clays: effect of Al content. **Clay Minerals,** v. 52, n. 4, p. 521-535, 2017. ISSN 0009-8558. Available at: https://www.cambridge.org/core/article/preparation-and-catalytic-activities-of-porous-clay-heterostructures-from-aluminiumintercalated-clays-effect-of-al-content/64CABFCF4912BCC8B69D6546B86CD52A. Access at: 29th march 2020.

231 WANG, Y., *et al.* The non-micellar template model for porous clay heterostructures: A perspective from the layer charge of base clay. **Applied Clay Science,** v. 116-117, p. 102-110, 2015/11/01/ 2015. ISSN 0169-1317. Available at: http://www.sciencedirect.com/science/article/pii/S0169131715300867. Access at: 16th june 2020.

232 LAI, C., *et al.* Nanocomposite films based on TEMPO-mediated oxidized bacterial cellulose and chitosan. **Cellulose,** v. 21, n. 4, p. 2757-2772, August 01 2014. ISSN 1572-882X. Available at: https://doi.org/10.1007/s10570-014-0330-3. Access at: 22nd august 2019.

233 MEZA-CONTRERAS, J. C., *et al.* XRD and solid state 13C-NMR evaluation of the crystallinity enhancement of 13C-labeled bacterial cellulose biosynthesized by Komagataeibacter xylinus under different stimuli: A comparative strategy of analyses. **Carbohydrate Research,** v. 461, p. 51-59, 2018/05/22/ 2018. ISSN 0008-6215. Available at: http://www.sciencedirect.com/science/article/pii/S0008621518300089. Access at: 5th december 2020.

234 XUE, Z., *et al.* Synthesis and characterization of ordered mesoporous zeolite LTA with high ion exchange ability. **Journal of Materials Chemistry,** v. 22, n. 6, p. 2532-2538, 2012. ISSN 0959-9428. Available at: http://dx.doi.org/10.1039/C1JM14740D. Access at: 5th december 2020.

235 GREISER, S., *et al.* Differentiation of the solid-state NMR signals of gel, zeolite phases and water species in geopolymer-zeolite composites. **Ceramics International,** v. 43, n. 2, p. 2202-2208, 2017/02/01/ 2017. ISSN 0272-8842. Available at: http://www.sciencedirect.com/science/article/pii/S0272884216320028. Access at: 5th december 2020.

236 ETIM, U. J., *et al.* Mechanistic insights into structural and surface variations in Y-type zeolites upon interaction with binders. **Applied Catalysis A: General,** v. 571, p. 137-149, 2019/02/05/ 2019. ISSN 0926-860X. Available at: http://www.sciencedirect.com/science/article/pii/S0926860X18306094. Access at: 5th december 2020.

237 WANG, G., *et al.* Synthesis of highly regular mesoporous Al-MCM-41 from metakaolin. **Applied Clay Science,** v. 44, n. 1, p. 185-188, 2009/04/01/ 2009. ISSN 0169-1317. Available at: http://www.sciencedirect.com/science/article/pii/S0169131708002834. Access at: 24th february 2018.

238 VOISIN, H., *et al.* Nanocellulose-Based Materials for Water Purification. **Nanomaterials,** v. 7, n. 3, p. 57-75, 2017.

239 MAUTNER, A., *et al.* Rapid Water Softening with TEMPO-Oxidized/Phosphorylated Nanopapers. **Nanomaterials,** v. 9, n. 2, p. 136-154, 2019.

240 WEN, J.;DONG, H.;ZENG, G. Application of zeolite in removing salinity/sodicity from wastewater: A review of mechanisms, challenges and opportunities. **Journal of Cleaner Production,** v. 197, p. 1435-1446, 2018/10/01/ 2018. ISSN 0959-6526. Available at: http://www.sciencedirect.com/science/article/pii/S0959652618319292. Access at: 15th april 2020.

241 MASTERS, A. F.;MASCHMEYER, T. Zeolites – From curiosity to cornerstone. **Microporous and Mesoporous Materials,** v. 142, n. 2, p. 423-438, 2011/07/01/ 2011. ISSN 1387-1811. Available at: http://www.sciencedirect.com/science/article/pii/S1387181110004592. Access at: 5th may 2020.

242 GUYO, U.;PHIRI, L. Y.;CHIGONDO, F. Application of Central Composite Design in the Adsorption of Ca(II) on Metakaolin Zeolite. **Journal of Chemistry,** v. 2017, p.

7025073, 2017/08/10 2017. ISSN 2090-9063. Available at: https://doi.org/10.1155/2017/7025073. Access at: 5th may 2020.

243 GUO, X.;NAVROTSKY, A. Hydration dynamics in zeolite A – An X-ray diffraction and infrared spectroscopic study. **Microporous and Mesoporous Materials,** v. 268, p. 197-201, 2018/09/15/ 2018. ISSN 1387-1811. Available at: http://www.sciencedirect.com/science/article/pii/S1387181118302257. Access at: 29th june 2020.

244 FISCHER, R. X., *et al.* Crystal structure and morphology of fully hydrated zeolite Na-A. **Zeitschrift für Kristallographie - Crystalline Materials,** v. 227, n. 7, p. 438, 2012. ISSN 2194-4946. Available at: https://www.degruyter.com/view/journals/zkri/227/7/article-p438.xml. Access at: 29th june 2020.

245 MOREIRA, J. C., *et al.* Evaluation of different reaction systems to obtain zeolite 4A via reverse microemulsion. **Microporous and Mesoporous Materials,** v. 279, p. 262-270, 2019/05/01/ 2019. ISSN 1387-1811. Available at: http://www.sciencedirect.com/science/article/pii/S1387181118306759. Access at: 5th december 2020.

246 SILVA FILHO, S. H., *et al.* LTA zeolite synthesis using natural materials and its evaluation by Green Star methodology. **SN Applied Sciences,** v. 2, n. 3, p. 344, 2020/02/05 2020. ISSN 2523-3971. Available at: https://doi.org/10.1007/s42452-020-2162-0. Access at: 23rd october 2020.

247 AMONI, B. C., *et al.* A method for NaA zeolite synthesis from coal fly ash and its application in warm mix asphalt. **Road Materials and Pavement Design,** v. 20, n. sup2, p. S558-S567, 2019/07/31 2019. ISSN 1468-0629. Available at: https://doi.org/10.1080/14680629.2019.1633766. Access at: 23rd october 2020.

248 ZHANG, C., *et al.* TPABr-grafted MWCNT as bifunctional template to synthesize hierarchical ZSM-5 zeolite. **Materials Letters,** v. 197, p. 111-114, 2017/06/15/ 2017. ISSN 0167-577X. Available at: http://www.sciencedirect.com/science/article/pii/S0167577X17304202. Access at: 20th june 2020.

249 XU, D.;CHE, S.;TERASAKI, O. A design concept of amphiphilic molecules for directing hierarchical porous zeolite. **New Journal of Chemistry,** v. 40, n. 5, p. 3982-3992, 2016. ISSN 1144-0546. Available at: http://dx.doi.org/10.1039/C5NJ02949J. Access at: 14th february 2018.

250 MINTOVA, S.;GILSON, J.-P.;VALTCHEV, V. Advances in nanosized zeolites. **Nanoscale,** v. 5, n. 15, p. 6693-6703, 2013. ISSN 2040-3364. Available at: http://dx.doi.org/10.1039/C3NR01629C. Access at: 6th september 2017.

251 VENKATESAN, C., *et al.* Facile synthesis of mesoporous zeolite Y using seed gel and amphiphilic organosilane. **Microporous and Mesoporous Materials,** v. 288, p. 109579, 2019/11/01/ 2019. ISSN 1387-1811. Available at:

http://www.sciencedirect.com/science/article/pii/S1387181119304366. Access at: 13rd april 2020.

252 CHEN, H., *et al.* Organosilane Surfactant-Directed Synthesis of Hierarchical ZSM-5 Zeolites with Improved Catalytic Performance in Methanol-to-Propylene Reaction. **Industrial & Engineering Chemistry Research,** v. 57, n. 32, p. 10956-10966, 2018/08/15 2018. ISSN 0888-5885. Available at: https://doi.org/10.1021/acs.iecr.8b00849. Access at: 17th october 2019.

253 HASAN, F. A., *et al.* Zeolite monoliths with hierarchical designed pore network structure: Synthesis and performance. **Chemical Engineering Journal,** v. 223, p. 48-58, 2013/05/01/ 2013. ISSN 1385-8947. Available at: http://www.sciencedirect.com/science/article/pii/S1385894713002751. Access at: 7th february 2018.

254 VAREDA, J. P.;DURÃES, L. Efficient adsorption of multiple heavy metals with tailored silica aerogel-like materials. **Environmental Technology,** v. 40, n. 4, p. 529-541, 2019/02/10 2019. ISSN 0959-3330. Available at: https://doi.org/10.1080/09593330.2017.1397766. Access at: 29th april 2020.

255 MENG, Q., *et al.* Zeolite A synthesized from alkaline assisted pre-activated halloysite for efficient heavy metal removal in polluted river water and industrial wastewater. **Journal of Environmental Sciences,** v. 56, p. 254-262, 2017/06/01/ 2017. ISSN 1001-0742. Available at: http://www.sciencedirect.com/science/article/pii/S1001074216310075. Access at: 15th april 2020.

256 ESAIFAN, M., *et al.* Synthesis of Hydroxy-Sodalite/Cancrinite Zeolites from Calcite-Bearing Kaolin for the Removal of Heavy Metal Ions in Aqueous Media. **Minerals,** v. 9, n. 8, p. 484-497, 2019.

257 NIGHTINGALE, E. R. Phenomenological Theory of Ion Solvation. Effective Radii of Hydrated Ions. **The Journal of Physical Chemistry,** v. 63, n. 9, p. 1381-1387, 1959/09/01 1959. ISSN 0022-3654. Available at: https://doi.org/10.1021/j150579a011. Access at: 29th april 2020.

258 OLIVERA, S., *et al.* Potential applications of cellulose and chitosan nanoparticles/composites in wastewater treatment: A review. **Carbohydrate Polymers,** v. 153, p. 600-618, 2016/11/20/ 2016. ISSN 0144-8617. Available at: http://www.sciencedirect.com/science/article/pii/S0144861716309523. Access at: 29th april 2020.

259 WERNERT, V., *et al.* Cancrinite synthesis from natural kaolinite by high pressure hydrothermal method: Application to the removal of Cd^{2+} and Pb^{2+} from water. **Microporous and Mesoporous Materials,** v. 301, p. 110209, 2020/07/01/ 2020. ISSN 1387-1811. Available at: http://www.sciencedirect.com/science/article/pii/S1387181120302122. Access at: 6th may 2020.

260 KHAMKEAW, A., *et al.* Synthesis of mesoporous MFI zeolite via bacterial cellulose-derived carbon templating for fast adsorption of formaldehyde. **Journal of Hazardous**

Materials, v. 384, p. 121161, 2020/02/15/ 2020. ISSN 0304-3894. Available at: http://www.sciencedirect.com/science/article/pii/S030438941931115X. Access at: 6th may 2020.

261 NAKAMOTO, K.;OHSHIRO, M.;KOBAYASHI, T. Mordenite zeolite—Polyethersulfone composite fibers developed for decontamination of heavy metal ions. **Journal of Environmental Chemical Engineering,** v. 5, n. 1, p. 513-525, 2017/02/01/ 2017. ISSN 2213-3437. Available at: http://www.sciencedirect.com/science/article/pii/S2213343716304754. Access at: 6th may 2020.

262 HONG, M., *et al.* Heavy metal adsorption with zeolites: The role of hierarchical pore architecture. **Chemical Engineering Journal,** v. 359, p. 363-372, 2019/03/01/ 2019. ISSN 1385-8947. Available at: http://www.sciencedirect.com/science/article/pii/S1385894718323210. Access at: 6th may 2020.

263 LI, J., *et al.* Efficient recovery of Cu(II) by LTA-zeolites with hierarchical pores and their resource utilization in electrochemical denitrification: Environmentally friendly design and reutilization of waste in water. **Journal of Hazardous Materials,** v. 394, p. 122554, 2020/07/15/ 2020. ISSN 0304-3894. Available at: http://www.sciencedirect.com/science/article/pii/S0304389420305434. Access at: 6th may 2020.

264 ISOBE, N., *et al.* TEMPO-oxidized cellulose hydrogel as a high-capacity and reusable heavy metal ion adsorbent. **Journal of Hazardous Materials,** v. 260, p. 195-201, 2013/09/15/ 2013. ISSN 0304-3894. Available at: http://www.sciencedirect.com/science/article/pii/S0304389413003403. Access at: 5th may 2020.

265 YU, X., *et al.* Adsorption of heavy metal ions from aqueous solution by carboxylated cellulose nanocrystals. **Journal of Environmental Sciences,** v. 25, n. 5, p. 933-943, 2013/05/01/ 2013. ISSN 1001-0742. Available at: http://www.sciencedirect.com/science/article/pii/S1001074212601454. Access at: 5th may 2020.

266 LI, C., *et al.* Highly efficient and sustainable carboxylated cellulose filters for removal of cationic dyes/heavy metals ions. **Chemical Engineering Journal,** v. 389, p. 123458, 2020/06/01/ 2020. ISSN 1385-8947. Available at: http://www.sciencedirect.com/science/article/pii/S1385894719328712. Access at: 5th may 2020.

267 JOSEPH, I. V.;TOSHEVA, L.;DOYLE, A. M. Simultaneous removal of Cd(II), Co(II), Cu(II), Pb(II), and Zn(II) ions from aqueous solutions via adsorption on FAU-type zeolites prepared from coal fly ash. **Journal of Environmental Chemical Engineering,** v. 8, n. 4, p. 103895, 2020/08/01/ 2020. ISSN 2213-3437. Available at: http://www.sciencedirect.com/science/article/pii/S2213343720302438. Access at: 6th may 2020.